Journal of Geophysical Research

The continuation of

[Ter]restrial Magnetism and Atmospheric Electricity (1896-1948)

An International Quarterly

[Vol]ume 62 March, 1957 Number 1

CONTENTS

(*Contents concluded on outside back cover*)

Published at

The William Byrd Press, Inc.

P. O. Box 2-W, Sherwood Ave. and Durham St.

RICHMOND 5, VIRGINIA

Address all correspondence to

Journal of Geophysical Research

5241 Broad Branch Road, Northwest

WASHINGTON 15, D.C., U.S.A.

[S]ix Dollars a Year Single Numbers, Two Dollars

JOURNAL OF GEOPHYSICAL RESEARCH

The continuation of

Terrestrial Magnetism and Atmospheric Electricity (1896-1948)

An International Quarterly

Founded 1896 by L. A. BAUER *Continued 1928-1948 by* J. A. FLEMING

Fields of Interest

Terrestrial Magnetism
Atmospheric Electricity
The Ionosphere
Solar and Terrestrial Relationships
Aurora, Night Sky, and Zodiacal Light
The Ozone Layer
Meteorology of Highest Atmospheric Levels
The Constitution and Physical States of the Upper Atmosphere
Special Investigations of the Earth's Crust and Interior, including experimental seismic waves, physics of the deep ocean and ocean bottom, physics in geology
And similar topics

This Journal serves the interests of investigators concerned with terrestrial magnetism and electricity, the upper atmosphere, the earth's crust and interior by presenting papers of new analysis and interpretation or new experimental or observational approach, and contributions to international collaboration. It is not in a position to print, primarily for archive purposes, extensive tables of data from observatories or surveys, the significance of which has not been analyzed.

Forward *manuscripts* to one of the Associate Editors, or to the editorial office of the Journal at 5241 Broad Branch Road, Northwest, Washington 15, D.C., U.S.A. It is preferred that manuscripts be submitted in English, but communications in French, German, Italian, or Spanish are also acceptable. A brief abstract, preferably in English, must accompany each manuscript. A *publication charge* of $8 per page will be billed by the Editor to the institution which sponsors the work of any author; private individuals are not assessed page charges. Manuscripts from outside the United States are invited, and should not be withheld or delayed because of currency restrictions or other special difficulties relating to page charges. Costs of publications are roughly twice the total income from page charges and subscriptions, and are met by subsidies from the Carnegie Institution of Washington and international and private sources.

Back issues and *reprints* are handled by the Editorial Office, 5241 Broad Branch Road, N.W., Washington 15, D.C., U.S.A.

Subscriptions are handled by the Editorial Office, 5241 Broad Branch Road, N.W., Washington 15, D.C., U.S.A.

Second-class mail privileges authorized at Richmond, Virginia

Journal of

GEOPHYSICAL RESEARCH

The continuation of

Terrestrial Magnetism and Atmospheric Electricity

OLUME 62 MARCH, 1957 No. 1

A STATISTICAL ANALYSIS OF MAGNETIC PROFILES*

BY P. H. SERSON AND W. L. W. HANNAFORD

The Dominion Observatory, Department of Mines and Technical Surveys, Ottawa, Canada

(Received October 11, 1956)

ABSTRACT

Autocorrelation functions are computed for profiles of D, H, and Z obtained by a three-component airborne magnetometer over Western Canada and over the Atlantic east of Bermuda. The accuracy of magnetic charts is computed as a function of the distance over which interpolation is made. The accuracy is not significantly increased by smoothing. A comparison with the autocorrelation functions of simple models indicates that most anomalies originate in a thin layer 11 km below sea level under the continent and 6.5 km below sea level under the ocean. Intense magnetization of the rocks (0.005 to 0.05 cgs) is indicated.

INTRODUCTION

A magnetic survey of the prairie provinces of Canada was made in 1955 by ans of the Dominion Observatory's three-component airborne magnetometer. velve lines were flown along parallels of latitude one degree apart, covering the a from latitude 49° to 60° north and longitude 95° to 120° west. In addition, ree north-south lines were flown at longitudes 97°, 103°, and 115° west. All ghts were made at an altitude of 3 km above sea level.

The three-component magnetometer presents its observations in two forms: continuous strip-chart recordings of D, H, and Z, and as average values of D,

*Published by permission of the Deputy Minister, Department of Mines and Technical rveys, Ottawa, Canada.

H, and Z automatically computed over successive 5-minute (30-km) segments of the flight path. When the 30-km averages were plotted on charts, they proved unexpectedly difficult to contour. In spite of the smoothing effect of the altitude and the 30-km averaging, irregularities of several hundred gammas occurred frequently in all parts of the region surveyed. It was apparent that if the profiles were smoothed enough to remove these irregularities, the resulting contours could have been obtained just as well from flight lines spaced several times farther apart. The line spacing of 110 km was perhaps not a good choice. It was too coarse to map most of the anomalies, and finer than necessary to map the smooth field.

Several questions naturally arise:

(*a*) How closely must observations be spaced to obtain a given accuracy of mapping?

(*b*) Does smoothing of the observations significantly increase the accuracy of the charts?

(*c*) If the relation between accuracy of charts and spacing of observations is not linear, what accuracy can be obtained in smoothed charts with an economically reasonable survey?

(*d*) What can be deduced concerning the origin of the anomalies?

The first part of this paper describes a statistical analysis of profiles of D, H, and Z obtained in Western Canada. A comparison is made with profiles obtained over the Atlantic Ocean east of Bermuda. In the second part, these results are used to compute interpolation errors in magnetic charts as a function of the spacing of observations and methods of smoothing. In the third part, it is shown that simple models will produce profiles with similar statistical properties to those observed over the continent and over the sea.

THE AUTOCORRELATION OF MAGNETIC PROFILES

The magnetic profiles obtained in Western Canada resemble gentle curves, with wavelengths of a few thousand kilometers, on which are superimposed irregular fluctuations of a much shorter wavelength, which we designate as noise. The noise appears remarkably constant in amplitude and frequency range over the whole area in spite of large differences in surface geology. Since this noise is obviously the largest source of error in magnetic charts, the analysis of chart errors is based on its statistical properties.

To analyse the noise, it was first separated from the smooth field. For simplicity, the smooth field was assumed to be a linear function of horizontal distance. In Western Canada, this assumption worked well for D and H, whose profiles were generally straight, but caused some trouble in the case of Z, where the profiles had a definite curvature.

The autocorrelation function $R(\tau)$ of $H(x)$, a function of x, is defined by

$$\left.\begin{aligned} R(\tau) &= \lim_{l\to\infty}\frac{1}{2l}\int_{-l}^{l} H(x)\cdot H(x+\tau)\,dx \\ &= \overline{H(x)\cdot H(x+\tau)} \end{aligned}\right\}\quad\ldots\ldots\ldots\ldots\ldots\ldots(1)$$

where the bar indicates an average taken over x [see 1 of "References" at end of

aper]. In the present case, x represents distance measured along the surface of e earth, and $H(x)$ is a component of the earth's magnetic field.

Another function, containing the same information as the autocorrelation funcon but whose physical meaning is perhaps more easily understood, is $\Delta(\tau)$, the ot-mean-square change in the component $H(x)$ over the interval τ. It is related the autocorrelation function by the following equation:

$$\left.\begin{aligned}\Delta^2(\tau) &= \overline{[H(x+\tau) - H(x)]^2} = \overline{H^2(x+\tau)} - \overline{2H(x+\tau)H(x)} + \overline{H^2(x)} \\ &= 2[R(0) - R(\tau)]\end{aligned}\right\} \quad \text{..(2)}$$

Calculation of autocorrelation functions from experimental data is extremely dious, and some short-cuts were used. The 30-km average values of the compoents had already been plotted as profiles. A straight line was drawn through each ofile, joining the mean of the first half of the plotted points with the mean of the cond half. The departures of the 30-km averages from the straight line were bulated and the autocorrelation function computed in the usual way for $\tau = 0$, , 60, $\cdots$, 270 km.

The autocorrelation function $R(\tau)$ of the instantaneous values will be equal the autocorrelation function $R_a(\tau)$ of the 30-km averages for large values of τ, suming that there are no narrow peaks in $R(\tau)$ for τ large. To obtain $R(\tau)$ for < 60 km, additional information must be derived from the continuous records the strip-chart recorders.

A graticule graduated in (gammas)^2 was laid over the continuous records, owing for the slope of the linear approximation to the profile, and the squared anges over 1, 2, 3, and 4 minutes were read. The averages of these readings are (τ) for $\tau = 6$, 12, 18, and 24 km. By combining these values with the function (τ) already determined, points on the curve $R(\tau)$ were obtained at $\tau = 0$, 6, 12, , and 24 km.

Figure 1 shows the average of the autocorrelation functions obtained in D, and Z from three north-south flights in Western Canada totaling 3,600 km. ere appeared to be no significant difference in the results from different flights, d no systematic variation from north to south, although H varied by a factor three over the area surveyed. In D and H, there is little correlation between ues more than 50 km apart. In Z, the correlation at large values of τ is due to poor fitting of the straight-line approximation to the curved profiles. The -frequency cut-off shows more clearly in the functions $\Delta(\tau)$ plotted in the lower rt of Figure 1. A few east-west flights in Western Canada were also analysed. tocorrelation functions very similar to those of Figure 1 were obtained.

An interesting point is that the autocorrelation function of H in Figure 1 initely goes negative, indicating a maximum in the spectrum of the anomaly d at a wavelength of about 200 km. This would seem to imply a periodicity in geology—a conclusion which is not justified, as will be seen later.

Figure 2 shows the autocorrelation functions and r.m.s. changes in H and Z ained from two east-west flights totaling 2,400 km over the Atlantic Ocean t of Bermuda (latitude 31° to 35° north, longitude 48° to 65° west). Here the rofiles were quite straight, while the H profiles showed a slight curvature.

A comparison of Figures 1 and 2 shows that the main difference in the anomaly

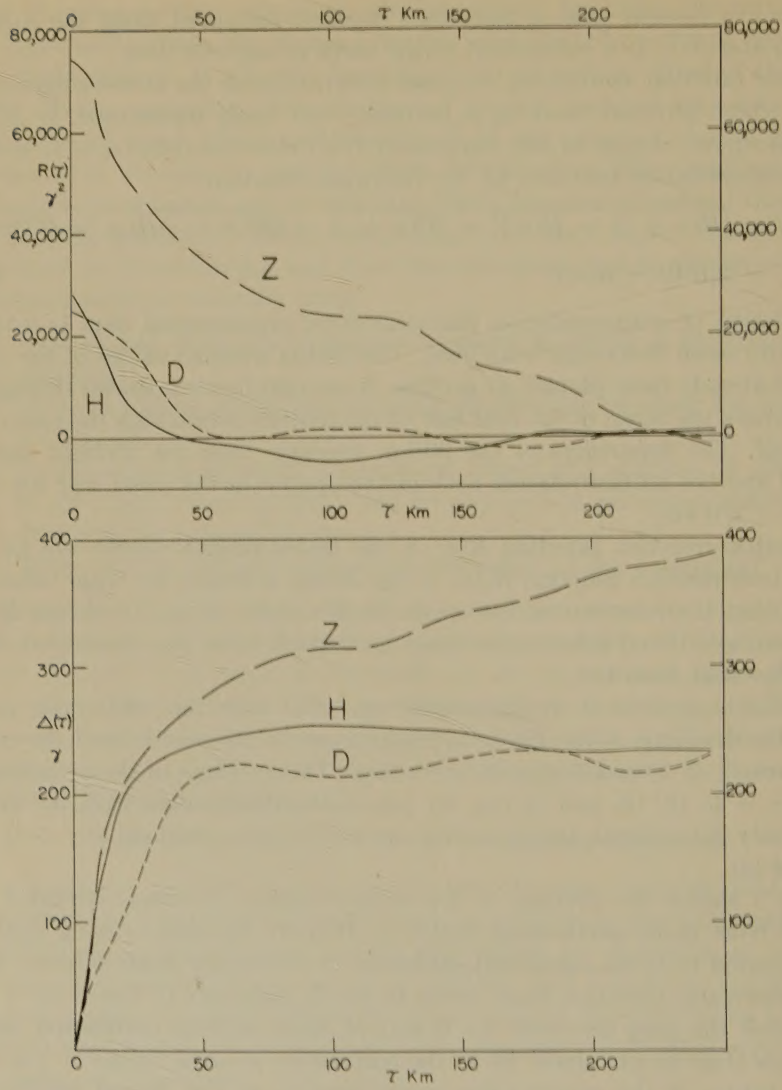

FIG. 1—Autocorrelation functions of magnetic profiles from three north-south flights in Western Canada (*above*), and corresponding r.m.s. changes in components over distance τ (*below*)

fields is in amplitude, the anomalies over the ocean being about one-third as large as those over the continent. A surprising feature, in view of the great depth of the Atlantic east of Bermuda (6 km), is that the wavelengths of anomalies observed over the ocean tend to be shorter than over the continent.

INTERPOLATION ERRORS IN MAGNETIC CHARTS

The root-mean-square error of a magnetic chart will now be computed as a function of the geographical density of the observations on which the chart is based. Root-mean-square error is chosen as a criterion of accuracy for the usual

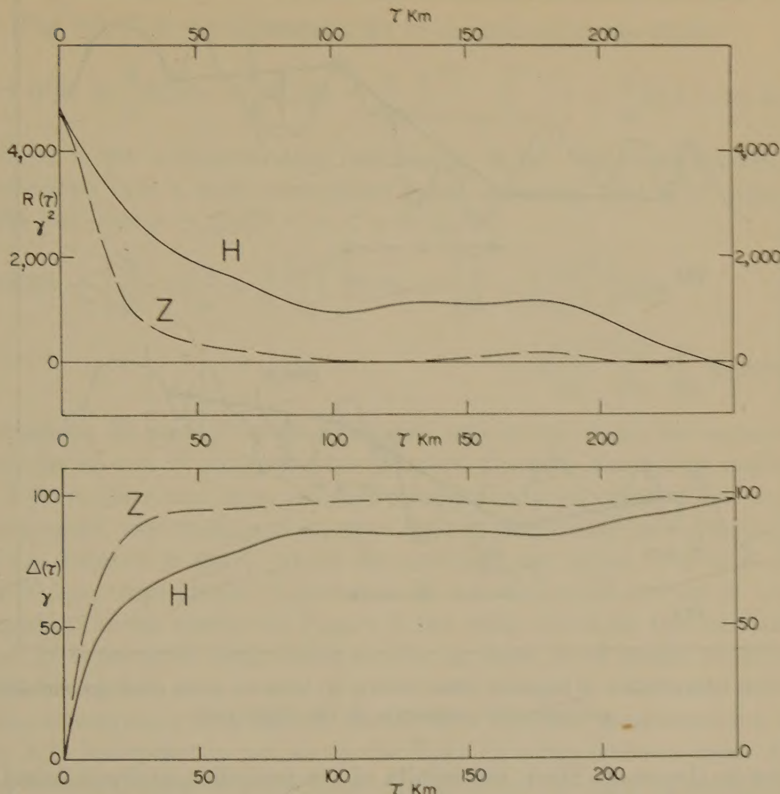

FIG. 2—Autocorrelation functions of magnetic profiles from two east-west flights over the Atlantic east of Bermuda (*above*), and corresponding r.m.s. changes in components over distance τ (*below*)

reasons—that it is easily calculated, and that n small errors of magnitude ϵ are less important than one large error of magnitude $n\epsilon$.

First, consider linear interpolation between observations with no smoothing. The component $H(x)$ has been measured at points spaced at equal intervals p along the x-axis. What is the r.m.s. error of the representation obtained by interpolating between successive observations [Fig. 3(a)]?

The interpolated representation of $H(x)$ is

$$\left(1 - \frac{\tau}{p}\right) H(np) + \frac{\tau}{p} H(np + p)$$

where n is an integer determined by $np \leq x \leq np + p$, and

$$\tau = x - np \qquad (3)$$

The error is

$$H(np + \tau) - \left(1 - \frac{\tau}{p}\right) H(np) - \frac{\tau}{p} H(np + p) \qquad (4)$$

If $H(x)$ is a linear function of x, the error is of course zero. If $H(x)$ is the sum of a linear function of x and an irregular function of x, only the irregular part

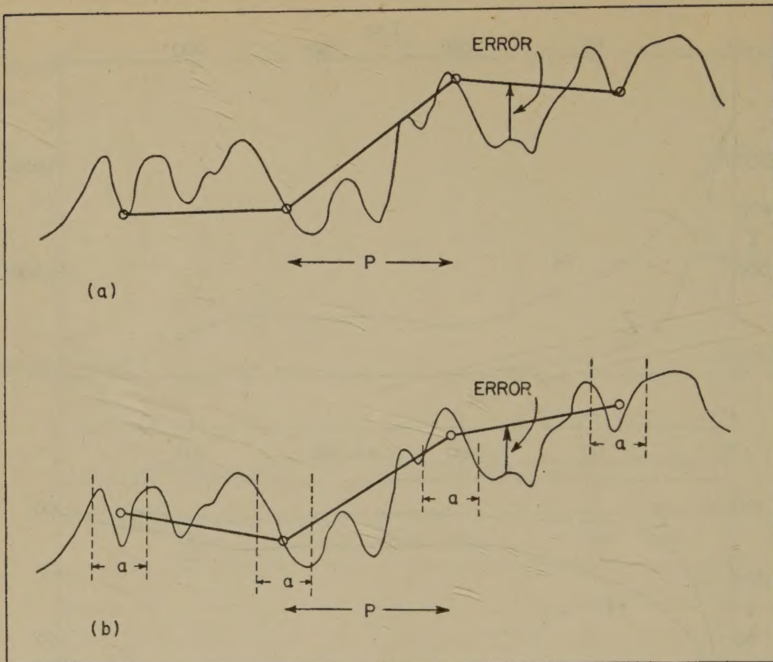

Fig. 3—Linear interpolation of magnetic observations (a) between point readings and (b) between averages over segments of the flight path

contributes to the error. Thus, the results of the preceding analysis based on the departure of the profile from a straight line are sufficient to calculate interpolation errors.

The average square error for a given τ and all values of n is found by squaring (4) and applying (1), giving

$$2\left[1 - \frac{\tau}{p} + \left(\frac{\tau}{p}\right)^2\right]R(0) + 2\left[\frac{\tau}{p} - \left(\frac{\tau}{p}\right)^2\right]R(p) - 2\left[\left(1 - \frac{\tau}{p}\right)R(\tau) + \frac{\tau}{p}R(\tau - p)\right] \quad (5)$$

The mean-square error $\epsilon^2(p)$ for all x is obtained by averaging (5) over all τ from 0 to p:

$$\left.\begin{aligned}\epsilon^2(p) &= 2\left(1 - \frac{1}{2} + \frac{1}{3}\right)R(0) + 2\left(\frac{1}{2} - \frac{1}{3}\right)R(p) \\ &\quad - \frac{2}{p}\int_0^p \left(1 - \frac{\tau}{p}\right)R(\tau)\,d\tau - \frac{2}{p}\int_0^p \frac{\tau}{p}R(\tau - p)\,d\tau \\ &= \frac{5}{3}R(0) + \frac{1}{3}R(p) - \frac{4}{p}\int_0^p \left(1 - \frac{\tau}{p}\right)R(\tau)\,d\tau\end{aligned}\right\} \quad (6)$$

Instead of interpolating between observations, interpolation may be made between points representing the mean of several observations. Carrying this procedure to the limit, the component $H(x)$ is averaged over intervals of x of length a to give a smoothed function $H_a(x)$. What is the r.m.s. error of the representation obtained by linearly interpolating between averages centered at points a distance

apart [Fig. 3(*b*)]? A calculation similar to the preceding one gives

$$\epsilon^2(p) = R(0) + \frac{2}{3}R_a(0) + \frac{1}{3}R_a(p) - \frac{4}{ap}\int_{\sigma=-a/2}^{a/2}\int_{\tau=0}^{p}\left(1 - \frac{\tau}{p}\right)R(\tau - \sigma)\,\mathrm{d}\sigma\,\mathrm{d}\tau \quad \ldots(7)$$

here $R_a(\tau)$ is the autocorrelation function of $H_a(x)$. For computation, (7) can e transformed into a more convenient form, assuming that $R(\tau)$ approximates straight line over $p - (a/2) < \tau < p + (a/2)$

$$\left.\begin{aligned}(p) \approx R(0) + \left[\frac{2}{3} - 2\frac{a}{p} + \frac{1}{2}\left(\frac{a}{p}\right)^2\right]R_a(0) + \left[\frac{1}{3} - \frac{1}{2}\left(\frac{a}{p}\right)^2\right]R_a(p)\\ - 4\left(\frac{a}{p}\right)^2\sum_{m=1}^{p/a-1}\sum_{r=1}^{m}R_a(ra)\end{aligned}\right\} \ldots(8)$$

Expressions (6) and (8) were evaluated numerically from the autocorrelation inctions for H and Z obtained over Western Canada. The curves marked (*a*) in igure 4 show the r.m.s. error for interpolation between observations at points a istance p apart. Curves (*b*) and (*c*) show the r.m.s. errors for interpolation between verages a distance p apart, where the averages are taken over intervals of 30 m and 90 km, respectively. Expression (6) was also evaluated for H and Z east Bermuda. Curves similar to Figure 4 but with one-third the amplitude were btained. It is assumed that curves similar to those for H would be obtained for eclination.

In the construction of magnetic charts from airborne measurements, the main roblem is in interpolation not along the flight lines but between them. For interolation between point observations, the direction of flight is immaterial, and quation (6) still applies. Equation (8), however, is based on a special case. When ne averaging and the interpolation are performed in the same direction, some or ll of the points at which the error is computed are included in the formation of the verages. The curves (*b*) and (*c*) of Figure 4 should be regarded as the lower limit f the r.m.s. error. In any case, it appears safe to conclude that the smoothing of bservations is not likely to increase significantly the accuracy of a magnetic hart, and, in fact, decreases it if the smoothing interval exceeds the interpolation terval. There may, of course, be other reasons for smoothing—to make the chart ore legible, to avoid giving an impression of great accuracy, or to reduce the fect of errors in measurement, errors in navigation, or magnetic disturbances.

Root-mean-square chart-errors were also computed for the case where obserations are smoothed by taking means weighted toward the centre of the interval. he results were hardly distinguishable from those shown in Figure 4, as would be xpected from the regularity of the autocorrelation functions. There are more laborate interpolation techniques, such as fitting algebraic or trigonometric ries to the observations, with or without satisfying the equations of potential heory. In the majority of cases, the most important source of error in magnetic harts is not in the errors of observation but in the lack of knowledge of anomalies etween the points of observation. If the purpose of magnetic charts is to show ne earth's field as it is rather than as one would like it to be, the use of methods ore elaborate than the simplest linear smoothing and interpolation would seem be unjustified.

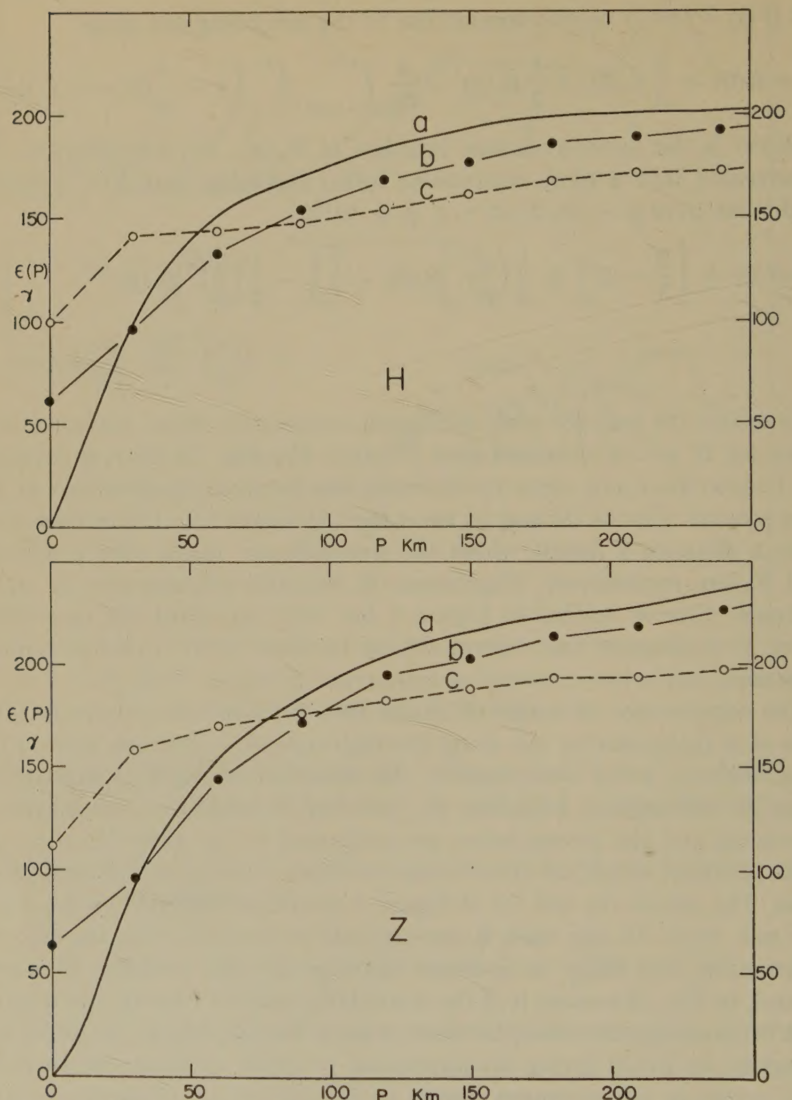

FIG. 4—R.M.S. errors in magnetic charts of Western Canada for linear interpolation over interval p (*a*) between point observations; (*b*) between averages over 30 km; (*c*) between averages over 90 km

The result of the investigation can be summarized as follows. When, as is generally the case, anomalies are the main source of error in magnetic charts, simple linear interpolation between observations is likely to produce as accurate a chart as any other method. Smoothing of observations does not increase the accuracy appreciably, and may reduce it. The root-mean-square error of a chart is proportional to the distance between observations if that distance is less than 50 km. The error increases more slowly as the distance between observations increases from 50 to 250 km. The r.m.s. errors of charts based on observations 50 and 250 km apart are 150 gammas and 230 gammas, respectively, over the conti-

nent and 50 gammas and 80 gammas, respectively, over the ocean. Errors tend to be larger in the vertical component than in the horizontal (by a factor of $\sqrt{2}$ for widely spaced observations, as will be shown).

It is concluded that an airborne survey with lines 50 km apart, costing five times as much as one with lines 250 km apart, will produce charts only 35 per cent more accurate. In the case of a chart based on a ground survey, where the cost will vary inversely as the square of the separation, the 35 per cent increase in accuracy would increase the cost 25 times. These conclusions, of course, are based on observations made at an altitude of 3 km, but as will be seen in the next section, there is reason to believe that similar results would be obtained on the ground.

THE AUTOCORRELATION OF MAGNETIC PROFILES OF MODELS

The autocorrelation functions of Figures 1 and 2 are similar in shape to the autocorrelation functions of series formed by subjecting random numbers to various smoothing processes [2]. This suggests the possibility of fitting to the observed functions theoretical functions based on a random arrangement of magnetic poles. In the present case, the smoothing arises from the fact that the anomalies are observed at some distance from their sources. The objection that there is, in general, no unique solution for an observed magnetic anomaly applies still more strongly to the interpretation of the autocorrelation functions of anomalies. In view of the remarkable uniformity of the autocorrelation over a large area, however, it seems likely that useful results would be obtained in an investigation of the simplest random models.

Consider first a random distribution of magnetic poles in a thin horizontal layer at a constant depth z beneath the aircraft. The layer extends to infinity horizontally. In Cartesian coordinates, with the origin at the aircraft (Fig. 5), a

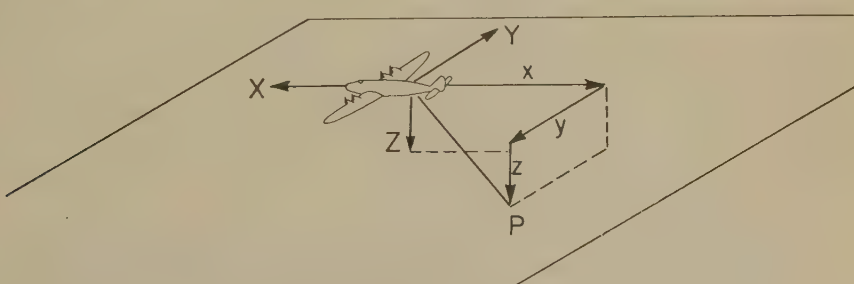

FIG. 5—Geometry of magnetic models

magnetic pole of strength m located at $P(x, y, z)$ produces at the aircraft anomalies mA_X, mA_Y, and mA_Z in the X, Y, and Z components, respectively, where

$$\left.\begin{aligned} A_X &= \frac{x}{(x^2+y^2+z^2)^{3/2}} \\ A_Y &= \frac{y}{(x^2+y^2+z^2)^{3/2}} \\ A_Z &= \frac{z}{(x^2+y^2+z^2)^{3/2}} \end{aligned}\right\} \qquad (9)$$

As the aircraft moves along the x-axis, this pole will make a contribution to the X autocorrelation function of

$$\Delta R_X(\tau) = \lim_{l \to \infty} \frac{m^2}{2l} \int_{-l}^{l} A_X(x, y, z) A_X(x + \tau, y, z)\, dx \qquad (10)$$

Because the magnetic poles are assumed to be distributed at random, there will be no correlation between the anomalies due to different poles. More precisely, any correlation which exists—for example, when all anomalies are positive—will be independent of τ, and could not be detected by the methods used to derive the experimental autocorrelation functions. Thus, the autocorrelation function $R_x(\tau)$ is simply the sum of the contributions $\Delta R_x(\tau)$ due to the magnetic poles scattered over the infinite plane. If σ is the average number of magnetic poles per unit area, and $\overline{m^2}$ the mean-square strength of the poles,

$$\left.\begin{aligned} R_X(\tau) &= \sigma\overline{m^2} \int_{-\infty}^{\infty} dy \int_{-\infty}^{\infty} A_X(x, y, z) A_X(x + \tau, y, z)\, dx \\ R_Y(\tau) &= \sigma\overline{m^2} \int_{-\infty}^{\infty} dy \int_{-\infty}^{\infty} A_Y(x, y, z) A_Y(x + \tau, y, z)\, dx \\ R_Z(\tau) &= \sigma\overline{m^2} \int_{-\infty}^{\infty} dy \int_{-\infty}^{\infty} A_Z(x, y, z) A_Z(x + \tau, y, z)\, dx \end{aligned}\right\} \qquad (11)$$

It will be noticed that the autocorrelation functions for this model are completely determined by two parameters: the quantity $\sigma\overline{m^2}$ and the depth z of the layer below the aircraft.

The expressions (11) were computed by numerical integration for the dimensionless case. Then, by choosing the two parameters, the theoretical function $R_X(\tau)$ was fitted to the experimental curve $R_H(\tau)$ obtained from the north-south flights in Western Canada. The horizontal component was selected because its original profiles fitted the straight-line approximation well, and its autocorrelation function had the most characteristic shape. The best fit, shown in Figure 6, was obtained for $\sigma\overline{m^2} = 7.0 \times 10^6$ gauss^{2}cm^2 and $z = 14$ km. Using the same value of the parameters, theoretical curves $R_Y(\tau)$ and $R_Z(\tau)$ were plotted for comparison with the observed $R_D(\tau)$ and $R_Z(\tau)$ (Fig. 6).

The agreement between the observed and theoretical autocorrelation functions is reasonably good, except in the case of Z, where the original profiles had a distinct curvature. The observed Z autocorrelation function was recalculated, using a smooth free-hand curve drawn through the profile instead of the straight-line approximation. The result is shown by the solid circles in Figure 6. It is apparent that by a proper choice of curvature for the baseline, good agreement could be obtained between the theoretical and experimental functions.

It will be noticed that the theoretical function $R_X(\tau)$ becomes negative for τ of the order of 50 km. The reason is that every pole which produces a positive anomaly in X as the aircraft approaches it will produce a negative anomaly as the aircraft leaves it behind, and positive and negative X anomalies occur in pairs, separated by a few tens of kilometers. Thus, the maximum in the spectrum of H, noted in connection with Figure 1, does not necessarily indicate a periodic geological structure, but can be explained by a random arrangement of magnetic bodies.

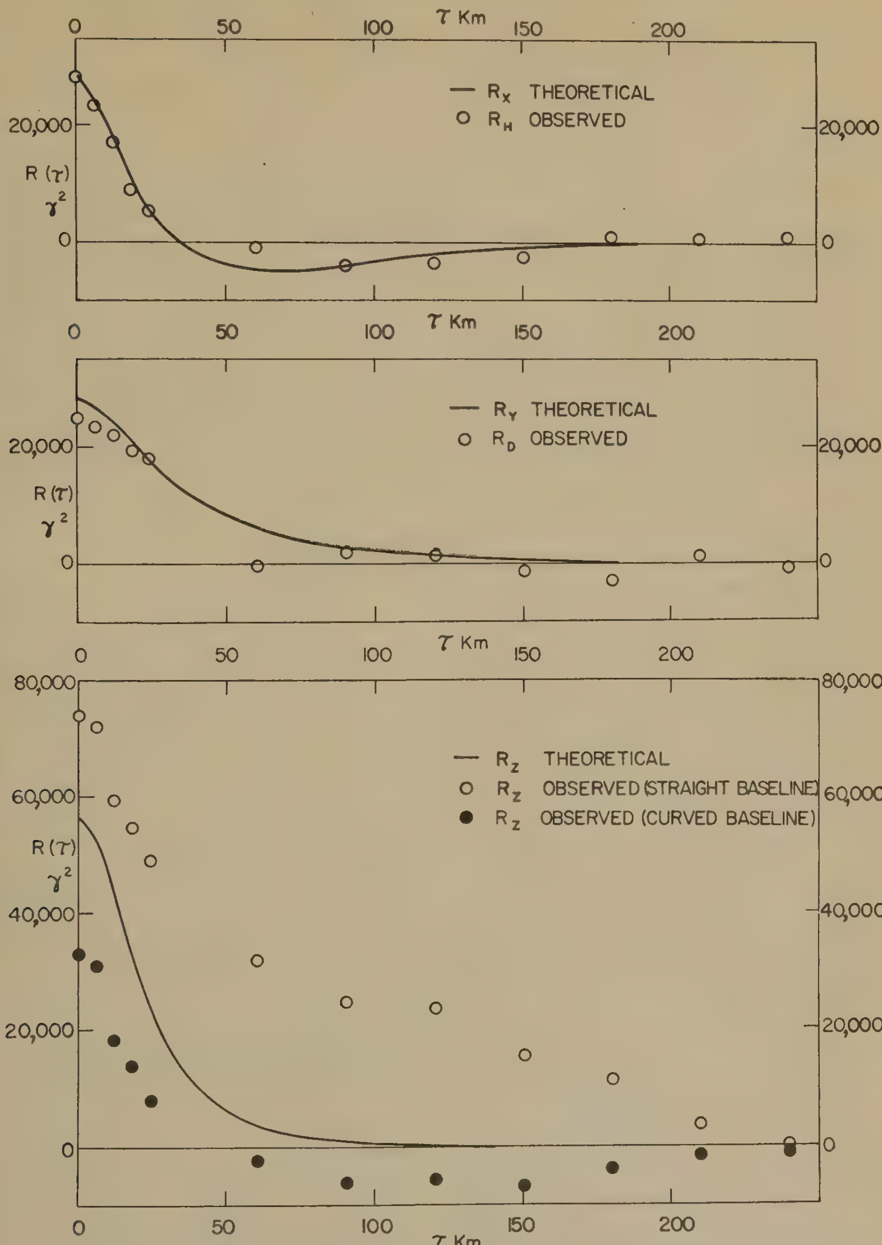

FIG. 6—Theoretical autocorrelation functions for a thin layer of magnetic poles of 14 km below the aircraft with $\sigma\overline{m^2} = 7.0 \times 10^6$ gauss²cm², and points on curves observed on north-south flights in Western Canada

Figure 7 shows theoretical and observed functions $\Delta(\tau)$ for the model of Figure 6. The agreement appears better here because the function $\Delta(\tau)$ is less sensitive to curvature of the profiles than $R(\tau)$.

The same model—a thin layer of poles at constant depth—was fitted to the results obtained over the Atlantic. Here the Z profiles were fairly straight, and the

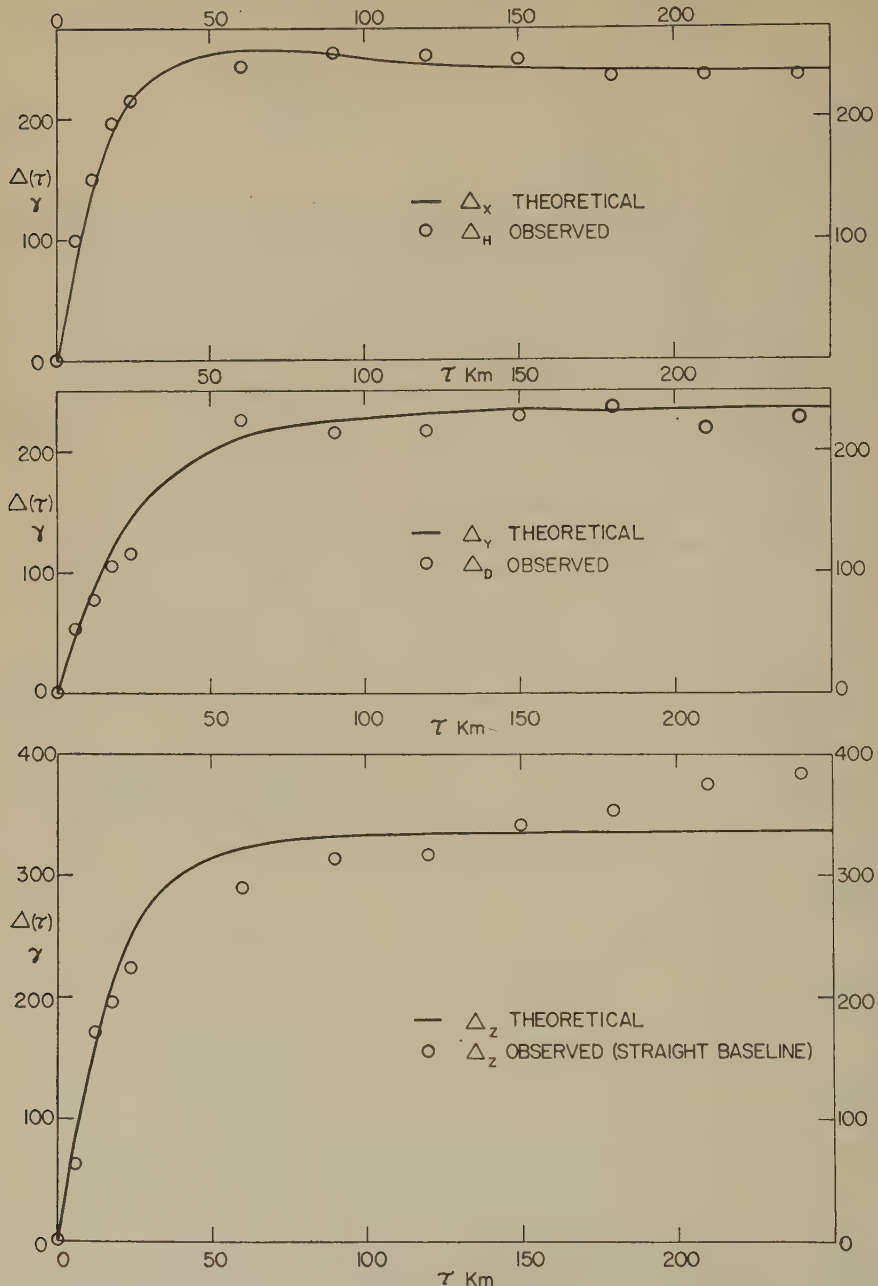

Fig. 7—Theoretical r.m.s. changes in components over distance τ for the model of Figure 6, and observed curves for Western Canada

parameters were obtained from $R_Z(\tau)$: $\sigma\overline{m^2} = 3.0 \times 10^5$ gauss^{2}cm^2, and $z = 9$ km. Since the depth of the ocean is practically constant at 5.5 km and the altitude of the aircraft was 2.5 km, the magnetic layer would be one kilometer below the

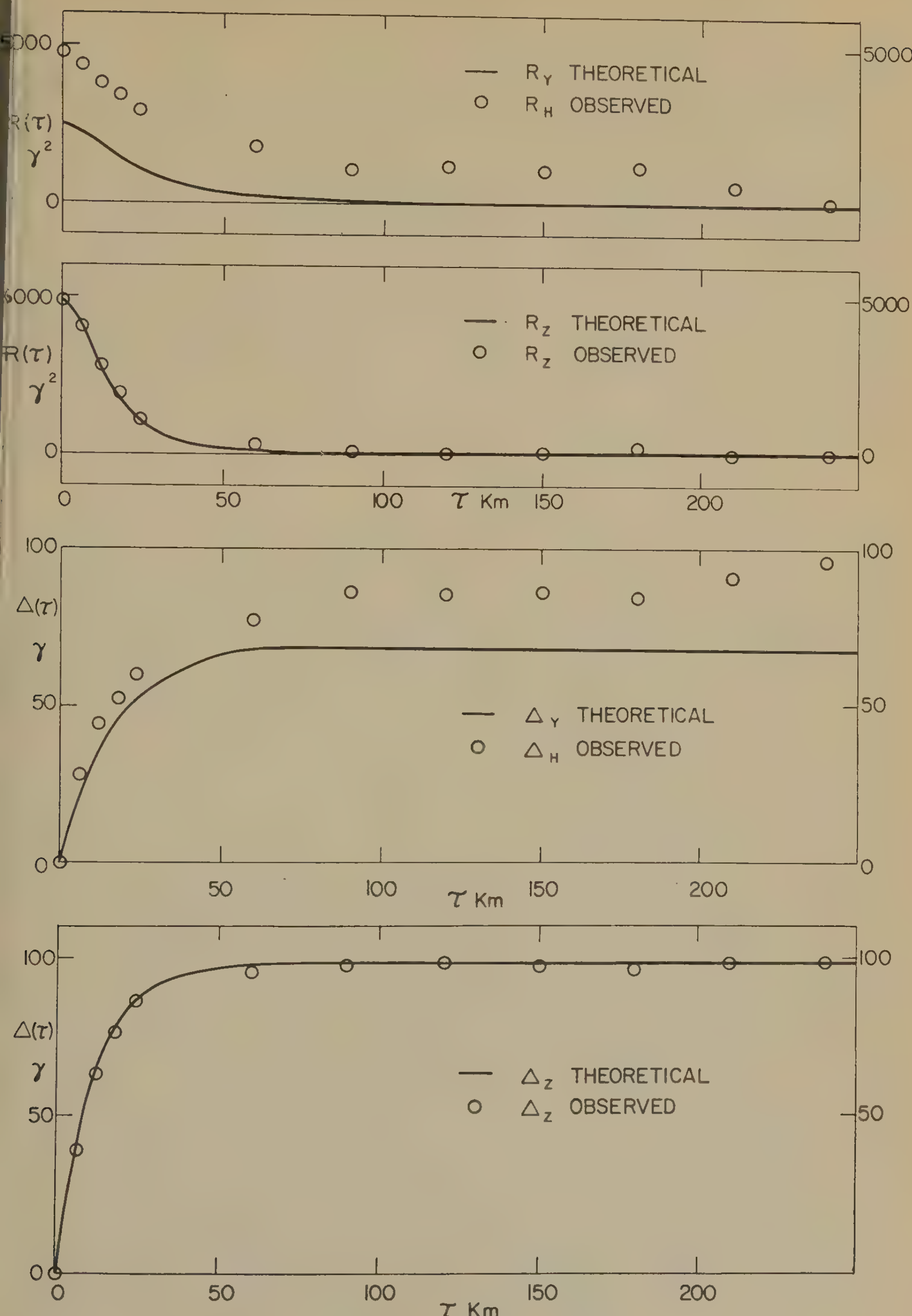

FIG. 8—Theoretical functions for a thin layer of magnetic poles 9 km below the aircraft with $\overline{m^2} = 3.0 \times 10^5$ gauss²cm², and points on curves observed on east-west flights over Atlantic

bottom of the ocean. Seismic evidence from blasts at sea shows that the usual depth of sediments is one kilometer [3].

Figure 8 shows that remarkably good agreement was obtained between the observed and theoretical functions for the vertical component. The difference in the case of the horizontal component could be due to slowly varying errors in the stabilizing system with an amplitude of one or two minutes of arc, but here again the curvature of the profiles, though slight, is sufficient to account for the discrepancy.

Another model whose autocorrelation functions are determined by two parameters is a random distribution of magnetic poles throughout a thick horizontal layer which extends from a depth d below the aircraft down to an infinite depth. For this model, when ρ is the average number of poles per unit volume in the layer, $\overline{m^2}$ the mean-square pole-strength as before,

$$R_X(\tau) = \rho\overline{m^2} \int_d^\infty dz \int_{-\infty}^\infty dy \int_{-\infty}^\infty A_X(x, y, z) A_X(x + \tau, y, z)\, dx \ldots\ldots (12)$$

etc.

By numerical integration, it was found that the autocorrelation functions of this model are so similar in shape to those of a thin layer of poles at a depth of about $2d$ that the two models would be indistinguishable experimentally. A model of a thick layer of poles extending from 7 km below the aircraft down to infinity would fit the experimental results from Western Canada just as well as the thin layer at 14 km, already considered. For the observations over the Atlantic, the thick layer would begin 4.5 km below the aircraft. Since the bottom of the ocean is 8 km below the aircraft, the model is physically inadmissible.

Models made up of dipoles can be investigated similarly, but additional parameters are necessary to specify the orientation of the dipole moments, unless the orientation is taken to be random—an assumption which is probably unjustified. Autocorrelation functions were computed for the special cases of thin and thick layers of dipoles whose axes are all vertical. The best fit to the functions observed in Western Canada was obtained for the thin layer 34 km below the aircraft, or the thick layer beginning at 24 km. For the ocean observations, the corresponding depths are 22 km and 15 km. The autocorrelation functions of the dipole models differ noticeably in shape from those of the single pole models. When the curves are matched as closely as possible, differences amounting to 10 per cent of the maximum correlation remain. It can be stated that the single pole models fit the ocean results appreciably better than the dipole models. In Western Canada, irregularities in the observed autocorrelation functions and the uncertain effects of curvature in the profiles confuse the picture, but is appears that the single pole models again give a better fit.

For each of the four models analysed, the following relation was found to hold exactly:

$$R_Z(0) = 2R_X(0) = 2R_Y(0) \ldots\ldots\ldots\ldots\ldots\ldots (13)$$

Accordingly, it would be expected that anomalies in the vertical field will generally be larger than those in the horizontal field by a factor of $\sqrt{2}$.

CROSS-CORRELATION

There is another statistical function which can be used to check on the pre-[ce]ding results—the cross-correlation [1] between different magnetic components. [Th]e cross-correlation function of Z and H, for example, is defined by

$$R_{ZH}(\tau) = \lim_{l\to\infty} \frac{1}{2l} \int_{-l}^{l} Z(x)H(x + \tau)\, dx = \overline{Z(x)H(x + \tau)} \quad \text{.........(14)}$$

Theoretical cross-correlation functions can be computed for the random [m]odels. For the thin layer of single poles,

$$R_{ZH}(\tau) = \sigma\overline{m^2} \int_{-\infty}^{\infty} dy \int_{-\infty}^{\infty} A_Z(x, y, z) A_X(x + \tau, y, z)\, dx \quad \text{........(15)}$$

[an]d, because of the symmetry of the model,

$$R_{XY}(\tau) = R_{ZY}(\tau) = 0$$

[F]or the thick layer of poles,

$$R_{ZX}(\tau) = \rho\overline{m^2} \int_{d}^{\infty} dz \int_{-d}^{\infty} dy \int_{-\infty}^{\infty} A_Z(x, y, z) A_X(x + \tau, y, z)\, dx \quad \text{......(16)}$$

[an]d again $R_{XY}(\tau) = R_{ZY}(\tau) = 0$.

It was hoped that the cross-correlation function would provide a method for [di]stinguishing between a thin and a thick layer of poles, for instance, but when [(1]5) and (16) were evaluated it was found that the thick layer starting at depth [d] was again practically indistinguishable from the thin layer at depth $2d$.

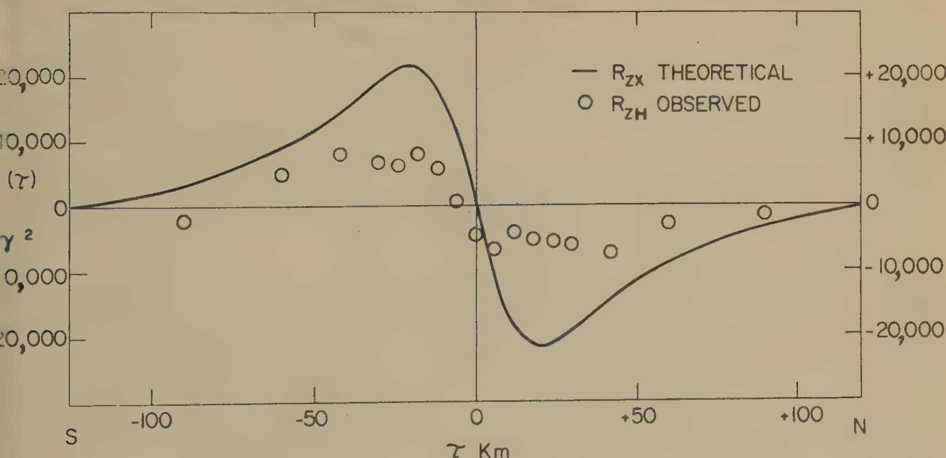

[FI]G. 9—Theoretical cross-correlation function for the model of Figure 6, and observed cross-correlation for one north-south flight in Western Canada

Figure 9 shows the theoretical cross-correlation function $R_{ZX}(\tau)$ for the model [of] Figures 6 and 7 (a thin layer of poles at 14 km with $\sigma\overline{m^2} = 7.0 \times 10^6$ gauss^{2}cm^2), [an]d the function $R_{ZH}(\tau)$ obtained by analysing one north-south flight of 1,200 [k]m in Western Canada. The difference in the amplitudes of the theoretical and the [o]bserved curves seems to indicate that there must be some H anomalies not

associated with Z anomalies, and *vice versa*. Even if this were physically possible, it would lead to the conclusion that the fact shown by Figure 7—that the ratio of the mean-square H-anomaly to the mean-square Z-anomaly is close to the theoretical value—is purely fortuitous. Another difficulty is that the experimental cross-correlation curve is shifted about 5 km toward the south from the theoretical curve. The explanation appears obvious: that magnetic poles do not occur at random but in pairs, with the deeper pole of a pair slightly to the north of the upper one. However, calculations on pairs of poles and dipoles dipping at various angles showed no appreciable asymmetry in the cross-correlation. It may be that the curvature of the Z profile is responsible for the discrepancies in both amplitude and phase, but it is difficult to estimate the magnitude of its effect.

INTENSITY OF MAGNETIZATION

It is not possible by an analysis of autocorrelation functions to distinguish between profiles containing many weak anomalies and profiles containing a few strong anomalies. The strength of the magnetic poles causing the anomalies cannot be calculated directly because the number of poles is not known. However, by introducing the condition that two differently magnetized bodies may not occupy the same space, it is possible to calculate a lower limit of the intensity of magnetization of the rock necessary to produce the anomalies observed.

Assume that the thin layer of poles is formed by the upper surfaces of a collection of long vertical cylinders of magnetized rock. For Western Canada, $\sigma\overline{m^2} = 7 \times 10^6$ (unit poles)^2/cm^2. Obviously, the poles must be large—much larger than one centimeter. Suppose the radius of the cylinders is 3 km—the largest radius which would allow them to appear as point sources from 15 km above. First, it is assumed that all poles are of the same strength, and the random distribution is geographical. To leave room for randomness, the poles must be separated on the average by 10 times their radius, and σ is of the order of 10^{-3}/km^2 or 10^{-13}/cm^2. Then the pole strength m is $\sqrt{7 \times 10^{19}}$ or 10^{10} cgs units. The intensity of magnetization is the pole strength divided by the area of the top of the cylinder, or $10^{10}/3 \times 10^{11} = 0.03$ cgs.

Another way to obtain a random distribution is to have the poles closely packed but varying in strength. The surface density σ is then 2×10^{-12}/cm^2, and the r.m.s. pole-strength is $\sqrt{4 \times 10^{18}}$ or 2×10^9 cgs. The stronger poles would have to be at least 10^{10} cgs, and the intensity of magnetization is again 0.03 cgs.

If the radius r of the poles had been assumed smaller than 3 km, the calculated intensity of magnetization would increase in the ratio $1/r$.

For the thick layer of poles in Western Canada, the parameter $\rho\overline{m^2}$ was found to be 3 (unit poles)^2/cm^3. Assume poles of equal strength formed at the ends of cylinders of radius $r = 3$ km, average length $l = 10$ km. The density ρ will be of the order of $2/(10^3 \times \text{volume of cylinder}) = 7 \times 10^{-21}$/cm^3. Then,

$$m = \sqrt{\frac{3}{7 \times 10^{-21}}} = 2 \times 10^{10} \text{ cgs}$$

The intensity of magnetization is $2 \times 10^{10}/3 \times 10^{11} = 0.07$ cgs, and will vary with $\sqrt{l/r}$.

For the vertical dipole models, similar calculations yield intensities of magneti-ation of the order of 0.7 cgs. From the four models considered, it appears that nder Western Canada there are many rocks magnetized to an intensity of at ast 0.05 cgs.

For the flights over the Atlantic, the model of the thin layer of poles one ilometer below the ocean floor gives $\sigma\overline{m^2} = 3 \times 10^5$ gauss^{2}cm^2, and the lower mit of intensity of magnetization is 0.005 cgs. This magnetization is very high ven for basic rocks [4], especially when it is remembered that the anomalies are ot isolated examples, but occur many times in 100 km. Miller and Ewing obtain ne same magnetization in their analysis of the anomaly associated with Caryn eak [5], and conclude that such a high value probably indicates thermo-remanent nagnetization of basic rock. It would appear that the values of magnetization btained in Western Canada, still larger by at least an order of magnitude, can nly be explained by basic rocks thermo-remanently magnetized.

DISCUSSION OF MAGNETIC MODELS

Four models have been investigated to account for the statistical properties f magnetic profiles obtained by airborne magnetometer. For the observations ver the Atlantic, there is little doubt that the model of a thin layer of magnetic oles one kilometer below the ocean floor supplies the correct explanation for e observed anomalies. For Western Canada, the interpretation is more difficult. ight possible models are listed, with all depths measured below sea level:

(*a*) A thick layer of poles from 4 km to infinity
(*b*) A thick layer of poles from 4 km to 30 km
(*c*) A thick layer of poles from 6 km to 24 km
(*d*) A thin layer of poles at 8 km plus another at 18 km
(*e*) A thin layer of poles at 9 km plus another at 33 km
(*f*) A thin layer of poles at 11 km
(*g*) A thick layer of vertical dipoles from 20 km to infinity
(*h*) A thin layer of vertical dipoles at 30 km

or a model of a given type, the depth of the top below the aircraft can be estimated ± 10 per cent, but there is a wide choice of models, even if the last two are ruled ut on account of the high intensity of magnetization necessary and the rather ubious evidence that they do not fit the observed autocorrelation functions as ell as the first six. Direct seismic evidence from blasts does not show under the ontinents any discontinuities in velocity above the Mohorovičić at 35 km. How-ver, Gutenberg suspects a decrease in velocity at about 12 km [6]. Perhaps the odels could be distinguished by making more flights over the same area at a onsiderably greater altitude.

An important question is whether the model (*a*) represents the minimum ossible depth for the sources of the observed anomalies. The answer is obviously o; circular patches of poles on the surface of the earth of the order of 100 km in iameter could produce the same sort of anomalies if the pole strength varied in a pecial way from strong at the center to weak at the edges. However, it is im-robable that features of such a special nature would be found scattered uniformly ver an area 1,200 km square. Furthermore, the areas of poles would have to

overlap without upsetting each other's special distributions of pole strength.

It is natural to look for the source of magnetic anomalies at the top of the Precambrian. The average depth of the Precambrian in the area surveyed is 0.5 km below sea level or 3.5 km below the aircraft, whereas the top of model (*a*) is 7 km below the aircraft. If the anomalies were associated with the top of the Precambrian, it would be expected that the three north-south flights for which the average depths of the Precambrian were 4.5, 3.0, and 2.7 km below the aircraft, would show systematic differences in the functions $\Delta(r)$. No significant differences could be found. This is not to deny that anomalies may originate at the top of the Precambrian; it means that such anomalies are too rare to affect the statistical properties of the profiles.

At the beginning of this investigation, it was hoped that some indication of the depth of the Curie point might be obtained. According to different authorities, it would be expected to lie somewhere between 20 and 100 km [7, 8]. Unfortunately, except for the dipole models which appear doubtful on other grounds, anomalies originating at such a depth would be masked by the stronger anomalies originating above, as can be seen by comparing models (*a*) and (*b*) in the above list. From the ocean results, it can at least be concluded that, if the magnetized bodies are long vertical cylinders, the lower poles must be at a depth greater than 30 km.

It is unfortunate that in obtaining the autocorrelation and cross-correlation functions, the signs of the anomalies are lost. It may be that if the autocorrelation functions of the positive and negative departures from the mean field were calculated separately, the ratio of normal magnetization to reversed magnetization could be estimated, throwing some light on the history of the earth's field. The possibility of distinguishing a positive pole from a gap in a group of negative poles, however, seems remote.

The simplest conclusions to be drawn from the investigation of magnetic models are as follows: Under the deep ocean, there are many bodies magnetized to an intensity of at least 0.005 cgs which produce magnetic poles one kilometer below the ocean bottom. If there are corresponding poles at greater depths, they must be deeper than 30 km. Under the continent, there are still more strongly magnetized bodies producing poles either in a layer at 10 to 12 km or scattered from 4 km downward. The most likely mechanism for producing such intense magnetization seems to be thermo-remanent magnetization of basic rocks.

References

[1] H. M. James, N. B. Nichols, and R. S. Phillips, Theory of Servomechanisms, McGraw-Hill Book Co., Inc., New York (1947); p. 273.

[2] M. G. Kendall, The Advanced Theory of Statistics, Charles Griffin and Co., Ltd., London, 3rd ed. (1955); Vol. II, p. 405.

[3] G. P. Woollard, Report of the Special Committee on the Geophysical and Geological Study of Continents, 1952-54, Trans. Amer. Geophys. Union, 36, 698 (1955).

[4] T. Nagata, Rock Magnetism, Maruzen Co., Ltd., Tokyo (1953).

[5] E. T. Miller and M. Ewing, Magnetic measurements in the Gulf of Mexico and in the vicinity of Caryn Peak, Geophysics, 21, 423 (1956).

[6] B. Gutenberg, Wave velocities in the earth's crust, Geol. Soc. Amer. Memoir 62, 19-34 (1955).

[7] V. Vacquier and J. Affleck, A computation of the average depth to the bottom of the earth's magnetic crust based on a statistical study of local magnetic anomalies, Trans. Amer. Geophys. Union, Pt. 2, 446-450 (1941).

[8] F. Birch, Physics of the crust, Geol. Soc. Amer. Memoir 62, 101-117 (1955).

LINEAR SECULAR OSCILLATION OF THE NORTHERN MAGNETIC POLE

BY E. R. HOPE

Defence Research Board, Ottawa, Canada

(Received June 8, 1956)

ABSTRACT

Modern data seem to support the thesis (van Bemmelen, 1899) that the secular motion of the northern magnetic pole is a nearly linear oscillation. This oscillation is along the axis of a great magnetic anomaly in the arctic. Except for the constraint of the anomaly, the motion would probably be circular or quasi-circular, as suggested by the historical declination-dip curves.

Figure 1 shows that the northern magnetic pole, displaced hundreds of kilo-…ers from the geomagnetic axis-pole, is the low end of a long magnetic trough, …ch has been characterized [see 1 of "References" at end of paper], without …rvations, as a fixed magnetic anomaly. The same term "magnetic anomaly" … previously applied by Fisk [2]. Comparison with earlier charts [2, 3] seems, …ed, to indicate that this distortion of the surface field is produced by something …obile and permanent; that is, necessarily a geological and doubtless a crustal …ure (deep-lying, but above the Curie-point level). In the anomaly-trough …ciated with this geological feature, the magnetic pole is trapped.

This would signify, and indeed the whole picture of Figures 1 and 2 suggests, … the secular variation of the magnetic north direction, as observed during the … three or four centuries in western Europe, was probably not reflected in a … wandering or circling of the dip-pole over the earth's surface; rather the …pole was, as now, confined to the trough and merely oscillated along it, either …arly or in a very compressed oval path. If so, the difference of aspect (Fig. 2), … the manner in which the magnetic meridians are gathered together into a long, …graphically fixed sheaf, suggests that in the China area (where early records …t) and in North America, the secular variation should be small as compared … that in Europe.

This conclusion seems to be borne out by the facts. In the China area, "from … remotest times for which reliable magnetic data could be obtained, the secular …ation was always very small" (de Moidrey [4], p. 217). Moreover, for reasons …ch will be clear from Figure 2, magnetic north in China is very nearly true …h, and this has been the case throughout the whole extent of the records. (A …t *easterly deviation* of the *magnetic needle* is mentioned in a book by a Chinese …onomer printed between 1089 and 1093 A.D.)

Off the North American end of the trough, the available records likewise show …mparatively narrow range of declination (Fig. 3). Whereas the north end of … total magnetic vector in Europe has traced a wide oval (variation of 35° in

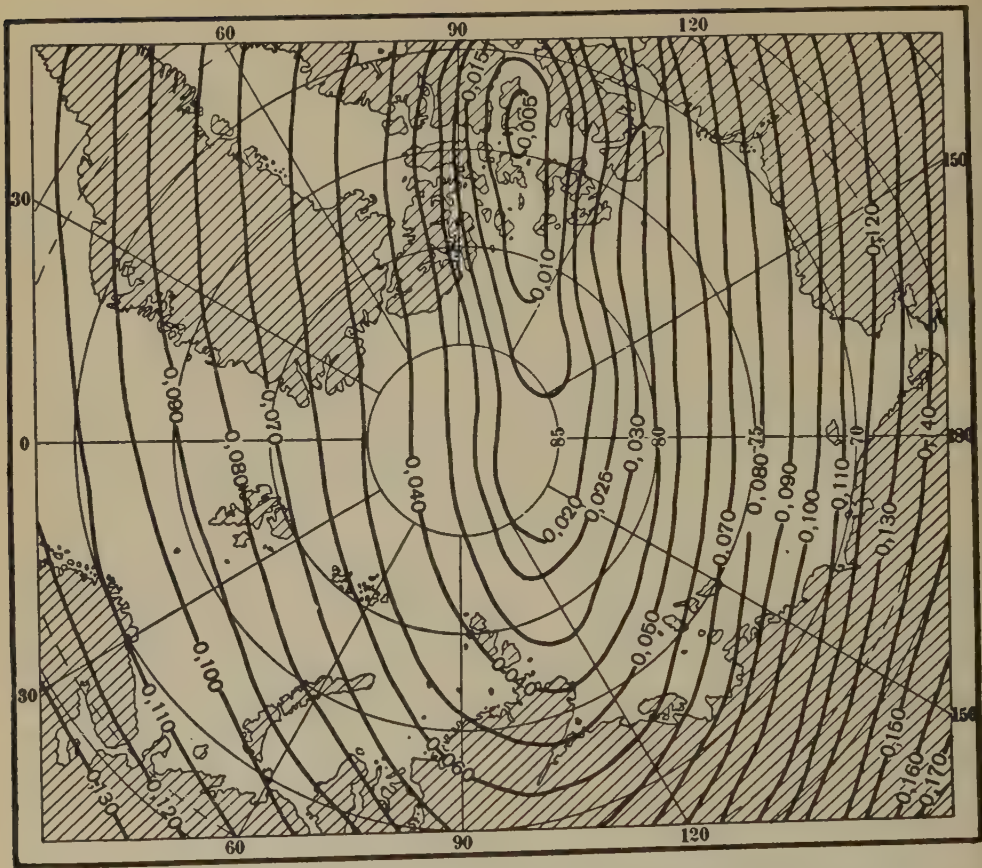

Fig. 1—Isomagnetic chart of horizontal component, epoch 1950, from [1]. Compare the very similar charts for epoch 1925, Fisk [2], p. 139, and for epoch 1945, Vestine [3], p. 505.

declination and 8° to 9° in dip), the oval at Boston and Baltimore is narrow and meridionally orientated. The same comparatively narrow secular range of declination is in evidence at San Francisco; see Fleming [5], p. 217. At Boston and Baltimore, the maximum dip occurred in 1850-1860, which is close to the time of maximum westward declination in Europe; that is, the phases are consistent with the longitude-difference. (After 1895, a disturbance occurred in the Boston and Baltimore curves, which we shall discuss elsewhere.)

It is interesting to compare the historical pole-path (Fig. 4) as deduced by van Bemmelen [6] at the beginning of this century. Van Bemmelen's positions for 1600 and 1700 A.D. represent the probable convergence-points of the magnetic meridians as determined by an extensive study of the available records. Similar convergence-points for later dates did not show too clear a picture, because of the reversal of the magnetic pole's motion and a generally more complicated behavior. The corresponding portion of the curve in Figure 4 may therefore be regarded as interpolation, to connect the earlier positions with the observed mid-nineteenth-century position of the magnetic pole. This interpolation is at least roughly correct; today the magnetic pole is proceeding northward along the left-hand side of the narrow ellipse suggested by van Bemmelen's curve.

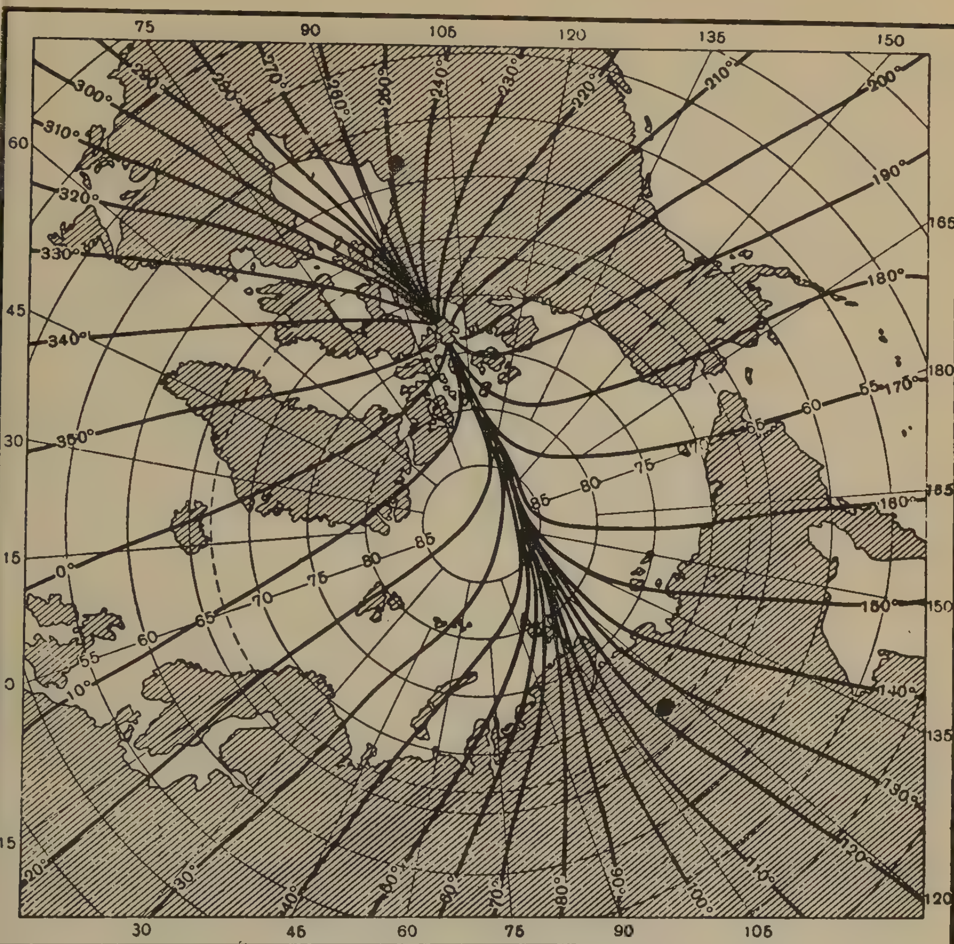

Fig. 2—Magnetic meridians, epoch 1950, from Ostrekin [16]. Compare Fisk's chart for epoch 1925 in [2], p. 136; also van Bemmelen for 1885, Figure 5 of [6]. The solid circlets mark the poles of maximum vertical intensity, epoch 1945, after Vestine [3], p. 522.

The ellipse coincides quite well with the magnetic trough of the arctic anomaly (compare Figs. 2 and 4); suprisingly so, when the circumstances of van Bemmelen's calculations are considered. The positions for 1600 and 1650 A.D. are probably a little too far to the west; the anomaly crosses the circle of 80° north at longitude 105° west. The recent motion of the magnetic pole is almost exactly parallel to the anomaly-axis, and its direction intersects van Bemmelen's curve.

Figure 4 is additional evidence for the permanence of the anomaly. It is also to be noted that van Bemmelen's magnetic meridians for 1885 (after Neumayer) show the existence of the anomaly-trough quite plainly, even though in rudimentary form ([6], Fig. 5).

The linear or nearly linear motion of the northern magnetic pole is not a new idea. Schütz [7] in 1902 emphasized that van Bemmelen's pole-path was far from circular. Madill ([8], p. 17) renewed the suggestion in 1948, on the basis of recent data. Yet from the declination-dip curves, particularly the wide oval-shaped

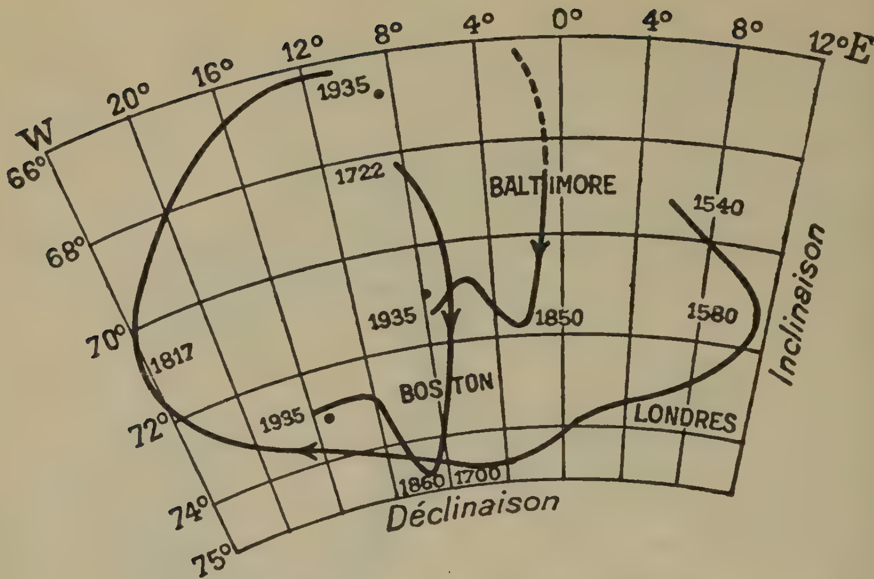

Fig. 3—Secular variation of declination and dip (L. A. Bauer), from Dauvillier [10]. The dots near the ends of the curves represent values for 1956 (unsmoothed).

London curve (Fig. 3), it appears that the primary mechanism of the variation is such that it ought to cause a quasi-circular motion of the dip-pole on the earth's surface (Woodward [9], p. 2). To explain why this is not the case, one must suppose a local distortion of the pole-path.

The local nature of the distortion is proved by the absence of any similar anomaly-trough or linear bunching of the magnetic meridians in the antarctic; this is seen from Vestine's declination charts [3]; compare pages 476-477 with 484-485, and page 522 with page 523. It is furthermore seen from Figure 1 that the ellipticity of the isolines, though still evident at great distances, even up to the edges of the chart, is radially decreasing. The cause is therefore central in this area, and it cannot, relatively speaking, lie very deep.

Thus, there are (at least) two successive effects in the displacement of the dip-pole from the geomagnetic axis-pole: first, the cyclic variation of Figure 3, and, second, the anomaly-distortion. We have the axis-pole (stationary or slow-moving), then a theoretical "cyclic pole," the motion of which would be circular or quasi-circular, and finally the dip-pole, which, in its restricted motion along the anomaly-trough, follows the "cyclic pole" as closely as possible.

The statement that the dip-pole is restricted or confined to the anomaly-trough really means this: the surface pattern of the geomagnetic field is contracted or foreshortened toward the anomaly-region from both sides, and the magnetic pole, which is no more than part of the said pattern, along with it. The cyclic variation moves the pattern through the distortion region, as though under a prismoidal lens. In the axial area of strongest distortion, the movement of the pole becomes nearly linear. The magnetic field at a distance exhibits a progressively freer circling motion of declination and dip, but nevertheless continues to be

4—Historical path of northern magnetic pole reconstructed by W. van Bemmelen in 1899. Compare with Figures 1 and 2, and particularly with Fisk [2], pp. 136, 137, and 139.

ected by the pull of the pattern-contraction in the anomaly-region. This, indeed, hat explains the difference between the shapes of the London and the Boston Baltimore curves (Fig. 3).

The above concepts, particularly that of the "cyclic pole," will be utilized further paper.

An unanswered question, of course, is that of the southern magnetic pole and motion deduced by van Bemmelen ([6], Fig. 1). Since the antarctic region ws nothing similar to our Figures 1 and 2, a similar pole-path is not to be ected, unless it be by way of an adjustment of the entire terrestrial field to ommodate the northern magnetic pole's motion. Actually, there is not much van Bemmelen's pole-paths to prove that there is any connection or ultimate ilarity of shape. The problem can scarcely be decided until we have better a for the antarctic.

The dip-pole is the minimum of the horizontal component, but it is not the maximum of the vertical component.

Indeed, the vertical component Z of the magnetic field has, in the northern hemisphere, two maxima, one in Canada and one in Siberia (Fig. 2). They lie off the ends of the anomaly-trough, and coincide approximately with the regions of maximum curvature of the isolines of horizontal intensity (Fig. 1). The most obvious explanation is that at each of these points the total magnetic field concentrates and dips to pass into the ends of the geological formation responsible for the anomaly. Such a concentration must occur at the ends of any elongated magnetically permeable mass.

The maxima of the vertical component change their positions, presumably according to the motions of the "cyclic pole" and the dip-pole. During the recent period when the dip-pole has been moving northward, the Canadian vertical maximum has also moved northward.

Many attempts have been made to describe the two vertical maxima, and the magnetic trough which extends between them, in terms of two local magnetic dipoles. Nevertheless, it will surely be simpler to account for the cyclic variation by a single deep-seated process rather than by two separately varying dipoles. For instance, there is the fact that at London (Fig. 3) the dip has both a maximum and minimum value midway between the extremes of declination. In any case, such dipoles (a theoretical abstraction) may be taken as merely a way of describing the concentrations produced at the ends of a bar-shaped inclusion, as above. The crux of the matter is, are these dipoles permanent or impermanent? Are they, aside from the cyclic displacement, mobile or immobile?

(Here it is appropriate, however, to note that A. Dauvillier [10] ascribes all secular variation to thermally induced fluctuations and waves in the Curie-point level. Whether this thesis can be defended or not, it is entirely possible that such a mechanism does contribute to secular variation. If so, it implies that even a geological magnetic anomaly is not necessarily either immobile or permanent.)

It may be significant that the arctic magnetic anomaly passes along a recently reported [11] strip of Mesozoic folding and subsidence across the floor of the Arctic Ocean (Figs. 5 and 6). Furthermore, this strip is shown by the Soviet authors as a corridor between Precambrian platforms, sunken continental blocks [11, 12, 13]. Between these blocks, a ferriferous magma may have welled up from beneath, that is, from below the Curie-point level (see, however, [14]).

On the other hand, the corridor has a sharp bend, and there is no sign that the anomaly is deflected to follow it. The magnetic meridians (Fig. 2) run very straight. The dip-pole has traveled far south of the bend, and the Canadian maximum of vertical intensity lies still farther south. Now this may be explained if it is assumed that the corridor, the Mesozoic folding, is no more than the surface trace of deeper movements. The deep formation responsible for the anomaly continues into and under the arctic archipelago, past the shattered arctic coast-line and even into the foundations of the continental shield. The superficial folding cannot follow; it will stop at the edge of the continental shelf (compare [1], Fig. 8) or turn to follow along the edge. This is, in fact, exactly what happens. The westward bend of the corridor (Figs. 5 and 6) is known to North American geologists

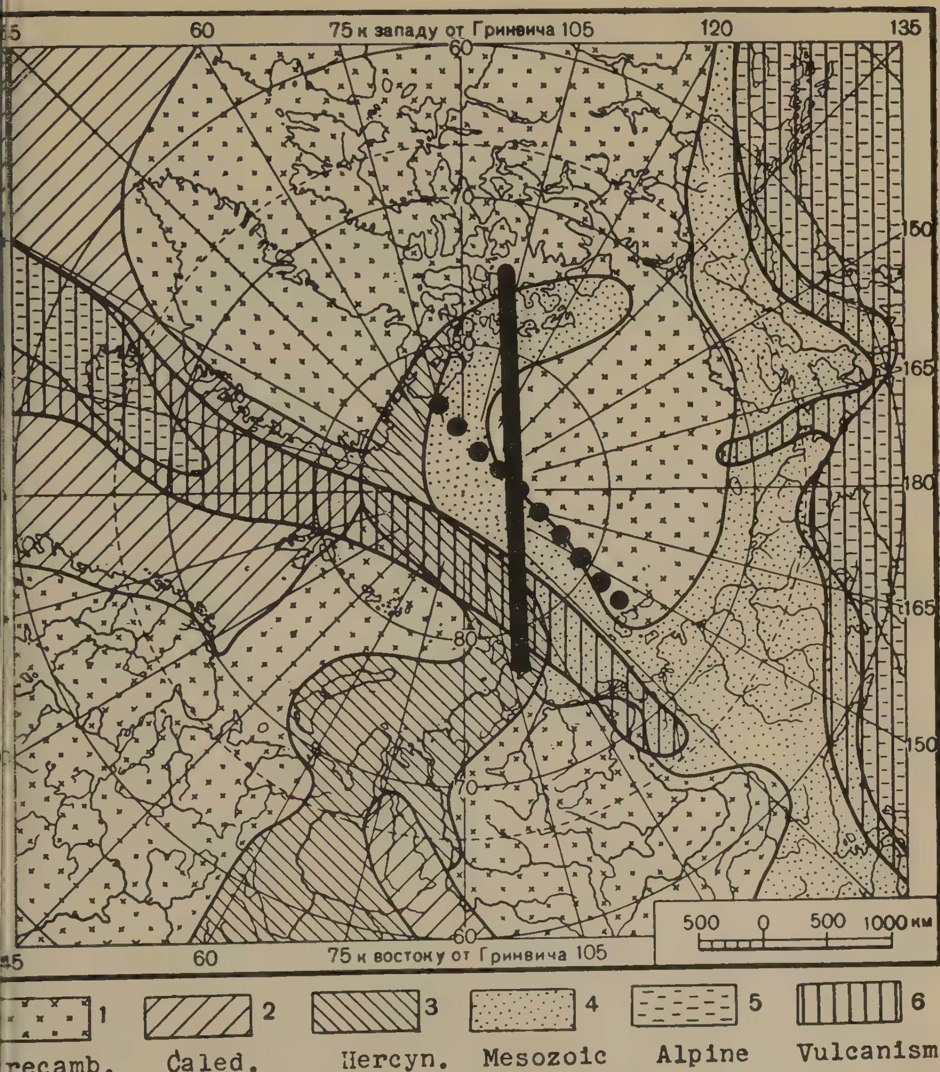

. 5—Geological structure of central arctic; regions of folding and zone of recent vulcanism; from Saks, *et al.* [11], with additions as follows:

Axis of arctic magnetic anomaly

Lomonosov suboceanic mountain range

15], p. 2077) as a belt of orogeny and a possible geosyncline—the Franklin osyncline—in northern Ellesmere Island and Axel Heiberg Island; it is thought extend westward as far as Prince Patrick Island. It traces the rim of the conti- ntal shelf.

Figure 2 shows that the anomaly crosses the whole Arctic Ocean on either a eat-circle course or in a very smooth arc (compare the positions of the vertical axima). Whatever its nature, the geological formation responsible for the anomaly on the same scale as the great seismic-orogenic belts and island arcs, or the

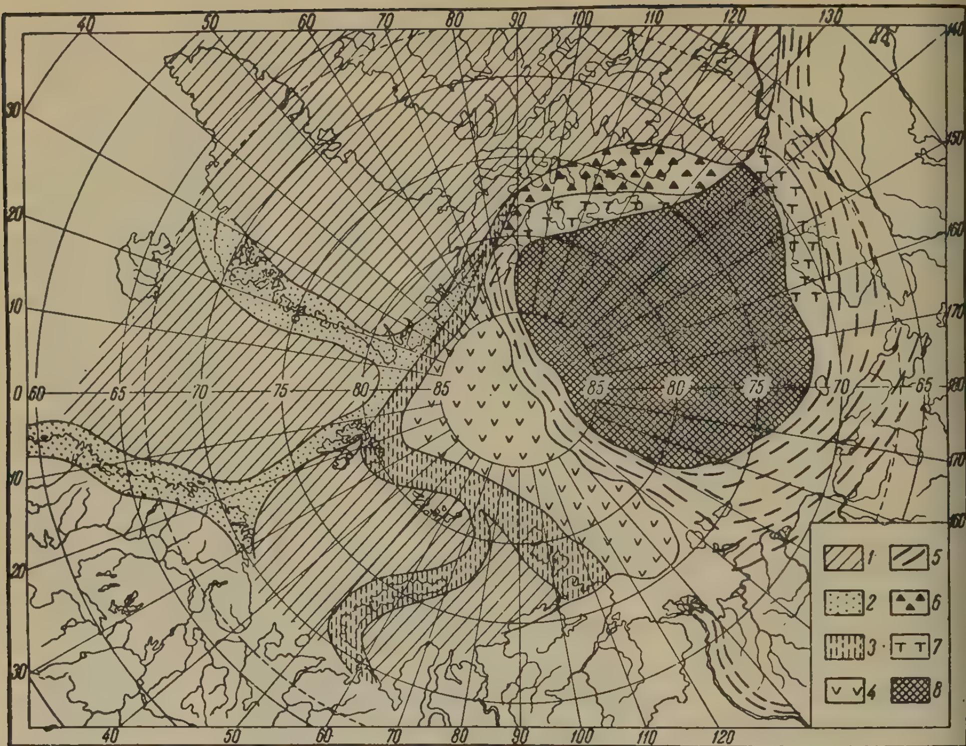

Fig. 6—Arctic tectonics, from Panov [13]: 1. Prepaleozoic platforms; 2. Caledonian folding; 3. Hercynian folding; 4. Paleozoic platform of western part of central arctic basin; 5. Mesozoic folding; 6. Marginal sags of Canadian arctic platform, of Paleozoic age; 7. Marginal sags of Canadian arctic platform and Alaska, of Mesozoic age; 8. Hyperborean platform (Prepaleozoic) in eastern part of central arctic basin.

smoothly arcuate coasts like that of the western United States, which are thought to be the final stages of island arcs. (Similar but smaller curves, both convex and concave, are found in the arctic; for example, the eastern shore of Hudson's Bay, which might have been laid out in a series of compass-sweeps, and the northern coast of Alaska).

The great arctic anomaly is unique as a magnetic feature, but this is probably due to the nearly vertical magnetic field, or in other words, the feeble and easily modified horizontal component. Similar geological formations may exist elsewhere, but apparently it is not in the isogons or isoclines that their magnetic effects show to best advantage. We note that in the magnetic charts for 1940 the zero isopor (line of zero change) of declination, which was sweeping slowly westward over Quebec, developed an impressive southwestward loop, opening in a narrow neck at Quebec City but enclosing the whole St. Lawrence valley and part of the Great Lakes.

The author thanks the Defence Research Board of Canada for permission to publish this communication. He is indebted to Mr. T. A. Harwood, Mr. R. G. Madill, and Dr. L. W. Morely for useful discussion, and to A. Dauvillier and Hermann et Cie., Paris, for the use of Figure 3.

References

New Soviet Researches, Explorations and Discoveries in the Central Arctic, Izvest. Akad. Nauk SSSR, Ser. Geog., No. 5, 3 (1954). Anonymous. English translation in Defence Research Board of Canada Pub. T 165 R. See also reference [16].

H. W. Fisk, Trans. Amer. Geophys. Union, Twelfth Annual Meeting, April 30 and May 1, p. 134 (1931).

E. H. Vestine, L. Laporte, C. Cooper, I. Lange, and W. C. Hendrix, Washington, D. C., Carnegie Inst. Pub. 578 (1947).

J. de Moidrey, Terr. Mag., **37**, 217 (1932).

J. A. Fleming, Proc. Phys. Soc., **58**, 213 (1946).

W. van Bemmelen, Die Säkular-Verlegung der magnetischen Axe der Erde, Batavia, Obsns. Mag. Met. Obs., **22**, Pt. 1 (App. 1), p. 159 (1900).

E. H. Schütz, Die Lehre von dem Wesen und den Wanderungen der magnetischen Pole der Erde. Ein Beitrag zur Geschichte der Geophysik. Dietrich Reimer, Berlin (1902).

R. G. Madill, Arctic, **1**, 8 (1948).

R. H. Woodward, Terr. Mag., **53**, 1 (1948).

A Dauvillier, Le magnétisme des corps célestes, Tome 2, Variations et origine du géomagnétisme, Hermann et Cie., Paris (1954).

V. N. Saks, N. A. Belov, and N. N. Lapina, Priroda, No. 7, 13 (1955). English translation in Defence Research Board of Canada Pub. T 196 R.

D. G. Panov, Doklady Akad. Nauk SSSR, **104**, 462 (1955). English translation in Defence Research Board of Canada Pub. T. 204 R.

D. G. Panov, Doklady Akad. Nauk SSSR, **105**, 339 (1955). English translation in Defence Research Board of Canada Pub. T 207 R.

J. E. Oliver, M. Ewing, and F. Press, Bull. Geol. Soc. Amer., **66**, 1063 (1955).

Y. O. Fortier, A. H. McNair, and R. Thorsteinson, Bull. Amer. Soc. Petrol. Geol., **38**, 2075 (1954).

M. Ye. Ostrekin, Priroda, No. 12, 3 (1954). English translation in Defence Research Board of Canada Pub. T 172 R.

(*Note*: Copies of Defence Research Board of Canada translations mentioned above have been deposited with the ntific Translation Center, Library of Congress, and with other libraries.)

ROTATION, PULSE-DISTURBANCE, AND DRIFT IN THE GEOMAGNETIC SECULAR VARIATION

BY E. R. HOPE

Defence Research Board, Ottawa, Canada

(Received September 4, 1956)

ABSTRACT

The *westward drift* of surface geomagnetic patterns (the rate of which is about 30° of longitude per century) has at least one superimposed *rotation* of period ~480 years (Fig. 1), and possibly another of period ~800 years; these are phenomena of a peculiarly localized nature. The 480-year rotation is demonstrable not only in the curves of declination *versus* dip, but also in the isoporic patterns. A strong *pulse-disturbance* which occurred in the relative rotation of the terrestrial core, and therefore in the westward drift, is shown to affect the 480-year rotation in a manner which helps to clarify the relationships.

1) In reference [1] at end of paper, it is argued that in the northern hemisphere e are (at least) two systematic displacements of the surface magnetic field ern from that of the dipole field, both of them relatively local phenomena. first of these is a regular rotary oscillation of the grid of magnetic meridians isoclines. This *rotation*, of period about 480 years, produces the curves of re 1 and must have a deep-seated cause; the pole of the undistorted oscillating would presumably move in a quasi-circular path, and might be called the clic pole." Superimposed on this is the effect of a more local distortion, the t arctic anomaly. The distortion decreases radially throughout the pattern, it nevertheless extends to very considerable distances (because the magnetic s of force repel each other, and thus produce a wide-spreading adjustment to strong local distortion of the anomaly). The extended effect of the distortion roughly account for the different shapes of the curves in Figure 1.

The 480-year rotation seems to be far too regular and too permanent to be to a westward-drifting focus of secular variation of the type discovered by k [2, 3], which would have a probable lifetime of the order of a century. On other hand, this rotation is not the westward drift itself, though it has the e direction: the westward drift is much slower, and is, moreover, a world-wide nomenon, whereas the 480-year rotation is relatively localized in the northern nisphere.

The present paper (largely descriptive) attempts to clarify these relationships; o to prove two descriptive theses which will be required as starting points in a er paper dealing with probable mechanisms, namely:

(a) That the undistorted, quasi-circular 480-year rotation is a reality, demonstrable not only in the declination-dip curves but independently in other features of the geomagnetic field; and

(b) That the same periodicity can be demonstrated in the secular motion of the dip-pole; that is, the 480-year rotation is, indeed, the guiding mechanism here.

The present paper will also account for the marked irregularity in Bauer's curves (Fig. 1), the fact that whereas the London curve is a fairly regular oval, the oval course of the American curves was abruptly broken around 1895 (Bauer [4], p. 208) or 1902 (Hazard [3], p. 207). Bauer's original curves showed no such irregularity; they were compiled before this "westward break" occurred. When it did occur, it was the occasion of some disgust among magnetologists, because evidently one could no longer be certain of discovering a simple law (Hazard [3], p. 207). Since then the tendency has been, perhaps, to ascribe the westward break to some local perturbation, something vaguely of the nature of westward-drifting disturbance-foci. We shall see that it is of a much more general character.

(2) It is necessary to note, however, an unavoidable lacuna in the discussion. The curves of Figure 1 are representative for the European and North American region, but it is not yet clear how the picture in other regions accords with these curves. There is doubtless a similar rotation, perhaps of different periodicity, in

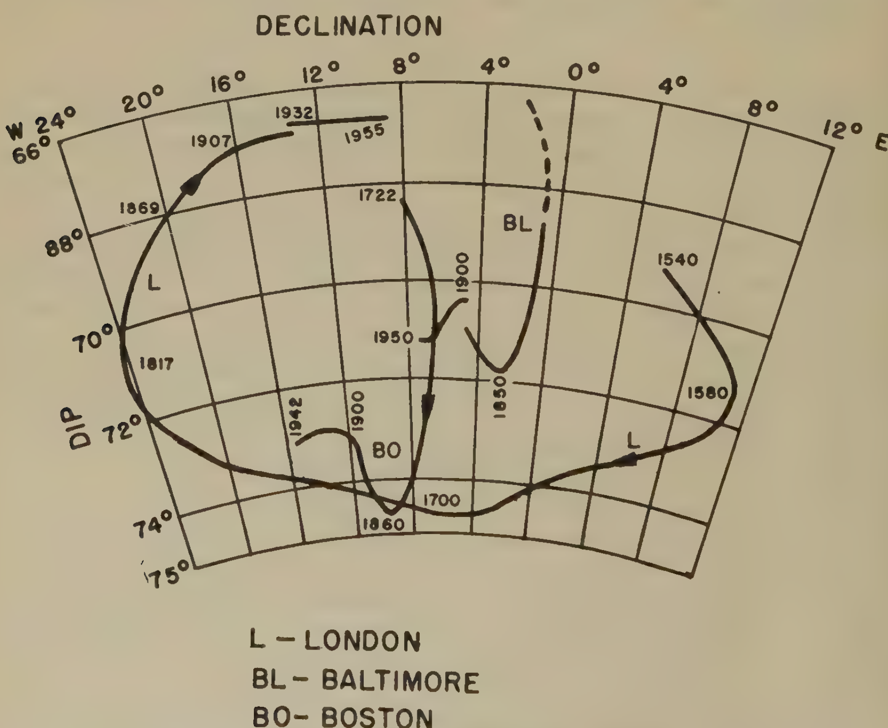

Fig. 1—*Rotation* as seen in the secular variation of magnetic declination and dip in Europe and North America, after L. A. Bauer. The phasing of the curves is consistent with the difference of longitude; thus, the most easterly deviation of the magnetic needle occurred at London about 1580-1590, at Halifax about 1750 (Hazard [18]), in Maine about 1770, at Boston 1785, at New York about 1800, at Baltimore 1802, in Indiana 1830, in Nebraska 1850 (Hazard [3], p. 214). The gap in the London curve (1925) represents the transition to Abinger data; in the Baltimore curve (1900), to Cheltenham data.

e southern hemisphere, but discussion of this point is impossible because of e scanty data. It is now reported (Imamiti [5]) that the secular variation of declition in the Japan area exhibits a periodicity of about 800 years, not 480 years. this proves to be correct, then there are *two* localized rotations in the northern misphere which will have to be explained.

It is remarkable that both the above periodicities may have been detected by rlheim-Gyllensköld, who discovered, in 1896, the general westward drift of e spherical harmonics in his analysis of the Gaussian potential of the geomagtic field. This analysis ([6], p. 24) shows one second-order and one third-order rm which should appear in local curves of declination and dip in the form of cillations with periods of 454 years and 815 years, respectively.

(3) To offset Imamiti's report and the puzzle which it sets, there are new cts testifying in favor of van Bemmelen's reconstructed pole-path, the essential rrectness of which was accepted in reference [1].

For over a century, magnetic charts have confined the dip-pole to a region on e west coast of the Boothia Peninsula, allowing it no motion other than local rations or wanderings. Ross' pole (1831), Neumayer's pole (1885), and mundsen's pole (1904) all lay close together. This apparent immobility casts ubt on all calculations such as those of van Bemmelen which, no matter how rupulously performed, were based on uncertain historical data. But in 1948, it s proved that the magnetic pole is on the move northward (Madill [7]), and on course which agrees very well with the extrapolated western side of van mmelen's pole-path. Today, its position is north of Prince of Wales Island. If r a century it wandered in nearly the same spot, this hold-up is definitely over. ne may even question that there ever was a hold-up. Whitham and Loomer [7] w report that the speed of the magnetic pole's northward movement is about four les or 0.07 degree per year. Exactly the same figure (1° in 14 years) is obtained an entirely different way by Jacobs [7]. This is just about the rate that is required take the pole from Amundsen's position of 1904 to its position in 1950 (about ° north, 100° west). In other words, it is highly possible that a uniform rate of rthward travel has been maintained for the last half-century. We point out that is is in remarkably close agreement with the motion shown by van Bemmelen ig. 4 of [1]) on the eastern side of his pole-path since 1600 A.D.—about 7° of c per century.

It now seems probable that the magnetic pole reached the southernmost int of its path in the middle of the last century (compare the American curves Fig. 1); that Ross' pole was on the eastern, descending side of the path and nundsen's pole on the westward, ascending side. It is true that the reported sitions (Fig. 4 of [1]) do not entirely accord with this hypothesis; Ross' position actually to the west of Amundsen's. But it is necessary to make allowances, st of all for the extreme observational difficulties at nearly vertical angles of p, for displacement due to local anomalies, and for the diurnal variation which, cording to Serson and Clark's observations on Prince of Wales Island in 1947, n displace the dip-pole by as much as 50 miles (Madill [7]) or, according to hitham and Loomer, by as much as 100 miles on magnetically disturbed days f. also Saxov [7], p. 23). Even if these effects are eliminated, it cannot by any eans be assumed that the actual motion of the pole will correspond to the smoothed

or averaged path shown by van Bemmelen. For instance, Whitham and Loomer find that the pole, between 1950 and 1955, moved 21 miles north and three miles *east*, while the total motion since 1904 has been *west* of north, in close agreement with the direction of van Bemmelen's path and the arctic anomaly. This means that considerable excursions from the mean path can take place, quite sufficient to account for the Ross and Amundsen positions.

Very likely more will have to be said about these excursions, because the dip-pole, being part of the pattern of magnetic meridians and isoclines, should be affected by any disturbance in this pattern, such as the westward break seen in the American curves.

(4) The westward break was simultaneous with

(*a*) Irregularities in the European variation of declination and dip which do not show in the London curve, and also with

(*b*) A widespread disturbance in the isoporic patterns (which we shall here discuss), and furthermore with

(*c*) A disturbance-pulse of such general nature that Vestine [8] detected it in the movements of the eccentric dipole which best represents the total distribution of the geomagnetic field over the earth's surface (Fig. 2).

Now modern theory ascribes the irregularity in the curves of Figure 2 to a sudden pulse in the westward drift-rotation of the earth's core relative to the mantle (Vestine, Runcorn [8, 9]). If the primary geomagnetic field is imbedded in the core and transported thereby, the pulse will naturally be exhibited in the motion of the eccentric dipole which approximately describes this field. The pulse, that is, the exchange of momentum between core and mantle, is fact and not hypothesis, for it is elsewhere demonstrable; it caused a slight irregularity in the rotation of the entire globe, and this irregularity has been detected in astronomical records.*

The above simultaneities suggest that the pulse in the westward drift is also the cause of the other disturbances. The idea is entirely reasonable, because much if not all of secular variation is due to disturbance-foci located in the core-surface and transported thereby. The resulting geomagnetic pattern will therefore show the influence of the pulse, not only because the transport-velocity of the foci is affected, but also because the above-mentioned exchange of momentum undoubtedly takes place by way of electromagnetic coupling, and the electromagnetic forces involved might be expected to modify the core-surface disturbance-foci themselves.

Thanks to Vestine, the disturbance-pulse can be accurately dated: the "longitude east" curve of Figure 2 shows that it occurred between 1880 and 1920. The westward break in the American curves of Figure 1 falls in the middle of this interval; that is, it corresponds to the top of the hump in Vestine's curve. If the westward break thus represents the center of the actual disturbance-interval at Boston and Baltimore, the magnetic needle must have been deflected eastward of its "proper" course since about 1880; the westward break initiates the recovery.

*See, however, Dauvillier ([10]), p. 35), who associates variation and pulses in the earth's rotation with changes in the total magnetic moment of the terrestrial field, and supposes that the mechanism is a magnetostrictive contraction in the ferromagnetic superficial structure of the earth. It might be remarked that the terrestrial magnetic moment has indeed varied, and magnetostriction, therefore, cannot possibly be ignored, no matter how much or how little its contribution to the effect in question.

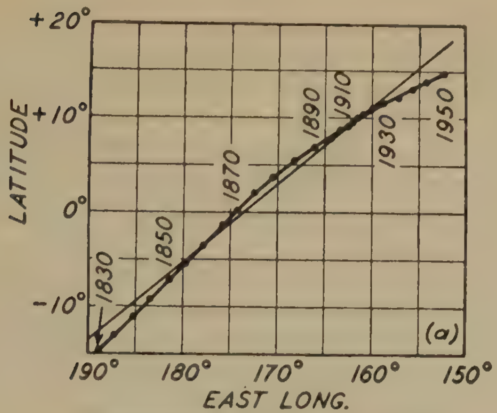

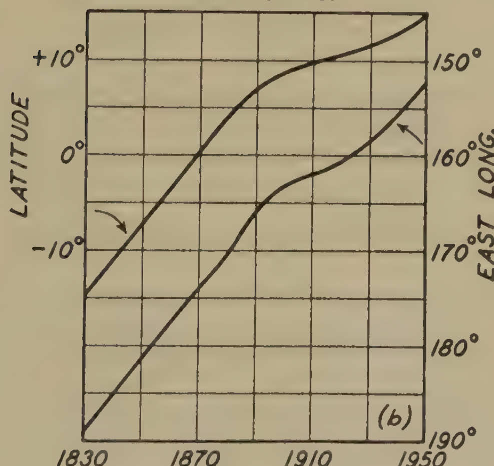

2—*Disturbance-pulse* in the *westward drift*, from Vestine [9]: (*a*) Motion of eccentric dipole, -1950, and (*b*) its latitude and longitude, 1830-1950. Compare, however, with Jory ([9], p. 1171, Fig. 4), who finds a different trend in the earlier part of the period.

The London curve shows nothing to correspond, but this is appearance only; changes of declination and dip happen to match each other, in such a way that curve is not noticeably deflected. These changes, however, are clearly seen ie separate time-curves of declination and dip, for instance at Potsdam ([11], 31); they both exhibit a marked change of slope toward 1910. Actually the urbance began about 1880. At London, the eastward movement of the needle lerated at that time, and even more after 1895 (for a detailed account, see p. 359). Between 1900 and 1910, it re-accelerated in the manner which is in the Potsdam curves, and which corresponds to Vestine's "remarkable ation in the spacing of the five-yearly points around 1910" ([8], p. 63) in the er curve of Figure 2.

5) We are taking it for granted that the motion in longitude exhibited by ine's eccentric dipole center does represent the same westward drift that is rved in the isoporic patterns on the earth's surface, in the residual non-dipole , and in the spherical harmonics. This assumption is reasonable, because the ntric dipole of Figure 2 has drifted 37° by longitude in 120 years, which agrees

closely with the rate of the westward drift in its surface manifestations—about 30° per century, or 360° in about 1200 years—as found by several investigators using different methods. (Compare, however, Bullard, *et al.* [13], Lowes [14], p. 94.)

The motion of the eccentric dipole in latitude (Fig. 2) can only correspond to the "general displacement of the whole system of magnetizing forces toward the north" (Fisk [2], p. 239), which has been recognized from analysis of the surface magnetic field.

It is important to note that the eccentric dipole, even though it is the best representation of the entire surface field and of the earth's field in exterior space, nevertheless does not represent the stable, primary terrestrial magnetization. The eccentric dipole participates in the westward drift; that is, its motion contains a component of secular variation. The primary geomagnetic field must be represented by the Gaussian centered dipole or something very close to it, because this centered dipole shows no influence of the westward drift, even though its axis is tilted 11.5° from the earth's rotational axis, and therefore should be affected by any magnetic motion in longitude. The northern axis-pole of the centered dipole has practically not moved since its discovery by Gauss over a century ago—certainly it has not moved anything like 30° per century. To repeat:

(*a*) The eccentric dipole analysis yields a global representation of a secularly varying field.

(*b*) Restriction of the analysis to a centered dipole representation discloses the existence of a basic geomagnetic field, secularly invariant or very slowly varying.

The meaning can only be that the eccentric dipole analysis does not point to the simplest physical reality, as far as the *origin* of the geomagnetic field is concerned.

It is true that van Bemmelen and Carlheim-Gyllensköld both found secular motions for the geomagnetic axis-pole, but these motions are in contradiction not only with the observed immobility of the Gaussian pole, but also with each other. Van Bemmelen's result was a southward movement, while Carlheim-Gyllensköld's was a constant westward rotation of the axis-pole around the geographic pole at an unvarying distance of 11° 44′ and with a period of 3,147 years. It is probable that the motion picked up by van Bemmelen's analysis belongs, not to the Gaussian centered-dipole axis-pole, but to the "pole" where the eccentric dipole axis intersects the earth's surface. The two points in question are not far apart (see Chapman and Bartels [11], pp. 652, 659). The eccentric dipole axis-pole, of course, has moved but even this motion cannot have been very great, for the curves of equal auroral intensity (isochasms) have not altered materially since they were mapped by H. Fritz in 1867 and 1881, on the basis of nearly five thousand auroral observations *over the period 1700-1872* ([11], p. 467). These isochasms must center on the eccentric dipole axis, since they are the termini of charged-particle orbits in space, and therefore dependent on the eccentric exterior field of the earth.

(6) The centered dipole axis-pole, then, is not displaced by the westward drift nor by the 480-year cyclic rotation. The absence of the drift-effect will be discussed in a later paper. The absence of any effect from the 480-year rotation

y be explained if the said rotation is a local phenomenon, and, moreover, ally compensated: that is, if it corresponds to a local regrouping of the magnetic es of force entirely within a certain area, so that there is no influence on the er-all surface field distribution which the geomagnetic dipole represents. That s explanation is likely to be correct is shown by the fact that the eccentric ole too is unaffected by the 480-year rotation; we can find nothing in Figure 2 correspond, in direction and phase, with the motion exhibited in Figure 1.

It would, however, be strange if neither the westward drift nor the 480-year lic rotation affected the dip-pole, which is part of the local magnetic pattern. he dip-pole is at present trapped in the arctic anomaly as we suppose, then the ect of the westward drift may be entirely obscured within the historical range data at our disposal. But the dip-pole's historical motion (van Bemmelen) is sistent with the curves of Figure 1; that is, it would appear to be controlled by cyclic rotation. This, of course, is only appearance. Moreover, there might other influences at work, for example, the 800-year periodicity apparently ibited by the declination in Japan. The immediate task is therefore to prove t the cyclic motion which controls the travel of the dip-pole actually does have eriodicity of about 480 years; that is, that it is the same cyclic motion, without nixture, as that which produces the variation of Figure 1.

The problem may be approached as follows. If the magnetic pole of a uniformly netized spherical earth were being displaced in a certain direction, then along e drawn through the pole in this direction there would be no change of declina- (except at the pole itself, which changes the declination by 180° as it passes n point to point along the line). This *zero isopor of declination*, then, shows the ction of the pole's movement. The variation of declination on one side of westward, and on the other side eastward, depending on how the motion of the e is seen from each side. In the uniformly magnetized sphere, the zero isopor ld be a great circle, passing through both magnetic poles and showing the ction of movement of both. In the distorted terrestrial field, however, this is y far from the case. Here there are (after local vagaries are smoothed out) rally two zero isoporic contours (distorted minor circles) instead of one. Each passes through one of the magnetic poles (which may, indeed, be moving e independently). This is shown schematically in Figure 3, which may be n as representing the situation in the early years of the present century. h of the zero isoporic loops more or less encircles a continental mass. The first d loop, which passes through the northern magnetic pole, encloses two isoporic of westward variation of declination in North and South America, respectively. second loop, which passes through the southern magnetic pole, encloses a sian focus and an Indian Ocean focus, again of westward variation. Between oops, on the Atlantic side of the globe, there are two foci, this time of eastward ation. Between the loops on the other side, that is, in the Pacific sector, there relative absence of foci—a strange but well-known fact (Fisk [2]).

n spite of all these complexities, the segment of the zero isopor at the magnetic should still show the motion of the pole. If we can roughly determine the ction of this segment from the positions of the two sides of the loops, insofar hese are known, then we know the direction of motion of at least an idealized netic pole.

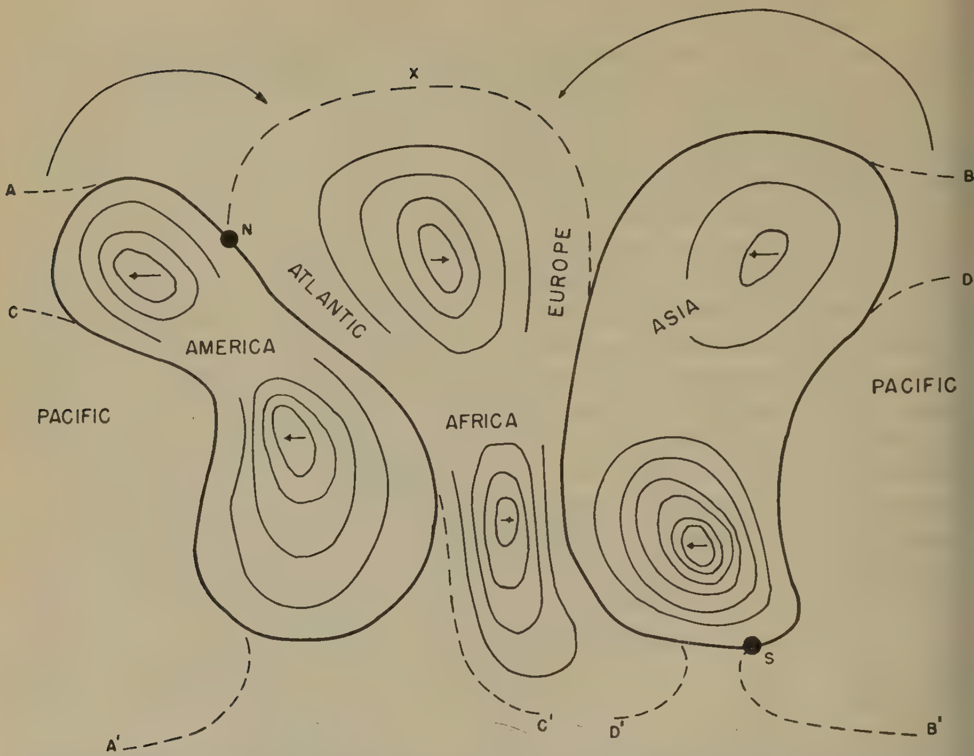

FIG. 3—Schematic chart (quasi-Mercator) of zero isopors of declination in the early part of this century, showing the westward-drifting foci and active areas, and suggesting the manner of *nodal redivision* (drawn after Fig. 4 of Fisk [3], or p. 115 of ref. [11]).

The northern pole is trapped in the anomaly and its motion strongly constrained thereby, but this effect is *local*; therefore, the motion of the isopors at a distance should more and more reflect, not the constrained motion of the dip-pole, but the true motion of the theoretical "cyclic pole." Moreover, if the cyclic rotation itself is a geographically localized phenomenon, then at still greater distances its influence should disappear from the isopor-motion; this indicates a method whereby we may, given adequate data, precisely determine the said localization.

Now the whole isoporic pattern will be carried along by the westward drift. But in North America, we find, exactly as we expect, that the motion has been at a much faster rate than can be explained by the general westward drift. There is a superimposed motion, a westward swing of the north end of the American loop and we suppose it to be due to the 480-year cyclic variation of Figure 1. Moreover as will appear, only the northern end of the loop is affected; the loop as a whole moves more sedately, no doubt in accordance with the westward drift. The 480-year cyclic variation, then, extends only to a certain distance.

The period during which we have sufficient data to construct detailed isoporic charts is so short in comparison with that of the westward drift (1,200 years or more) that it is difficult to judge how the isoporic loops drift as a whole. We may venture the conclusion that when one side of a loop drifts into the Pacific, *where the foci which it encloses must disappear*, it will swing comparatively rapidly

ross the whole ocean and close itself into a minor circle on the other side of the obe. How it will react with the other loop, during this process, is not clear.

Let us, however, disregard for the moment the slow westward drift of the loops a whole, and consider what happens to the rapidly swinging northern end of at loop which in Figure 3 encloses the Americas and passes through the northern agnetic pole. This motion, of course, cannot continue to distort the loop indefitely without something radical happening, and, in fact, what happens is this. hen the north part of the American loop swings toward the Pacific Ocean, the ading edge of the loop comes into contact, in the Alaska region, with the Eurasian op, the loop which passes through the southern magnetic pole. The approach of e two loops, in Alaska, may be seen in the Canadian magnetic chart [15] for 22; also in Fisk's chart for 1922 ([16], p. 219), and in that chart on which our gure 3 is based. After contact, the loops *redivide.* One side of the American loop, A, joins one side of the Eurasian loop at B (Fig. 3); then it contracts across the ctic to the position of the broken line X, enclosing the North Atlantic focus. the Pacific Ocean, the western side of the North American loop, at C, joins the irasian loop at D. A similar nodal redivision may occur in the antarctic: A' B' and C' to D'. The two loops have now reformed, and in positions far to the st. The difference is that eastward variation is now inside the loops and westward riation outside (between them). The top of the new Atlantic loop may now be pected to swing westward until it too breaks away, flips across the arctic, and onstitutes a loop still farther east, corresponding to the original Eurasian loop Figure 3 and like it enclosing foci of westward variation. Indeed, we may infer t the whole process is a cycle, in which the *status quo* is continually restored, ept for the changes introduced by the slow westward drift of the entire pattern, d these too will form a longer cycle.

A nodal redivision, practically simultaneous in the arctic and antarctic, appears have occurred in the early years of the present century, starting from the position things shown in Figure 3. In the process and in subsequent developments, we see features belonging to the 480-year cyclic variation as the immediate ise of the redivision, and also features which must belong to the westward drift. new loop, enclosing foci of eastward variation, has been formed in the Atlantic. is loop is drifting westward as though it had every intention of reconstituting American loop, but again its northern part is traveling faster, so that the ocess will necessarily be interrupted by further redivisions. In the Pacific also, expected new loop has formed. The effect of the westward drift on it is to make slip around south of the Pacific Ocean, *the region where there are no foci,* and vel up over Australia and the East Indies to re-form the Eurasian loop. The st steps of the process may be seen with fascinating clarity in Vestine's charts], pp. 346, 348, 350, 352, which we summarize in Figure 4. It may be interrupted further nodal redivisions, but it is evidently the long-term trend and will in e end be accomplished.

Incidentally, we note that it is hard to pin down the exact time when the revision occurred in Alaska. The earlier charts (Canadian and United States) ow the situation of Figure 3 persisting until 1922. That is, redivision was imminent t not yet accomplished; the loops were still approaching each other in Alaska. the other hand, the picture shown by Vestine [17] implies that redivision had

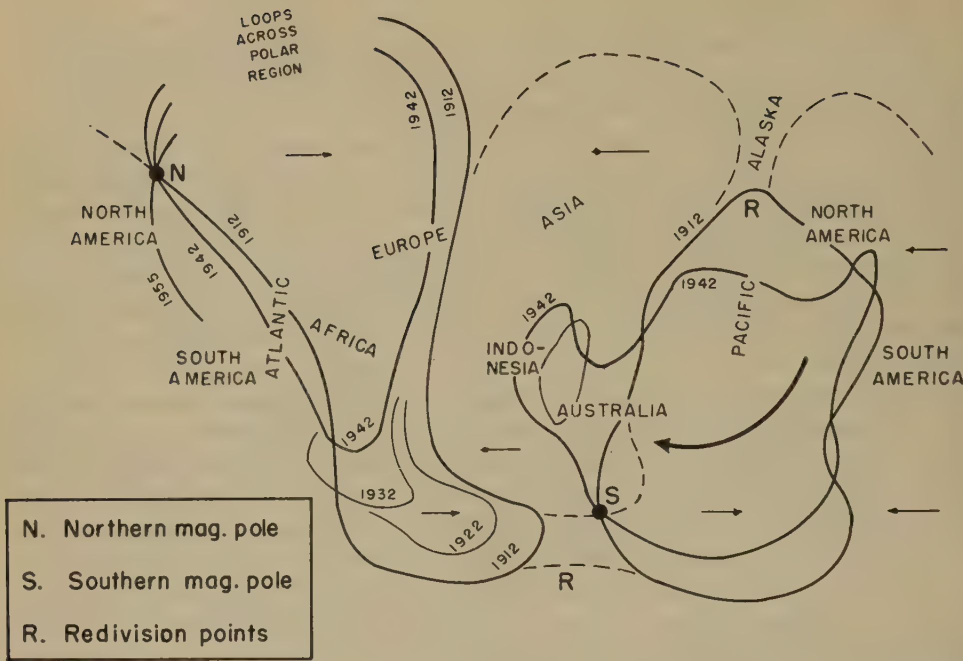

Fig. 4—Zero isopors of declination, 1912-1942, schematized from Vestine [17], pp. 346, 348, 350, 352. Nodal redivision has occurred in Alaska (before 1912 according to Vestine), and also in the antarctic south of Australia, as shown. (Sizes in the arctic and antarctic are exaggerated by the Mercator projection.) Dotted lines indicate the former Eurasian and American loops, as in Figure 3. Small arrows indicate the direction of the magnetic variation. The effect of the westward drift is well exhibited. The loop through the southern magnetic pole, which will ultimately become the Eurasian loop, is contracting southwestward from North America and simultaneously thrusting out a horn over Australia and the East Indies toward Asia (large arrow); that is, it is detouring south of the Pacific Ocean area where foci of variation are absent or very weak. The other loop (through the northern magnetic pole) is contracting swiftly across Africa toward the Atlantic; it will ultimately become the American loop.

already taken place before 1912. There is reason to question this result, even though Vestine's charts (1947) are, in other particulars, a manifest improvement over the earlier ones (compare [17], p. 261). The segment of Vestine's zero isopor north of the magnetic pole (broken line in Fig. 5*B*), which he shows in practically the same position in 1912, 1922, 1932, and 1942, is farther to the right than the Canadian isopor for 1955.5. Since the latter is based on the intensive ground and air surveys of recent years, it is unlikely to be mistaken; thus, there is little probability that the isopor could have already rotated farther than this in 1912. It will be seen in Figure 5*B* that Vestine's 1922 zero isopor (broken line) in the Pacific has an extremely sharp bend just off the Alaskan coast. This might be expected if redivision in Alaska had just taken place, but according to Vestine it had already occurred before 1912.

The sequence of six Canadian magnetic charts [15] displays an entirely consistent picture. The zero isopor north of the dip-pole rotates rapidly between 1922 and 1932; that is, there is an *unflexing* of the zero isopor upon redivision, as one would expect. After 1932, there is only a moderate clockwise rotation, and the

direction of the zero isopor closely agrees with the direction of the arctic anomaly, with the recent northward movement of the magnetic pole, and with the extrapolation of van Bemmelen's curve (Fig. 4 of [1]).

(7) The northern part of the American zero isoporic loop of Figure 3 has had the following history. In 1700 A.D., it lay far to the east, as in Figure 5*A*. Its left-hand side was in the western Atlantic; it passed over Halifax about 1750 A.D. (Hazard [18], table on p. 89), over Quebec City and the State of Maine about 1770 (compare data in caption of Fig. 1). Its right-hand side was somewhere in Russia···it swept over Danzig about 1770 A.D. (Olczak [18]). London and Paris thus lay in the region of westward variation of declination enclosed by the loop. In North America, outside the loop, the variation was eastward.

During the next two centuries, the top of the loop swung steadily to the west, pivoting around the magnetic pole. In 1812, the right-hand side passed over London, changing the variation there from westward to eastward (Fig. 1). By 1875, the left-hand side of the loop had traveled from Maine to Oregon and California, so that nearly all of North America lay within the loop and thus in the area of westward variation of declination.

FIG. 5—(*A*) Reconstructed zero isopors of declination, 1700 to 1875 A.D. The curve for 1700 is drawn through van Bemmelen's magnetic pole for that date, as in Figure 4 of reference [1], and east of Halifax (where it passed in 1750). The 1815 and 1875 loops are drawn through the magnetic pole in the Boothia Peninsula, which is approximately correct. Their paths through the United States are according to N. H. Heck's charts, as reproduced in [11]. The right-hand side of the loop swept over London, England, in 1812; in 1875, it was not far from the position shown, as may be seen from Heck's charts, [11], pp. 124-125. The path of the 1875 curve across Labrador is based on comparison with the zero isopor in 1922 [15].

(*B*) Zero isopors of declination, 1922 and 1955.5, according to [15] and [17]. The northern part of the 1922 isopor is positioned according to the Canadian magnetic chart for that year and is drawn through the magnetic pole on King William Island given on the same chart. Redivision with the Eurasian loop (here shown passing through Alaska as in the Canadian chart) is imminent, but not yet accomplished. According to Vestine, however, redivision had already taken place, in the manner shown by the broken lines.

(*C*) Approximate directions (as viewed from New England) of the zero isopor of declination through the (idealized) magnetic pole. Compare with the Boston and Baltimore curves of Figure 1. The sense in which the arrows point, of course, is determined by the direction of the variation on either side of the zero isopor.

If we now pass over the period of the disturbance-pulse (1880-1920), we find that in recent years the westward swing has continued as in Figure 5*B*. The right-hand side of the loop has entered North America from the Atlantic, and today lies north and south in almost mid-continent; accordingly, the variation in the eastern half of the continent is now eastward. Meanwhile, the left-hand side of the loop has ceased to exist as such; it has met the Eurasian loop in Alaska and *redivided.*

The arrows in Figure 5*C* represent the approximate relative directions of the smoothed zero isopor through the magnetic pole for 1700, 1815, 1875, 1922, and 1955. They indicate that there has been a rotation of somewhat over 180° in 255 years. This agrees closely with the 480-year rotation estimated from the London curve of Figure 1, and shows that the magnetic pole's secular motion has this same periodicity (Q.E.D.).

The effect of the anomaly-distortion is exhibited in the comparatively rapid rotation of the polar segment of the zero isopor between 1815 and 1875; during this period, the magnetic pole was rounding the end of its narrow elliptical orbit (compare Fig. 4 of [1]) and its direction of motion was therefore changing rapidly. Farther away, the isoporic movement shows less of this effect. At the level of the United States-Mexican border, the zero isopor between 1815 and 1875 (the period of comparatively rapid rotation at the pole) progressed only 25° in longitude, that is, at a rate not much greater than the westward drift.

The much slower rotation of the polar segment between 1922 and 1955 corresponds to the recent movement of the dip-pole northward along the side of its oval path—almost a linear movement. This slower rotation, the effect of the anomaly distortion, is again less evident at a distance; farther south, the zero isopor, better reflecting the undistorted cyclic rotation, has kept moving steadily from Newfoundland to beyond Lake Superior. Since the movement here is faster than the movement both farther north and farther south, that is, faster than the rotation of the polar segment and faster than the westward drift of the isopor in the tropical regions, it is obviously not in the nature of an accommodation or averaging between these two rotations. It is proof of the independent reality of the *undistorted* cyclic rotation (Q.E.D.).

(8) The continuous clockwise rotation exhibited in Figure 5*C* was violently upset in the period 1875-1922. Details are shown in Figure 6. Shortly after 1875, the directional arrow reversed its rotation, and retrograded (with increasing speed after ~1890) until ~1900; then it turned again and, in an abrupt jump of nearly 90°, fell in step once more with the smooth rotation of Figure 5*C*, almost as though nothing had happened.

The disturbance thus began after 1875 and was all over by 1922; compare the 1880-1920 pulse in Figure 2. The end of the retrograde motion (1900) coincides exactly with the center of the hump in Vestine's "east longitude" curve, and also with the westward break in Figure 1. Compare also the disturbance in the variation at London: the eastward movement of the needle decreased markedly after 1880; still more so after 1895; then accelerated between 1900 and 1910.

The polar segment of the zero isopor of declination, in the period 1875-1900, was twisted counter-clockwise against its previous rotation. The right-hand side of the loop accordingly receded eastward, bringing London and Potsdam into a region of less rapid eastward variation. Meanwhile the left-hand side of the loop

FIG. 6—(*A*) Zero isopors of declination, 1875 to 1922, during the disturbance-pulse, shown according to N. H. Heck's charts, as in [11], pp. 124-126. The curve for 1922 is according to Vestine, except for the broken-lined portion across Alaska, which is from the Canadian chart. To avoid disagreement with Vestine's chart for 1912, the zero isopor for 1915 ([11], p. 126) is omitted. (*B*)Approximate directions of the zero isopor through the magnetic pole, 1875 to 1922. The direction for 1922, if redrawn due north according to Vestine, would not conflict with the general picture.

drew back from California to the Mississippi Basin. After 1900, the twist was abruptly relaxed. The variation-rate at London and Potsdam increased again, and the Boston and Baltimore curves broke westward. The zero isopor across the United States was suddenly convulsed, rotating from a north-south to a west-east direction (compare Heck's curves in [11], p. 126). Figure 6 shows that this was due to the abrupt clockwise rotation of the polar segment; the zero isopor was thrown out westward in a great arc, like the snap of a whip, to meet the Eurasian loop and redivide. Or to look at it in another way, a wave of westward variation of declination rolled west and south over the American continent. In the Alaska region, it burst through the area of eastward variation (between the isoporic loops) to make contact with the area of westward variation in Asia. The most rapid propagation of the wave would be, according to the Canadian charts, between 1910 and 1920. Since 1930, the movements have been moderate: a slow clockwise rotation of the zero isopor which passes through the northern magnetic pole, and a slow southwestward contraction of the zero isopor crossing the southern United States, which is now part of the loop passing through the southern magnetic pole (Fig. 4).

The changing directions of the polar segment of the zero isopor suggest that

the movements of the dip-pole during the pulse-disturbance may have been spectacular, but there is nothing to indicate their amplitude. Probably there was a net westward or southwestward displacement, a westward break of the magnetic pole itself. The Canadian chart [15] for 1922 shows such a displacement; it locates the magnetic pole at the northern tip of King William Island. (It is probably significant that the Canadian cartographers, in 1922, were unable to make the magnetic meridians converge in the Boothia Peninsula, where all historical data indicated that the northern magnetic pole should lie.) The eastward component of the dip-pole's motion in 1950-1955, as reported by Whitham and Loomer, is perhaps a still-continuing recovery from the displacement.

It is to be noted that the whole disturbance was later than the rapid rotation of the polar segment during the period 1815-1875 when the dip-pole was making its turn-about at the southern end of its path. This motion has nothing to do with the pulse-disturbance, and, though rapid, it did not convulse the isoporic pattern.

Finally, by no means the least outcome from the above comparisons is the multiple confirmation which they provide for Vestine's results in Figure 2.

The author thanks the Defence Research Board of Canada for permission to publish this communication; also Dr. E. H. Vestine and the Carnegie Institution of Washington for permission to reproduce Figure 2; and Messrs. R. G. Madill and W. E. Scott for their courteous assistance in obtaining data.

References

[1] E. R. Hope, J. Geophys. Res., **62**, 19 (1957).
[2] H. W. Fisk, Terr. Mag., **37**, 235 (1932).
[3] H. W. Fisk, Trans. Amer. Geophys. Union, Eleventh Annual Meeting, May 1 and 2, p. 215 (1930); D. L. Hazard, *ibid.*, p. 206.
[4] L. A. Bauer, Annual Report of Smithsonian Institution, p. 195 (1913).
[5] S. Imamiti, Mem. Kakioka Magnetic Observatory, **7**, No. 2, 49 (1956).
[6] V. Carlheim-Gyllensköld, Stockholm, Astr. Iaktt., **5**, No. 5 (1896).
[7] R. G. Madill, Arctic, **1**, 8 (1948); K. Whitham and E. I. Loomer, J. Atmos. Terr. Phys., **8**, 349 (1956); J. A. Jacobs, Nature, **178**, 35 (1956); Svend Saxov, Geografisk Tidskrift, **53**, 19 (1956).
[8] E. H. Vestine, Trans. Amer. Geophys. Union, **35**, 63 (1954); S. K. Runcorn, *ibid.*, p. 49.
[9] E. H. Vestine, J. Geophys. Res., **58**, 127 (1953); F. S. Jory, Phys. Rev., **102**, 1167 (1956).
[10] A. Dauvillier, Le magnétisme des corps célestes, Tome 2, Variations et origine du géomagnétisme, Hermann et Cie., Paris (1954).
[11] S. Chapman and J. Bartels, Geomagnetism, Clarendon Press, Oxford (1940).
[12] Encyclopedia Britannica, Eleventh Edition, volume 14 (1911).
[13] E. C. Bullard, C. Freedman, H. Gellman, and J. Nixon, Phil. Trans. R. Soc., A, **243**, 67 (1950).
[14] F. J. Lowes, Ann. Géophys., **11**, 91 (1955).
[15] Magnetic Charts: **1922**, **1927**, **1932**, Topographical Survey, Dept. of Interior, Canada; *1940*, Surveys and Engineering Branch, Dept. of Mines and Resources, Canada; **1948**, Surveys and Mapping Bureau, Dept. of Mines and Resources, Canada; **1955.5**, Division of Geomagnetism, Dominion Observatories Branch, Dept. of Mines and Technical Surveys, Canada.
[16] J. A. Fleming, Proc. Phys. Soc., **58**, 213 (1946).
[17] E. H. Vestine, L. Laporte, I. Lange, and W. C. Hendrix, Washington, D. C., Carnegie Inst. Pub. 578 (1947).
[18] D. L. Hazard, U. S. Coast and Geodetic Survey Special Publication No. 44 (1917). T. Olczak, Acta Geophys. Polonica. **3**, 27 (1955).

Journal of Geophysical Research Volume 62, No. 1 March, 1957

CALCULATIONS OF IONOSPHERIC REFLECTION COEFFICIENTS AT VERY LOW RADIO FREQUENCIES

By James R. Wait and Loris B. Perry
National Bureau of Standards, Boulder, Colorado

(Received September 10, 1956)

ABSTRACT

A set of calculated curves are presented for the reflection coefficients at a sharply bounded homogeneous ionized medium with a superimposed magnetic field. The results are plotted parametrically to permit general comparisons with experimental data. Both steady-state and transient cases are considered.

Introduction

Propagation of radio waves at low radio frequencies (below 100 kc) is appreciably affected by the presence of the ionosphere for distances greater than 100 miles or so. A large number of investigations on this subject have been carried out over a period of 40 years. An excellent survey of this work prior to 1949 is given by Bremmer [see 1 of "References" at end of paper] in his treatise on wave propagation. Recently the problem of the reflection from a sharply bounded ionosphere has been considered by Budden [2], who presents a number of curves of reflection coefficients *versus* angle of incidence for fixed values of the electric properties of the ionosphere. It is the purpose of the present paper to extend these results, and in particular to illustrate the behavior of the reflection coefficients as a function of frequency. It is believed that this will facilitate comparison with data derived from variable-frequency ionospheric soundings and from frequency spectra of atmospheric waveforms. Finally, the steady-state results are used to derive the form of the transient reflected wave for an incident wave in the form of a step function.

Theoretical Basis

The derivation of the reflection coefficients for a plane wave at arbitrary incidence on a plane boundary of an anisotropic homogeneous ionosphere has been solved rigorously by Bremmer [1]. The resulting formulas are exceedingly cumbersome for purposes of computation. The same problem has also been attacked by Budden [2], who obtains somewhat more tractable results as a consequence of certain simplifying assumptions. Since Budden's results are to be the basis of the subsequent calculations, it seems desirable to outline briefly the significant features of his derivation. In what follows, M.K.S. units are used and the time factor exp $(i\omega t)$ is implied.

The starting point is the magneto-ionic formula of Appleton and Hartree [3] for the complex refractive index μ for a homogeneous ionized medium with super-

imposed magnetic field. In the region from 70 to 90 km in the ionosphere, where very low frequencies are reflected, it is permissible to employ the quasi-longitudinal approximation of Booker [4]. It is then implied that the waves after they are transmitted into the ionosphere are steeply refracted toward the vertical. Essentially this means that the refractive index does not depend to any great extent on the direction of propagation for temperate and polar latitudes, so that

$$\mu^2 \simeq 1 - i(\omega_r/\omega) \exp(\pm i\tau) \quad \text{(1)}$$

where

$$\tan \tau = \omega_L/\nu$$

and

$$\omega_r = \omega_0^2(\nu^2 + \omega_L^2)^{-\frac{1}{2}}$$

In the above,

$\omega_0^2 = Ne^2/\epsilon_0 m$

N = number of electrons per meter^3

e and m = charge and mass of electrons

$\epsilon_0 = 8.854 \times 10^{-12}$

ν = collision frequency

$\omega_L = (4\pi \times 10^{-7})\, H\, e/m$

and

H = strength of the earth's magnetic field

It is now desirable to consider four reflection coefficients $_{\|}R_{\|}$, $_{\|}R_{\perp}$, $_{\perp}R_{\|}$, and $_{\perp}R_{\perp}$ to indicate the complex ratio of a specified electric field in the wave after reflection to a specified electric field in the wave before reflection. The first subscript denotes whether the electric field in the wave is parallel ($\|$) or perpendicular ($\perp$) to the plane of incidence, and the second subscript refers in the same way to the reflected wave. A Cartesian coordinate system (x, y, z) is now taken with z measured vertically upwards. The incident wave has its normal in the xz plane inclined at an angle θ to the z axis. The components of the electric field are $E_{\|}$ in the xz plane and $E_{\perp}$ perpendicular to this plane (that is, in the direction of increasing y). When the + sign is taken in equation (1), the refractive index is denoted μ_o, corresponding to the ordinary wave; and when the − sign is taken, the refractive index is denoted μ_e, corresponding to the extraordinary wave. With this convention, it can be shown that [4]

$$E_{\perp o}/E_{\| o} = -i \qquad \text{and} \qquad E_{\perp e}/E_{\| e} = i$$

in the northern hemisphere.

The Reflection Coefficients

The incident wave is now characterized by a factor exp $[-i\omega(x \sin\theta + z \cos$

/c], and the reflected wave, therefore, contains a factor exp $[-i\omega(x \sin \theta - z$ s $\theta)/c]$. Furthermore, the transmitted waves have factors exp $[-i\omega(x \sin \theta_o + z$ s $\theta_o)\mu_o/c]$ and exp $[-i\omega(x \sin \theta_e + z \cos \theta_e)\mu_e/c]$. The reflection coefficients are w obtained in the usual way by matching tangential field components at the r-ionosphere interface. The results, expressed in a form suitable for computation, e listed below.

$$_{\parallel}R_{\parallel} = \{(\mu_o + \mu_e)(C^2 - C_oC_e) + (\mu_o\mu_e - 1)(C_o + C_e)C\}/D \quad \text{(2a)}$$

$$_{\parallel}R_{\perp} = 2iC(\mu_oC_o - \mu_eC_e)/D \quad \text{(2b)}$$

$$_{\perp}R_{\parallel} = 2iC(\mu_oC_e - \mu_eC_o)/D \quad \text{(3a)}$$

$$_{\perp}R_{\perp} = \{(\mu_o + \mu_e)(C^2 - C_oC_e) - (\mu_o\mu_e - 1)(C_o + C_e)C\}/D \quad \text{(3b)}$$

here

$$\left.\begin{array}{l} \mu_e \sin \theta_e = \mu \sin \theta, \qquad \mu_o \sin \theta_o = \mu \sin \theta \\ D = (\mu_o + \mu_e)(C^2 + C_oC_e) + (\mu_o\mu_e + 1)(C_o + C_e)C \\ C = \cos \theta, \qquad C_o = \cos \theta_o, \qquad C_e = \cos \theta_e \end{array}\right\} \quad \text{(4)}$$

nd

When ω/ω_r is small compared to one, the above formulas can be approximated

$$\begin{smallmatrix}\parallel\\ \perp\end{smallmatrix}R\begin{smallmatrix}\parallel\\ \perp\end{smallmatrix} \simeq \frac{(1 + i)(\omega/\omega_r)^{\frac{1}{2}} \cos \tau/2\,(\cos^2 \theta - 1) \pm 2^{\frac{1}{2}}[1 - i\omega/\omega_r] \cos \theta}{(1 + i)(\omega/\omega_r)^{\frac{1}{2}} \cos \tau/2\,(\cos^2 \theta + 1) + 2^{\frac{1}{2}}[1 + i\omega/\omega_r] \cos \theta} \quad \text{(5)}$$

d

$$\begin{smallmatrix}\parallel\\ \perp\end{smallmatrix}R\begin{smallmatrix}\perp\\ \parallel\end{smallmatrix} \simeq \frac{-2(\omega/\omega_r)^{\frac{1}{2}}(1 + i) \cos \theta \sin (\tau/2)}{(1 + i)(\omega/\omega_r)^{\frac{1}{2}} \cos \tau/2\,(\cos^2 \theta + 1) + 2^{\frac{1}{2}}[1 + i\omega/\omega_r] \cos \theta} \quad \text{(6)}$$

It is clearly evident from the preceding equations that if the earth's magnetic eld is removed the value of τ is zero, and consequently $_{\parallel}R_{\perp} = {}_{\perp}R_{\parallel} = 0$. In general, owever, the reflected waves are elliptically polarized and the polarization ellipse epends on τ. To illustrate the numerical nature of all four of these reflection oefficients as a function of frequency, they are shown plotted in Figures 1 to 6 a function of the frequency parameter ω/ω_r for fixed values of the angle of cidence. Two values of τ are considered, namely, 0° corresponding to the isotropic nosphere and 60° which is believed to be of the correct order of magnitude for w radio frequencies. The calculations were carried out using the complete formulas dicated by equations (2), (3), and (4). The approximate relations [equations) and (6)] were used to check the computations for small values of (ω/ω_r).

Discussion of the Frequency Spectrum Curves

It is interesting to note that the general shapes of the $_{\parallel}R_{\parallel}$ and $_{\perp}R_{\perp}$ curves e not appreciably different for the two values of τ. This is particularly true for rge angles of incidence. The pronounced dip in the $_{\parallel}R_{\parallel}$ curves for large angles incidence is a quasi-Brewster effect, being where the incident wave is most early matched to the ionosphere. This brings up immediately an interesting estion. Suppose that the reflection coefficient $_{\parallel}R_{\parallel}$ at $\theta = 80°$ was deduced

Figs. 1 to 6—The amplitude and phase of the reflection coefficients $_{\parallel}R_{\parallel}$, $_{\perp}R_{\perp}$, $_{\parallel}R_{\perp}$, and $_{\perp}R_{\parallel}$ are shown plotted for various angles of incidence as a function and the angular frequency ω expressed as ratio to ω_r. It is believed that ω_r, which is approximately proportional to the ratio N/ν, is of the order of 5×10^5 for a summer night and 1.5×10^6 for a summer day at frequencies of the order of 16 kc.

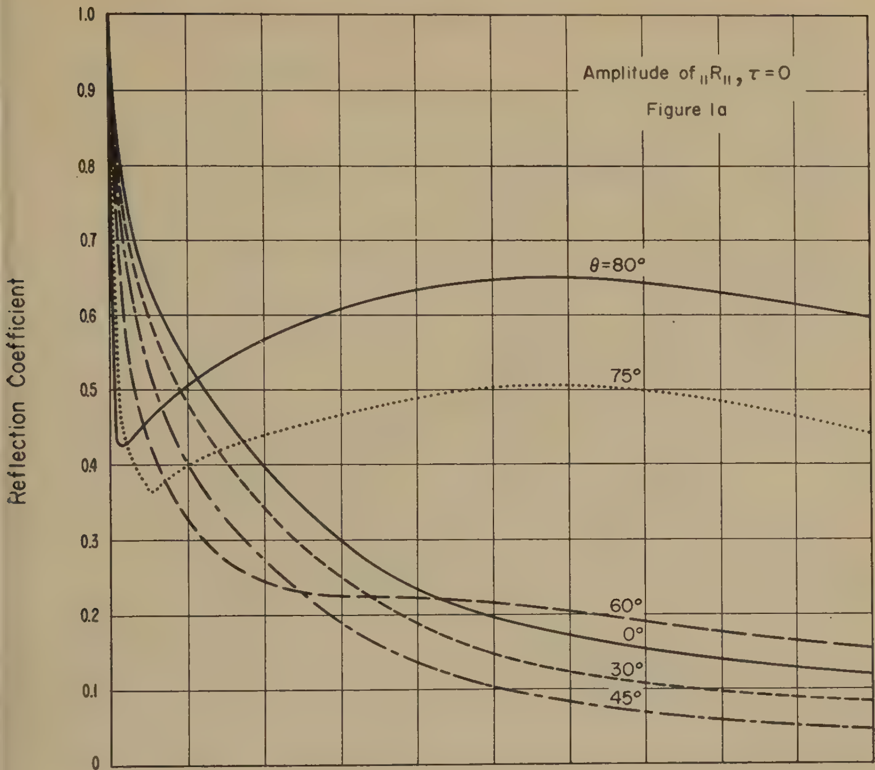
Amplitude of ${}_{\parallel}R_{\parallel}$, $\tau = 0$
Figure 1a
Reflection Coefficient
1.0
0.9
0.8
0.7
0.6
0.5
0.4
0.3
0.2
0.1
0
θ=80°
75°
60°
0°
30°
45°

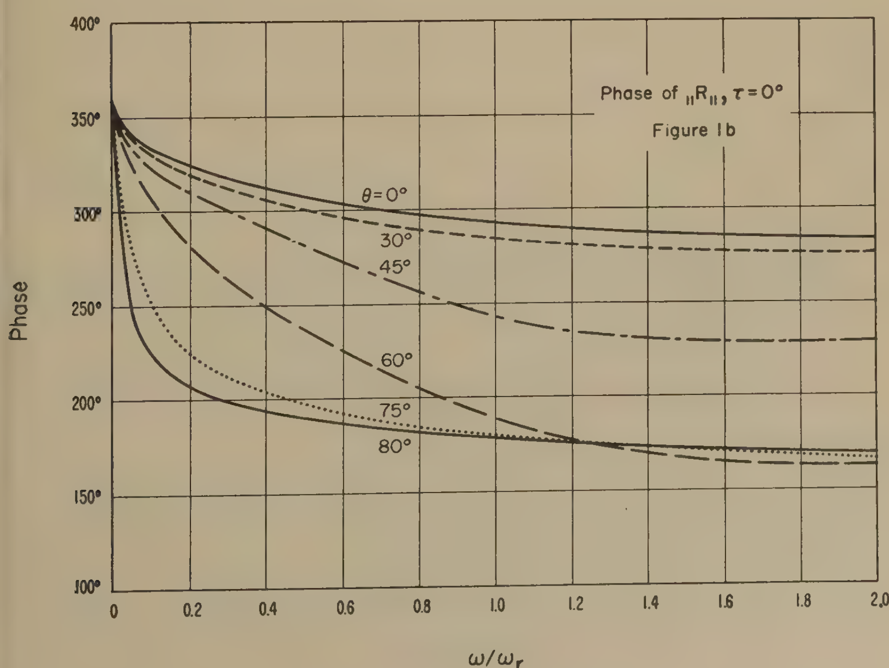
Phase of ${}_{\parallel}R_{\parallel}$, $\tau = 0°$
Figure 1b
Phase
400°
350°
300°
250°
200°
150°
100°
θ= 0°
30°
45°
60°
75°
80°
0
0.2
0.4
0.6
0.8
1.0
1.2
1.4
1.6
1.8
2.0
ω/ω_r

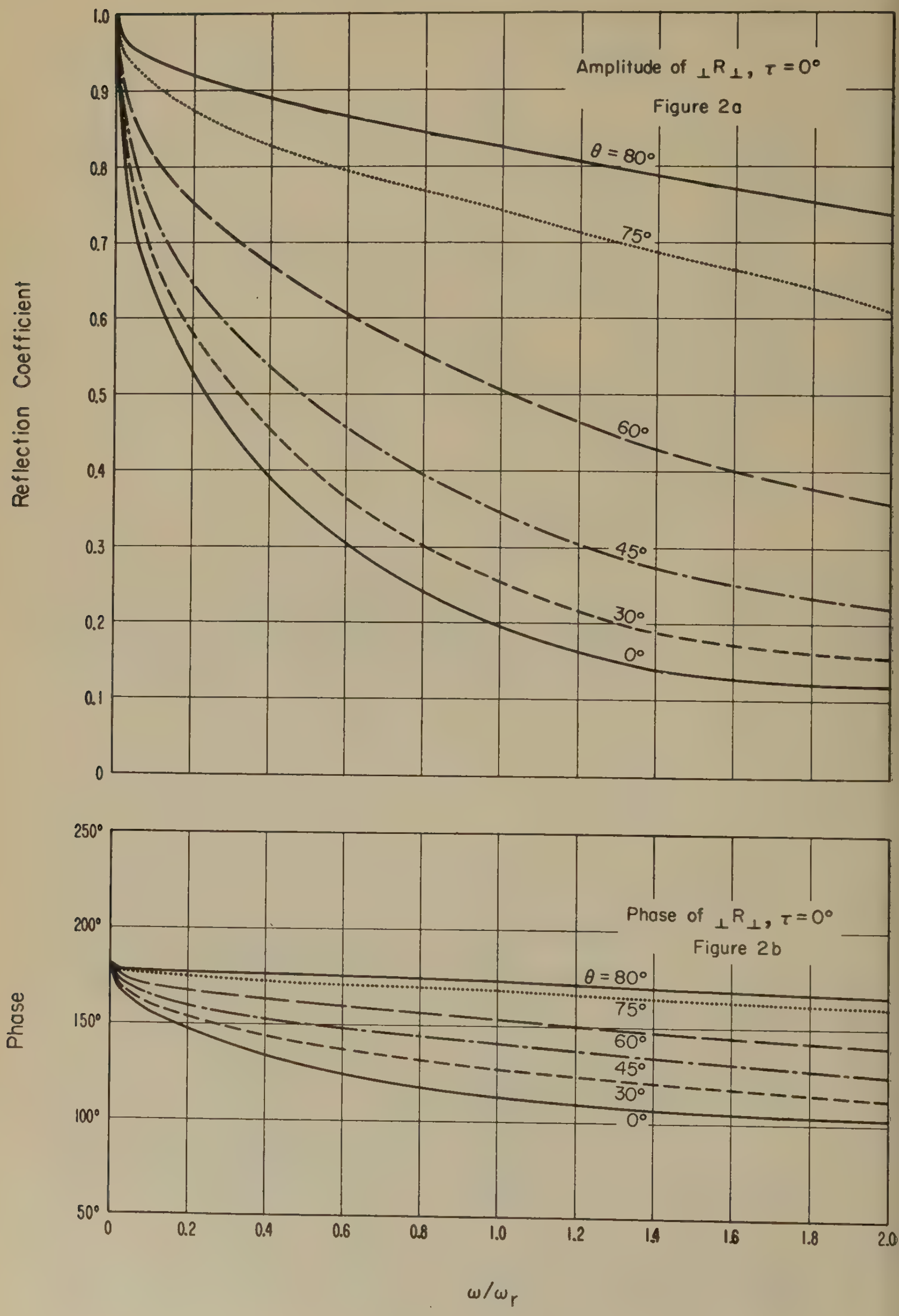
Amplitude of ⊥R⊥, τ = 0°
Figure 2a
Reflection Coefficient
1.0
0.9
0.8
0.7
0.6
0.5
0.4
0.3
0.2
0.1
0
θ = 80°
75°
60°
45°
30°
0°
Phase of ⊥R⊥, τ = 0°
Figure 2b
Phase
250°
200°
150°
100°
50°
θ = 80°
75°
60°
45°
30°
0°
0
0.2
0.4
0.6
0.8
1.0
1.2
1.4
1.6
1.8
2.0
ω/ω_r

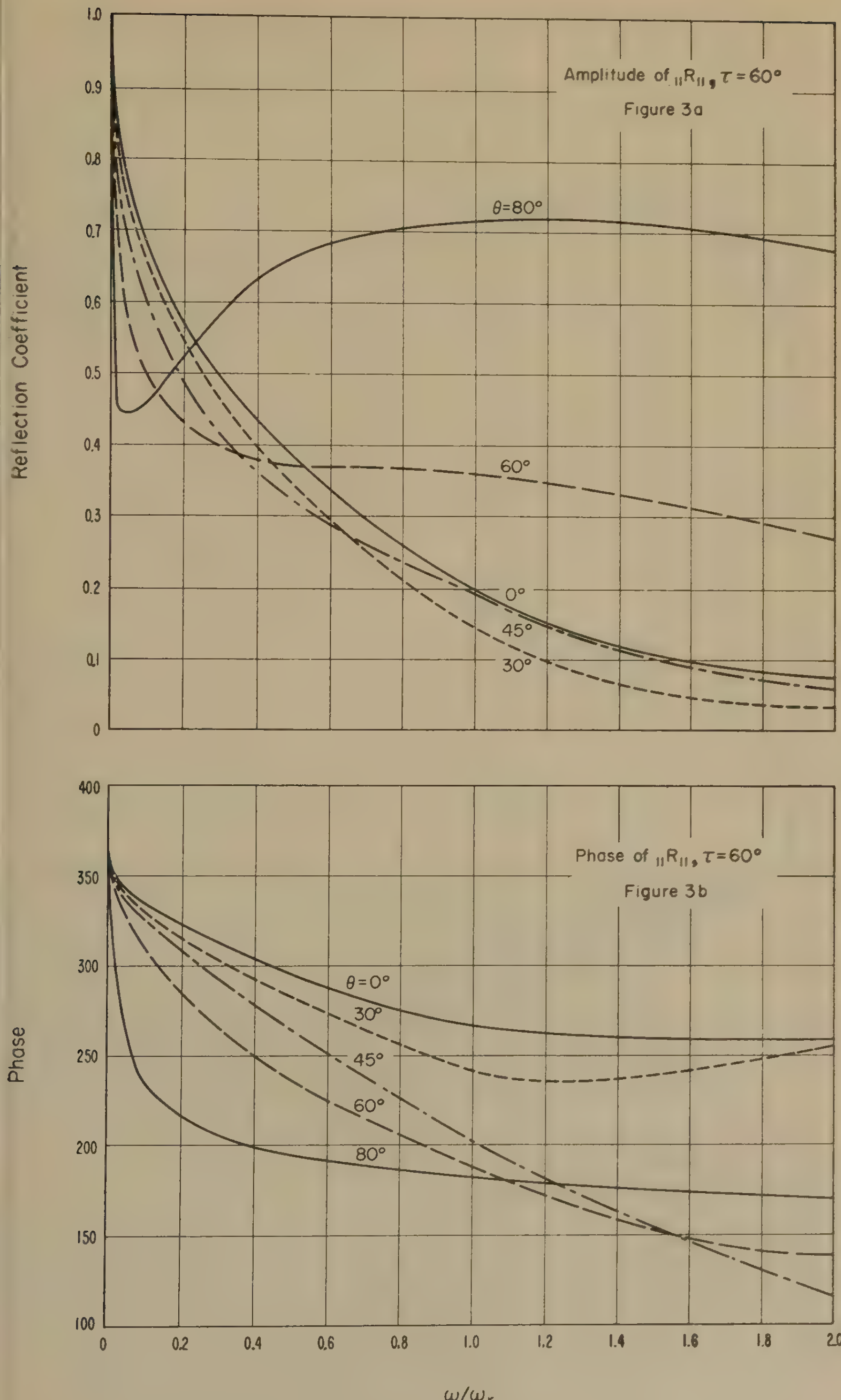
Amplitude of $_{11}R_{11}$, $\tau = 60°$
Figure 3a
θ=80°
60°
0°
45°
30°
Reflection Coefficient
1.0
0.9
0.8
0.7
0.6
0.5
0.4
0.3
0.2
0.1
0
Phase of $_{11}R_{11}$, $\tau = 60°$
Figure 3b
θ=0°
30°
45°
60°
80°
Phase
400
350
300
250
200
150
100
0
0.2
0.4
0.6
0.8
1.0
1.2
1.4
1.6
1.8
2.0
ω/ω_r

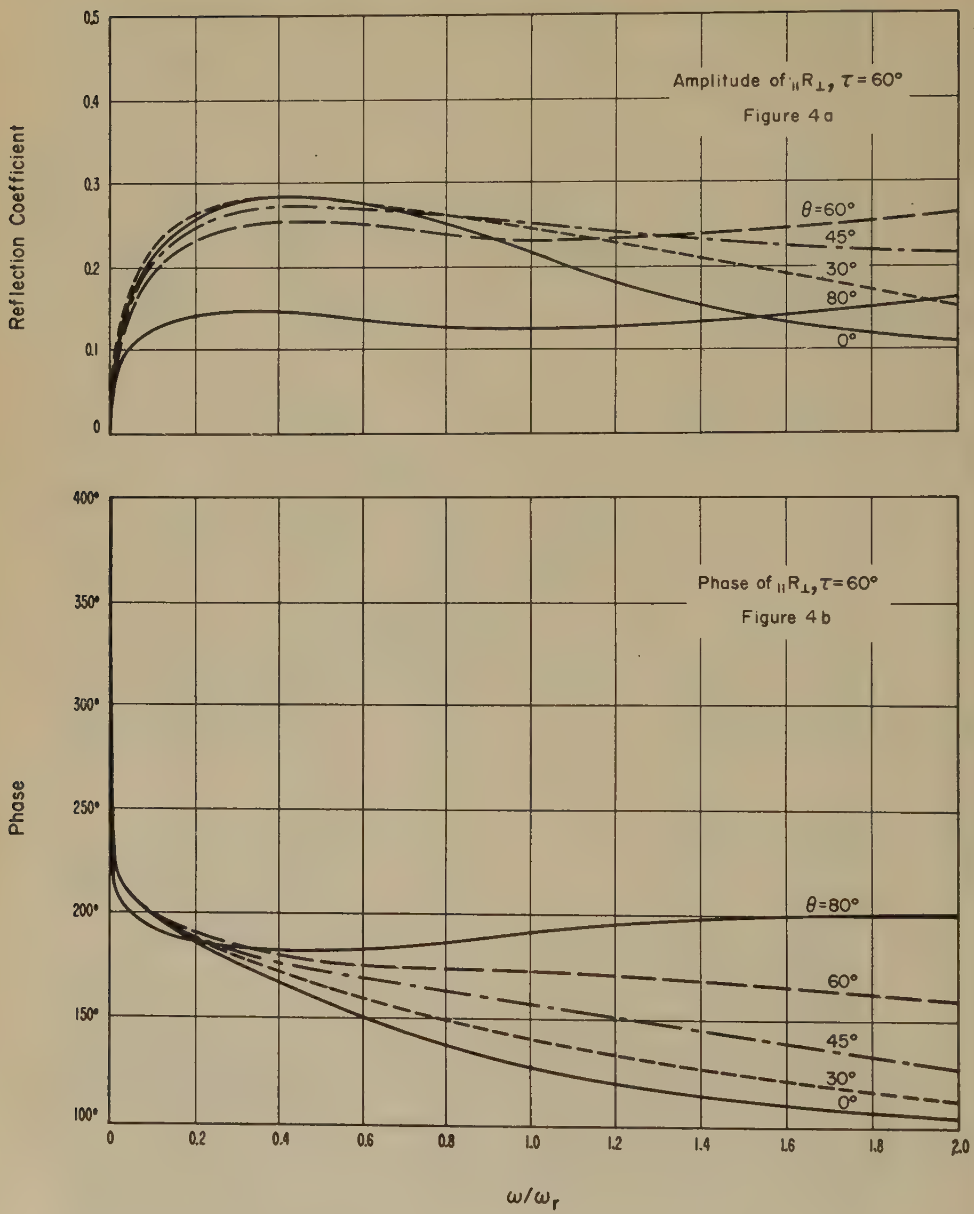
Reflection Coefficient
0.5
0.4
0.3
0.2
0.1
0
Amplitude of $_{\parallel}R_{\perp}$, $\tau = 60°$
Figure 4a
$\theta = 60°$
45°
30°
80°
0°
Phase
400°
350°
300°
250°
200°
150°
100°
Phase of $_{\parallel}R_{\perp}$, $\tau = 60°$
Figure 4b
$\theta = 80°$
60°
45°
30°
0°
0
0.2
0.4
0.6
0.8
1.0
1.2
1.4
1.6
1.8
2.0
ω/ω_r

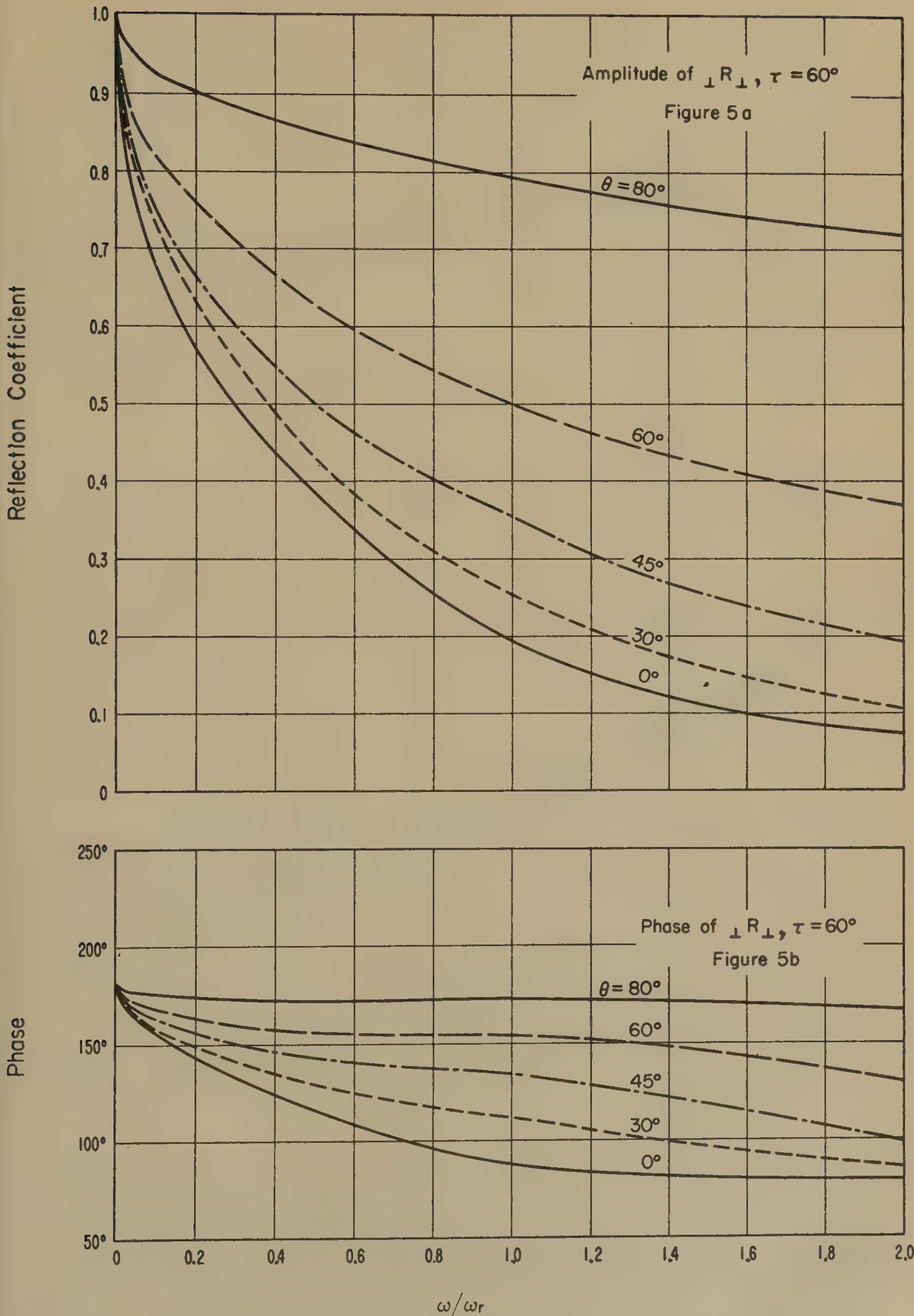
Amplitude of $_\perp R_\perp$, $\tau = 60°$
Figure 5a
Reflection Coefficient
1.0
0.9
0.8
0.7
0.6
0.5
0.4
0.3
0.2
0.1
0
$\theta = 80°$
60°
45°
30°
0°
Phase of $_\perp R_\perp$, $\tau = 60°$
Figure 5b
Phase
250°
200°
150°
100°
50°
$\theta = 80°$
60°
45°
30°
0°
0
0.2
0.4
0.6
0.8
1.0
1.2
1.4
1.6
1.8
2.0
ω/ω_r

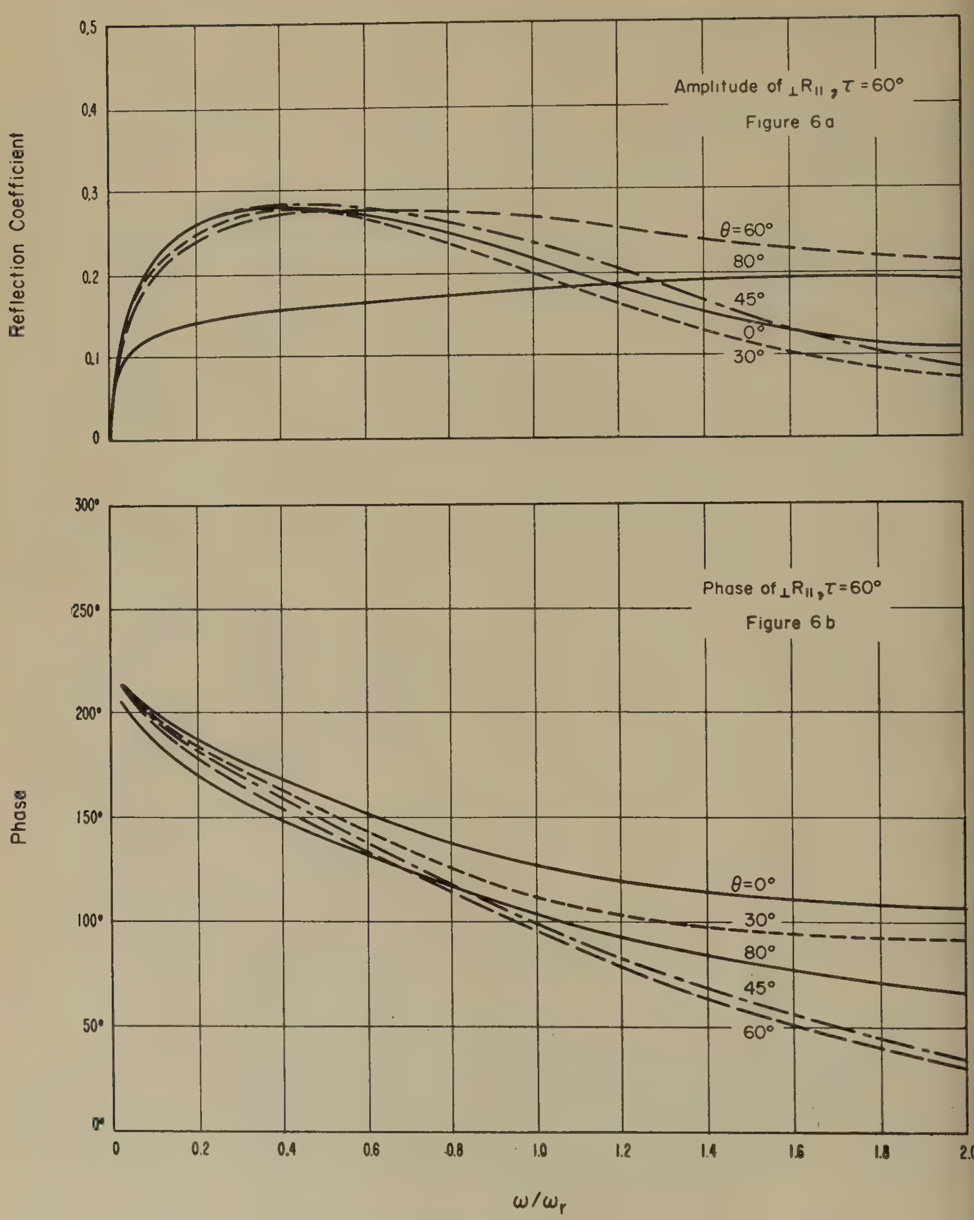

from experimental observations and found to be 0.5. Then ω/ω_r could be either about 0.16 or about 0.02, as indicated in Figure 3*a*. The choice of these two values is best ascertained by measuring the value of $_{\parallel}R_{\perp}$. As seen from Figure 4*a*, this would be about 0.25 for $\omega/\omega_r = 0.16$ and less than 0.05 for $\omega/\omega_r = 0.02$. Experimental results [5] at 16 kc indicate that $_{\parallel}R_{\perp}$ is comparable to $_{\parallel}R_{\parallel}$ at these oblique angles and hence a value of $_{\parallel}R_{\parallel}$ equal to 0.25 would not be unreasonable, and consequently the correct choice for ω/ω_r would be 0.16.

The above example was chosen to illustrate the complicated behavior of the ospherically reflected wave at large oblique angles of incidence. Most earlier k on the propagation theory of V.L.F. is based on the premise that the iono-ere can be represented as a mirror reflector with the finite conductivity being sidered as a perturbation to the case of lossless reflection. This assumption underlies the derivation of the Austin-Cohen formula given by Bremmer [1] the recent work of Schumann [6]. It is believed that these calculations indicate electron-density values derived by these workers are too high by a factor of or so, as a result of assuming that the effective ω/ω_r values are to the left of minima in the curves in Figure 1*a* or 3*a*. This matter has been pursued further rigorously solving for the wave-guide modes that can exist between the earth the ionosphere without making the assumption that the losses can be accounted by a perturbation of the lossless case.*

Further Comparison with Experimental Data

It is worth while to make some further comparisons of the calculated reflection fficients ${}_{\|}R_{\|}$ and ${}_{\|}R_{\perp}$ with the experimental results at 16 kc taken by Bain, acewell, Straker, and Westcott [9]. One of the most striking features of their a was the consistent change of the state of polarization of the downcoming ve, being nearly circular at short ranges (that is, when $\theta < 30°$) and becoming ar at larger ranges (that is, when $\theta > 60°$). On examining Figures 3*b* and 4*b*, seen that the phase difference between ${}_{\|}R_{\|}$ and ${}_{\|}R_{\perp}$ for $\theta \leq 30°$ is of the er of 100°, corresponding to approximately circular polarization for a range of ω_r from about 0.4 to 1.0 or more. Furthermore, from these same curves, it is that the phase difference, for $\theta \simeq 80°$, is less than 10°, corresponding to roximately linear polarization.

They also find that $| {}_{\|}R_{\|}/{}_{\|}R_{\perp} |$ is about 1.25 for most of their results. On mining Figures 3*a* and 4*a*, it would appear that this would be valid within 20 cent for angles of incidence $\leq 60°$ for ω/ω_r in the range from 0.2 to 0.6. At ger ranges, corresponding, say, to $\theta = 80°$, the ratio would still be near 1.25 ω/ω_r was somewhat smaller, say, 0.1 to 0.3.

It has been found also that the reflection coefficient ${}_{\|}R_{\|}$ on a summer night of the order of 0.5 both at short and larger ranges (that is, $\theta < 80°$) [9]. This ıld be compatible with Figure 3*a* if ω/ω_r is anywhere in the range from about 5 to 0.3. On the other hand, the reflection coefficient ${}_{\|}R_{\|}$ on a summer day is the order of 0.2 for short ranges (that is, $\theta \leq 45°$) and about 0.35 for larger ges ($\theta \geq 60°$). This most closely corresponds to the curves in Figure 3*a* when ω_r is near 0.8.

Values of ω/ω_r at 16 kc that are most nearly representative of a summer night a summer day could be taken as 0.2 and 0.6, respectively.

The Transient Response

Although the preceding set of curves plotted on a frequency basis are probably equate for interpreting future experimental measurements, it is possible that ne benefit might be gained in examining the transient response. If the source

*To be published in collaboration with Dr. H. H. Howe.

were a lightning stroke, the waveform of the current variation can be very complicated; however, invoking the principle of superposition, the waveform of the ionospherically reflected wave can be derived from the response to a step-function incident field. Therefore, the electric field of the incident wave is taken to be $E_0u(t)$ polarized in the plane of incidence [$u(t) = 1$ for $t > 0$, $= 0$ for $t < 0$]. The frequency spectrum of the incident wave is then given by

$$\int_{-\infty}^{\infty} e^{-i\omega t} E_0 u(t)\, \mathrm{d}t = E_0/i\omega \qquad (7)$$

and therefore the spectrum of the reflected wave is $(E_0/i\omega)R(\omega)$, where $R(\omega)$ is an appropriate reflection coefficient expressed as a function of frequency. The waveform of the appropriate field component $E(t)$ is then obtained by an inverse Fourier transformation,

$$E(t) = \frac{E_0}{2\pi i} \int_{c-i\infty}^{c+i\infty} [R(\omega)/i\omega]\, \mathrm{d}(i\omega) \qquad (8)$$

where c is a small positive real constant introduced to insure that the integration contour passes to the right of any pole on the imaginary axis of $i\omega$. $R(\omega)/i\omega$ is, of course, the Laplace transform of $E(t)$. It was shown in an earlier paper [7] that the integral could be evaluated directly if the ionosphere was isotropic (that is, $\tau = 0$). In the general case, it appears to be preferable to employ a numerical technique, since $R(\omega)/i\omega$ has a very complicated analytical form. It is not difficult, however, to show that [8]

$$E(t) = E_0\left[A + \frac{2}{\pi} \int_0^{\infty} \frac{[Im.\, R(\omega)]}{\omega} \cos \omega t\, \mathrm{d}\omega \right] u(t) \qquad (9)$$

where $A = \lim_{\omega \to 0} R(\omega)$ and where $Im.$ indicates that the imaginary part is to be taken. This integral has been evaluated by writing it in dimensionless form, as follows:

$$I = \frac{2}{\pi} \int_0^{\infty} P(\Omega) \cos \Omega T\, \mathrm{d}\Omega \qquad (10)$$

where

$$P(\Omega) = \frac{Im.\, R(\Omega)}{\Omega}$$

with $\Omega = \omega/\omega_r$ and $T = \omega_r t$. Now it can be shown that ${}_{\parallel}R_{\parallel}$ and ${}_{\perp}R_{\perp}$ are proportional to $(\omega/\omega_r)^{\frac{1}{2}}$ as ω approaches zero, so for these cases

$$P(\Omega) = P(\delta)(\delta/\Omega)^{1/2} \qquad (11)$$

where δ is some very small value (say 10^{-3}). Therefore,

$$\left.\begin{aligned} I &= \frac{2P(\delta)}{\pi} \int_0^{\delta} (\delta/\Omega)^{\frac{1}{2}} \cos \Omega T\, \mathrm{d}\Omega + \frac{2}{\pi} \int_{\delta}^{\infty} P(\Omega) \cos \Omega T\, \mathrm{d}\Omega \\ &\simeq \frac{4\delta}{\pi} P(\delta) + \frac{2}{\pi} \int_{\delta}^{\infty} P(\Omega) \cos \Omega T\, \mathrm{d}\Omega \end{aligned}\right\} \qquad (12)$$

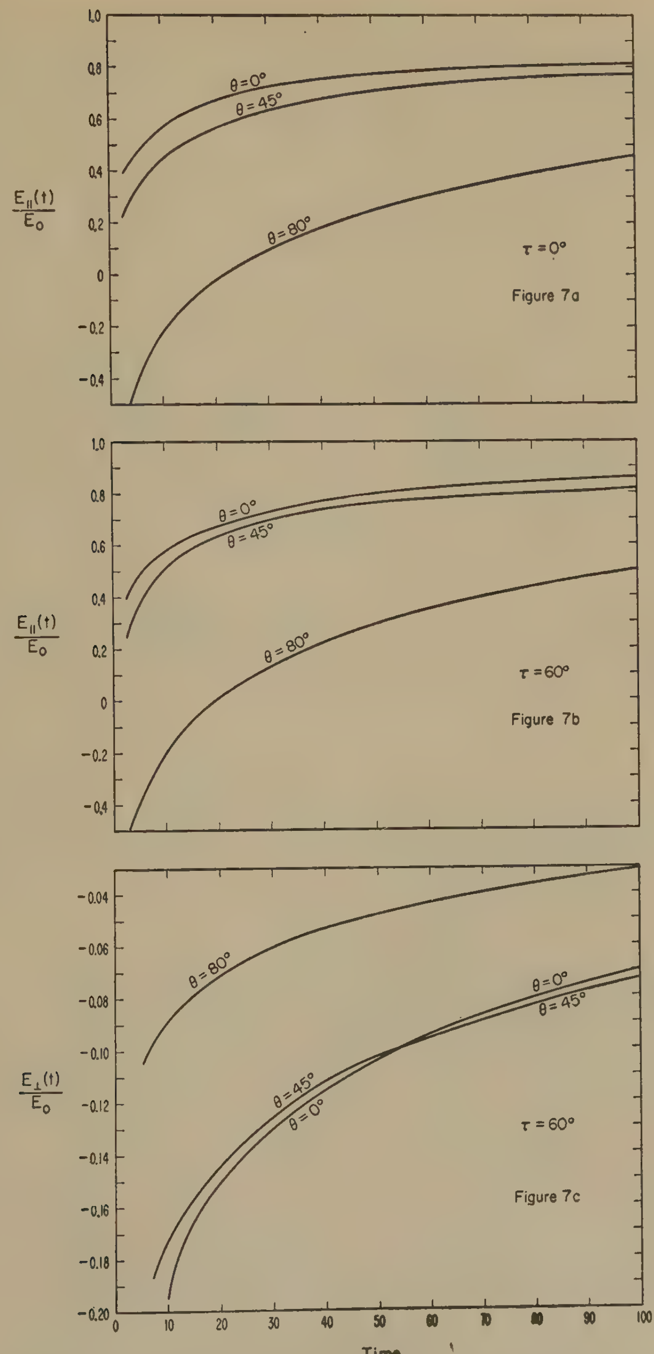

7—The waveform of the electric field in the reflected wave is shown for an incident wave se electric field is in the plane of incidence and varies with time as a step function. The abscissa oted as "TIME" is actually $\omega_r t$, where t is the time in seconds measured from the point of the initial rise of the waveform.

subject to $\delta T \ll 1$. The integrand $P(\Omega)$ is now always finite over the integration range. In carrying out the calculations for the cross-polarized reflection fields involving ${}_{\|}R_{\perp}$ and ${}_{\perp}R_{\|}$, the function $P(\Omega)$ does not have a singularity at $\Omega = 0$ and consequently δ can be set equal to zero.

Employing numerical integrations of the integral I, the waveform of the electric field in the reflected waves is obtained for a step-function incident field. The results are shown in Figure 7 plotted as a function of $T(= \omega_r t)$ for the case where the electric field of the incident wave is in the plane of incidence. The subscripts $\|$ and $\perp$ on $E(t)$ refer to the polarization of the reflected wave. For the case $\tau = 0°$, the ionosphere is effectively isotropic and consequently $E_{\|}(t)$ can be compared with some previous calculations where the integral can be evaluated in closed form [7]. The agreement is very good, indicating that the numerical procedure adopted here is probably quite adequate. The field components $E_{\|}(t)$ and $E_{\perp}(t)$ are also shown in Figure 7 for the case $\tau = 60°$, which is probably typical of the ionosphere for the range of time T indicated on the curves. Again it is noted that $E_{\|}(t)$ is very similar for the two cases of $\tau = 0°$ and $\tau = 60°$. On the other hand, the cross-polarized field $E_{\perp}(t)$ vanishes for $\tau = 0°$ and is quite appreciable for $\tau = 60°$.

The reflected field waveforms shown here could be employed, in conjunction with the superposition theorem, to calculate the response for an incident wave with an arbitrary electric-field variation. This is believed to be a worthy subject for future study.

References

[1] H. Bremmer, Terrestrial Radio Waves, Elsevier Publishing Co., New York and Amsterdam; also see Dr. Bremmer's contribution to the new edition of Handbuch der Physik to be published by Julius Springer, Berlin.

[2] K. G. Budden, Phil. Mag., **42**, 833 (1951).

[3] E. V. Appleton, J. Inst. Elec. Eng., **71**, 642 (1932).

[4] H. G. Booker, Proc. R. Soc., A, **150**, 267 (1935).

[5] K. Weekes, Proc. Inst. Elec. Eng., **97**, Pt. III, 100 (1950).

[6] W. O. Schumann, Zs. angew. Phys., **6**, 35 (1954).

[7] J. R. Wait and C. Froese, J. Geophys. Res., **60**, 97 (1955).

[8] J. R. Wait, Can. J. Tech., **31**, 127 (1953).

[9] W. C. Bain, R. N. Bracewell, T. W. Straker, and B. A. Westcott, Proc. Inst. Elec. Eng., **99**, Pt. IV, 250 (1952).

UPPER AIR PRESSURE AND DENSITY MEASUREMENTS FROM 90 TO 220 KILOMETERS WITH THE VIKING 7 ROCKET

By R. HOROWITZ AND H. E. LAGOW

U. S. Naval Research Laboratory, Washington 25, D. C.

(Received October 6, 1956)

ABSTRACT

The density and pressure of the atmosphere from 90 to 220 km above White Sands, New Mexico, were determined from the Viking 7 rocket flight on 7 August 1951 at 11:00 a.m. MST. A Philips ionization gage was used to measure pressure and pressure changes on the side of the nose cone of the rolling rocket. Measured pressure in the 90 to 105 km region were corrected for velocity ram and residual gas, and were approximately one-fourth of the Rocket Panel values. The derived pressure of 3×10^{-7} mm Hg at 220 km is twice the corresponding Rocket Panel value. Densities were measured from 120 to 185 km and at 220 km. The 220 km density value of 9×10^{-8} gm/m^3 agrees with the Rocket Panel value. However, the density values at the lower altitudes are one-fourth to one-half those of the Rocket Panel. These lower density values in the 100 to 130 km region are in good agreement with values obtained from X-ray absorption experiments. Scale heights, (RT/Mg), derived from the density data above 140 km, are approximately a factor of two higher than Rocket Panel values.

INTRODUCTION

Upper atmosphere pressure, temperature, and density values have been obtained by several groups using various rocket-borne and ground-based techniques. The rocket techniques and results are described by Newell [see 1 of "References" at end of paper], the Rocket Panel [2], and Boyd, Seaton, and Massey [3]. The ground-based measurements have been summarized by Mitra [4].

Havens, Koll, and LaGow [5] showed that, while gage pressure measurements for pressures less than about 10^{-4} mm Hg were affected by residual rocket gas, atmospheric density measurements could be made in this region provided the rocket rolled rapidly, and complete rocket aspect and trajectory information were available. The experiment reported here was flown to increase the altitude range of measurements and to check the values already obtained. The telemetered records showed pressure changes having a frequency equal to that of rocket roll. The peak altitude density was deduced and published immediately [15]. However, at the lower altitudes, the ascent densities were incompatible with those obtained during descent. After considering possible sources for the observed discrepancies, it was plausibly concluded that interference from rocket gas on the descent at-

tenuated and distorted the pressure signal. Hence, preliminary figures taken from ascent data were released giving gage pressure at 100 km and a density value at 160 km [2, 16]. The effect of residual gas on the roll pressure signals could be studied after a similar experiment was flown on the Viking 10 rocket in May 1954, since on this flight strong gas interference was known to have taken place. The dissimilarity between the Viking 7 and Viking 10 a.c. pressure signals led the authors to reexamine the Viking 7 records, and to perform further laboratory tests on a similar gage. This paper contains the results of their effort.

THEORY

The pressure in a gage chamber mounted on the side of a yawed rocket is, in general, a function of the rocket's velocity relative to the atmosphere, angle of attack, and both ambient pressure and density. In the lower atmosphere, it is necessary to use empirical methods for determining the relationship between gage pressure and ambient conditions, except for a few special cases, for example, stagnation pressures and cone pressures for small angles of attack [5]. In the upper atmosphere, where the mean free path is large compared to rocket dimensions, it is possible to use the flow principles of kinetic theory to relate gage pressure to ambient atmospheric pressure and density. A careful interpretation of theory [5, 6] shows that both atmospheric pressure and density can be measured relatively independently of temperature and the average molecular weight of the gas, if an absolute pressure gage is mounted on the side of a rapidly rolling rocket having a large angle of attack. Further considerations and measurements described below show that ambient density can be determined even in the presence of a residual gas cloud, provided that, on the average, the incoming atmospheric air molecules reach the gage without striking molecules of the gas cloud. The equations relating gage pressure to atmospheric pressure and density are derived below.

a. *Vector Notation*

Since the pressure gage readings are affected by velocity ram, it is necessary to evaluate the component of the relative velocity between rocket and atmosphere parallel to the gage axis. Hence, for a given yaw position of the rocket, one seeks an expression showing the explicit relationship between the velocity ram into a gage mounted on a rocket nose cone and the roll position of the rocket.

Consider the two sets of right-handed orthogonal axes shown in Figure 1. The $\hat{X}_i$ $(i = 1, 2, 3)$ axes are fixed on earth and are oriented as follows:

$$\hat{X}_1 = \text{unit vector in north direction}$$

$$\hat{X}_2 = \text{unit vector in west direction}$$

$$\hat{X}_3 = \text{unit vector in up direction}$$

The $\hat{X}_i'$ axes are defined by

$$\hat{X}_i' = C_{ij}\hat{X}_j\ , \ i, j = 1, 2, 3 \quad \ldots\ldots\ldots\ldots\ldots\ldots\ldots (1)$$

here the repeated index indicates summation, and C_{ij} is the matrix

$$C_{ij} \equiv \begin{Bmatrix} \cos\theta\cos\phi & \cos\theta\sin\phi & -\sin\theta \\ -\sin\phi & \cos\phi & 0 \\ \sin\theta\cos\phi & \sin\theta\sin\phi & \cos\theta \end{Bmatrix} \quad \text{(2)}$$

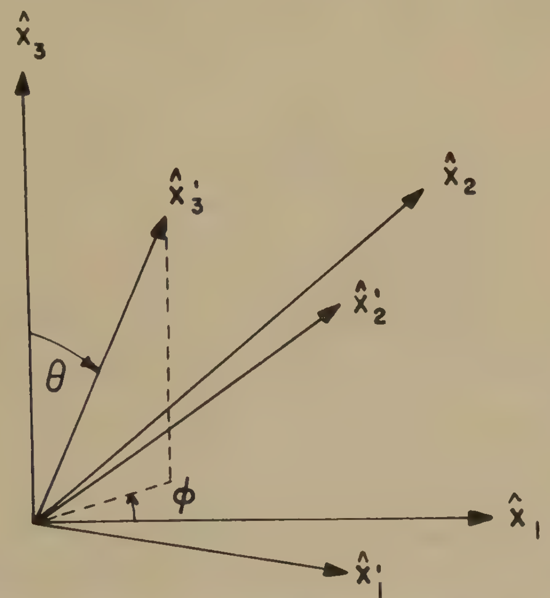

FIG. 1—Orientation of rocket at zero roll position with respect to earth fixed axes

Here,

$\hat{X}_1' \equiv$ unit vector along the north fin of the rocket at zero roll position

$\hat{X}_2' \equiv$ unit vector along the west fin of the rocket at zero roll position

$\hat{X}_3' \equiv$ unit vector along rocket axis

$\theta \equiv$ zenith angle, defined as the angle between the vertical and rocket axes

$\phi \equiv$ azimuth angle, defined as the angle between the projection of the rocket axis on the north-west plane and north, measured positive moving from north to west.

To introduce rocket roll and gage orientation, consider Figure 2. The $\hat{X}_i'$ axes remain fixed during a roll cycle, while the $\hat{X}_i''$ axes rotate with the rocket. Define:

$\beta \equiv$ angle between rocket axis and gage axis

$\psi \equiv$ roll angle of rocket

$\hat{n} \equiv$ unit outward drawn vector parallel to gage axis

$\alpha \equiv \pi/2 - \beta$

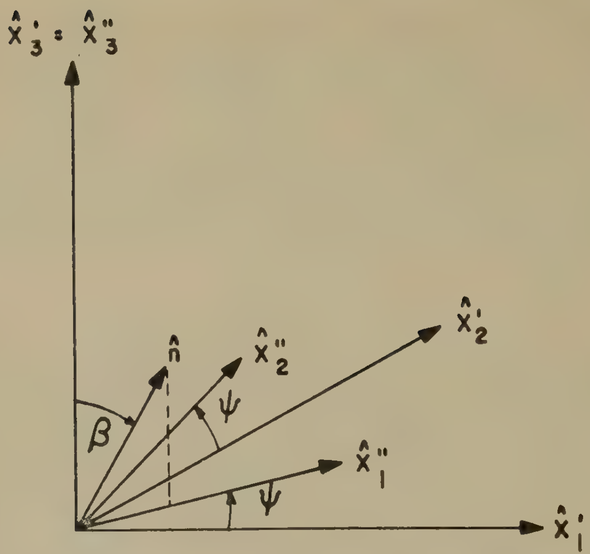

Fig. 2—Orientation of gage axis during a roll cycle relative to zero roll position

For $\psi = 0$, $\hat{X}_i' \equiv \hat{X}_i''$. From Figure 2, it is seen that

$$\hat{n} = \cos\alpha \cos\psi \hat{X}_1' + \cos\alpha \sin\psi \hat{X}_2' + \sin\alpha \hat{X}_3' \quad \text{(3)}$$

If V_1, V_2, V_3 are the components of the rocket velocity $\vec{V}$, relative to the atmosphere in the north, west, and vertical directions, respectively, then

$$\vec{V} = V_1\hat{X}_1 + V_2\hat{X}_2 + V_3\hat{X}_3$$

Alternatively, one may write

$$\vec{V} = V_1'\hat{X}_1' + V_2'\hat{X}_2' + V_3'\hat{X}_3' \quad \text{(4)}$$

where

$$V_i' = C_{ij}V_j, \qquad i, j = 1, 2, 3 \quad \text{(5)}$$

and C_{ij} is given by matrix (2). From equations (3) and (4), it is seen that the relative velocity ram into the gage may be written as

$$(\vec{V}\cdot\hat{n}) = \cos\alpha \cos\psi V_1' + \cos\alpha \sin\psi V_2' + \sin\alpha V_3' \quad \text{(6)}$$

Therefore, if V_1, V_2, V_3, θ, and ϕ are given, $(\vec{V}\cdot\hat{n})$ can be evaluated as a function of ψ. Equation (6) may be simplified to

$$(\vec{V}\cdot\hat{n}) = D\sin(\psi + E) + C \quad \text{(7)}$$

where

$$C \equiv V_3' \sin\alpha$$

$$D \equiv \cos\alpha \sqrt{(V_1')^2 + (V_2')^2}$$

$$E \equiv \tan^{-1}\frac{V_1'}{V_2'}$$

Since C, D, and E are independent of ψ, equation (7) gives the desired explicit relationship between velocity ram into the gage and roll angle.

Observations: For the Viking 7 rocket, C, D, and E remained constant during a roll cycle; that is, during a roll period neither the velocity nor aspect of the rocket changed significantly: Hence:

1. The angle through which the rocket rolled, ψ_P, in order for the pressure gage to experience the maximum velocity ram and hence record its maximum pressure, is given by

$$\psi_P = \frac{\pi}{2} - E \qquad (8)$$

2*a*. The values of ψ for zero velocity ram are obtained from equation (7) by setting $(\vec{V}\cdot\hat{n}) = 0$ to get

$$\sin(\psi + E) = -\frac{C}{D} \qquad (9)$$

2*b*. The relative time the gage spends in experiencing a ram and rarefaction is obtained by examining the values of "ψ" which make $(\vec{V}\cdot\hat{n})$ positive and negative, respectively.

3. The included angle "δ" between $\vec{V}$ and $\hat{n}$ at time of maximum ram is given by

$$\delta = \cos^{-1}\frac{D + C}{|\vec{V}|} \qquad (10)$$

Since the direction of $\vec{V}$ and the values for θ and ϕ are known, δ can be uniquely determined.

4. When the gage is mounted on a cylinder, then $\alpha \equiv 0$ and

$$(\vec{V}\cdot\hat{n}) = D\sin(\psi + E) \qquad (11)$$

b. *Assumptions*

In order that the following relationships be valid, these conditions must exist or be suitably amended:

1. The pressure inside the gage is low enough so that the mean free path is greater than the gage dimensions.
2. The gage mouth is directly exposed to the atmosphere through an orifice.
3. The molecules in the upper atmosphere and those leaving the gage possess Maxwellian velocity distributions.
4. At any altitude, the average mass of the molecules entering the gage is equal to that of the molecules leaving.
5. The rocket's aspect, altitude, and velocity remain essentially constant over a roll cycle.
6. Electrical, magnetic, and tidal forces are small compared to the gravitational force, so that the hydrostatic equation is valid. This is required to derive pressure and scale heights, but is not necessary for determining density.

c. *Pressure and Density Formulae*

Accepting the above assumptions as valid, one calculates (6) the number of atmospheric molecules entering and leaving the gage per second. When the gage response time is much faster than the time necessary to obtain the change in pressure it experiences, then at any time the gage may be considered to be in equilibrium. Hence, one equates the expression for the number of atmospheric molecules entering the gage per second due to directed and thermal velocities to the number leaving per second due to thermal velocities alone. The resulting equation is

$$P_g = P_a \left(\frac{T_g}{T_a}\right)^{1/2} F(S) \qquad (12)$$

where

P_g ≡ gage pressure

P_a ≡ ambient atmospheric pressure

T_g ≡ absolute temperature of gage case

T_a ≡ absolute temperature of atmosphere, and

$F(S)$ ≡ velocity function given by

$$F(S) = S\sqrt{\pi}\,[1 + \operatorname{erf}(S)] + e^{-S^2} \qquad (13)$$

Here,

$$S \equiv \frac{(\vec{V}\cdot\hat{n})}{V_{P_0}} \qquad (14)$$

V_{P_0} ≡ most probable speed of atmospheric molecules

$$\operatorname{erf}(S) \equiv \frac{2}{\sqrt{\pi}} \int_0^S e^{-x^2}\, dx$$

A plot of "$F(S)$ *vs* S" appears in the literature [7].

The change in gage pressure over a roll cycle, "ΔP_g", is

$$\Delta P_g = \rho_a R' (T_a T_g)^{1/2} \Delta F(S) \qquad (15)$$

since $F(S)$ is the only quantity on the right-hand side of equation (12) varying over a roll cycle. In equation (15),

ρ_a ≡ ambient atmospheric density

R' ≡ gas constant for 1 gram $= K/m$

K ≡ Boltzmann constant

m ≡ Mass in grams of one molecule

Rewriting (15), one obtains

$$\rho_a = \frac{\Delta P_g}{\Delta F(S)} \cdot \frac{1}{R'(T_a T_g)^{1/2}} \qquad (16)$$

Observations: From equation (16), it is seen that:

1. The change in gage pressure, ΔP_g, over a roll cycle is related to the change in velocity function $\Delta F(S)$ by a constant. Hence, if ΔP_g is small compared to P_g, or the gage calibration is linear, and if the associated gage electronics has a linear response, and if the gage time constant is short compared to the period of pressure change, then the shape of the a.c. pressure signal over a roll cycle should be the same as that obtained by plotting "$F(S)$ *vs* ψ."

2. For the case where the gage is mounted on a cylinder $\alpha \equiv 0$, and

$$\rho_a = \frac{\Delta P_g}{V_{P_i} \sqrt{\pi}\,(\vec{V}\cdot\hat{n})_{\max}} \qquad (17)$$

Hence, for this gage orientation, the measured ambient density is independent of atmospheric temperature. In equation (17), $V_{P_i} \equiv$ most probable speed of molecules inside the gage.

THE PRESSURE GAGE

The pressure gage [8, 9] was a cold cathode ionization gage which had a usable range from 10^{-3} to 10^{-6} mm Hg. The gage was a commercial model obtained from Distillation Products, Inc., modified for rocket mounting, as shown in Figure 3.

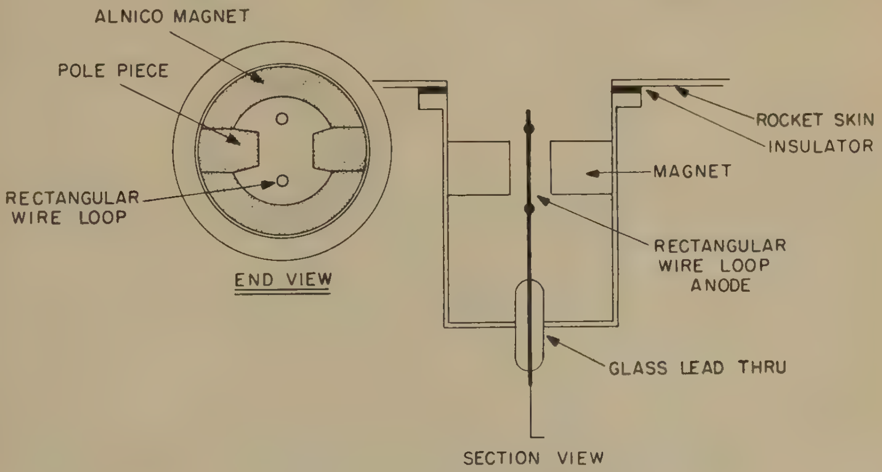

Fig. 3—Philips ionization gage

It consisted of a small internal magnet ($\approx$ 1,500 gauss) and a central rectangular loop of wire for the anode. The volume of the gage was equal to 33 cm^3. The gage, including the evacuating tube, was connected to the atmosphere outside the rocket through a 2.2 cm diameter orifice in the nose section. The gage's rugged construction and cold cathode operation made it well suited for rocket flight.

Figure 4 shows the gage circuit. A 3,000 volt, 10 pound dry battery was in series with the gage and four resistors. The voltages across the resistors were fed to three channels as shown. The 1.0 μfd condenser between the 400 K ohm resistor and cathode follower limited the signal from the 400 K ohm resistor to a.c. voltages.

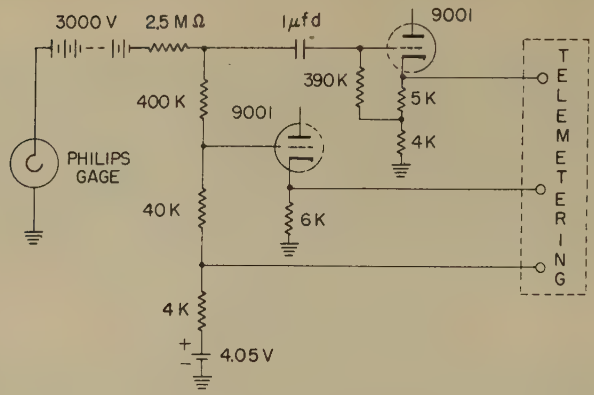

FIG. 4—Schematic of gage circuit

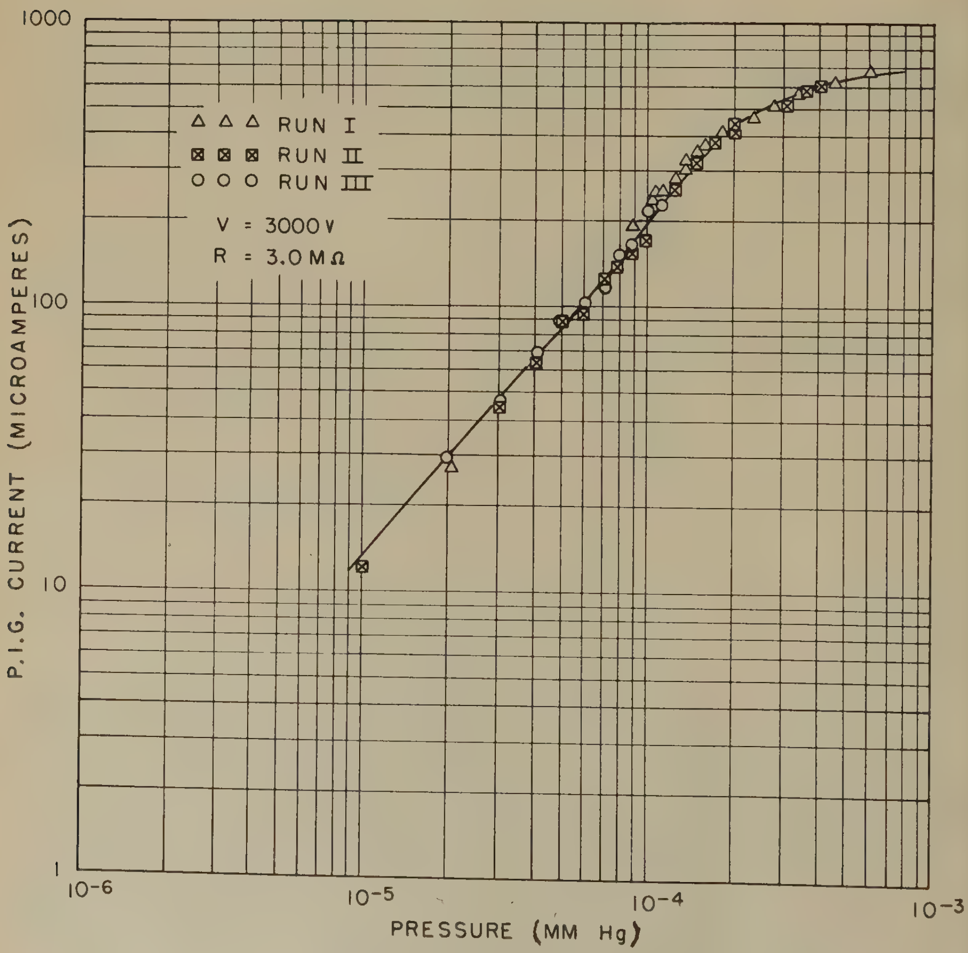

FIG. 5—P.I.G. d.c. calibration

These voltages were proportional to the a.c. pressure change in the gage and were in phase with the roll of the rocket. An a.c. signal of 0.04 volt at the input of the telemetering corresponded with a cyclic pressure change in the gage of 10^{-7} mm Hg.

The flight P.I.G. (Philips Ionization Gage) was calibrated in the laboratory against a D.P.I.-VGIA ionization gage which had been checked with a McLeod gage. Figure 5 shows the gage calibration curve for a 3,000 volt supply and 3.0 M ohm load resistance. The calibration was performed under conditions of dynamic equilibrium, with gage current and VGIA control meter readings remaining unchanged at any one system pressure for periods exceeding five minutes. The scatter in experimental points is less than 25 per cent for pressures between 7×10^{-4} mm Hg and about 10^{-5} mm Hg. It should be noted that no hysteresis effect was observed in gage operation. Thus, within the experimental error, a given pressure P corresponded to a gage current I, regardless of whether P was approached from higher or from lower pressure.

In addition to the d.c. calibration, several other tests were performed, including the following: The evacuation of a P.I.G. from atmospheric pressure to 10^{-6} mm Hg in five minutes time; a comparison between the performance of a P.I.G. recently brought to low pressure from atmospheric pressure and a P.I.G. kept at pressures equal to 10^{-5} mm Hg; the direct measurement of a.c. sensitivity of the P.I.G. by mounting the gage in a chamber whose volume could be cycled a known amount at frequencies of from 0.5 to 5.0 c.p.s.; and, finally, the measurement of the gage time constant. The results of these tests can be summarized as follows:

(1) The P.I.G. was capable of reading pressures of about 2×10^{-6} mm Hg within five minutes (approximate peak time) after it had been energized at atmospheric pressure even with laboratory pumping speeds less than those calculated to exist during flight.

(2) The a.c. sensitivity of the gage was equal to the slope of the d.c. calibration curve. As Figure 6 shows, the a.c. gage sensitivity is a function of gage current.

(3) The time constant of the pressure gage volume and its evacuating tube was short enough to cause no significant amplitude reduction in the gage pressure changes at the frequency involved. Within 5 milliseconds, the gage would see 99 per cent of a 1.5 c.p.s. periodic pressure change.

EXPERIMENTAL DATA

All gage data were obtained *via* telemetering. In the telemetering system [10] used in this rocket, all channels were calibrated sequentially at intervals of 16 seconds by five one-volt steps applied to the data channel inputs. The stability of the system, together with the calibrations, made it possible to read absolute voltages with an error of less than 0.05 volt, and voltage changes occurring in a few seconds with an error of less than 0.01 volt.

The Viking rocket reached an altitude of 219 kilometers [10], 268 seconds after take-off. Its north and west velocities were measured to be 180 m/sec and

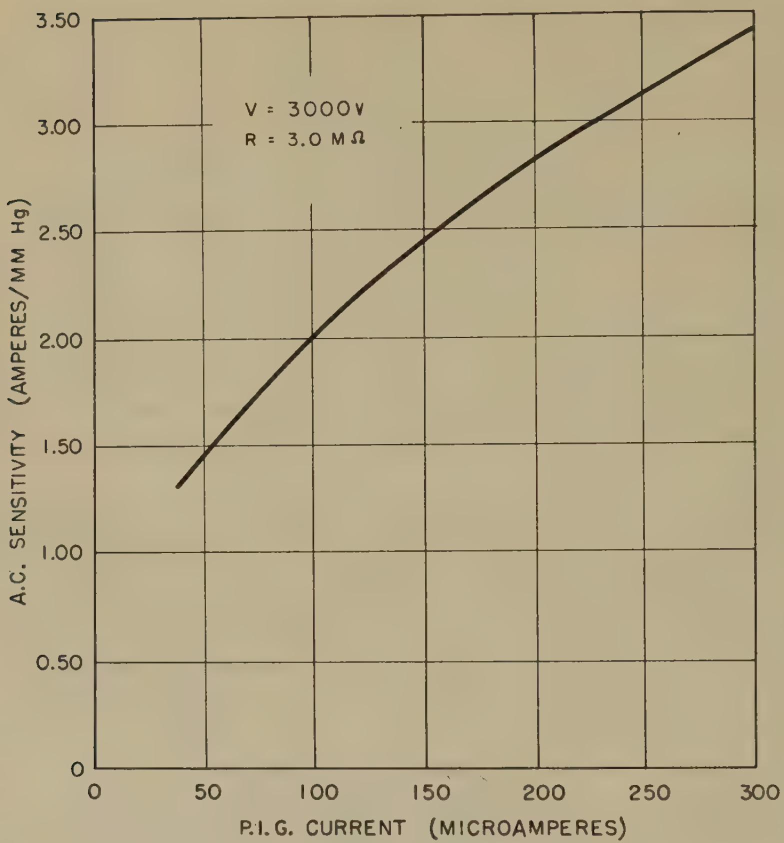

FIG. 6—P.I.G. a.c. sensitivity *vs* gage current

16 m/sec, respectively, and remained essentially constant through that portion of flight of interest. The rocket's attitude history, as determined from aspect camera data,* is shown in Figure 7.

Figure 8 show the gage d.c. pressure in mm Hg as a function of time of flight. The pressure plateau at 110 seconds is due to the firing of small spin jets located on the rocket's tail fins. It should be noted that there is a striking asymmetry between ascent and descent pressure, which is attributed to gas escaping from unsealed compartments. Previous flights also showed this asymmetry. The dashed lines at each extremity of the graph represent the best estimate of the residual gas surrounding the rocket as a function of time.

As the rocket rolled, the pressure gage recorded an a.c. signal corresponding to the change in gage pressure over a roll cycle. Figure 9 is a plot of the peak to peak amplitude of the change in gage pressure as a function of time of flight. The small build-up at 143 seconds is due to a rapid increase in velocity ram which the gage experienced at this time, and was caused by changing aspect. Since the

*Reduced for the Naval Research Laboratory by the New Mexico College of Agriculture and Mechanical Arts.

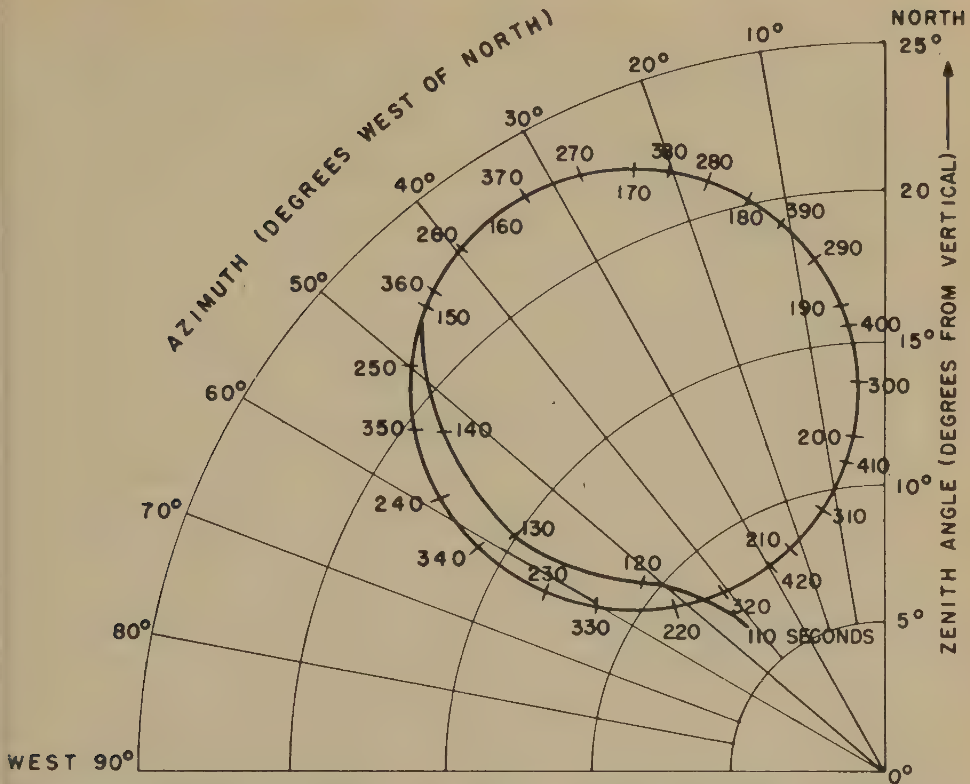

FIG. 7—Inclination and bearings of the rocket's longitudinal axis during coasting flight

shape of the a.c. pressure signal was different on the ascent from that observed on descent, it was important to show that the observed difference was a function of rocket velocity and geometry rather than of instrumentation and/or gas interference. It was noted earlier, in connection with equation (16), that when the listed conditions existed, the predicted shape of a.c. pressure signal could be obtained by plotting "$F(S)$ *vs* ψ." Since these conditions did apply to the Viking 7 experiment, it was possible to examine the predicted wave shapes. Referring to Figure 10, one notes that the dots, $\cdots$, are the observed a.c. output signal plotted with abscissa as roll angle, ψ, in degrees and ordinate of arbitrary units. The crosses, xxx, show the calculated values of $F(S)$ for corresponding values of ψ. It is seen that the difference in signal shape observed on ascent with that on descent is predicable and is due to a combination of rocket velocity, aspect, and gage orientation.

To check rocket aspect and to furnish roll phase reference, a coil of wire was mounted inside the rocket nose cone. As the rocket rolled, the coil cut the earth's magnetic field and generated an a.c. voltage proportional to the roll and rocket aspect, but not to air motion. Using a method similar to that developed here to obtain equation (7), it was possible to determine the angles through which the rocket rolled in order for the coil to generate a maximum signal. From equation

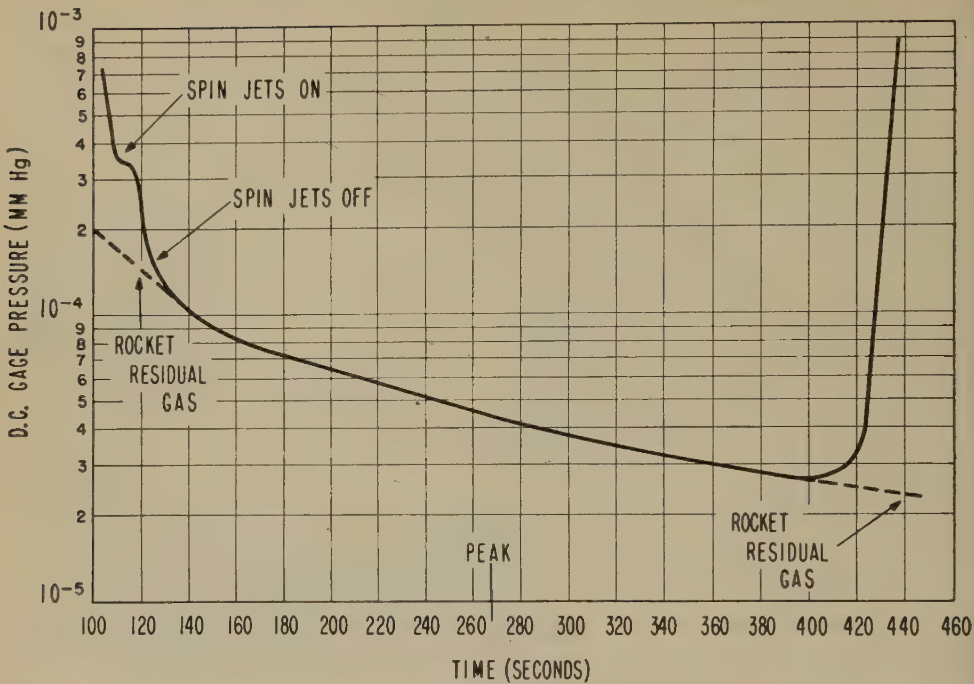

FIG. 8—D.c. gage pressure *vs* time of flight

(8), it was possible to calculate the angle through which the rocket rolled in order for the P.I.G. to record maximum pressure, assuming no winds. Correcting for the phase angle due to gage electronics, and for the different orientations within the rocket, it was possible to predict the difference between the time of coil maximum signal and the time of P.I.G. maximum pressure. This difference was measured directly from the telemetered record. Over that portion of flight where the pressure signal amplitude was large enough to permit making reliable phase measurements, during both ascent and descent, the predicted and measured time differences agreed to ±15 milliseconds (±8° of roll), the measuring accuracy. It is interesting to note that at one time during the flight, shortly before 200 seconds, the roll position at which ram pressure was a maximum shifted rapidly from the south and upward direction to an easterly direction. In the preliminary analysis of the data [13], it was estimated that this phase shift was significantly delayed from the time it was computed to occur based on rocket aspect and trajectory data. This delay was interpreted as an atmospheric wind. However, after reexamining the data at this time, the authors concluded that the phase of the extremely small and somewhat irregular pressure signals could not be accurately measured. Hence, the time when the phase had moved 90° was not determined well enough to enable a significant wind calculation to be made.

ANALYSIS OF DATA

Figure 11 shows atmospheric pressure in mm Hg plotted against altitude in

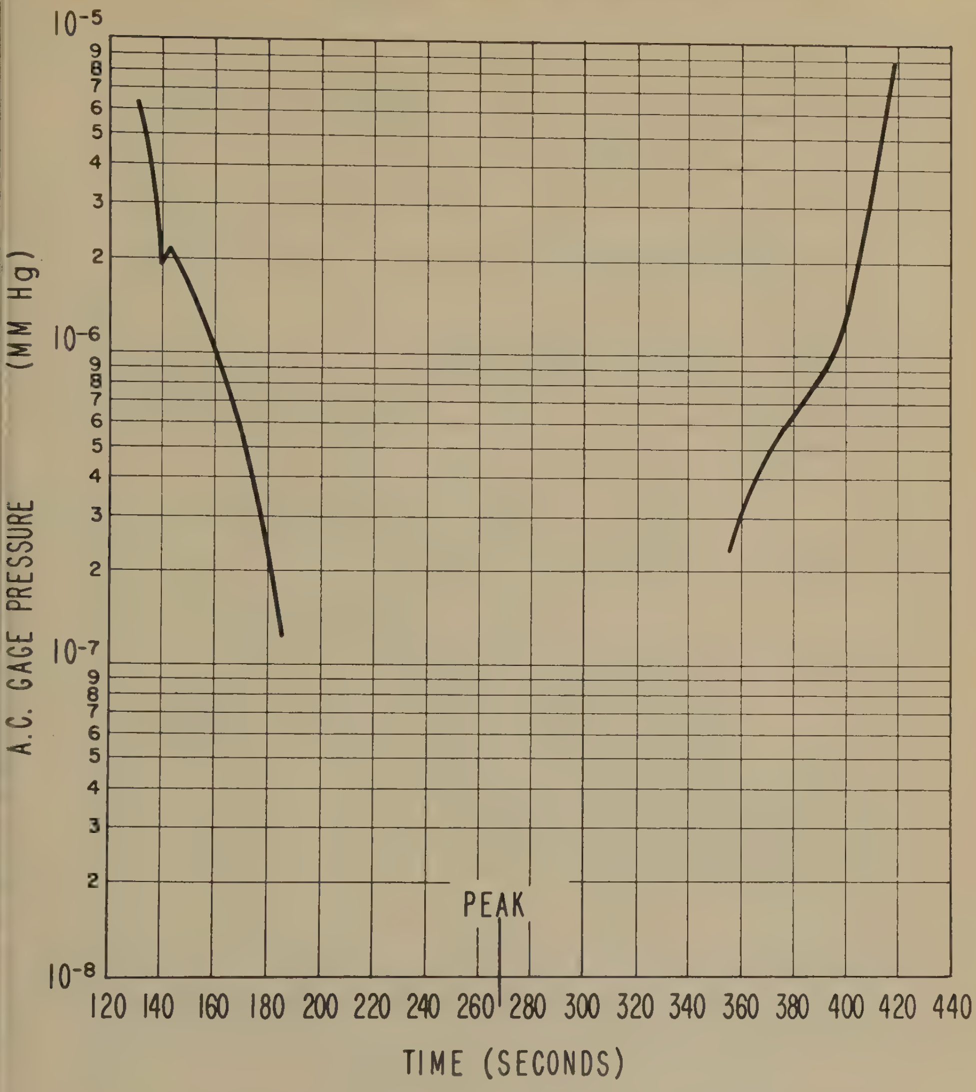

Fig. 9—Peak to peak a.c. gage pressure *vs* time of flight

kilometers. Atmospheric pressure values were obtained from gage pressure by first subtracting the residual gas (see Fig. 8) and then correcting for velocity ram *via* equation (12). The scatter is seen to be less than 25 per cent, and part of it might be due to small errors involved in subtracting the residual pressure. Above 105 km, the pressure curve is based on measured densities and computed scale heights described below. A plot of the Rocket Panel [2] pressures is shown for comparison. It is noted that the Viking 7 pressures are about a factor of four less than Rocket Panel values until 140 km, where the agreement improves. At 185 km, the two pressure curves intersect. At 220 km, interpretation of flight data yields pressures about a factor of two higher than that of the Rocket Panel atmosphere.

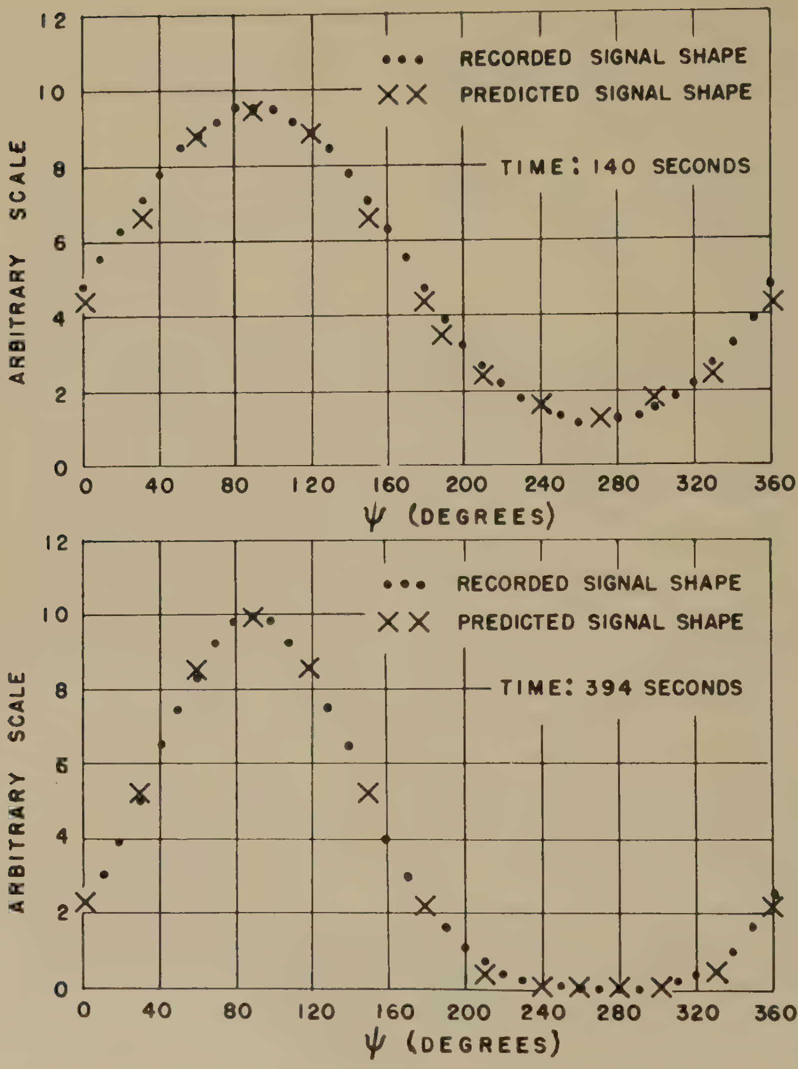

FIG. 10—Comparison between observed and predicted signal shapes

Figure 12 shows atmospheric density in gms/m^3 as a function of altitude in kilometers. Density data points were taken from 120 to 220 km. Density values from 92 to 102 km were obtained from the slope of the pressure curve. There is a systematic difference between the up and down data. All of the ascent density values are higher than the corresponding descent values. The following are possible explanations for the observed systematic differences. It was noted earlier that the a.c. sensitivity of the gage was equal to the slope of the d.c. calibration curve. An error of 30 per cent in evaluating the slope is possible. Yet, if the measured slope at about 10^{-4} mm Hg were lower than the true slope by 30 per cent, and if the measured slope at 3×10^{-5} mm Hg were too high by 30 per cent, then using the correct slopes would bring the ascent and descent values into agreement to within

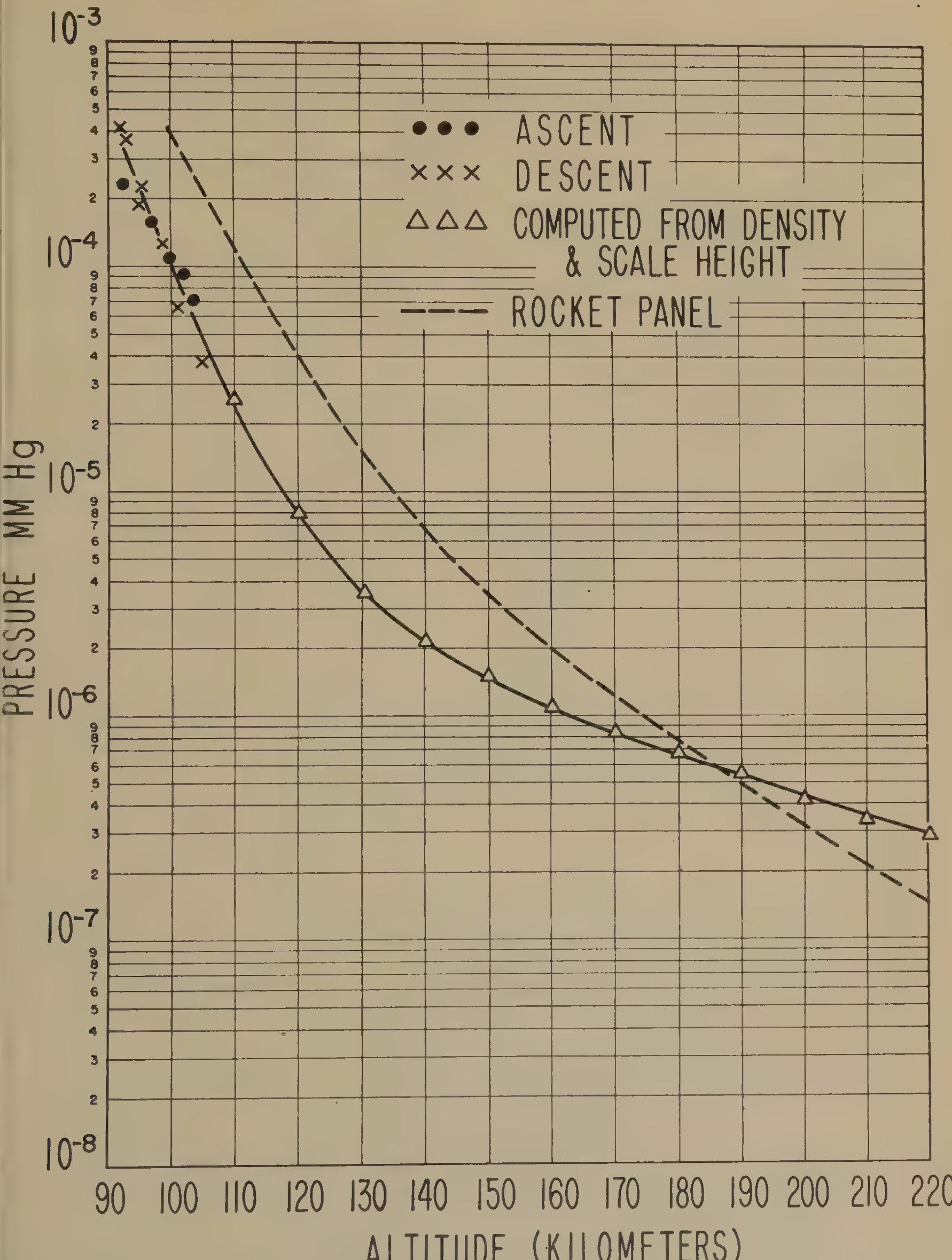

FIG. 11—Pressure *vs* altitude

50 per cent. A second possible explanation for this observed difference is horizontal atmospheric winds. A moderate wind coming from a southerly direction would be so oriented as to significantly affect the amplitude of the relative velocity between rocket and atmosphere without causing a measurable phase shift in the

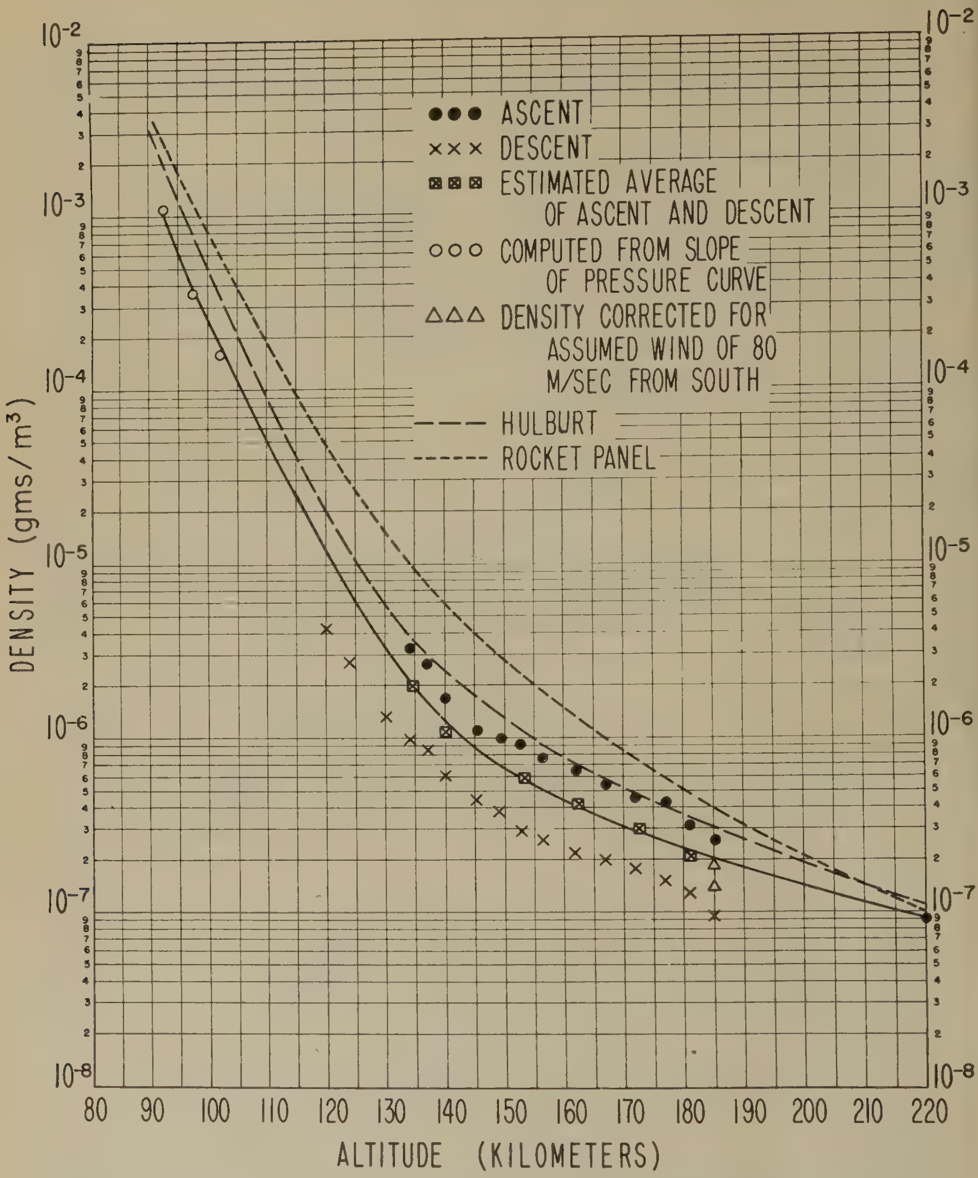

FIG. 12—Density *vs* altitude

pressure signal. For an assumed wind of 80 m/sec from the south, the ascent and descent density values at 185 km are brought into approximately 30 per cent agreement (see Fig. 12). A third possible source of discrepancy might be the short evacuating tube connecting the gage mouth to the rocket skin. The presence of this tube, coupled with the fact that the gage spent a greater portion of its roll cycle experiencing a velocity ram on the ascent than on the descent, could possibly account for the observed difference in density values. Finally, it should be noted

that it is not reasonable to attribute the observed difference to the gas composition sensitivity of the gage. First, calibration tests with the P.I.G. using different gases [11] reveal that for air, nitrogen, and oxygen the gage sensitivity is essentially the same. Second, and more important, it is unreasonable to believe that the air composition on ascent was significantly different from that on descent. From the available information, one could not favor either set of data points. Hence, an average of the two sets was taken as the best values of atmospheric density. It appears that making the corrections for any of the above listed possible sources of the discrepancy, will have the effect of bringing the experimental points into closer agreement with the average density curve.

The density values are not very sensitive to atmospheric temperature. Calculations show that an error of more than 50°K would, under normal conditions, not cause more than a 5 per cent error in the density measurements. Furthermore, it should be noted that at the peak of flight when the velocity ram is almost directly into the gage, the density value is independent of atmospheric temperature. The 220 km density value of 9×10^{-8} gm/m^3 agrees with the Rocket Panel value. However, the density values at the lower altitudes are approximately one-fourth of those given by the Rocket Panel. Finally, it is seen that the measured densities agree with those of Hulburt [12] to better than a factor of two from 100 to 180 km. Above this altitude, the difference continually decreases to 20 per cent at 220 km.

The scale height shown in Figure 13 was computed from the "density *vs* altitude" curve using the equation

$$\frac{\rho_1}{\rho_2} = \frac{H_2}{H_1} e \frac{-2(h_1 - h_2)}{H_1 + H_2} \qquad (18)$$

where

h_1 and h_2 are altitudes in kilometers

H_1 is the scale height at h_1

ρ_1 is the density at h_1

H_2 is the scale height at h_2

ρ_2 is the density at h_2

Since the "density *vs* altitude" curve does not uniquely determine scale height, it was necessary to make the following two assumptions:

1. The scale height from 180 to 220 km is essentially constant. This is based on the belief that in this region the ratio of the thermal conductivity of the atmosphere to its energy absorption capacity is large enough that temperature gradients would be negligible. Furthermore, it is believed that changes in molecular weight would be small over about one scale height when the mean free path is about 1 per cent of H.

2. The scale height monotonically decreases from 220 to 90 km. This is in agreement with current theories. Accepting the first assumption as valid, it was possible to compute the scale height in the 180 to 220 km region. The value obtained

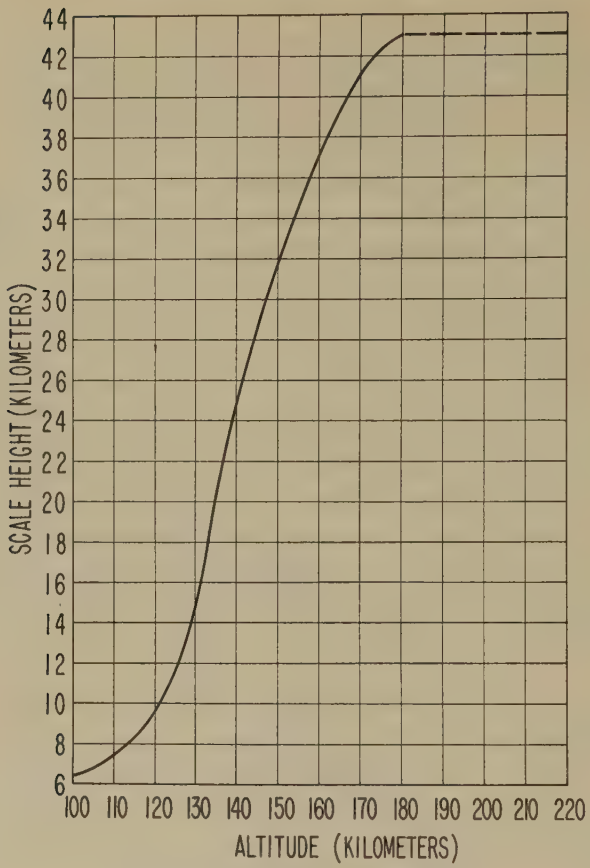

FIG. 13—Scale height *vs* altitude

was 43 km. Using the second assumption and equation (18), one can compute the scale height down to 100 km. It should be noted that the scale height at 220 km would be higher if the assumption of a slight increase in scale height with altitude between 180 to 220 km were made. Hence, the values for H given at this altitude should be regarded as a lower limit, for this flight time and season.

DISCUSSION OF RESULTS

Considering the nature of the data, the authors made no attempt to apply statistical methods in considering data accuracy. With regard to measured pressure values, it is believed that the values presented are correct to ± 30 per cent. The accuracy was determined after considering possible gage calibration error, possible errors in rocket velocity and aspect, possible systematic errors, such as , for example, gas composition, and the good agreement between ascent and descent values. After considering the accuracy with which the a.c. gage sensitivity was determined, and the difference between the density ascent and descent values with the possible explanations for these differences, the authors believe that the measured density values obtained from the average density curve are accurate to within a factor

Altitude (KM)	Pressure (M.M.Hg)	Density (gms M^{-3})	Scale Height (KM)	Assumed Mol. Wt. (gm/mol)	Temperature (°K)	Scale Height (KM) R.P.	Scale Height (KM) Hulburt
100	1.1×10^{-4}	2.5×10^{-4}	6.4	28.8	210	7.3	6.0
110	2.6×10^{-5}	5.0×10^{-5}	7.4	27.0	228	8.2	7.2
120	8.0×10^{-6}	1.2×10^{-5}	9.4	25.3	270	10	9.8
130	3.5×10^{-6}	3.3×10^{-6}	15	25.2	428	12	15
140	2.1×10^{-6}	1.2×10^{-6}	25	25.0	700	14	21
150	1.5×10^{-6}	6.6×10^{-7}	32	24.5	880	15	27
160	1.1×10^{-6}	4.3×10^{-7}	37	23.7	980	17	33
170	8.6×10^{-7}	3.0×10^{-7}	41	23.0	1050	19	36
180	6.9×10^{-7}	2.3×10^{-7}	43	22.3	1070	21	39
190	5.5×10^{-7}	1.8×10^{-7}	43	22.3	1070	23	42
200	4.2×10^{-7}	1.4×10^{-7}	43	22.3	1070	25	45
210	3.3×10^{-7}	1.1×10^{-7}	43	22.3	1070	27	
220	2.7×10^{-7}	9.0×10^{-8}	43	22.3	1070	28	50

FIG. 14—Atmospheric pressure, density, temperature, and scale height from Viking 7 measurements

of two. These measurements, along with computed scale heights and temperatures, are tabulated in Figure 14. Rocket Panel and Hulburt's scale heights are included for comparison.

In view of the significant difference between the Rocket Panel atmosphere, based on measurements made up to 1952, and that obtained from this firing, it is of interest to examine the basis of the Rocket Panel atmosphere. Up to 80 km altitude, data obtained from several methods were available. Above 100 km, the results were limited to Philips gage pressure measurements made on two V-2 rockets and a preliminary analysis of a part of the ascent data of the Viking 7 flight. The data published in this report differ significantly from the earlier data in two respects, as follows: (1) Pressures in the 100 to 120 km region, and (2) densities in the 155 to 160 km range. There is agreement in the 220 km density value. While it is conceivable that the V-2 data and the data presented here are different due to atmospheric variations, there are several reasons listed below for believing that the Viking 7 results are more accurate.

1. Rocket aspect was poorly known for the V-2 rockets. Hence, while the d.c. gage pressures were corrected for residual gas, they could not be properly corrected for velocity ram. Descent pressures measured on one of the V-2 flights [5] were found to be more than a factor of two lower than those on ascent. On the Viking 7 flight, aspect was known, and ram velocity corrections were made. This reduced the ascent pressure data by a factor of 2.7. The value 2.7 was obtained from kinetic flow equations. However, even if one were to extrapolate the data in Kopal's "Supersonic flow around yawing cones" to fit the particular Viking 7 flight conditions, he would obtain a correction of 2.5.

2. Density values on the V-2 rockets were measured under unfavorable conditions of very slow rocket roll rates and poor rocket aspect. Hence, interpretation of data was limited to peak altitudes with attendant low velocity ram, which may have been significantly affected by atmospheric winds.

3. Soft X-ray measurements [14] agree with the Viking 7 data in the 100 to 130 km region.

4. The $F2$ ionospheric scale height and collision frequency estimates are in better agreement with the Viking 7 data.

Hulburt's atmosphere [12] is essentially the Rocket Panel atmosphere up to 80 km. In the region just above 100 km, he follows the soft X-ray pressure values ($\approx$ 1/3 Rocket Panel). For temperature, he assumed (1) 1100° K ($F2$-layer) at 300 km, and (2) an energy balance between radiation energy absorbed and heat energy conducted downward. The resulting density and pressure distribution up to 220 km agrees very well with the Viking 7 data.

The agreement between the atmospheric pressures determined from solar X-ray absorption experiments [14, 17] and that obtained from gage measurements is very significant. The two methods are different and common systematic errors are unlikely. Thus, for example, principal errors in the gage measurements could be caused by uncertainties in the distribution of the rocket gas cloud and gas kinetics on a yawing rocket, and by gage and cone geometry. These effects should be absent in the absorption measurements. When the X-ray measurements are made with the sun near the horizon to take advantage of greater absorption and

extend the measurements to higher altitudes, a possible systematic error is introduced when an altitude-density distribution must be assumed. The Philips gage pressure measurements are free from this systematic error.

Both the Philip's gage experiment and X-ray absorption experiment will be flown together on five rockets to be fired at Fort Churchill during the International Geophysical Year. A direct comparison of the results should greatly improve our knowledge of the atmospheric structures up to 250 km, and permit seasonal and diurnal effects to be studied.

ACKNOWLEDGMENTS

Assistance from many people and groups were essential in performing these measurements. Particular thanks are due to former members of the Section; Dr. R. J. Havens for directing the experimental measurements and in performing the preliminary analysis of the data, and Mr. O. E. Berg, Miss M. Bond, and Mr. J. E. Bush for laboratory and field work with the experiment. For launching and tracking the rockets, thanks are due Mr. Milton W. Rosen and colleagues of the Naval Research Laboratory, Mr. W. Purdy and colleagues of the Glenn L. Martin Company, and to many of the civilian and military personnel of the White Sands Proving Ground. The authors wish to acknowledge valuable discussions with Dr. H. E. Newell, Jr., Mr. J. W. Townsend, Jr., Mr. J. Ainsworth, and Mr. D. Kleitman in analyzing the results. Thanks are also due Mr. H. Benton for assistance in determining the gage's response to rapid evacuation and small pressure changes. The authors are also indebted to Mr. H. Spitz of the Naval Research Laboratory and to the New Mexico College of Agriculture and Mechanic Arts for the camera aspect data.

References

[1] H. E. Newell, Jr., High Altitude Rocket Research, Academic Press, Inc., New York (1953).
[2] The Rocket Panel, Phys. Rev., 88, 1027 (1952).
[3] R. L. F. Boyd and M. J. Seaton (Editors), Rocket Exploration of the Upper Atmosphere, Pergamon Press, Ltd., London (1954).
[4] S. K. Mitra, The Upper Atmosphere, The Asiatic Society, Calcutta (1952).
[5] R. J. Havens, R. T. Koll, and H. E. LaGow, The pressure, density, and temperature of the earth's atmosphere to 160 kilometers, J. Geophys. Res., 57, 62 (1952).
[6] R. Horowitz and D. Kleitman, A method for determining density in the upper atmosphere during rocket flight, Naval Research Laboratory Rep. No. 4246 (1953).
[7] B. Wiener, Ambient pressure determination at high altitudes by use of free-molecule theory, National Advisory Comm. Aeronaut. Rep. No. 1821 (1949).
[8] F. M. Penning, High vacuum gauges, Phillips Tech. Rev., 2, 201 (1937).
[9] J. Backus, Theory and Operation of a Philips Ionization Gage Type Discharge, Characteristics of Electrical Discharges, Guthrie and Wakerling (Editors), McGraw-Hill Book Co., Inc., New York (1949); pp. 345-369.
[10] M. W. Rosen, J. M. Bridger, and A. E. Jones, The Viking 7 firings, Naval Research Laboratory Rep. No. 3946 (1952).
[11] L. R. Foote, Effect of different gases on Philips gages, University of California, Rad. Lab. AECD No. 2672 (1944).
[12] E. O. Hulburt, Advances in the physics of the upper air since 1950, Naval Research Laboratory Rep. No. 4600 (1955).

[13] R. J. Havens and H. Spitz, (Abstract) Atmospheric winds at 200 kilometers, Trans. Amer. Geophys. Union, 33, 317 (1952).
[14] E. T. Byram, T. A. Chubb, and H. Friedman, Dissociation of O_2 in upper atmosphere, Phys. Rev., 98, 1594-1597 (1955).
[15] R. J. Havens and H. E. LaGow, (Extrait) Mém. Soc. roy. sci. de Liége, 12, Fasc. 1-2 (1952).
[16] H. E. Newell, Jr., (Extrait) Ann. Géophys., 11 (1955).
[17] E. T. Byram, T. A. Chubb, and H. Friedman, The solar X-ray spectrum and the density of the upper atmosphere, J. Geophys. Res., 61, 251 (1956).

JOURNAL OF GEOPHYSICAL RESEARCH VOLUME 62, No. 1 MARCH, 1957

METEOR ECHOES AT ULTRA-HIGH FREQUENCIES

By WALTER A. FLOOD

Cornell Aeronautical Laboratory, Inc., of Cornell University, Buffalo 21, New York

(Received August 13, 1956)

ABSTRACT

It is proposed that, at ultra-high frequencies, underdense meteor echoes have an effective scattering length L, which is much less than a Fresnel zone. Consequently, UHF meteoric echoes may be analyzed in terms of Fraunhofer diffraction theory, resulting in a relaxation of the requirement that a meteor trail be perpendicular to the radar line-of-sight before an echo can be received. Formulas for the back-scattered power, time duration, and echo rate are deduced.

LIST OF SYMBOLS

dZ = amplitude reflection coefficient per unit trail length
R_0 = perpendicular range to the meteor trail
μ_0 = permeability of free space
e = charge on an electron
m = mass of an electron
D = ionospheric diffusion coefficient
λ = wavelength
k = propagation constant = $2\pi/\lambda$
q = electronic line charge
v_0 = average meteoric velocity
r_0 = initial radius of meteor trail
l_0 = average length of meteor trail = 25×10^3 meters

I. INITIAL CONSIDERATIONS

If a meteor column of ionization expands from a line source according to the diffusion equation, $\delta N/\delta t = D\,\nabla^2 N$, the density of the trail as a function of time and radial position is given by

$$N = \frac{q}{4\pi Dt}\exp\left\{-\frac{r^2}{4Dt}\right\} = N_0 \exp\left\{-\left(\frac{r}{r_0}\right)^2\right\} \quad (1)$$

where N = electron density and D = diffusion coefficient ≈ 5 meter^2/sec at an altitude of 100 km. The reflection coefficient per unit incident field strength per unit column length for underdense meteor trails with a Gaussian distribution of electron density [see 1 of "References" at end of paper] is

$$dZ = \frac{\mu_0 e^2}{4\pi m R}\, q \exp\{-(kr_0)^2\} \quad (2)$$

Combining (1) and (2),

$$dZ = \frac{\mu_0 e^2}{4\pi m R} q \exp\{-4k^2 Dt\} \qquad (3)$$

Now considering that the meteor trail may be formed with an initial radius r_0, equation (3) may be modified to take this into account, as follows:

$$dZ = \frac{\mu_0 e^2}{4\pi m R} q \left[\exp\left\{-4k^2 Dt - \frac{4\pi^2 r_0^2}{\lambda^2}\right\}\right] \qquad (4)$$

$$r_0 = 10 \text{ cm at an altitude of } 100 \text{ km}$$

This formula is generally used to indicate the duration of the echo once the trail has been formed. However, the rate of trail formation is finite—meteors have velocities ranging from 11 km/sec to 70 km/sec, averaging 40 km/sec. Therefore, the time factor in (4) may be made a function of position in the following manner. Consider:

$Y = v_0 t$

Y = distance of the scattering element from the head of the meteor trail

v_0 = average meteor velocity

Then,

$$dZ = \frac{\mu_0 e^2}{4\pi m R} q \exp\left\{-\frac{16\pi^2 Dy}{\lambda^2 v_0} - \frac{4\pi^2 r_0^2}{\lambda^2}\right\} \qquad (5)$$

Equation (5) may be used to calculate the back-scattered field per unit incident field strength, per unit trail length. As a meteor column forms, the contributions of the various elements along the column must be summed, taking into account the effect of diffusion by equation (5) and the phase difference due to path geometry.

1.2 *Formulation of the Problem*

Radiation from an element dy is dE.

$$dE = \frac{A}{4\pi R_0} \exp\left\{-\frac{4\pi i}{\lambda} R_0\left[1 + \left(\frac{S+y}{R_0}\right)^2\right]^{1/2} - \frac{16\pi^2 Dy}{\lambda^2 v_0} - \frac{4\pi^2 r_0}{\lambda^2}\right\}$$

where $A = (\mu_0 e^2/m)q$. The total field due to the entire length of the meteor trail is

$$E = \frac{A}{4\pi R_0} \exp\left\{-\frac{4\pi^2 r_0^2}{\lambda^2}\right\} \cdot I \qquad (6)$$

$$I = \int_0^\infty \frac{\exp\left\{-\frac{4\pi i}{\lambda} R_0\left[1 + \left(\frac{S+y}{R_0}\right)^2\right]^{1/2} - \frac{16\pi^2 Dy}{\lambda^2 v_0}\right\}}{\left[1 + \left(\frac{S+y}{R_0}\right)^2\right]^{1/2}} dy \qquad (7)$$

Equation (7) may be rewritten in terms of a Fresnel integral with complex argument. However, such formulations do not lend themselves to analysis with emphasis on physical insight.

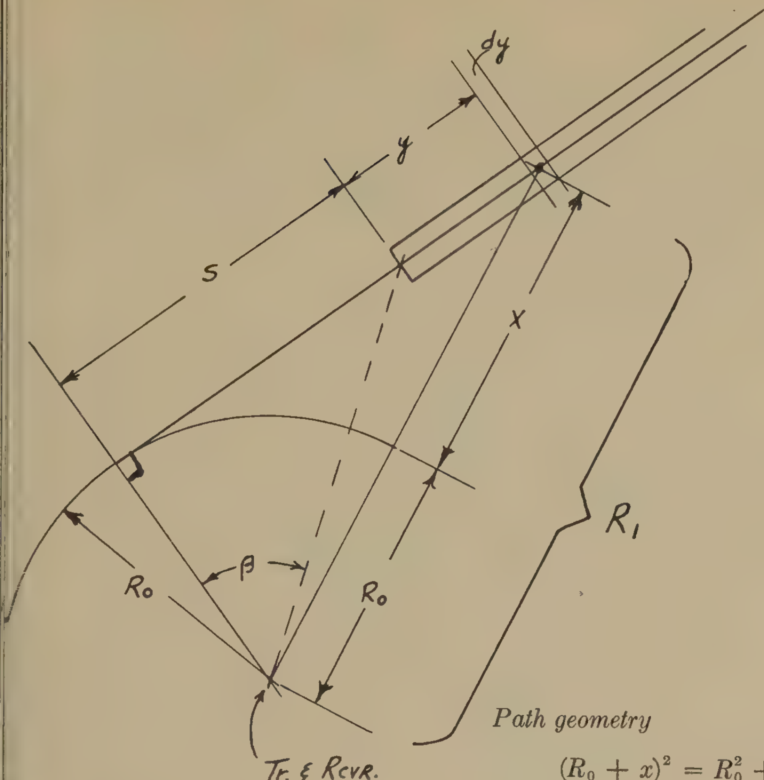

Path geometry

$$(R_0 + x)^2 = R_0^2 + (S + y)^2$$

$$R_1 = R_0 + x = R_0\left[1 + \left(\frac{S + y}{R_0}\right)^2\right]^{1/2}$$

FIG. 1

.3 *Approximate Analysis*

The maximum value of the integrand (7) occurs at $y = 0$, while the point of stationary phase occurs outside the limits of integration. For positive values of S, the main contribution to the integral must come from small values of y—the exponential factor of $(-16\pi^2 Dy/\lambda^2 v_0)$ will cause the integrand to vanish for large values of y. Let us arbitrarily limit the integration from $y = 0$ to $y = L$, where L is defined as that value of y which makes the real part of the exponential equal to 0.367, and further approximate by replacing exp $(-16\pi^2 Dy/\lambda^2 v_0)$ by unity. This may tend to overestimate the integral. Moreover, since we are now restricted to values of y less than L, and since L is on the order of meters whereas R is measured in hundreds of kilometers, we may expand the square root in the exponential phase factor, taking only the first two terms of the binomial expansion. The square root in the denominator can be approximated by unity. With these substitutions,

equation (7) becomes

$$I = \exp\left\{-\frac{4\pi i}{\lambda} R_0\right\} \frac{\sqrt{R_0\lambda}}{Z} \int_{2S/\sqrt{R_0\lambda}}^{2(S+L)/\sqrt{R_0\lambda}} \exp\left\{-i\frac{\pi}{2}v^2\right\} dv$$

$$I = \exp\left\{-\frac{4\pi i}{\lambda} R_0\right\} \frac{\sqrt{R_0\lambda}}{Z} \left[F\left(\frac{2(S+L)}{\sqrt{R_0\lambda}}\right) - F\left(\frac{2S}{\sqrt{R_0\lambda}}\right)\right] \quad\ldots\ldots\ldots(8)$$

where $F(u)$ is the Fresnel integral defined by

$$F(u) = \int_0^u \exp\left\{-i\frac{\pi}{2}v^2\right\} dv$$

and

$$L \equiv \frac{\lambda^2 v_0}{16\pi^2 D}$$

Let us estimate some of the parameters

$$L = \frac{\lambda^2 v_0}{16\pi^2 D} \leq 50 \text{ meters}$$

$$\sqrt{R_0\lambda} \geq 450 \text{ meters}$$

$$v_0 = 40 \times 10^3 \text{ meters/sec}$$

$$D = 5 \text{ meters}^2\text{/sec}$$

$$\lambda \leq 1 \text{ meter}$$

$$R_0 \geq 200 \text{ km}$$

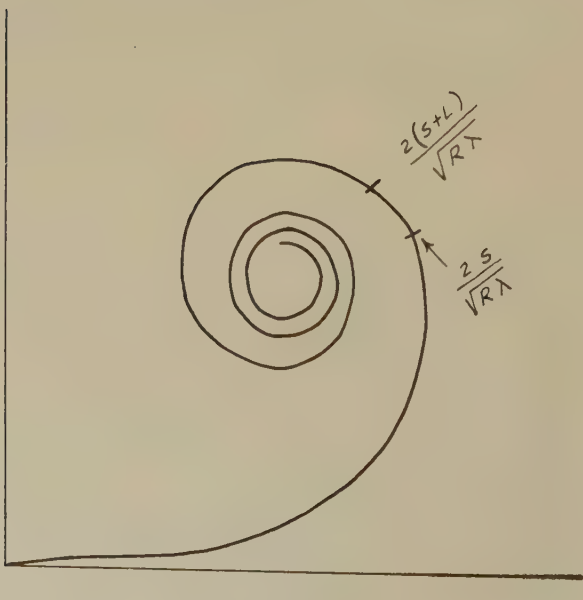

FIG. 2

The difference of the two Fresnel functions in equation (8) can be visualized by means of the Cornu Spiral. The difference of the two functions is the chord corresponding to the arc of length $2L$ positioned at a distance $2S$, as depicted in Figure 2. Since L is small compared to $\sqrt{R_0\lambda}$, the chord length and arc length will be equal for all values of S up to the point where the spiral is very tight. If L is sufficiently small, one would expect (8) to be independent of the value of S over a restricted range of S. Therefore, setting $S = 0$,

$$I = \exp\left\{-\frac{4\pi i}{\lambda} R_0\right\} \frac{\sqrt{R_0\lambda}}{Z} F\left(\frac{2L}{\sqrt{R_0\lambda}}\right) \qquad (8a)$$

Now it may be shown that for $(2L/\sqrt{R_0\lambda}) \leq 0.45$,

$$F\left(\frac{2L}{\sqrt{R_0\lambda}}\right) \approx \frac{2L}{\sqrt{R_0\lambda}} \qquad (9)$$

To set a limit on the range of λ for which (9) is valid, consider

$$\frac{2L}{\sqrt{R_0\lambda}} = \frac{100\lambda^2}{\sqrt{R_0\lambda}} \leq 0.45 \qquad R_{\min} = 100 \times 10^3 \text{ meters}$$

$$\lambda \leq 1.25 \text{ meters}$$

Substituting (9) into (8a),

$$I = \exp\left\{-\frac{4\pi i}{\lambda} R_0\right\} \cdot L$$

Therefore,

$$E = \left[\frac{\mu_0 e^2}{4\pi m R_0} q \exp\left\{-\frac{4\pi^2 r_0^2}{\lambda^2}\right\}\right] \cdot \left[\frac{\lambda^2 v_0}{16\pi^2 D}\right] \qquad (10)$$

The quantity in the first bracket is recognizable as the scattering from a Gaussian column, per unit length, per unit incident field strength. The quantity in the second bracket has the dimension of length and is the effective scattering length. We have already seen that for $\lambda \leq 1.25$ meters, L, the effective scattering length, is less than one-tenth of a full Fresnel zone. Under these circumstances, we may view the problem as one of Fraunhofer diffraction rather than Fresnel diffraction, and can use Fraunhofer theory to indicate the restricted range of S over which equation (8) is substantially constant and equal to equation (8a). Consequently, over a restricted range of S, the back-scattered field intensity per unit incident field strength from a meteor trail is given by (10) and the effective length of scatterer L is

$$L = \frac{\lambda^2 v_0}{16\pi^2 D} \qquad (11)$$

1.4 *Comparison with Previous Results*

Eshleman [2] has considered the effects of radio wavelength and diffusion upon meteoric echoes, deriving essentially equation (6). He approximated this as follows: "Since the maximum signal strength for trails of low line density occurs

at minimum radius, the maximum echo power, including the finite velocity and initial size effects, should occur at the instant of complete trail formation." Complete trail formation occurs when the first Fresnel zone is uncovered. Accordingly, Eshleman approximated the integral by neglecting the phase factor $\exp\{-(4\pi i/\lambda) R_0 [1 + (y/R)^2]^{1/2}\}$ over the range from 0 to $\sqrt{R_0\lambda}$ and setting the integral to zero over the rest of the range of integration.

Then, according to Eshleman,

$$E = \frac{A}{4\pi R_0} \exp\left\{-\frac{4\pi^2 r_0^2}{\lambda^2}\right\} \int_0^\infty \frac{\exp\left\{\frac{4\pi i}{\lambda} R_0\left[1 + \left(\frac{y}{R_0}\right)^2\right]^{1/2} - \frac{16\pi^2 D y}{\lambda^2 v_0}\right]}{\sqrt{1 + (y/R_0)^2}} dy$$

$$E \approx \frac{A}{4\pi R_0} \exp\left\{-\frac{4\pi^2 r_0^2}{\lambda^2}\right\} \int_0^{\sqrt{R_0\lambda}} \exp\left\{-\frac{16\pi^2 D y}{\lambda^2 v_0}\right\} dy$$

$$E \approx \frac{A}{4\pi R_0} \exp\left\{-\frac{4\pi^2 r_0^2}{\lambda^2}\right\} \frac{\lambda^2 v_0}{16\pi^2 D}\left[1 - \exp\left\{-\frac{16\pi^2 D\sqrt{R_0\lambda}}{\lambda^2 v_0}\right\}\right] \qquad (12)$$

Eshleman proceeded to develop the square of equation (12)—proportional to power. Comparison of equation (12) with equation (10) will show that they differ only in the factors

$$\frac{\lambda^2 v_0}{16\pi^2 D} \quad \text{and} \quad \frac{\lambda^2 v_0}{16\pi^2 D}\left[1 - \exp\left\{-\frac{16\pi^2 D\sqrt{R_0\lambda}}{\lambda^2 v_0}\right\}\right]$$

For

$$\frac{\lambda^2 v_0}{16\pi^2 D} \ll \sqrt{R_0\lambda}, \qquad \frac{\lambda^2 v_0}{16\pi^2 D}\left[1 - \exp\left\{-\frac{16\pi^2 D\sqrt{R_0\lambda}}{\lambda^2 v_0}\right\}\right] \to \frac{\lambda^2 v_0}{16\pi^2 D}$$

For UHF, Eshleman has, in reality, defined an effective scattering length equal to that given in equation (11). To this extent, the two approximations to the scattering integral give essentially the same results. In this paper, the integral was approximated by defining an effective scattering length (less than a Fresnel zone), and, therefore, one can expect a relaxation of the perpendicularity requirement. Because the form of his development required the use of a Fresnel zone, Eshleman may not have recognized the fact that at UHF the effective scattering length is less than the first Fresnel zone.

II. FRAUNHOFER DIFFRACTION

The important result of Part I is the realization that, when dealing with meteor echoes at UHF, one is not truly concerned with diffraction by an infinite plane. There is an important scattering distance L which is a measure of the effective diffraction aperture. For the wavelengths and ranges considered, the magnitude of L is such that Fraunhofer diffraction theory may be used.

Fraunhofer diffraction theory indicates that a beam of angular width θ is produced when an aperture of length L is illuminated by energy of wavelength λ according to the relation $\theta = \lambda/L$. If the aperture itself is illuminated from an angle β, the beam will be directed away from the normal by an angle β. There-

fore, in the meteor case, if we are to receive any back-radiation from a line source illuminated at an angle β, the beam-width of the line source must be 2β. Since $\theta = 2\beta = \lambda/L$, β_{max}, the greatest angle from the normal to the trail which will permit back-scattering to be observed, is (refer to Fig. 1)

$$\beta = \frac{\lambda}{2L} = \frac{S}{R_0} \qquad (13)$$

Equation (13) is important in two respects: (1) It can be used to estimate the range of S over which (10) is valid; (2) it can be used to estimate the maximum angle a meteor trail may deviate from the perpendicular to the line-of-sight and still qualify as a back-scatter source.

2.1 *The Distance from the Perpendicular Point*

Solving equation (13) for S_{max},

$$S_{max} = \frac{R_0\lambda}{2L} = \frac{8\pi^2 DR_0}{\lambda v_0} \approx \frac{R_0}{100\lambda} \qquad (14)$$

for $\lambda = 1$ meter, $R = 200$ km, $S_{max} = 2$ km.

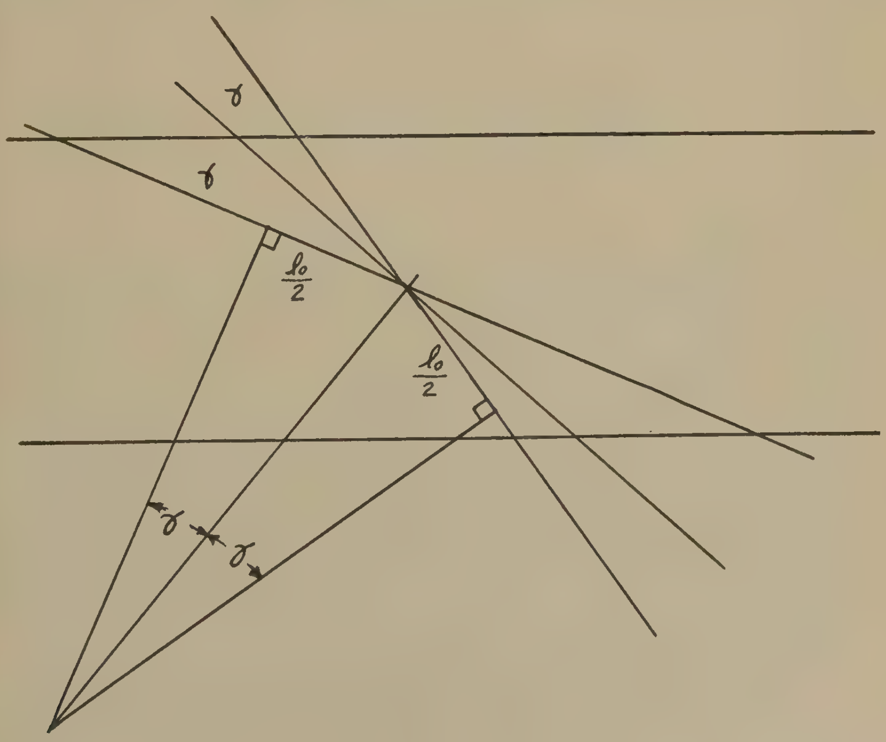

FIG. 3

2.2 *Maximum Deviation from Perpendicularity*

$$\beta_{max} = \frac{\lambda}{2L} = \frac{8\pi^2 D}{\lambda v_0} \approx \frac{10^{-2}}{\lambda} \quad \text{(15)}$$

for $\lambda = 1$ meter, $\beta_{max} \approx 1/2°$; for $\lambda = 50$ cm, $\beta_{max} \approx 1°$.

If the theory of meteor echoes at HF and VHF were used to predict the echo rate at UHF, only those trails which were perpendicular to the line-of-sight in the meteor plane could qualify as potential echoes. If meteor trails have an average length l_0, only those trails contained in the cone of semi-angle γ may qualify as echoes. Assuming that the distribution of sporadic meteor radiants is uniform, the echo rate will be proportional to γ.

$$\tan \gamma \approx \gamma = l_0/2R \quad \text{(16a)}$$

Taking into account the limited length of the scattering aperture by equation (15), the meteor echo rate at UHF will be proportional to $(\gamma + \beta)$.

$$M = \text{meteoric echo rate} = \alpha\left(\frac{l_0}{2R_0} + \frac{10^{-2}}{\lambda}\right) \quad \text{(16b)}$$

where α is a constant of proportionality.

The correction for the relaxation of the perpendicularity requirement is illustrated below by the cross-hatched area in Figure 4.

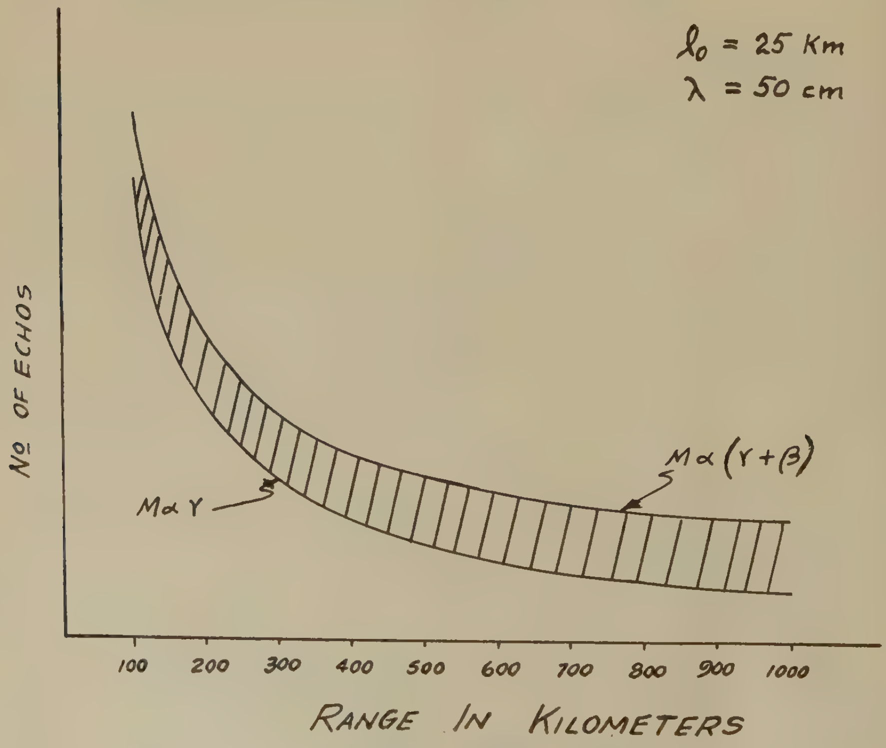

FIG. 4

2.3 *Calculation of Back-scattered Power*

The back-scattered field intensity from a meteor trail of initial density q, at a distance R from the receiver, per unit incident field intensity, is by equation (10)

$$E = \frac{\mu_0 e^2}{4\pi m R} q \exp\left\{-\frac{4\pi^2 r_0^2}{\lambda^2}\right\} \frac{\lambda^2 v_0}{16\pi^2 D} = 50\lambda^2 \frac{\mu_0 e^2}{4\pi m R} q \exp\left\{-\frac{4\pi^2 r_0^2}{\lambda^2}\right\}$$

The back-scattered field due to a transmitter of power P_0 is

$$E = \left[\frac{\rho P_0 G_T}{2\pi R_0^2}\right]^{1/2} 50\lambda^2 \frac{\mu_0 e^2}{4\pi m R_0} q \exp\left\{-\frac{4\pi^2 r_0^2}{\lambda^2}\right\}$$

The back-scattered power density at the receiver is

$$S = \frac{P_0 G_r}{4\pi R_0^2} 2500\lambda^4 \left(\frac{\mu_0 e^2}{m}\right)^2 \frac{q^2}{16\pi^2 R_0^2} \exp\left\{-\frac{8\pi^2 r_0^2}{\lambda^2}\right\}$$

The power abstracted from this back-scattered field by an antenna and matched load is

$$P_r = S\frac{\lambda^2}{4\pi} G_R = \frac{2500 P_0 G_T G_R}{16\pi^4 R^4} \left(\frac{\mu_0 e^2 q}{4m}\right)^2 \lambda^6 \exp\left\{-\frac{8\pi^2 r_0^2}{\lambda^2}\right\} \quad \ldots\ldots\ldots(17)$$

Equation (17) will hold for all $\lambda < 1.25$ meters. For certain values of λ, the Lovell-Clegg formula should hold.

$$P_r = \frac{P_0 G_r G_R}{32\pi^4} \left(\frac{\mu_0 e^2}{m}\right)^2 q^2 \left(\frac{\lambda}{R}\right)^3 \quad \ldots\ldots\ldots(18)$$

Equation (18) should hold for λ_{VHF} satisfying the relation

$$L = \frac{\lambda^2 v_0}{16\pi^2 D} = 50\lambda^2 \geq \sqrt{R\lambda}$$

for $R_{\min} = 100$ km and $\lambda_{VHF} > 2.7$ meters. Equation (18) is valid for $\lambda > 2.7$ meters. For $1.25 < \lambda < 2.7$, the formula in Eshleman's paper should be used.

$$P_r = \frac{P_0 G_r G_R}{32\pi^4} \left(\frac{\lambda}{R}\right)^3 \left(\frac{\mu_0 e^2 q}{4m}\right)^2 \frac{\lambda^3 v_0^2}{64\pi^4 D^2 R} \exp\left\{-\frac{16\pi^2 D\sqrt{R\lambda}}{\lambda^2 v_0}\right\} \sinh^2\left(\frac{8\pi^2 D\sqrt{R\lambda}}{\lambda^{3/2} v_0}\right) \quad ..(19)$$

2.4 *Meteor-Echo Duration Time*

Conventionally, one calculates that meteors do not give appreciable echoes until the entire trail (or at least the first Fresnel zone) has formed and the rate of decay of the echo strength is governed by the diffusion equation (eq. 3).

If the minimum detectable received power of the radar is $P_{r_{\min}}$,

$$P_{r_{\min}} = \frac{2500 P_0 G_r^2}{16\pi^4 R^4} \left(\frac{\mu_0 e^2}{4m}\right)^2 q_{\min}^2 \lambda^6 \exp\left\{-\frac{8\pi^2 r_0^2}{\lambda^2}\right\}$$

we can solve for the minimum detectable value of $q = q_{\min}$:

$$q_{\min} = 8.92 \times 10^{13} \left[\frac{P_{r_{\min}}}{P_0 G_r^2}\right]^{1/2} \exp\left\{\frac{4\pi^2 r_0^2}{\lambda^2}\right\} \lambda^{-3} R^2 \quad \ldots\ldots\ldots(20)$$

The time necessary for a meteor trail, initially of line density q_i, to decay to the minimum detectable value q_{min} is given by

$$t = \frac{\lambda^2}{16\pi^2 D} \ln\left(\frac{q_i}{q_{min}}\right) \quad (21)$$

For sensitive radars operating at wavelengths less than one meter, duration times of 2 to 3 milliseconds are to be expected.

However, it has been demonstrated that at UHF, the echo arises from a short length of trail moving with the velocity of the meteoric particle. Moreover, we have seen that meteoric returns at UHF are explainable in terms of Fraunhofer diffraction.

Equation (14) shows that the meteoric echoes can be observed at distances from the perpendicular point up to S_{max}.

$$S_{max} \leq \frac{R_0}{100\lambda}$$

The duration time

$$t_0 = \frac{S_{max}}{v_0} \approx \frac{R_0}{4\lambda} \times 10^{-6} \text{ sec} \quad (22)$$

For a minimum range of $R \doteq 100$ km, a wavelength of one meter, the minimum duration time of a meteoric echo is approximately 25 milliseconds. This should be contrasted with the duration times of 2 to 3 milliseconds given by the diffusion considerations of equation (21). It becomes apparent that meteoric echoes at UHF are "head echoes" and are observed during the process of trail formation. It may be argued that the meteor should still be seen after it passes the perpendicular point and that, therefore, equation (23) should be written $t_0 = 2S/v_0$. However, when meteor Doppler shifts are measured, they are primarily decreasing in frequency, implying that relatively few of the incoming meteoric particles have sufficient energy to penetrate through the meteor plane below the perpendicular point.

2.5 *Sporadic Meteor Echo Rate at UHF*

McKinley [3] has assumed that the number of sporadic meteors with mass m_0 or greater is inversely proportional to m_0, and that the ionization efficiency of a meteoric particle is independent of the mass of the particle. With these assumptions, at VHF and HF wavelengths, substantial agreement between the theoretical prediction of the effect of wavelength upon the echo rate of underdense sporadic meteors and experimental results has been obtained. Accordingly, let us assume that the number of meteor trails with line density greater than q_{min} is given by

$$n = \frac{K}{q_{min}} \quad (23)$$

where K is a proportionality constant and n is the average number of meteor trails with line density greater than q passing through one square meter of the meteor plane per second.

At a given instant of time, the average number of meteors N with line density greater than q_{min} present in one square meter of the meteor plane is

$$N = n \cdot t_0 = \frac{K}{q_{min}} \frac{R_0}{4\lambda} \times 10^{-6}$$

If we look for a finite period of time (a pulse length), then in addition to the number of meteors initially seen, during the pulse period, an additional number of meteors will be created. This number, ΔN, is equal to $\Delta N = n \cdot t_p$ meteors per square meter when t_p is the pulse length. The total number of meteors per look is $(N + \Delta N)$:

$$(N + \Delta N) = \frac{K}{q_{min}} \left[\frac{R_0}{4\lambda} \times 10^{-6} + t_p \right] \quad \text{.......} (24)$$

The fraction of meteor trails (assuming the radiants to be uniformly distributed in space) properly oriented to return an echo is given essentially by equation (16*a*). This fractional number has duration times given by (22). Echoes from trails satisfying (16*b*) but not (16*a*) have duration times proportionately less. The number of meteors properly oriented which can be seen per square meter per look is approximately

$$(N + \Delta N)\gamma = \frac{K}{q_{min}} \left[\frac{R_0}{4\lambda} \times 10^{-6} + t_p \right] \frac{l_0}{2R_0} \text{ meteors per square meter} \dots (25)$$

The echoing area of the meteor plane will be defined by the intersection of the antenna pattern and the meteor plane. The total number of meteor echoes per look will then be

$$T = \phi_0 \int_{\theta_{max}}^{\theta_{min}} - H^2 \csc^2 \theta \cot \theta \left[\frac{K}{q_{min}} \left(\frac{10^{-6} l_0}{8\lambda} + \frac{t_P l_0}{2R_0} \right) \right] d\theta \dots\dots (26)$$

where H = height of meteor plane $\approx 10^5$ meters, $R = H \csc \theta$, ϕ_0 = azimuthal beam-width, θ = elevation angular coverage from θ_{min} to θ_{max}, and T = number of echoes per look or per pulse.

Multiplying (26) by the pulse repetition frequency (r) of the radar will give the expected number of meteor echoes per second.

$$\left. \begin{aligned} M = r\phi_0 K \lambda^2 \exp\left\{ -\frac{0.395}{\lambda^2} \right\} 10^{-15} \left[\frac{P_0 G_T^2}{P_{r_{min}}} \right]^{1/2} \\ \cdot \left[3.5 \times 10^{-2} \ln\left(\frac{\sin \theta_{max}}{\sin \theta_{min}} \right) - 1.4 t_P \lambda (\sin \theta_{max} - \sin \theta_{min}) \right] \end{aligned} \right\} \dots (27)$$

If the pulse length is short enough (so that $\Delta N \ll N$), equation (27) may be further approximated:

$$M = 3.5 \times 10^{-17} r \phi_0 K \lambda^2 \left[\frac{P_0 G_T^2}{P_{r_{min}}} \right]^{1/2} \exp\left\{ -\frac{0.395}{\lambda^2} \right\} \left[\ln\left(\frac{\sin \theta_{max}}{\sin \theta_{min}} \right) \right] \dots\dots (28)$$

References

[1] V. R. Eshleman, Tech. Rep. No. 49, Electronics Research Laboratories, Stanford University (July 15, 1952).

[2] V. R. Eshleman, The effect of radar wavelength on meteor echo rate, Trans. Inst. Radio Eng., Professional Group on Antennas and Propagation, AP-1, No. 2 (1953).
[3] D. W. R. McKinley, Variation of meteor echo rates with radar system Parameters, Can. J. Phys., 29, 403-426 (1951).

APPENDIX I

In essence, what we have calculated is the back-scatter from a meteor as it approaches the perpendicular point. The arguments for evaluating the integral in this manner may be summarized by stating that under these conditions the maximum value of the integrand occurs closest to the point of stationary phase. Arguments of this sort led us to an integral which gives the correct answer when the maximum value of the integrand occurred at the point of stationary phase. We are now faced with the problem of what happens after the head of the meteor trail has passed the perpendicular and has traveled a distance S, as indicated by Figure 5. In the body of this paper, we have indicated that the echo should be substantially

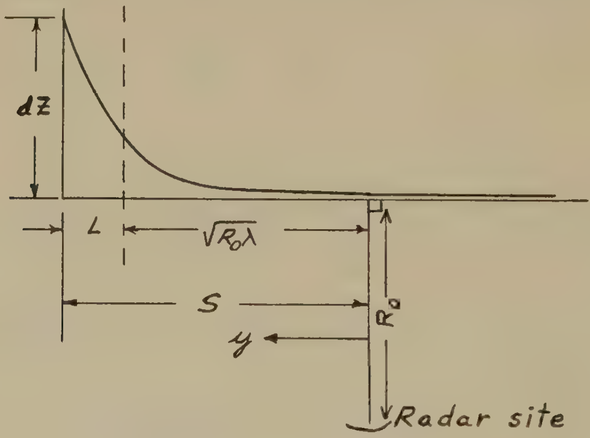

FIG. 5

constant just so long as the angle β satisfies equation (14) or the distance S is less than that distance given by equation (22). However, when the head of the meteor trail has passed the perpendicular point, there is a contribution at the point of stationary phase which must be considered in addition to the contribution from the maximum part of the integrand. If S is less than the first Fresnel zone, the development in Section I should hold and the result given by equation (11) is substantially correct. We are primarily concerned, therefore, with values of S greater than one Fresnel zone.

Consider

$$S \geq \sqrt{R_0\lambda} + L$$

Then the contribution from the point of maximum amplitude (given by eq. 11) is

$$E_{\text{amp}} = \frac{\mu_0 e^2}{4\pi m R_0} q \exp\left\{-\frac{4\pi^2 r_0^2}{\lambda^2}\right\} \frac{\lambda^2 v_0}{16\pi^2 D}$$

The contribution from the area of stationary phase (the first Fresnel zone) is

$$E_{\text{phase}} = \frac{\mu_0 e^2}{4\pi m R_0} q \exp\left\{-\frac{4\pi^2 r_0^2}{\lambda^2}\right\} \frac{\lambda^2 v_0}{16\pi^2 D}\left[\exp\left\{\frac{16\pi^2 D\sqrt{R_0\lambda}}{\lambda^2 v_0}\right\} - 1\right]\exp\left\{-\frac{16\pi^2 DS}{\lambda^2 v_0}\right\}$$

The ratio of the field due to region of stationary phase to the field due to the maximum value of the integrand is given by

$$\frac{E_{\text{phase}}}{E_{\text{amp}}} = \exp\left\{-\frac{S}{L}\right\}\left[\exp\left\{\frac{\sqrt{R_0 L}}{L}\right\} - 1\right] \approx \exp\left\{-\frac{S - \sqrt{R_0\lambda}}{L}\right\}$$

The contribution of the region of stationary phase is maximized for $S = \sqrt{R_0\lambda} + L$.

$$\left.\frac{E_{\text{phase}}}{E_{\text{amp}}}\right|_{\max} = \exp\left\{-\frac{L}{L}\right\} = \exp\{-1\}$$

As S becomes larger, $S = \sqrt{R_0\lambda} + z \leq R_0/100\,\lambda$.

$$\frac{E_{\text{phase}}}{E_{\text{amp}}} = \exp\left\{-\frac{z}{L}\right\}$$

For $R_0 = 300 \times 10^3$ meters, $\lambda = 1$ meter, and $z = 2.45 \times 10^3$ meters,

$$\frac{E_{\text{phase}}}{E_{\text{amp}}} = \exp\{-50\}$$

The above calculations show that after the meteor has passed the perpendicular point, the maximum contribution of the region of stationary phase is but 37 per cent of the field due to the maximum value of the integrand. If we consider that, at worst, the back-scattered field from the stationary phase point may be in antiphase with respect to the field from the effective scattering length, then the total field will be reduced to 63 per cent of the value given by equation (11). Under these circumstances, the back-scattered power will be reduced by approximately 4 decibels from the values given by (17). This correction to the back-scattered power is present for only a very short period of time—as the head of the meteor trail passes beyond the perpendicular point, the back-scattered field will rapidly return to its initial value. Consequently, it is felt that these calculations indicate that the meteor echo is substantially constant over the range of S given by equation (14).

RADIO FREQUENCY AND SCATTERING ANGLE DEPENDENCE OF IONOSPHERIC SCATTER PROPAGATION AT VHF

By ALBERT D. WHEELON

The Ramo-Wooldridge Corporation, Los Angeles, California

(Received September 3, 1956)

ABSTRACT

The weak and fluctuating radio signals observed at distances of 1,500 km on VHF are attributed to scattering from E-region turbulence. It is noted that propagation constants $k = 4\pi/\lambda \sin(\theta/2)$, corresponding to the experimental frequencies (28 to 108 Mc), just straddle the viscosity cutoff wave-number $k_s = (2 \text{ meters})^{-1}$ of the region, thereby giving a qualitative explanation for the curious dichotomy found in the experimental data. The two competitive turbulence theories are then developed in detail near the viscosity transition range. It is found that pressure fluctuations of the ionosphere's neutral gases induce a spectrum of dielectric variations which reproduce the frequency and scattering angle dependence of the experimental results quite well. A theory of turbulent mixing of ionization gradients is then developed along the lines of Heisenberg's original treatment of the velocity field. This process predicts a frequency variation of power levels which is also satisfactory. It is concluded that more precise, simultaneous measurements will be required to choose between the two theories on this basis.

1. INTRODUCTION

The chance observation of unexplicably high field strengths beyond the optical orizon ($\sim$ 300 km) at microwave frequencies [see 1 of "References" at end of aper] gave the first hint of "scatter propagation." Subsequent experiments howed that the received signal was weak but significantly greater than that redicted by round earth diffraction theory. The field strength decreased very owly with distance and was observed to fade about its mean value ($\sim$ 70 db elow free space) several times a second. These facts suggested a statistical theory f scattering from turbulent fluctuations of the troposphere's dielectric constant 2], a theory which has been developed and fitted to increasingly refined experiments 3].

This experience suggested that a similar propagation mode might be sustained 1 the ionospheric E layer at frequencies above the maximum usuable frequency MUF) by large angle scattering from turbulent concentrations of free electrons. uch a mechanism was immediately observed at VHF for ranges extending to ,500 km [4], thus providing an important new mode of radio propagation. To

explain the *average power level* of these scatter transmissions, several hydrodynamic theories of turbulent fluctuations were advanced.

Villars and Weisskopf [5] first proposed a theory based on pressure fluctuations of the ionosphere's neutral gases. The ionized electrons were imagined to be frozen into the neutral viscous fluid, which they described by the Navier-Stokes equations. Percentile variations in electron density, fluid density, fluid pressure, and fluid velocity were thus related. Using a Born approximation for the electromagnetic scattering by such turbulence, they were able to tie the received signal's statistical properties to those of the turbulent velocity field in the ionosphere, thereby bringing the considerable literature on homogeneous turbulence [6] to bear on the problem.

The initial success of this approach in predicting average power levels was later challenged by Gallet [7] and the original authors [8] themselves. They now feel that a more careful evaluation of the meteorological parameters gives a power which is one thousand times smaller than that measured (others disagree—see section 3). These writers suggest that much less turbulence in the presence of ionization gradients can stir up enough fluctuations to provide ample scattered power. The balanced state between this mixing and diffusion-recombination effects is imagined to scatter the electromagnetic waves, and the signal's statistical properties are again related to those of the (convective) velocity field.

This paper is concerned with the radio frequency and scattering angle dependence of the received power. The results of an important series of experiments designed to establish these two scaling laws have recently been declassified and published by Bailey, Bateman, and Kirby [9]. They measured the power ratios amongst three VHF transmissions over the same path with scaled antennae. To establish the angle variation, 50-Mc signals were monitored with three identical receivers spaced along a great-circle path. The great virtue of these experiments is that they give relative values, which are thus free from transmitter-receiver properties and presumably refer to the scattering agency alone.

We shall investigate both the pressure fluctuation and turbulent mixing theories to see what predictions they make for this radio frequency and scattering angle dependence of the received power. Theoretically, one finds that these scaling laws depend upon but one physical quantity—the viscosity cutoff wave-number k_s of the velocity decay spectrum. Comparison of theory with experiment then allows one to estimate this parameter and extrapolate present data to other transmission conditions.

2. SUMMARY OF OBSERVATIONS

Let us review briefly the experimental findings of Bailey, Bateman, and Kirby [9] which the theories must explain. The standard transmission geometry is shown in Figure 1. The power received at R may be described as the product of (1) the power per unit area incident on the scatterers, P_T/D; (2) the scattering cross-section per unit volume per unit solid angle $\sigma(\theta, \lambda)$; (3) the scattering volume, $V = Db \csc(\theta/2)$;* and (4) the solid angle subtended by the receiving antenna

*We imagine the turbulence to be confined within a layer of thickness b, as shown in Figure 1.

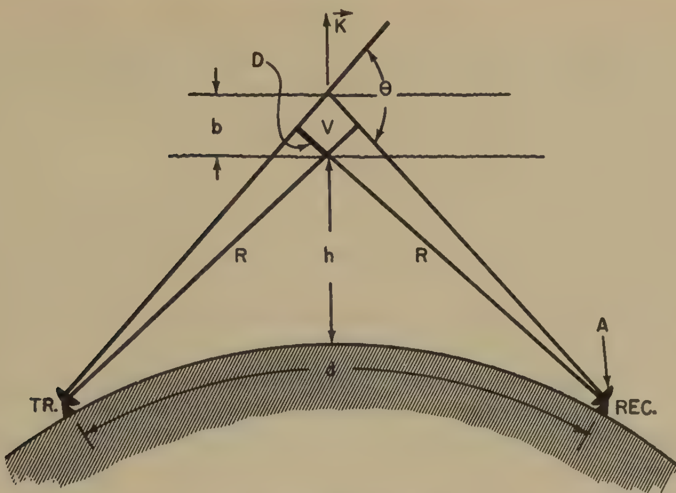

FIG. 1—Scatter propagation geometry

$\Omega = A/R^2$.

$$P_R = \frac{P_T b A}{R^2} \csc\left(\frac{\theta}{2}\right) \sigma(\theta, \lambda) \quad (2.1)$$

Except for the geometrical factor $R^{-2} \csc(\theta/2)$, all of the frequency and scattering angle dependence arises in σ.

The scattering cross-section $\sigma(\theta, \lambda)$ represents the electromagnetic response of the turbulent fluctuations to radiation of wavelength λ, for scattering at an angle θ to the primary beam. It may be expressed [8] in terms of the (spatial) Fourier transform of the variation in electron density* $\delta N(r, t)$ from the mean N_0 and the classical electron radius $r_0 = e^2/mc^2 = 2.8\ 10^{-13}$ cm.

$$\left.\begin{aligned} \sigma(\theta, \lambda) &= r_0^2 \frac{1}{V} \cdot \overline{\left| \int d^3 r e^{i\vec{k}\cdot\vec{r}} \delta N(r, t) \right|^2} \\ &= r_0^2 \frac{1}{V} \cdot \overline{| \eta(k, t) |^2} \end{aligned}\right\} \quad (2.2)$$

The "scattering vector" $\vec{k}$ is the difference between the incoming and outgoing propagation vectors, and its magnitude is given by [10]

$$|\vec{k}| = \frac{4\pi}{\lambda} \sin\left(\frac{\theta}{2}\right)\left[1 - \left(\frac{\text{MUF}}{\omega}\right)^2\right]^{1/2} \quad (2.3)$$

*An equivalent, and perhaps more familiar, representation is obtained if the turbulence is assumed to be homogeneous and isotropic, for then

$$\overline{\delta N(r, t)\, \delta N(r + \rho, t)} = \overline{\delta N^2}\, C(\rho)$$

and the cross-section is defined in terms of the space correlation's Fourier transform.

$$\sigma(\theta, \lambda) = r_0^2 \overline{\delta N^2} \int d^3\rho\, e^{i\vec{k}\cdot\vec{\rho}} C(\rho)$$

The third factor contains the maximum usable frequency (MUF) and represents the refractive correction to scattering in an ionized medium. Numerically, one finds that such effects are unimportant for *relative* power levels, and we shall set MUF = 0 in this paper.

(*a*) *Scattering angle dependence*

To determine the variation of P_R with θ, the National Bureau of Standards (NBS) group used three identical receivers to monitor three 49.7-Mc pulse transmitters at Sterling, Virginia. The three receivers were placed along a great-circle path at distances of 491, 592, and 811 km and their median signal levels compared. They [9] found that the power received at 592 km was between 5 and 7 db below the corresponding median at 811 km. The mean level at 491 km was found to be between 7 and 9 db below that at 811 km. The experimental data are *not* well fitted by a single inverse power of sin $(\theta/2)$.

(*b*) *Frequency dependence*

To investigate how the receiver signal depends on the radio frequency employed, a series of simultaneous transmissions were begun on the Sterling, Virginia, to Cedar Rapids, Iowa, path (d = 1,250 km, $h \simeq 85$ km). Scaled transmitting and receiving aerial sizes and heights were used to ensure that the results so obtained would reflect the frequency dependence of σ alone (that is, not A). These tests were made in two stages.

The first experiment compared simultaneous mean power levels at 49.8 and 107.8 Mc. The results were expressed as a power-law variation of the wavelength ratio.

$$\frac{P(108)}{P(50)} = \left[\frac{\lambda_{108}}{\lambda_{50}}\right]^n \qquad (2.4)$$

Bailey, *et al.* [9], found that n was not constant but varied diurnally and seasonally from 4 to 12. "Under conditions of strong scattered signal for the lower frequency, the median effective exponent tends to be the order 8. Under conditions of weak signal, the median effective exponent is smaller, values of 6 to 7 are typical." These averages refer to the exponents observed most often on a mass-density plot of data. A second series of tests were instituted somewhat later (and not simultaneous with the first series, unfortunately) to compare 27.8- and 49.8-Mc transmissions on this same path. Writing

$$\frac{P(50)}{P(28)} = \left[\frac{\lambda_{50}}{\lambda_{28}}\right]^m, \qquad (2.5)$$

the NBS group [9] found that m is also variable. "Under conditions of strong signal, as observed at the lower frequency, $\cdots$ it may be as high as 6 to 6.5 $\cdots$ under conditions of weak signals $\cdots$ a value of 4 to 4.5 is representative." A similar comparison of 24.3- and 48.9-Mc signals in Alaska showed roughly the same behavior.

More recently, Kirby [11] has reported on the diurnal and seasonal variation of m and n. During 1952, the 50 to 108 exponent (n) was found to vary between 6

n the evening to 8 at midday in December, and between 6.3 and 7.7 at the same imes in June. The tests on 28 and 50 Mc in 1954 show a much smaller diurnal variation; m varies from 4.5 to 5.5 (uncorrected for absorption) between night and day, respectively, in December, and from 3.5 to 5 in June. The striking point n these data is that n has almost twice as much diurnal variation as m at all easons.

c) *Evaluation*

These results are, indeed, bewildering. Disregarding for the moment the variability of both m and n, it is difficult to understand why their median values hould differ. If a scaling law has any meaning at all, it should hold over a three-o-one range of the independent variable! Our conclusion is that something rather drastic takes place in the turbulence decay scheme at a size comparable with the wave-number of the 50-Mc transmission. This idea is supported by turbulence heory [6], which says that atmospheric viscosity begins to control and *destroy* he subdividing blobs at a wave-number $k_s = \frac{1}{2}$ meters^{-1}. When this is compared with the propagation constant $k = 4\pi/\lambda \sin(\theta/2)$ of the transmissions, one sees hat k_s just divides the frequency band used to establish the frequency dependence. The curious dichotomy of the scaling laws is thus explained as a natural effect of the "smallest blob" cutoff imposed by viscosity effects. This idea was developed n a qualitative fashion in an earlier publication [12] and will now be studied in detail for the two turbulence theories, paying special attention to the high wave-number end of their spectra.

3. TURBULENT PRESSURE FLUCTUATIONS

Villars and Weisskopf [5] imagined the ionized electrons to be frozen into he turbulent neutral carrier so that their percentile density variations could be equated, $\delta N/N_0 = \Delta\rho/\rho_0$. If compressions and rarefactions of the neutral fluid's turbulent blobs are accomplished adiabatically, pressure and density fluctuations are connected by $\Delta\rho/\rho_0 = \gamma\Delta p/p_0$, where γ is the ratio of specific heats. The turbulent velocity and pressure fields are related to one another by he Navier-Stokes equations for viscous flow.*

$$\frac{\partial V_\alpha(r, t)}{\partial t} + V_\beta(r, t)\frac{\partial}{\partial r_\beta}V_\alpha(r, t) = \nu\nabla^2 V_\alpha(r, t) - \frac{\partial}{\partial r_\alpha}\frac{p(r, t)}{\rho_0} \quad \text{(3.1)}$$

To this equation, we adjoin the incompressibility condition

$$\frac{\partial}{\partial r_\alpha}V_\alpha(r, t) = 0 \quad \text{(3.2)}$$

which is valid so long as the velocity fluctuations are small compared with the ocal speed of sound, as they surely are.

In this and the following section, we shall deal directly with the Fourier integral epresentations

* $\nu = \mu/\rho$ is the kinematic viscosity and one is to sum over repeated indices.

$$V_\alpha(r, t) = \int d^3k\, e^{i\vec{k}\cdot\vec{r}} V_\alpha(k, t) \quad \text{(3.3a)}$$

$$p(r, t) = \int d^3k\, e^{i\vec{k}\cdot\vec{r}} p(k, t) \quad \text{(3.3b)}$$

where the transforms satisfy $p^*(k, t) = p(-k, t)$, etc., since the space functions are all real. The field equations (3.1) become

$$ik_\alpha \frac{p(k, t)}{\rho_0} + \left[\frac{\partial}{\partial t} + k^2\nu\right] V_\alpha(k, t) + i \int d^3l\, k_\beta V_\beta(l, t) V_\alpha(k - l, t) = 0 \quad \text{(3.4)}$$

and the divergence condition $k_\alpha V_\alpha(k, t) = 0$ permits one to relate the pressue and velocity spectra.

$$p(k, t) = -\rho_0 \int d^3l \frac{k_\alpha k_\beta}{k^2} V_\alpha(k - l, t) V_\beta(l, t) \quad \text{(3.5)}$$

A given Fourier component $p(k, t)$ is determined principally by space-like conditions which are localized to a dimension $L = 2\pi/k$. The ambient pressure corresponds to $k = 0$, and all other $p(k, t)$ represent pressure fluctuations (that is, Δp). By the identification of δN with Δp described above, we find that

$$\eta(k, t) = -\frac{N_0}{u_0^2} \int d^3l \frac{k_\alpha k_\beta}{k^2} V_\alpha(k - l, t) V_\beta(l, t) \quad \text{(3.6)}$$

where $u_0 = [\gamma p_0/\rho_0]^{\frac{1}{2}}$ is the local velocity of sound. The scattering cross-section (2.2) is computed from this result directly.

$$\sigma(k) = \left[\frac{r_0 N_0}{u_0^2}\right]^2 \frac{1}{V} \int d^3l \int d^3\lambda \frac{k_\alpha k_\beta k_\mu k_\nu}{k^4} \Omega\alpha\beta\mu\nu \quad \text{(3.7)}$$

where

$$\Omega\alpha\beta\mu\nu = \overline{V_\alpha(k - l, t) V_\beta(l, t) V_\mu(-k - \lambda, t) V_\nu(\lambda, t)} \quad \text{(3.8)}$$

The received power is thus identified with a time average over the velocity field. To evaluate (3.8), Batchelor [13] and Heisenberg [14] assumed that the $V_\alpha(k, t)$ could be treated as Gaussian random variables, namely,

$$\overline{V_\alpha V_\beta V_\mu V_\nu} = \overline{V_\alpha V_\beta}\; \overline{V_\mu V_\nu} + \overline{V_\alpha V_\mu}\; \overline{V_\beta V_\nu} + \overline{V_\alpha V_\nu}\; \overline{V_\beta V_\mu} \quad \text{(3.9)}$$

This ansatz is mathematically very valuable, for it relates the fourth order average of (3.8) to the fundamental spectrum [6] of kinetic energy $E(k)$ *via*

$$\overline{V_\alpha(k, t) V_\beta(k', t)} = (2\pi)^3 \delta(k + k') \frac{E(k)}{4\pi k^2} \left[\delta\alpha\beta - \frac{k_\alpha k_\beta}{k^2}\right]^* \quad \text{(3.10)}$$

The physical justification for (3.9) is more difficult to find. Although the largest (k_0) blobs may well be Gaussian,† it is doubtful if the redistribution of their energy

*The factor $(2\pi)^3$ only sets the normalization in our integral framework and is unimportant for power ratio predictions.

†As a result of a Central Limit Theorem analysis applied to their formation mechanism.

amongst higher k by the *non-linear* term in (3.4) could fail to alter significantly the initial probability characteristics. This is especially true "by the time" the smallest blobs appear, for $k_s = 10^4 k_0$ represents an enormous range over which this inertial (non-linear) term must operate. Nonetheless, we shall employ the assumption (3.9) in this analysis as a working hypothesis, to be discarded if it gives wrong answers or when a better theory is devised.

With the results of (3.9) and (3.10), one may reduce the integrations of (3.7) to a simple form.*

$$\sigma(k) = \left[\frac{r_0 N_0}{u_0^2}\right]^2 \pi \int d^3 l \, \frac{E(l) E(|\overrightarrow{k - l}|)}{|\overrightarrow{k - l}|^4} \sin^4 \psi \ldots\ldots\ldots\ldots (3.11)$$

Here ψ is the angle between $\vec{k}$ and $\vec{l}$. Since the spectra are proportional to v_0^2, the cross-section takes a factor $(v_0/u_0)^4$. At a height of 90 km, one finds $u_0 \simeq 400$ m/sec. The most recent estimate of Villars and Weisskopf [8] and Gallet [7] is $v_0 = 5$ m/sec and gives an absolute power level 40 db below the observed value. On the other hand, Booker [15] now finds good reason to believe that $v_0 = 30$ m/sec at these heights, which gives ample signal. The matter cannot be settled at this time on the basis of absolute power levels alone, and gives added incentive to study the frequency and scattering angle dependence of the transmission contained in the integral term of (3.11).

To proceed further, one must express a preference for one of the various theories predicting $E(k)$. We shall use Heisenberg's generalization [14] of Kologomoroff's similarity result ($k^{-5/3}$) to describe the transition to the high wave-number ($> k_s$) range.

$$E(k) = \frac{v_0^2}{l_0^{2/3}} \frac{1}{k^{5/3}} \frac{1}{[k^4/k_s^4 + 1]^{4/3}} \ldots\ldots\ldots\ldots (3.12)$$

The smallest blob wave-number k_s is given in terms of the large blob parameters and ν by

$$k_s^4 \simeq \frac{3}{8} \frac{v_0^3}{l_0 \nu^3} \ldots\ldots\ldots\ldots (3.13)$$

The result (3.11) is conveniently written in spherical polar coordinates centered on the vector $\vec{k}$.

$$\left.\begin{aligned} \sigma(k) = \left[\frac{r_0 N_0}{u_0^2}\right]^2 \pi \int_{k_0}^{\infty} dl \, l^2 \int_0^{\pi} d\psi \sin \psi \int_0^{2\pi} d\phi \, E(l) \sin^4 \psi \\ \frac{E[\sqrt{k^2 + l^2 - 2lk \cos \psi}]}{[k^2 + l^2 - 2lk \cos \psi]^2} \end{aligned}\right\} \ldots (3.14)$$

Combining (3.12) with (3.14) and introducing the dimensionless variables,

*Noting that

$$\int d^3 l \, \delta^2(l + a) = \int d^3 l \, \delta(l + a) \frac{1}{(2\pi)^3} \int_V d^3 x \, e^{i \vec{x} \cdot (\overrightarrow{l + a})} = \frac{V}{(2\pi)^3}$$

$$l = tk \text{ and } y = 1 + t^2 - 2t\cos\psi$$

one finds

$$\sigma(k) = \frac{2\pi^2}{l_0^{4/3}}(r_0N_0)^2\left(\frac{v_0}{u_0}\right)^4\frac{1}{k^{13/3}}W\left[\frac{k}{k_s}\right] \qquad (3.15)$$

with

$$W(\alpha) = \frac{1}{32}\int_0^\infty \frac{dt}{t^{14/3}[1+\alpha^4t^4]^{4/3}}\int_{(1-t)^2}^{(1+t)^2} dy\,\frac{[(1+t)^2-y]^2[(1-t)^2-y]^2}{y^{17/6}[1+\alpha^4y^2]^{4/3}} \qquad (3.16)$$

The lower limit k_0/k has been relaxed to zero here, since the integrand behaves like $t^{1/3}$ for small t. By ingenious analysis, E. Levin has derived the asymptotic results (see also ref. [5]).

$$W(\alpha) = \begin{Bmatrix} 1.326, & \alpha \ll 1 \\ \dfrac{1.600}{\alpha^{20/3}}, & \alpha \gg 1 \end{Bmatrix} \qquad (3.16a)$$

The experimental data reviewed in Part 2 indicated that the k range just near k_s is critical for the VHF experiments. To bridge the gap between these asymptotic expressions, the double integral $W[\alpha]$ of (3.16) was computed numerically on an ERA 1103 digital machine and the results plotted in Figure 2.

To investigate the frequency dependence of the scattered power predicted by this approach, we replace k by the propagation constant in equation (2.3). The angle θ is equated to 21°, corresponding to a scattering height of 85 km for the 1,250-km path (see Fig. 5). The ratio between two powers on different frequencies may thus be written in the form of equation (2.4).

$$\left[\frac{\lambda_{108}}{\lambda_{50}}\right]^n = \left[\frac{k_{50}}{k_{108}}\right]^{13/3}\cdot\frac{W\left[\frac{k_{108}}{k_s}\,0.564\right]}{W\left[\frac{k_{50}}{k_s}\,0.564\right]}, \qquad k = \frac{2\pi}{\lambda}$$

This expression was solved for n as a function k_s and is plotted in Figure 3. The experimental mean value $n = 8$ is shown on the same graph and corresponds to a cutoff wave-number $k_s = (2 \text{ meters})^{-1}$, in good agreement with meteorological data for this height [8]. One should also note that the large diurnal and seasonal variations observed for n can now be understood in terms of small changes in k_s.

A similar comparison was made for the 50- and 28-Mc transmissions, and the frequency scaling exponent m plotted as a function of k_s in Figure 4. The reported value $m = 6$ corresponds to a value $k_s^{-1} = 3$ meters. If one does not correct the observed value 4 to 4.5 for non-deviative absorption (to 6), a smaller value $k_s^{-1} = 2$ meters is found, in substantial agreement with the conclusions reached in Figure 3. In any case, a precise agreement with Figure 3 cannot be demanded, since the experiments were not performed simultaneously and seasonal variations of the signal are pronounced.

The diurnal variation of these exponents reported by Kirby [11] shows that

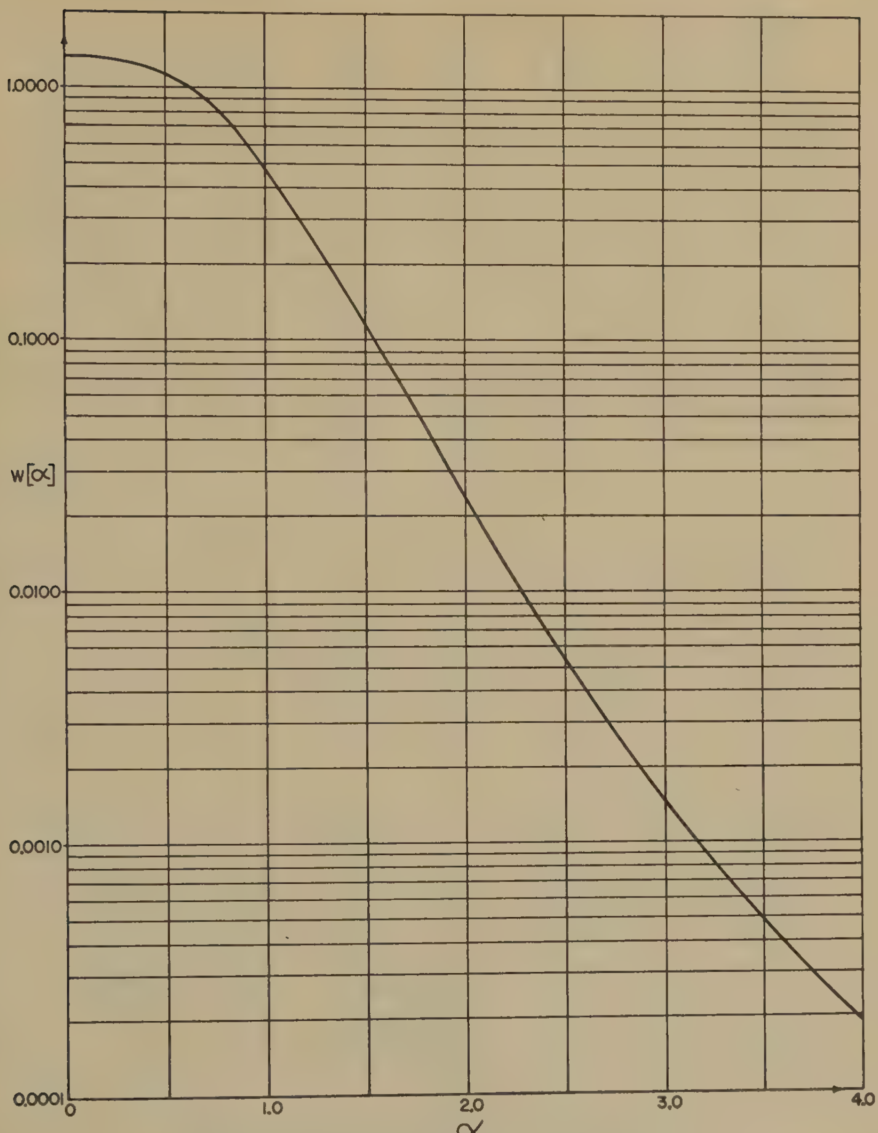

FIG. 2—Plot of double integral $W(\alpha)$ in equation (3.16)

n varies almost twice as much as m at any season. One might think that this ratio variation is caused by the familiar change of MUF with time of day (compare eq. 2.3). If this were so, however, the 50- to 28-Mc comparison should show the greatest effect. Just the reverse seems to be the case, so that we conclude that k_s itself must enjoy a diurnal variation. Comparing the slopes of Figures 3 and 4, one sees that $n(k_s)$ rises almost twice as steeply as $m(k_s)$ in the significant range, so that the same change in k_s would produce the observed variations.

To investigate the distance dependence of scattered power on a fixed frequency (50 Mc), we return to (2.1) and (3.15).

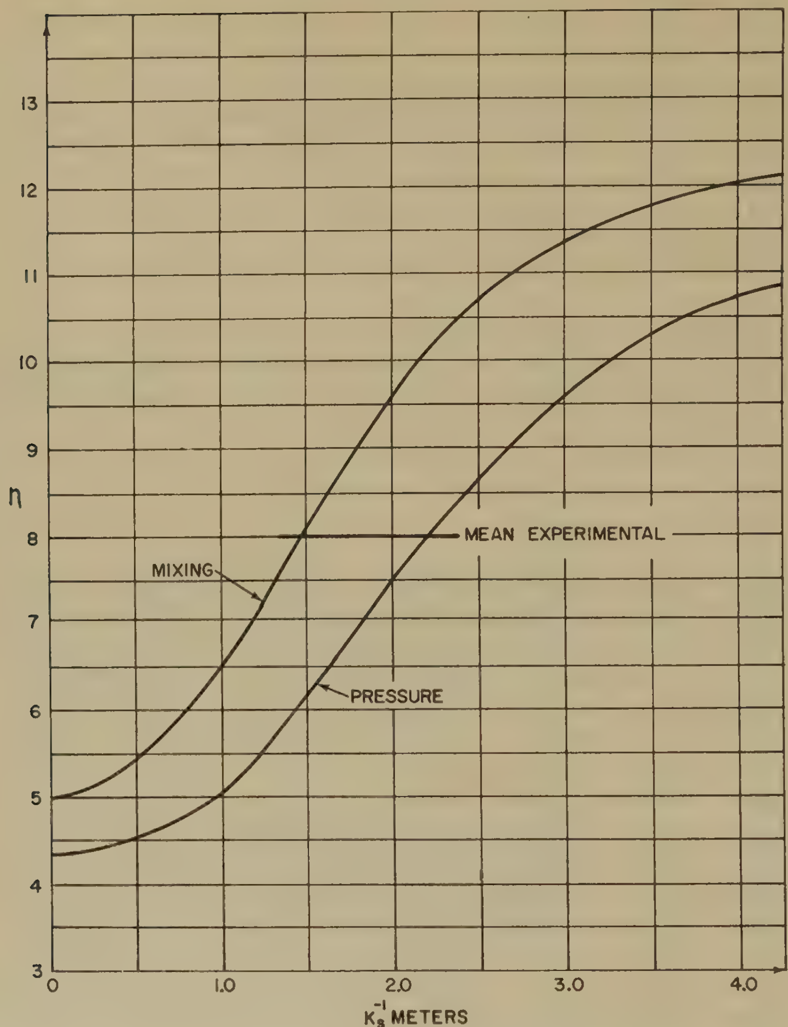

FIG. 3—Frequency scaling exponent for 50- to 108-Mc comparison; d = 1,250 km and h = 85 km

$$P(d) \simeq \frac{1}{[\sin\ \theta/2]^{13/3+1}} \frac{1}{R^2} W\left[\frac{1}{k_s} \frac{4\pi}{6} \sin\left(\frac{\theta}{2}\right)\right] \qquad (3.17)$$

The scattering angle θ corresponding to a given surface range d and scattering height h is computed from

$$\tan\left(\frac{\theta}{2}\right) = \frac{2h}{d} + \frac{d}{4a} \qquad (3.18)$$

where a = 6,400 km is the earth's radius. Sin $(\theta/2)$ is plotted in Figure 5 for various d and h values. The ray path length is given quite accurately by $R = \frac{1}{2}d$ for short ranges. Using (3.17), we have computed the ratio of measured power at 491 and 592 km to that at 811 km as functions of k_s and recorded the results in Figure 6.

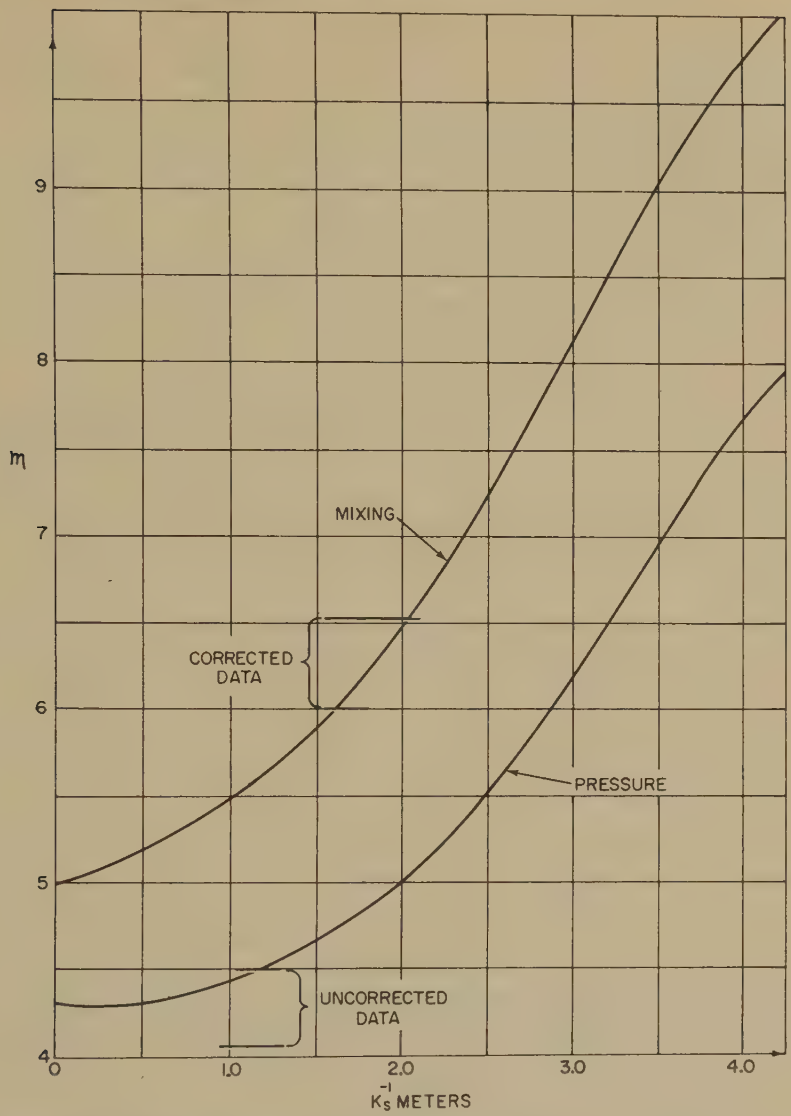

FIG. 4—Frequency scaling exponent for 28- to 50-Mc comparison; $d = 1{,}250$ km and $h = 85$ km

The experimental data are indicated on these graphs and good agreement indicated for

$$1.5 < k_s^{-1} < 2.5 \text{ meters}$$

On the whole, agreement between the pressure fluctuation theory and experimental results is remarkably good. Were it not for the uncertainty in absolute power levels discussed before, one would be inclined to accept this model and use it to extrapolate present data to other transmission situations with a working value $k_s^{-1} = 2$ meters.

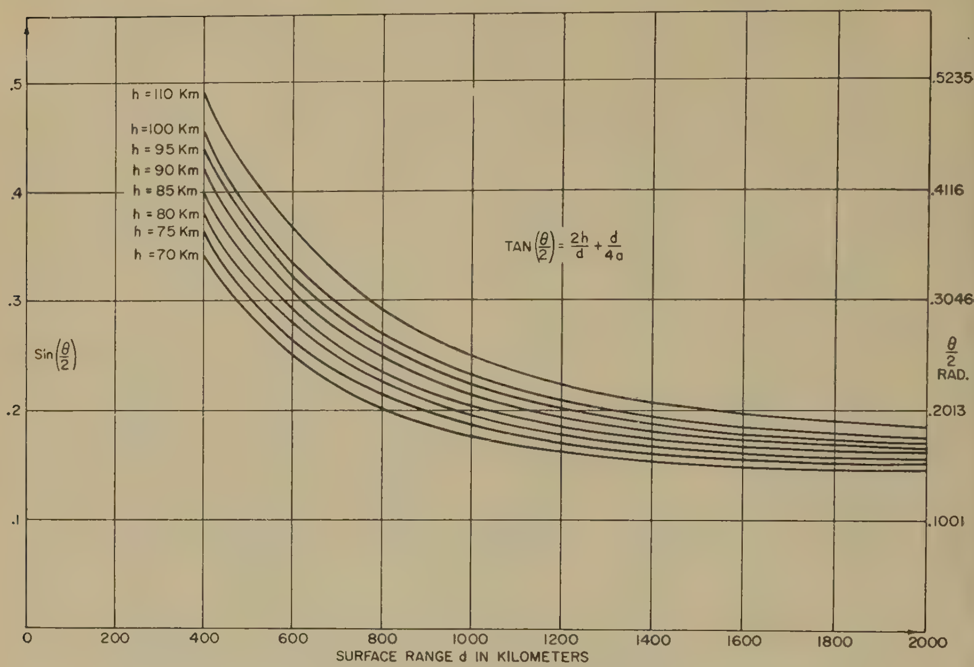

FIG. 5—Scattering angle *vs* distance for fixed heights and $a = 6{,}400$ km

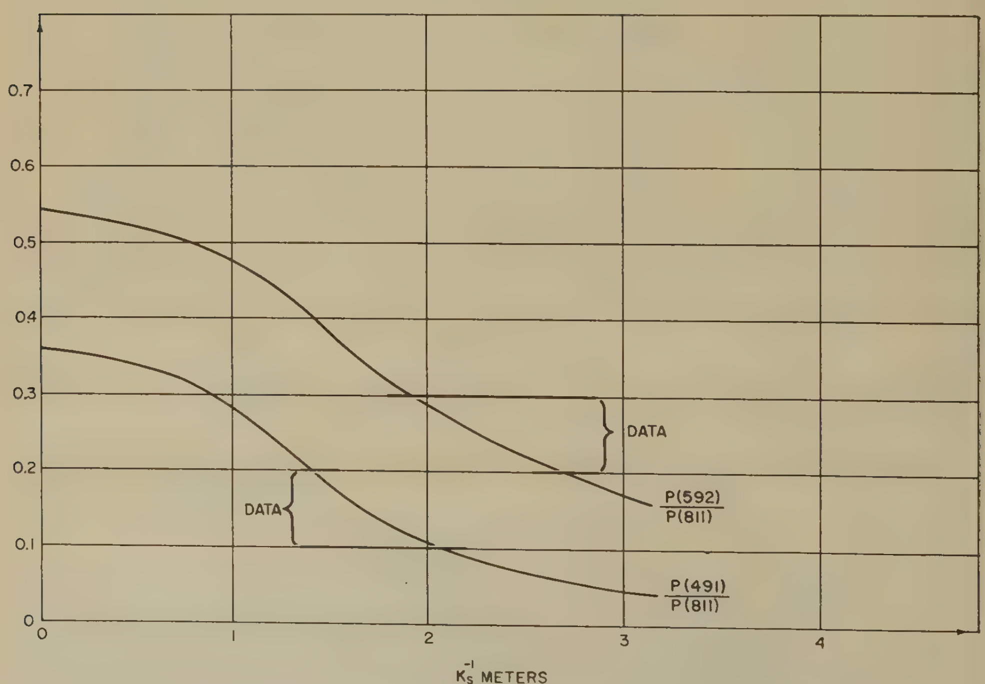

FIG. 6—Scattering angle variation, power ratios for 50 Mc, pressure theory, $h = 80$ km

4. TURBULENT MIXING FLUCTUATIONS

Again imagine the electrons to be frozen into the neutral turbulent fluid (gas). Now consider what happens to an initial gradient of ionization, such as is established in the standard ionospheric layers or by meteor trails [15]. Turbulent motions of the neutral carrier transfer electrons from low to high density points on this gradient's profile, and *vice versa*. These intruding cells appear as fluctuations against the ambient profile and scatter accordingly. In an unpublished paper, Villars and Weisskopf [16] have formulated these ideas mathematically.

Let $N(r, t)$ be the local electron density in the mixing medium. Its total time change is related to the ionization rate $I(r)$, recombination coefficient α, and diffusion constant D by the continuity equation.

$$\frac{\partial N(r, t)}{\partial t} + V_\alpha(r, t) \frac{\partial}{\partial r_\alpha} N(r, t) = I(r) - \alpha N^2(r, t) + D\nabla^2 N(r, t) \quad \text{(4.1)}$$

The convective velocity $V_\alpha(r, t)$ is the divergence-free solution of the Navier-Stokes equations (3.1) and (3.2). Since it is a statistical function itself, it induces statistical fluctuations in the mixed electron configuration. If there were no turbulence, a static profile $N_0(r)$ would be established, satisfying

$$0 = I(r) - \alpha N_0^2(r) + D\nabla^2 N_0(r) \quad \text{(4.2)}$$

and such solutions have been discussed frequently [17].

We are interested here in the density fluctuation,

$$\delta N(r, t) = N(r, t) - N_0(r) \quad \text{(4.3)}$$

Subtracting (4.2) from (4.1) and neglecting non-linear terms, we find that δN satisfies

$$\frac{\partial \delta N}{\partial t} + [2\alpha N_0 - D\nabla^2]\delta N = -V_\alpha \frac{\partial}{\partial r_\alpha} [N_0 + \delta N] \quad \text{(4.4)}$$

It is quite a good approximation to hold N_0 constant in the recombination (α) term and to let the gradient of N_0 be constant on the right-hand side. Introducing Fourier transforms for δN and V_α as before, we find that $\eta(k, t)$ satisfies the integro-differential equation

$$\left.\begin{aligned} &\frac{\partial \eta(k, t)}{\partial t} + [2\alpha N_0 + Dk^2]\eta(k, t) + \frac{dN_0}{dh} j_\alpha V_\alpha(k, t) \\ &\qquad + i \int d^3 l\, k_\alpha V_\alpha(k - l, t)\eta(l, t) = 0 \end{aligned}\right\} \quad \text{(4.5)}$$

where j_α is a unit factor in the direction of the (initial) ionization gradient—probably vertical.

If the integral or self-mixing term in this equation were negligible, one could provide an analytic solution; $\eta(k, t)$ then behaves like the output of an R-L filter driven by a random input. In the lower E region [18], $2\alpha N_0 \simeq 10^{-3}$ sec^{-1} and $D \simeq 10^4$ cm^2 sec^{-1}, but, since we are interested in values of $k \simeq 1/200$ cm, we may neglect recombination effects in comparison with diffusion "damping." As

a first approximation then,

$$\eta(k, t) = -\frac{dN_0}{dh} \int_0^\infty du\, e^{-Dk^2u} j_\alpha V_\alpha(k, t - u) \qquad (4.6)$$

To average this expression, we extend the result (3.10) to account for two $V(k, t)$ displaced in *time*.

$$\overline{V_\alpha(k, t) V_\beta(k', t + \tau)} = (2\pi)^3 \delta(k + k') \frac{E(k)}{4\pi k^2} \left[\delta_{\alpha\beta} - \frac{k_\alpha k_\beta}{k^2} \right] C[k, |\tau|] \qquad (4.7)$$

The scattering cross-section (2.2) may now be computed,* as

$$\sigma(k) = r_0^2 \left[\frac{dN_0}{dh}\right]^2 \frac{E(k)}{4\pi k^2} \left[1 - \frac{(\vec{j}\cdot\vec{k})^2}{k^2}\right] \int_0^\infty du \int_0^\infty dv\, e^{-k^2(u+v)} C[k, |u - v|] \qquad (4.8)$$

In the *high* wave-number range, a reasonable assumption** for the time correlation is

$$C[k, \tau] = e^{-k^2|\tau|\nu}$$

where $\nu \simeq 10^4$ cm^2/sec (at 80 km) is the kinematical viscosity† appearing in (3.1). The integrations are now easily performed and the spectrum (3.12) introduced to give

$$\sigma(k) = r_0^2 \left[\frac{dN_0^2}{dh}\right] \frac{v_0^2}{l_0^{2/3}} \frac{\sin^2\phi}{4\pi} \frac{1}{D(D + \nu)} \frac{1}{k^{23/3}} \frac{1}{\left[1 + \frac{k^4}{k_s^4}\right]^{4/3}} \qquad (4.9)$$

The angle ϕ is that included between $\vec{k}$ and $\vec{j}$, and hence very nearly zero for symmetrical scattering and a *vertical* gradient (see Fig. 1).

The point of the matter here is that local gradients in the mixed plasma can be as steep or steeper than the ambient profile, and the integral term in (4.5) *cannot* be omitted. The ambient profile provides a non-isotropic gradient source which is stirred into the spectrum $\eta(k, t)$ by blobs of *all* sizes simultaneously. This initial inmixing retains most of the parental anisotropy, so that the resulting spectrum (4.6) does not scatter forward, as we found. The next step is one of self-mixing, which redistributes the fluctuation "energy" of the larger blobs to smaller ones. The integral term in (4.5) evidently describes this transfer mechanism, for it couples different wave-number ranges together.‡ Since the velocity field itself is assumed isotropic, it acts progressively to erase the anisotropy of the

*Noting that

$$\delta(0) \quad \frac{1}{(2\pi)^3} \int_V d^3x\, e^{i\vec{x}\cdot 0} = V/(2\pi)^3$$

**This $C(k, \tau)$ implies infinite values for the fluid's (RMS) acceleration and is hence quite improper for small t, where it should have zero slope.

†Note that $\nu = D$, since space-charge effects bind the electrons to their ionized carrier's frictional experience.

‡In analogy with the inertial (non-linear) term in the Navier-Stokes equations (3.1).

parent source and to create a stable isotropic scalar field which does scatter forward. This redistribution or self-mixing continues until the fluctuations are damped at high wave-numbers by diffusion. The frequency dependence of electromagnetic scattering evidently depends critically on just how this energy is distributed down the spectrum and how long it takes a given input to reach isotropy by self-mixing.

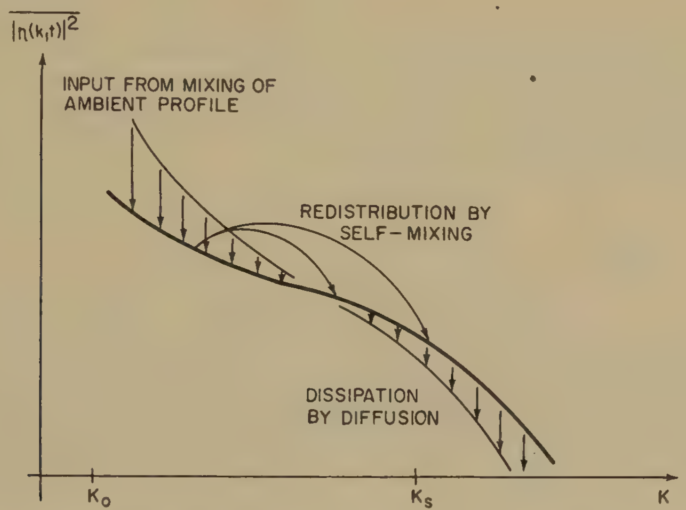

FIG. 7—Introduction, redistribution, and dissipation of fluctuation "energy" by turbulent mixing, as described by equation (4.5)

These intuitive ideas are represented schematically in Figure 7, which shows the stable spectrum and the mechanisms which maintain it. We should note an important difference between our turbulent mixing model and the more familiar decay of homogeneous turbulence. In the latter, one adds an external source of large eddies (k_0) at a rate $\epsilon(\text{cm}^2/\text{sec}^3)$ to balance the dissipation. The source of turbulent mixing appears *explicitly* in (4.5), however, and makes contributions to *each* wave-number interval, according to the (decreasing) magnitude of $V(k, t)$. If one assumes that this energy enters the spectrum only at k_0, the input

$$\overline{\delta N^2} = l_0^2 \left[\frac{dN_0}{dh} \right]^2$$

computed by Gallet [7] and Silverman [19]* would overestimate the total scattered power, as has been found.

In the similarity range $k_0 < k < k_s$, one may use purely dimensional arguments to predict the spectrum. As the self-mixing proceeds, one may expect isotropy and so represent

$$\overline{\eta(k, t)\eta(k', t)} = \delta(k + k') \frac{B(k)}{4\pi k^2} \quad \text{(4.10)}$$

*The writer has unfortunately not had access to the work of Obukhoff and Yaglom, so that the results presented here cannot be related to their earlier studies.

The mean-square fluctuation at a given point in space is thus

$$\left.\begin{aligned}\overline{|\,\delta N(r,t)\,|^2} &= \int d^3k \int d^3k'\, e^{i(\overrightarrow{k+k'})\cdot\vec{r}}\,\overline{\eta(k,t)\eta(k',t)} \\ &= \int_0^\infty dk\, B(k)\end{aligned}\right\} \quad \ldots\ldots\ldots (4.11)$$

The only quantity appearing in (4.5) which has the units of δN (that is, electrons/cc) is dN_0/dh, so that $B(k)$ must be proportional to its square. Since D and ν are approximately equal, the only other parameters are ϵ and ν, out of which one constructs (again by purely dimensional arguments) the characteristic speed and length of the velocity field [6].

$$v = [\epsilon\nu]^{1/2} \qquad l = [\nu^3/\epsilon]^{1/4} \ldots\ldots\ldots\ldots\ldots\ldots (4.12)$$

We need only assume that

$$B(k) = \left[\frac{dN_0}{dh}\right]^2 l^3 \psi(kl) \ldots\ldots\ldots\ldots\ldots\ldots\ldots (4.13)$$

for $\psi(x)$, a dimensionless function, to insure the dimensionality of (4.11). In the inertial range $k < k_s$, redistribution alone is important, so that the spectrum $B(k)$ ought to be independent of ν (or D). One satisfies this condition with the choice $\psi(x) = x^{-3}$, so that

$$\overline{\frac{1}{V}\,|\,\eta(k,t)\,|^2} = (2\pi)^{-3}\left[\frac{dN_0}{dh}\right]^2 \frac{C_0}{k^5} \ldots\ldots\ldots\ldots\ldots\ldots (4.14)$$

quite independent of the velocity field! This result agrees with Villars and Weisskopf's treatment [8], but is at variance with both Silverman [19] and Batchelor [20], who assumed a k-independent external source of turbulent input.

The loss of fluctuations by diffusion at high wave-numbers is described by the second term in (4.5). Neglecting recombination, the power loss is computed as

$$\left.\begin{aligned}S &= 2\int_0^\infty dk k^2 B(k) \\ &= 2D\left[\frac{dN_0}{dh}\right]^2 \lambda_0\end{aligned}\right\} \ldots\ldots\ldots\ldots\ldots\ldots\ldots (4.15)$$

where λ_0 is a constant determined by the spectrum's shape alone. On purely dimensional basis, one would have argued from (4.12) that

$$S = Vl\left[\frac{dN_0}{dh}\right]^2$$

which is again equivalent to (4.15) for $D = \nu$. The spectrum at high wave-numbers cannot be computed from dimensional arguments, since (4.15) is satisfied identically by (4.13). The iteration approach which leads to (4.9) can be pursued to the next step by substituting (4.6) into the integral term of (4.5). This approach converges rapidly only in the high wave-number range, where one finds a spectrum proportional to k^{-13}, as in (4.9). This calculation is tedious and unsound in the (k_s)

transition range, where self-mixing is still quite the largest redistribution mechanism.

To bridge the gap between our similarity (k^{-5}) and dissipation (k^{-13}) results, we introduce the concept of a transfer diffusion $D'(k)$ to describe the removal of fluctuation energy from a wave-number interval k to all higher k. Heisenberg [14] exploited this same concept in treating the non-linear, inertial transfer of velocity spectra as an equivalent viscosity, and so derived the transition spectrum of equation (3.12). In this spirit, we rewrite (4.5) as

$$\frac{\partial \eta(k, t)}{\partial t} + [D + D'(k)]k^2 \eta(k, t) = -\frac{\mathrm{d}N_0}{\mathrm{d}h} j_\alpha V_\alpha(k, t) \qquad (4.16)$$

The equivalent diffusion constant $D'(k)$ should depend principally on the convective velocity field, so that by purely dimensional arguments one has

$$D'(k) = \gamma \int_k^\infty \mathrm{d}\lambda \left[\frac{E(\lambda)}{\lambda^3}\right]^{1/2} \qquad (4.17)$$

γ is an absolute constant of order unity. One can also argue that $\eta(l, t)$ in (4.5) can be brought outside the integral as $\eta(k, t)$, since $V_\alpha(k - l, t)$ is largest and hence most effective as a convective mixer for k near l. The further condition $k_\alpha V_\alpha(k, t) = 0$ tells one that small values of l contribute little to the integration. When $\eta(l, t)$ is so removed, it is not difficult to infer (4.17).

One may wonder that we treat the *removal* action of the transfer term in (4.5) without also recognizing the transfer *input* from lower wave-numbers. An equivalent self-mixing term

$$\text{Input} = \lambda_\alpha V_\alpha(k, t) \int_0^k \mathrm{d}l \sqrt{lB(l)}$$

was again constructed by purely dimensional arguments and added to the balance (4.16). The vector λ_α is now strictly random in direction and ρ is an absolute constant of order unity. The theory with this additional term becomes quite complicated, so that we do not reproduce it here. The results are substantially the same as those which follow and are certainly consistent with Heisenberg's derivation of the spectrum (3.12), for which he neglected the explicit transfer of kinetic energy from the low wave-numbers.

The transfer diffusion evidently depends only on the similarity range of the velocity spectrum $E(k)$, so that one may substitute from (4.12) and find

$$D'(k) = \frac{3}{4} \frac{\gamma}{l_0^{1/3}} \frac{v_0}{k^{4/3}} \qquad (4.17a)$$

When this result is inserted into (4.16), one sees that $\eta(k, t)$ may be expressed exactly as in (4.6), except now with an additional damping term. Using the results (4.8) through (4.9) and dropping the viscosity ν when it appears with D (equivalent to an infinite time correlation) for convenience, we have

$$\sigma(k) = r_0^2 \left[\frac{\mathrm{d}N_0}{\mathrm{d}h}\right]^2 4\pi \frac{v_0^2}{l_0^{2/3}} \frac{\sin^2\phi}{k^{23/3}\left[D + \frac{3}{4}\gamma \frac{V_0}{l_0^{1/3} k^{4/3}}\right]^2} \frac{1}{\left[1 + \frac{k^4}{k_s^4}\right]^{4/3}} \qquad (4.18)$$

If k is small, this gives the similarity k^{-5} expression (4.14), and at high numbers it approaches the k^{-13} result adduced before. It would thus appear that we have succeeded in describing the diffusion transition range (k_s), where both self-mixing and dissipation are competing.

The persistant angle (ϕ) dependence in (4.18) requires a word of explanation. By replacing the self-mixing integral term by a transfer diffusion constant, we have destroyed the directional properties of this term (see 4.5). At this stage, however, we are quite sure that considerable self-mixing has taken place, since the direct input mechanism at these wave-numbers is small. To enforce this physical picture on the oversimplified representation (4.16), we average over all angles ϕ relating to the original gradient orientation. This is quite important for vertical gradients associated with ionospheric layers and probably not so critical for meteor trails which have gradients in all directions.

Our result (4.18) can be cast in more convenient form by recalling the definition (3.13) of the cutoff wave-number. Combining these suggestions, we have

$$\sigma(k) = r_0^2\left[\frac{\mathrm{d}N_0}{\mathrm{d}h}\right]^2 \frac{1}{k^5} \frac{\frac{8}{9}\gamma^{-2}}{\left[1 + \frac{D}{\gamma\nu}\left(\frac{k}{k_s}\right)^{4/3}\right]^2} \frac{1}{\left[1 + \frac{k^4}{k_s^4}\right]^{4/3}} \qquad (4.18a)$$

For our purposes, one may set $D = \gamma\nu$, and the transition to high wave-numbers depends only on k/k_s.

To investigate the frequency dependence of the mixing theory, one must substitute for k from (2.3) and take the ratio of two such expressions. For the 1,250-km path, one computes the frequency scaling exponents m and n in (2.4) and (2.5) as functions of k_s. This was done numerically and the results plotted in Figures 3 and 4. From these curves, one sees that the mixing theory implies a somewhat lower value for k_s^{-1} for a given power exponent than the pressure theory. The mean experimental value $n = 8$ gives $k_s^{-1} = 1.5$ meters for the mixing theory, in agreement with Booker [15]. The 28- to 50-Mc comparison, Figure 4, shows that the corrected values 6 to 6.5 correspond to $k_s^{-1} = 2$ meters, while the bare results of 4 to 4.5 are inadmissible on this theory.

The variation of power with scattering angle is plotted in Figure 8, using values at 491 and 592 km relative to those at 811 km as the variable. Experimental values indicate that a value of k_s^{-1} between 1 and 2 meters is appropriate to the mixing theory. This lower value agrees with the frequency-dependence deductions above.

5. CONCLUSIONS

We have studied the dependence of ionospherically-scattered fields on frequency and scattering angle, and compared the results of two theories with experiment. The pressure theory gives a satisfactory account of both scaling laws with an average value for the single undetermined parameter $k_s^{-1} = 2$ meters. It correctly explains the relative diurnal changes in scaling laws for 28 to 50 and 50 to 108 Mc comparisons. Diurnal and seasonal variations in the scaling laws can be understood in terms of small changes in the viscosity wave-number k_s.

A physical model of gradient mixing by a turbulent carrier was developed and also compared with experiment. It is characterized by a stronger dependence on

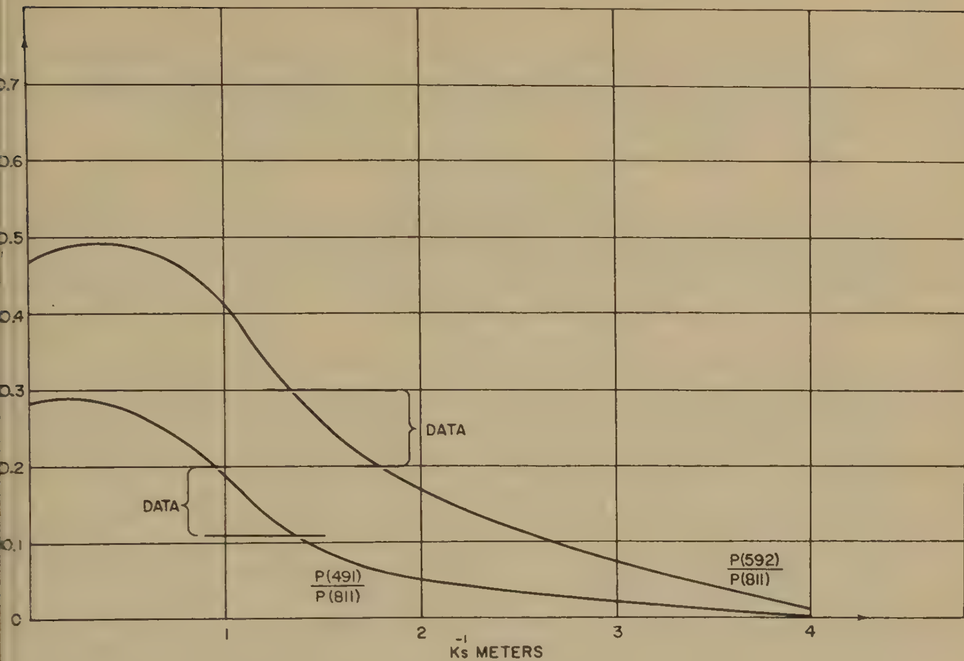

FIG. 8—Power ratios on 50-Mc mixing theory; $h = 80$ km

both frequency and scattering angle, so that if one is to fit the data, a somewhat smaller value $k_s^{-1} = 1.5$ meters should be chosen. Variability in the scaling laws is again understood in terms of small changes in the viscosity wave-number k_s.

To choose between the two theories, one must make simultaneous measurements on three or more frequencies and/or three scattering angles (that is, path lengths). This would permit one to calibrate k_s by comparing two, and then to predict the third power level. It is hoped that such simultaneous experiments can soon be arranged. It would also be desirable to clarify the role of absorption on the lower (28-Mc) frequency, for the suitability of mixing theory may be decided by the final choice for absorption corrections. Another experiment which would strengthen our present understanding would measure fading rates on three frequencies simultaneously. All of these relative measurements provide excellent means for studying the ionosphere at a distance.

There are also a number of theoretical questions which are worth clarifying. In the pressure theory, one makes two major assumptions: (1) The normality of the velocity field, which allows the decomposition of fourfold averages like (3.9); and (2) the choice of the spectrum (3.12). The first problem has already been discussed. Heisenberg's result for $E(k)$ implies infinite derivatives at some order for the velocity field and one cannot feel secure in such a state. It is probable that a further transition to exponential form is later effected, although this result may be correct just near k_s. In any case, our results depend critically on the form of $E(k)$, and a better form should be exploited when it becomes available.

In our derivation of the turbulent mixing spectrum, we also made two assumptions: (1) By introducing an equivalent diffusion constant, to represent the re-

distribution of fluctuations to higher wave-numbers by self-mixing; and (2) through the use of Heisenberg's spectrum (3.12) again. The degree of approximation in both areas is the same, as one can verify by considering the Navier-Stokes and diffusion equations as average forms of the Maxwell-Boltzmann equations.

Acknowledgments

I should like to thank D. Bailey, R. Bateman, R. C. Kirby, and especially Prof. Felix Villars for valuable discussions of these matters. E. Levin and Glen Culler kindly helped with the numerical computations. Prof. A. G. Hill suggested the problem.

References

[1] See, for example, the review paper by K. Bullington, Characteristics of beyond-the-horizon radio transmission, Proc. Inst. Radio Eng., **43**, 1175-1180 (1955).
[2] H. G. Booker and W. E. Gordon, A theory of radio scattering in the troposphere, Proc. Inst. Radio Eng., **38**, 401-412 (1950).
[3] See papers in "Scatter Propagation Issue," Proc. Inst. Radio Eng., **43**, (Oct. 1955).
[4] D. K. Bailey, R. Bateman, L. V. Berkner, H. G. Booker, G. F. Montgomery, E. M. Purcell, W. W. Salisbury, and J. B. Wiesner, A new kind of radio propagation at very high frequencies observable over long distances, Phys. Rev., **86**, 141-145 (1952).
[5] F. Villars and V. F. Weisskopf, The scattering of electromagnetic waves by turbulent atmospheric fluctuations, Phys. Rev., **94**, 232 (1954).
[6] See, for instance, G. K. Batchelor, The Theory of Homogeneous Turbulence, Cambridge, University Press (1953).
[7] R. M. Gallet, Aerodynamical mechanisms producing electron density fluctuations in turbulent ionized layers, Proc. Inst. Radio Eng., **43**, 1240-1252 (1955).
[8] F. Villars and V. F. Weisskopf, On the scattering of radio waves by turbulent fluctuations of the atmosphere, Proc. Inst. Radio Eng., **43**, 1232-1239 (1955).
[9] D. K. Bailey, R. Bateman, and R. C. Kirby, Radio transmission at VHF by scattering and other processes in the lower ionosphere, Proc. Inst. Radio Eng., **43**, 1181-1230 (1955).
[10] A. D. Wheelon, Refractive effects for ionospheric scatter propagation (to be published).
[11] R. C. Kirby, VHF propagation by ionospheric scattering—A survey of experimental results, IRE-GWU Symposium on Scatter Communication, Washington, D. C., November 14, 1955.
[12] A. D. Wheelon, A note on scatter propagation with a modified exponential correlation, Proc. Inst. Radio Eng., **43**, 1381-1383 (1955).
[13] G. K. Batchelor, Pressure fluctuations in isotropic turbulence, Proc. Cambridge Phil. Soc., **47**, 345 (1952).
[14] W. Heisenberg, Zur Statistischen Theorie der Turbulenz, Zs. Physik, **124**, 628 (1948).
[15] H. G. Booker and Robert Cohen, A theory of long-duration meteor-echoes based on atmospheric turbulence with experimental confirmation, J. Geophys. Res., **61**, 707-733 (1956).
[16] F. Villars and V. F. Weisskopf, Scattering of radio waves by turbulent fluctuations, II. Fluctuations produced by turbulent mixing in an inhomogeneous medium (unpublished as yet).
[17] S. K. Mitra, The Upper Atmosphere, Calcutta, Asiastic Society of Bengal, 2nd ed. (1952). [Vol. 5, Asiastic Society Monograph Series.]
[18] Report of the Physical Society Conference on "The Physics of the Ionosphere," Cavendish Laboratory, Cambridge, September 1954.
[19] R. A. Silverman, Turbulent mixing theory applied to radio scattering, J. Appl. Phys., **27**, 699-705 (1956).
[20] G. K. Batchelor, The scattering of radio waves in the atmosphere by turbulent fluctuations in refractive index, Cornell University, E. E. Res. Rep. No. 262 (Sept. 15, 1955).

JOURNAL OF GEOPHYSICAL RESEARCH VOLUME 62, No. 1 MARCH, 1957

SEISMIC EXPLORATION OF THE CONTINENTAL SHELF OFF THE WEST COAST OF INDIA

By J. N. NANDA

Office of Scientific Research and Development, Naval Headquarters, New Delhi, India

(Received August 20, 1956)

ABSTRACT

Some recent observations in connection with seismic exploration of the continental shelf off the west coast of India are described. A single ship with a single sono-buoy was used. Five shots were fired at distances up to six miles from the sono-buoy. Roughly, the depth of the ocean was about 80 fathoms, and a negative temperature gradient existed. The exact times of shots were calculated from the observed arrival of direct waves. The loose sediments are surmised to be about 2.8 km thick, and seismic velocity in these sediments is found to be 1.2 miles per second. The depth of sediments has been calculated from assigning a broad maximum in the records to reflection from the bottom of the loose sediments.

On 15th December 1953, the ocean bottom was investigated about 30 miles west of Cochin. The depth charges were fired from a vessel and the disturbance was monitored by a radio sono-buoy. The transmissions from the sono-buoy were received on the vessel, which fired charges exploding at about 30 fathoms depth, while the ship was moving westwards from the sono-buoy. The recording on the cathode-ray oscilloscope camera was started ten seconds before the explosion and was continued for about one minute. The sono-buoy radiated 62 Mc F.M. The film of the camera was moved at a speed of 66.6 inches per minute, providing the necessary time-base. Half-second pulses were fed from the chronometer to the flashing bulb in the camera, giving time-marks on the film. The instant of explosion was approximately noted to the nearest second of the chronometer on hearing the sound of the explosion. It is intended in future experiments to record this also in the camera from the output of a hydrophone suspended from the firing ship and then cutting off the output of the hydrophone instantaneously by a suitable thyratron.

Another vessel was also placed at about 25 miles east of this sono-buoy. This ship remained stationary and recorded on tape the arrival of sound at a hydrophone suspended from this ship. Since the generator on this vessel was very noisy, the tape recorder did not indicate any arrivals through water. Only the sound coming *via* air was recorded about 2.5 minutes after the shot. The speed of sound in air as calculated from times of arrival at this distant station was 327 meters per second, the temperature and humidity being 25°C and 50 per cent. The distance is not very accurately known and, therefore, the discussion of the error in the calculated velocity in air will be out of place.

The records as received from the sono-buoy were as follows. Usually a distinct arrival lasted for a few seconds before a second arrival was imposed. The amplitude after the second arrival increased for a few seconds, and then it decreased slowly and lasted for about 15 seconds or so. Assuming that the first arrival for near ranges was due to direct travel of the waves from shot to the sono-buoy, and for relatively longer ranges this was due to the refracted ray through loose sedimentary deposits below the water, one can roughly estimate the relative velocities. The observations and results are tabulated below.

Table 1—*Observations and results*

Shot No. (1)	Approx. distance between shot and sono-buoy (2)	Approx. time of shot (3)	Time of first arrival (4)	Time of second arrival (5)	Subsequent maximum (6)	Calculated time of shot (7)	Calc. vel. in loose sediments (8)	Calc. depth of sediments (9)
	miles	*h m s*	*h m s*	*h m s*	*h m s*	*h m s*	*miles/sec*	*miles*
1	1	12 35 02	*12 35 03.7*	12 35 05.3*	12 35 07.0	12 35 02.6	...	2.6
2	2	12 38 32	*12 38 35.1*	12 36 38.2*	12 38 38.4	12 38 33.0	...	2.8
3	3	12 42 04	12 42 06.2	*12 42 07.0*	12 42 09.1	12 42 03.8	1.2	2.8
4	4	12 45 34	12 45 36.6	*12 45 37.3*	12 45 39.2	12 45 33.1	1.2	3.0
5	6	12 52 37	12 52 41.2	*12 52 42.5*	12 52 43.1	12 52 36.1	1.2	2.9

Observations

(1) The timings that are in italics are presumed to be arrivals of direct waves. The velocity of sound in sea water for calculating time of shot from direct arrival was taken to be 0.94 mile per second for the existing average temperature and salinity values.

(2) The timings marked * are only apparent second arrivals, since the record was overloaded before these instants indicated by suppression of all noise and spuriously low amplitude. No account has been taken of these times.

(3) The B.T. observation taken under similar conditions next day indicated a steady fall of temperature. The depths for various shots extended from about 60 fathoms to about 100 fathoms.

Discussion

Beyond two miles, the direct waves arrive later than the first arrival, which are assigned to refracted waves in the loose sediments. In column (7) are given the calculated shot-times, as explained above. From first arrivals at 3, 4, and 6 miles, as given in column (4) and the times of shot in column (7), the velocity in sediments is seen to be 1.2 miles per second, as indicated in column (8). This has been found to be of the same order in the North Sea.

The maximum intensity in the record after the second arrival [times of incidence iven in column (6)] can be ascribed to reflection from the lower boundary of the oose sediments. Approximate treatment based on ray geometry gives the depth of his boundary as about 2.8 miles, which has been entered in column (9). The eflection is not sharp, since reverberations from the uneven bottom must be eaching the receiver at about the same time. Possibly the speed in the sediments vill slightly increase as one goes down to the lower boundary, in which case the lepth will work out to be somewhat more than 2.8 miles.

Experiments using sono-buoys cannot give much more information, as range of ny series of observations is limited. It is intended to extend the work using two hips at progressively increasing distances and see if distant arrivals can give elocities corresponding to rocks beneath the loose sediments. From the slow ading of the intensity after the maximum, it is suspected that propagation at ntermediate distances follows mode theory, where the lower boundary of sediments nd not just sea bottom is involved. Further observations are necessary to confirm his.

Acknowledgment

Thanks are due to Shri V. N. Rao, H. M. Iyer, and other scientists at the ndian Naval Physical Laboratory for assistance in this work, and to the Indian Navy for use of the vessels and for exploding the depth charges.

Journal of Geophysical Research Volume 62, No. 1 March, 1957

PENETRATION OF THE GEOMAGNETIC SECULAR FIELD THROUGH A MANTLE WITH VARIABLE CONDUCTIVITY*

By Keith Leon McDonald

Department of Physics, University of Utah, Salt Lake City, Utah

(Received October 20, 1956)

ABSTRACT

The work reported on here is an investigation of the radial distribution of electrical conductivity σ in the earth's mantle. Previously this function had been inferred only to about the 800-km depth from the geomagnetic transient variations of external origin (see Lahiri and Price). Throughout the remaining lower portion of the mantle, we make use here of the longer wave periods which characterize the geomagnetic secular variation. Choosing a power law for σ, the wave attenuation and phase retardation after propagation through the mantle are investigated, using sinusoidal input functions, and an equivalent conductivity is established on the basis of amplitude attenuation. Aperiodic models at the core are solved by the method of Laplace transforms and a time discontinuity in H_r (δ-function in H_r) is treated in detail. The elapsed time for a pulse to reach the earth's surface is expressed in terms of an equivalent conductivity. The latter quantity is then gotten indirectly from a study of the time-dependent magnetic observatory records. Judged somewhat better than an order of magnitude, in these calculations, σ is shown plotted throughout the mantle.

I. INTRODUCTION

Aside from the uppermost layers of the crust, our knowledge of the electrical conductivity σ in the earth's mantle is inferred from the geomagnetic transient variations, primarily, the periodic solar daily variations, and the aperiodic magnetic storms. By an extended Gaussian analysis, these variations are separated into their induced and exciting components. A comparison of the total fields at the earth's surface thereby enables one to compute the conductivity to depths penetrated by the induced current. Analyzing the geomagnetic field into its external and internal components was first considered by Schuster in 1889, wherein he applied Lamb's theory of induction in a uniform sphere to the daily magnetic variation. Since that time, S. Chapman and his collaborators have successfully inferred the distribution of σ to about the 800-km depth (roughly, the maximum depth penetrated by the induced currents). Aside from order of magnitude compu-

*This research was supported by the U. S. Office of Naval Research. Author is now at Los Alamos Scientific Laboratory, Los Alamos, New Mexico.

tations involving an equivalent conductivity,* however, the lower two-thirds portion of the mantle has never been discussed. Runcorn (1955), for example, considered a plane polarized pulse propagated through an infinite uniform slab. Later, we shall consider a refinement of this method which incorporates the equivalent conductivity in a spherical space.

To compute σ throughout the remaining portion of the mantle, we make use of the large wave periods which characterize the geomagnetic secular variation. Using a formalism similar to that of Lahiri and Price (1939) and, later, Rikitake (1950-51), we catalog in Section II the quasi-stationary field equations. Choosing a power law for σ $(=\sigma_0\rho^{-\gamma}$, where $\rho = r/R_c$ and R_c is the core radius), the equations are integrated in terms of Bessel functions. Using sinusoidal input functions, the amplitude attenuation and phase retardation after propagation through the mantle are plotted in Section III. In Section IV, an equivalent conductivity is established on the basis of amplitude attenuation. The equivalence allows one to transfer from a homogeneous medium to one of variable conductivity. In Section *V*, the electrical conductivity of the mantle is estimated by a method which replaces the time average of the space-averaged squared field at the core by a random static distribution. This quantity, attenuated by the mantle, is termwise compared with its observed image at the earth's surface. The method has the advantage of combining a large amount of data, so that the instantaneous details of the field at the core are incidental. The sinusoidal analysis is corroborated with results using aperiodic models in Section VI. Section VII contains the final conclusions.

II. MANTLE EQUATIONS

For later reference, we catalog the quasi-stationary field equations applicable to the mantle. Since a general treatment of electromagnetic induction in non-uniform conductors was presented by Lahiri and Price (1939), the following work draws to some extent on their formalism. Equating the electric displacement current to zero, we obtain the field equations (in Gaussian units) for a general linear isotropic medium,

$$\nabla \times \mathbf{E} = -\frac{1}{c}\dot{\mathbf{B}} \qquad \nabla \cdot \mathbf{B} = 0 \qquad (1)$$

$$\nabla \times \mathbf{H} = \frac{4\pi}{c}\mathbf{J} \qquad \nabla \cdot \mathbf{D} = 4\pi\epsilon \qquad (2)$$

The material equations are $\mathbf{D} = K\mathbf{E}$, $\mathbf{B} = \mu\mathbf{H}$, $\mathbf{J} = \sigma\mathbf{E}$. From the first of Eqs. (2), it follows that $\mathbf{J}$ is approximately solenoidal. Neglecting $\dot{\epsilon}$ compared to $\epsilon\sigma/K$, the second of Eqs. (2) gives the approximation $4\pi\epsilon = \mathbf{J}\cdot\nabla(K/\sigma)$. Thus, the space-charge density vanishes only if $\mathbf{J}$ lies in the iso-level surfaces K/σ = constant, or if K/σ is uniform. From (1) and (2), $\mathbf{E}$ and $\mathbf{H}$ must satisfy the equations

$$\nabla \times \left[\frac{1}{\mu}\nabla \times \mathbf{E}\right] + k\sigma\dot{\mathbf{E}} = 0, \qquad \nabla \times \left[\frac{1}{\sigma}\nabla \times \mathbf{H}\right] + k\mu\dot{\mathbf{H}} = 0$$

*In Section IV, an equivalent conductivity which depends on the order n of the solid harmonic is established, approximately, on the basis of amplitude attenuation. The whole secular field would, therefore, be roughly represented by an intermediary harmonic, say $n = 6$.

where $k = 4\pi/c^2$. On the other hand, in terms of the vector potential $\mathbf{A}$, we have $\mathbf{B} = \nabla \times \mu\mathbf{A}$, $\mathbf{E} = -\mu/c\,\dot{\mathbf{A}}$, where $\mathbf{A}$ is *any* solution of

$$\nabla \times \left[\frac{1}{\mu} \nabla \times (\mu \mathbf{A})\right] + k\mu\sigma\dot{\mathbf{A}} = 0$$

subject only to the auxiliary condition $\nabla \cdot (\mu\sigma\dot{\mathbf{A}}) = 0$. Here we neglect stationary magnetic fields. Our choice of the vector potential is such as to include the potential of the free-charge distribution.

Applying these equations to the mantle, we set $\sigma = \sigma(\rho)$, where $\rho = r/R_c$ and R_c is the radius of the core. Hereafter, we shall always take μ = constant. Under these conditions, standard solutions leading to the poloidal magnetic field ($\nabla \cdot \mathbf{A} = 0$) have the same form as in the homogeneous case (σ = constant), namely,

$$\mathbf{A} = \nabla \times \mathbf{r}\psi \qquad \nabla^2\psi = k\mu\sigma \frac{\partial}{\partial t}\psi \qquad \text{(3)}$$

General solutions leading to toroidal magnetic fields ($\nabla \cdot \sigma\mathbf{A} = 0$) are unknown. These solutions, however, are of little interest in the study of the secular variation, since they give rise to fields which are not observable at the earth's surface (Elsasser, 1950). Standard solutions of Eq. (3) are

$$\psi_{nm} = \mathfrak{R}_{nc}^m(\rho, t) \cdot S_{nc}^m(\theta, \phi) + \mathfrak{R}_{ns}^m(\rho, t) \cdot S_{ns}^m(\theta, \phi)$$

where $\mathfrak{R}_n(\rho, t)$ satisfies the differential equation

$$\frac{\partial^2}{\partial\rho^2}(\rho\mathfrak{R}_n) = \frac{1}{\rho}\frac{\partial}{\partial\rho}\left(\rho^2 \frac{\partial\mathfrak{R}_n}{\partial\rho}\right) = \left\{\frac{n(n+1)}{\rho^2} + k\mu\sigma R_c^2 \frac{\partial}{\partial t}\right\}\rho\mathfrak{R}_n \qquad \text{(4)}$$

$S_n^m(\theta, \phi)$ is the usual surface harmonic $P_n^m(\cos\theta)$ multiplied by $\sin m\phi$ or $\cos m\phi$. Outside the conductive medium, σ is identically zero and $\mathfrak{R}_n$ is computed from the resulting equation, homogeneous in ρ. In this special case, ψ_{nm} is a harmonic function which satisfies the relations $\mathbf{H} = \nabla \times \mathbf{A} = -\nabla\psi$. For later reference, the components of $\mathbf{A}$ and $\mathbf{H}$ are listed below ($R_c \leq r \leq R_e$, the earth's radius):

$$\left.\begin{aligned}
A_r &= 0 & H_r &= \rho^{-1}\sum_{nm} n(n+1)\psi_{nm} \\
A_\theta &= \frac{R_c}{\sin\theta}\sum_{nm}\frac{\partial}{\partial\phi}\psi_{nm} & H_\theta &= \rho^{-1}\sum_{nm}\frac{\partial}{\partial\rho}\left(\rho\frac{\partial}{\partial\theta}\psi_{nm}\right) \\
A_\phi &= -R_c\sum_{nm}\frac{\partial}{\partial\theta}\psi_{nm} & H_\phi &= \frac{\rho^{-1}}{\sin\theta}\sum_{nm}\frac{\partial}{\partial\rho}\left(\rho\frac{\partial}{\partial\theta}\psi_{nm}\right)
\end{aligned}\right\} \qquad \text{(5)}$$

Outside the mantle it is more convenient to replace R_c by R_e and ρ by r/R_e, where they occur explicitly in Eq. (5).

III. PERIODIC SOLUTIONS OF MANTLE EQUATIONS

Aside from an insulating mantle, the simplest earth model is that of an infinite conductive medium surrounding the core. We wish to examine this model, using various distributions of electrical conductivity. Waves introduced at the core boundary are investigated as to their attenuation and phase retardation. For the

electrical conductivity, we choose the three-parameter distribution (γ real)

$$\sigma(\rho) = \sigma_0 \rho^{-\gamma} + \sigma_1 \rho^{-2}$$

After Lahiri and Price, we make the following substitutions in Eq. (4):

$$\left.\begin{aligned} &\mathfrak{R}_n = \rho^{-1/2} W_{\nu_n}, \qquad \zeta = i^{3/2}(\omega k \mu R_c^2 \sigma_0)^{1/2} \\ &\frac{\partial}{\partial t} = i\omega, \qquad \rho^{1-\gamma/2} = \frac{|\gamma - 2|}{2\zeta} z, \qquad \gamma \neq 2 \\ &\nu_n = 2[(n + \tfrac{1}{2})^2 - \zeta^2 \sigma_1/\sigma_0]^{1/2} / |\gamma - 2|, \qquad n = 1, 2, 3, \cdots, \end{aligned}\right\} \quad \ldots\ldots(6)$$

and find that $W_\nu(z)$ obeys Bessel's differential equation of order ν_n and argument z. For simplicity, we choose $\sigma_1 \equiv 0$, so that ν_n is real.

In the computations, we consider only the radial component $\dot{H}_r$ for a sinusoidal input wave. In terms of the constant coefficients $\dot{H}_{rn}^m$ of a general expansion of $\dot{H}_r$ at the core, we then write, from (5),

$$\frac{\partial}{\partial t} H_r(\rho, \theta, \phi, t) = e^{i\omega t} \sum_{nm} B_n e^{-i\phi_n} \dot{H}_{rn}^m S_n^m \ldots\ldots\ldots\ldots\ldots\ldots(7)$$

where

$$B_n e^{-i\phi_n} = \rho^{-3/2} \left\{ \frac{W_{\nu_n}(z)}{W_{\nu_n}(z_c)} \right\}$$

z_c denotes the value of z at $r = R_c$. B_n is the real *total attenuation* and ϕ_n the real *phase retardation*. Three cases arise, depending upon whether γ is greater, equal, or less than 2.

Case I ($\gamma > 2$)—The equation (6) connecting ρ and z shows that $\rho \to \infty$ implies $z \to 0$. Since $|\mathbf{A}| = 0\ (\rho^{-2})$ when $\sigma = 0$, it follows that for $\sigma_0 > 0$, $\mathbf{A}$ must vanish to at least this order. Therefore, $W(z)$ must vanish to the appropriate order when $z \to 0$. The only solution of Bessel's differential equation satisfying this condition is that of the first kind, the series expansion being regular over the whole cut plane. For large values of ρ, therefore,

$$\rho^{-1}\mathfrak{R}_n(\rho, t) = e^{i\omega t} \rho^{-3/2} J_{\nu_n}(z) \sim \frac{|\zeta|^{\nu_n} e^{i(\omega t - 3\pi\nu_n/4)}}{\Gamma(1 + \nu_n)\,|\gamma - 2|^{\nu_n}} \rho^{-n-2} = 0(\rho^{-n-2})$$

Case II ($\gamma = 2$)—This case is singular for the substitutions (6). Eq. (4), however, is homogeneous in ρ, and a direct integration gives the general solution

$$\rho^{-1}\mathfrak{R}_n(\rho, t) = C^{\pm} \exp\{i[\omega t \mp b_n \log \rho] - [3/2 \pm a_n] \log \rho\}$$

where a_n and b_n are obtained from the expression

$$\sqrt{\epsilon \tfrac{1}{2}(n + \tfrac{1}{2})^2 + \tfrac{1}{2}\sqrt{|\zeta|^4 + (n + \tfrac{1}{2})^4}}$$

according as ϵ is $+1$ or -1. We are interested only in the expanding wave-front. The total attenuation B_n and phase retardation ϕ_n in (7) are, therefore, $\phi_n = b_n \log \rho$ and $B_n = \rho^{-3/2-a_n}$. For large $|\zeta|$, $a_n \doteq b_n \doteq |\zeta|\, 2^{-\frac{1}{2}}$, so that $\phi_n \doteq 2^{-\frac{1}{2}} |\zeta| \log \rho$ and $B_n = \exp\{-(3/2 + |\zeta|\, 2^{-\frac{1}{2}}) \log \rho\}$. For $|\zeta|$ small, $a_n \doteq (n + \frac{1}{2}) + |\zeta|^4 (2n + 1)^{-3}$, $b_n \doteq |\zeta|^2/(2n + 1)$ and therefore $\phi_n \doteq |\zeta|^2 (2n + 1)^{-1} \log \rho$, $B_n \doteq \exp\{[-n - 2 - |\zeta|^4 (2n + 1)^{-3}] \log \rho\}$.

Case III ($\gamma < 2$). Referring to Eq. (6), we see that $\rho \to \infty$ implies $|z| \to \infty$. Since the attenuation here is greater than in the two preceeding cases, it follows that W_ν must vanish as $|z| \to \infty$. From all the cylinder functions, we must, therefore, choose one of the two Hankel functions, since they alone vanish in a neighborhood of the point $z = \infty$. Consistent with our choice of ζ and the positive time-factor, we therefore write, in terms of the Hankel function of the first kind,

$$\rho^{-1}\mathfrak{R}_n(\rho, t) = e^{i\omega t}\rho^{-3/2}H^{(1)}_{\nu_n}(z)$$

For large $|z|$,

$$H^{(1)}_{\nu_n}(z) \sim \left[\frac{2}{\pi z}\right]^{1/2} \cdot e^{i(z-\nu_n\pi/2-\pi/4)}$$

Therefore,

$$B_n e^{-i\phi_n} \sim \rho^{\gamma/4-2} \cdot \exp\{-(1+i)2^{1/2}\,|\zeta|\,(\rho^{1-\gamma/2}-1)/|\gamma-2|\}$$

To investigate the effects of a material medium, we define the *physical attenuation* C_n as the ratio of the total attenuation B_n to the *geometrical attenuation* G_n:

$$C_n = B_n/G_n\,, \qquad G_n = \rho^{-n-2} \ldots\ldots\ldots\ldots\ldots\ldots (8)$$

In free space, $C_n = 1$. Observe that in the asymptotic expressions in the above three cases C_n (I) is a constant, (II) varies as a negative power law, (III) varies as the complex of an exponential attenuation and a power law. In Case I, the phase retardation is constant; the conductivity rapidly approaches zero; and $\dot{H}_r$ approaches the gradient of a scalar time-dependent potential, the equipotential surfaces varying isochronously.

Tables 1 and 2 include tabulated values of B_n and ϕ_n for the γ-values indicated. In the calculations, we take $\rho^{-1} = R_c/R_e = 0.546875$, $|\zeta| = 5.4986 \times 10^5$ $(\delta\text{yr/emu})^{\frac{1}{2}}$, $\delta = \sigma_0/T$, where $T = 2\pi/\omega$. σ_0 is measured in emu and T in years. δ is dimensionless. Standard asymptotic expansions of $H^{(1)}_\nu$ and J_ν (not contained in this paper) were employed for those larger values of δ for which the series representations fail to converge rapidly. The series expansions for B_n and ϕ_n were, in general, carried out to four significant figures. Computational errors were checked only by continuity of graphs. The values of $\gamma = 4.730$, 9.440, 14.16, 18.90, and 28.33 were chosen such that the conductivity at the 700-km depth would be 10^{-1}, 10^{-2}, 10^{-3}, 10^{-4}, and 10^{-6} times σ_0, the value at the core surface. Figure 1 shows the plot of the first 12 harmonics for $\gamma = 4.730$. The left-hand horizontal part of each curve indicates the geometrical attenuation. That the first and twelfth harmonics approach each other as δ increases, clearly shows that *lower order harmonics are physically attenuated more than higher order*. Thus, for $\delta = 10^{-9}$ emu/yr, Figure 1 shows that the first harmonic is attenuated some 25 times the twelfth harmonic. With larger values of δ, the effect is considerably enhanced.

The *travel time* t_n required for waves leaving the core to reach the earth's surface is obtained from the expression $t_n = \phi_n T/2\pi$. For a wave period $T = 1$ yr, $\gamma = 4.730$, $\delta = 10^{-9}$ emu/yr, we find from Table 2 for the first and twelfth harmonics, $t_1 = 0.80$ yr and $t_{12} = 0.47$ yr; the first harmonic arrives four months later. This *space-*

TABLE I—TOTAL ATTENUATION B_n

γ = 0.000

σ	B_1	B_2	B_3	B_4	B_5	B_6	B_7	B_8	B_9	B_{10}	B_{11}	B_{12}
$.0^{8}5$*	$.0^{10}3793$	$.0^{10}3731$	---	---	---	$.0^{10}3215$	---	---	---	---	---	---
$.0^{8}3$	$.0^{8}6425$	$.0^{8}6291$	---	---	---	$.0^{8}5188$	---	---	---	---	---	---
$.0^{8}2$	$.0^{6}1634$	$.0^{6}1591$	---	---	---	$.0^{6}1256$	---	---	---	---	---	---
$.0^{8}1$	$.0^{4}1105$	$.0^{4}1065$	---	---	---	$.0^{5}7607$	---	---	---	---	---	---
$.0^{9}5$	$.0^{3}2168$	$.0^{3}2058$	---	---	---	$.0^{3}1273$	---	---	---	---	---	---
$.0^{9}3$	$.0^{2}1091$	$.0^{2}1020$	---	---	---	$.0^{3}5457$	---	---	---	---	---	---
$.0^{9}1$	.01128	.01003	---	---	---	$.0^{2}3434$	---	---	---	---	---	---
$.0^{10}5$	.02830	.0241	---	---	---	$.0^{2}574$	---	---	---	---	---	---
$.0^{10}1$	.09160	.0664	---	---	---	$.0^{2}794$	---	---	---	---	---	---
$.0^{11}1$	.1523	---	---	---	---	---	---	---	---	---	---	[illegible]
$.0^{12}1$	.163	.089	---	---	---	$.0^{2}80$	---	---	---	---	---	---

γ = 2.000

σ	B_1	B_2	B_3	B_4	B_5	B_6	B_7	B_8	B_9	B_{10}	B_{11}	B_{12}
$.0^{6}1$	$.0^{32}2518$	---	---	---	---	---	$.0^{32}2357$	---	---	---	---	---
$.0^{7}1$	$.0^{10}2621$	$.0^{10}2581$	$.0^{10}2522$	$.0^{10}2446$	$.0^{10}2353$	$.0^{10}2243$	$.0^{10}2125$	$.0^{10}1995$	$.0^{10}1858$	$.0^{10}1717$	$.0^{10}1574$	[illegible]
$.0^{8}3$	$.0^{5}1051$	---	---	---	---	---	$.0^{6}7122$	---	---	---	---	[illegible]
$.0^{8}1$	$.0^{3}2367$	$.0^{3}2253$	$.0^{3}2090$	$.0^{3}1890$	$.0^{3}1664$	$.0^{3}1425$	$.0^{3}1185$	$.0^{4}9573$	$.0^{4}7501$	$.0^{4}5700$	$.0^{4}4203$	[illegible]
$.0^{9}3$	$.0^{2}6619$	$.0^{2}6039$	$.0^{2}5246$	$.0^{2}4325$	$.0^{2}3376$	$.0^{2}2493$	$.0^{2}1744$	$.0^{2}1161$	$.0^{3}7405$	$.0^{3}4562$	$.0^{3}2734$	[illegible]
$.0^{9}1$	.03546	.03007	.02322	.01631	.01055	$.0^{2}6429$	$.0^{2}3765$	$.0^{2}2151$	$.0^{2}1211$	$.0^{3}6753$	$.0^{3}3745$	[illegible]
$.0^{10}1$	.1421	.08584	.04815	.02655	.01457	$.0^{2}7980$	$.0^{2}4368$	$.0^{2}2390$	$.0^{2}1307$	$.0^{3}7151$	$.0^{3}3911$	[illegible]
$.0^{11}1$	.1632	.08941	.04891	.02675	.01463	$.0^{2}8000$	$.0^{2}4375$	$.0^{2}2393$	$.0^{2}1308$	$.0^{3}7156$	$.0^{3}3913$	[illegible]
$.0^{12}1$	.1635	.08944	.04891	.02675	.01463	$.0^{2}8000$	$.0^{2}4375$	$.0^{2}2393$	$.0^{2}1308$	$.0^{3}7156$	$.0^{3}3913$	[illegible]

γ = 4.730

σ	B_1	B_2	B_3	B_4	B_5	B_6	B_7	B_8	B_9	B_{10}	B_{11}	B_{12}
$.0^{11}1$	.1635	0.08944	.04891	.02675	.01463	$.0^{2}8000$	$.0^{2}4375$	$.0^{2}2392$	$.0^{2}1308$	$.0^{3}7156$	$.0^{3}3913$	[illegible]
$.0^{10}1$	.1626	0.08921	.04885	.02673	.01462	$.0^{2}7997$	$.0^{2}4374$	$.0^{2}2392$	$.0^{2}1308$	$.0^{3}7155$	$.0^{3}3913$	[illegible]
$.0^{9}1$	.1087	0.07192	.04316	.02476	.01391	$.0^{2}7728$	$.0^{2}4268$	$.0^{2}2349$	$.0^{2}1290$	$.0^{3}7079$	$.0^{3}3881$	[illegible]
$.0^{9}3$	.03678	0.03107	.02325	.01581	.01004	$.0^{2}6082$	$.0^{2}3569$	$.0^{2}2051$	$.0^{2}1161$	$.0^{3}6516$	$.0^{3}3631$	[illegible]
$.0^{8}1$	$.0^{2}3764$	$0.0^{2}3491$	$.0^{2}3099$	$.0^{2}2612$	$.0^{2}2081$	$.0^{2}1569$	$.0^{2}1121$	$.0^{3}7703$	$.0^{3}5077$	$.0^{3}3239$	$.0^{3}2010$	[illegible]
$.0^{8}2$	$.0^{3}4682$	$.0^{3}4437$	$.0^{3}4087$	$.0^{3}3652$	$.0^{3}3159$	$.0^{3}2637$	$.0^{3}2124$	$.0^{3}1647$	$.0^{3}1231$	$.0^{4}8894$	$.0^{4}6224$	[illegible]
$.0^{8}3$	$.0^{4}9429$	$.0^{4}9023$	$.0^{4}8442$	$.0^{4}7712$	$.0^{4}6873$	$.0^{4}5967$	$.0^{4}5039$	$.0^{4}4134$	$.0^{4}3295$	$.0^{4}2549$	$.0^{4}1915$	[illegible]

γ = 9.440

σ	B_1	B_2	B_3	B_4	B_5	B_6	B_7	B_8	B_9	B_{10}	B_{11}	B_{12}
$.0^{7}3$	$.0^{6}1186$	---	---	---	---	---	$.0^{7}7067$	---	---	---	---	[illegible]
$.0^{7}2$	$.0^{5}2381$	---	---	---	---	---	$.0^{5}1161$	---	---	---	---	[illegible]
$.0^{7}1$	$.0^{3}1193$	$.0^{3}1089$	$.0^{4}9492$	$.0^{4}7875$	$.0^{4}6325$	$.0^{4}4923$	$.0^{4}3727$	$.0^{4}2754$	$.0^{4}1991$	$.0^{4}1411$	$.0^{5}9818$	[illegible]
$.0^{8}7$	$.0^{3}5488$	---	---	---	---	---	$.0^{3}1332$	---	---	---	---	[illegible]
$.0^{8}3$	$.0^{2}7542$	$.0^{2}5962$	$.0^{2}4474$	$.0^{2}3220$	$.0^{2}2237$	$.0^{2}1510$	$.0^{3}9935$	$.0^{3}6306$	$.0^{3}4040$	$.0^{3}2510$	$.0^{3}1536$	[illegible]
$.0^{8}1$	.05138	.03540	.02322	.01466	$.0^{2}8985$	$.0^{2}5376$	$.0^{2}3157$	$.0^{2}1827$	$.0^{2}1045$	$.0^{3}5928$	$.0^{3}3338$	[illegible]
$.0^{9}3$	.1298	---	---	---	---	---	$.0^{2}4221$	---	---	---	---	[illegible]
$.0^{9}1$	.1586	.08766	.04827	.02650	.01453	$.0^{2}7958$	$.0^{2}4357$	$.0^{2}2385$	$.0^{2}1305$	$.0^{3}7141$	$.0^{3}3906$	[illegible]
$.0^{10}1$	.1635	.08942	.04891	.02675	.01463	$.0^{2}8000$	$.0^{2}4375$	$.0^{2}2393$	$.0^{2}1308$	$.0^{3}7156$	$.0^{3}3913$	[illegible]
$.0^{11}1$	.1635	.08944	.04891	.02675	.01463	$.0^{2}8000$	$.0^{2}4375$	$.0^{2}2393$	$.0^{2}1308$	$.0^{3}7156$	$.0^{3}3913$	[illegible]

γ = 14.16

σ	B_1	B_2	B_3	B_4	B_5	B_6	B_7	B_8	B_9	B_{10}	B_{11}	B_{12}
$.0^{7}5$	$.0^{5}2212$	---	---	---	---	---	$.0^{6}4807$	---	---	---	---	[illegible]
$.0^{7}3$	$.0^{4}4581$	$.0^{4}3604$	$.0^{4}2761$	$.0^{4}2069$	$.0^{4}1520$	$.0^{4}1097$	$.0^{5}7800$	$.0^{5}5467$	$.0^{5}3784$	$.0^{5}2582$	$.0^{5}1752$	[illegible]
$.0^{7}1$	$.0^{2}3270$	$.0^{2}2354$	$.0^{2}1653$	$.0^{2}1135$	$.0^{3}7653$	$.0^{3}5075$	$.0^{3}3316$	$.0^{3}2139$	$.0^{3}1363$	$.0^{4}8597$	$.0^{4}5368$	[illegible]
$.0^{8}3$	.03740	.02448	.01565	$.0^{2}9802$	$.0^{2}6034$	$.0^{2}3660$	$.0^{2}2187$	$.0^{2}1297$	$.0^{3}7603$	$.0^{3}4417$	$.0^{3}2547$	[illegible]
$.0^{8}1$	.1083	.06453	.03766	.02166	.01231	$.0^{2}6940$	$.0^{2}3887$	$.0^{2}2167$	$.0^{2}1203$	$.0^{3}6661$	$.0^{3}3680$	[illegible]
$.0^{9}1$	.1626	.08906	.04876	.02668	.01460	$.0^{2}7988$	$.0^{2}4369$	$.0^{2}2390$	$.0^{2}1307$	$.0^{3}7150$	$.0^{3}3913$	[illegible]
$.0^{10}1$	.1635	.08944	.04891	.02675	.01463	$.0^{2}8000$	$.0^{2}4375$	$.0^{2}2393$	$.0^{2}1308$	$.0^{3}7156$	$.0^{3}3913$	[illegible]
$.0^{11}1$	.1635	.08944	.04891	.02675	.01463	$.0^{2}8000$	$.0^{2}4375$	$.0^{2}2383$	$.0^{2}1308$	$.0^{3}7156$	$.0^{3}3913$	[illegible]

γ = 18.90

σ	B_1	B_2	B_3	B_4	B_5	B_6	B_7	B_8	B_9	B_{10}	B_{11}	B_{12}
$.0^{6}1$	$.0^{5}1454$	$.0^{5}1079$	$.0^{6}7889$	$.0^{6}5688$	$.0^{6}4051$	$.0^{6}2854$	$.0^{6}1990$	$.0^{6}1375$	$.0^{7}9421$	$.0^{7}6404$	$.0^{7}4321$	[illegible]
$.0^{7}5$	$.0^{4}6845$	---	---	---	---	---	$.0^{5}7368$	---	---	---	---	[illegible]
$.0^{7}3$	$.0^{3}6950$	$.0^{3}4810$	$.0^{3}3279$	$.0^{3}2216$	$.0^{3}1465$	$.0^{4}9634$	$.0^{4}6274$	$.0^{4}4049$	$.0^{4}2593$	$.0^{4}1647$	$.0^{4}1040$	[illegible]
$.0^{7}1$	.01384	$.0^{2}8984$	$.0^{2}5748$	$.0^{2}3623$	$.0^{2}2269$	$.0^{2}1403$	$.0^{3}8601$	$.0^{3}5229$	$.0^{3}3155$	$.0^{3}1891$	$.0^{3}1126$	[illegible]
$.0^{8}5$	.04195	.02618	.01611	$.0^{2}9801$	$.0^{2}5890$	$.0^{2}3508$	$.0^{2}2072$	$.0^{2}1214$	$.0^{3}7065$	$.0^{3}4060$	$.0^{3}2349$	[illegible]
$.0^{8}1$	.1393	.07934	.04400	.02451	.01359	$.0^{2}7524$	$.0^{2}4153$	$.0^{2}2288$	$.0^{2}1259$	$.0^{3}6920$	$.0^{3}3797$	[illegible]
$.0^{9}1$	.1632	.08931	.04886	.02673	.01462	$.0^{2}7995$	$.0^{2}4373$	$.0^{2}2392$	$.0^{2}1308$	$.0^{3}7153$	$.0^{3}3912$	[illegible]
$.0^{10}1$	.1635	.08944	.04891	.02675	.01463	$.0^{2}8000$	$.0^{2}4375$	$.0^{2}2393$	$.0^{2}1308$	$.0^{3}7156$	$.0^{3}3913$	[illegible]
$.0^{11}1$	.1635	.08944	.04891	.02675	.01463	$.0^{2}8000$	$.0^{2}4375$	$.0^{2}2393$	$.0^{2}1308$	$.0^{3}7156$	$.0^{3}3913$	[illegible]

γ = 28.33

σ	B_1	B_2	B_3	B_4	B_5	B_6	B_7	B_8	B_9	B_{10}	B_{11}	B_{12}
$.0^{6}3$	$.0^{6}2588$	$.0^{6}1749$	$.0^{6}1173$	$.0^{7}7809$	$.0^{7}5167$	$.0^{7}3398$	$.0^{7}2222$	$.0^{7}1446$	$.0^{8}9360$	$.0^{8}6097$	$.0^{8}3869$	[illegible]
$.0^{6}2$	$.0^{5}4412$	$.0^{5}2938$	$.0^{5}1942$	$.0^{5}1276$	$.0^{6}8328$	$.0^{6}5407$	$.0^{6}3491$	$.0^{6}2244$	$.0^{6}1435$	$.0^{7}9244$	$.0^{7}5802$	[illegible]
$.0^{6}1$	$.0^{3}1705$	$.0^{3}1106$	$.0^{4}7123$	$.0^{4}4559$	$.0^{4}2900$	$.0^{4}1835$	$.0^{4}1155$	$.0^{5}7230$	$.0^{5}4511$	$.0^{5}2802$	$.0^{5}1733$	[illegible]
$.0^{7}3$	$.0^{2}8008$	$.0^{2}4965$	$.0^{2}3057$	$.0^{2}1871$	$.0^{2}1138$	$.0^{3}6891$	$.0^{3}4151$	$.0^{3}2489$	$.0^{3}1486$	$.0^{4}8838$	$.0^{4}5237$	[illegible]
$.0^{7}1$	.04938	.02940	.01739	.01022	$.0^{2}5977$	$.0^{2}3477$	$.0^{2}2014$	$.0^{2}1161$	$.0^{3}6670$	$.0^{3}3817$	$.0^{3}2177$	[illegible]
$.0^{8}3$	.1264	.07142	.04015	.02248	.01254	$.0^{2}6978$	$.0^{2}3873$	$.0^{2}2146$	$.0^{2}1187$	$.0^{3}6553$	$.0^{3}3614$	[illegible]
$.0^{8}1$	.1579	.08681	.04769	.02616	.01435	$.0^{2}7867$	$.0^{2}4311$	$.0^{2}2361$	$.0^{2}1293$	$.0^{3}7082$	$.0^{3}3844$	[illegible]
$.0^{9}1$	.1635	.08942	.04890	.02674	.01463	$.0^{2}7999$	$.0^{2}4374$	$.0^{2}2393$	$.0^{2}1308$	$.0^{3}7155$	$.0^{3}3913$	[illegible]
$.0^{11}1$	.1635	.08944	.04891	.02675	.01463	$.0^{2}8000$	$.0^{2}4375$	$.0^{2}2393$	$.0^{2}1308$	$.0^{3}7156$	$.0^{3}3913$	[illegible]

* The notation $.0^{8}5$ denotes 5×10^{-9}.

TABLE 2—PHASE RETARDATION ϕ_n

$\gamma = 0.000$

φ_1	φ_2	φ_3	φ_4	φ_5	φ_6	φ_7	φ_8	φ_9	φ_{10}	φ_{11}	φ_{12}
22.773	22.756	---	---	---	22.61	---	---	---	---	---	---
17.64	17.61	---	---	---	17.43	---	---	---	---	---	---
14.395	14.37	---	---	---	14.15	---	---	---	---	---	---
10.17	10.14	---	---	---	9.832	---	---	---	---	---	---
7.180	7.132	---	---	---	6.73	---	---	---	---	---	---
5.550	5.491	---	---	---	5.0	---	---	---	---	---	---
3.174	3.08	---	---	---	---	---	---	---	---	---	---
2.216	2.1	---	---	---	---	---	---	---	---	---	---
.9163	---	---	---	---	---	---	---	---	---	---	---
.2013	---	---	---	---	---	---	---	---	---	---	---
.03007	---	---	---	---	---	---	---	---	---	---	---

$\gamma = 2.000$

φ_1	φ_2	φ_3	φ_4	φ_5	φ_6	φ_7	φ_8	φ_9	φ_{10}	φ_{11}	φ_{12}
74.16	---	---	---	---	---	74.09	---	---	---	---	---
23.44	23.43	23.40	23.37	23.33	23.29	23.23	23.17	23.10	23.03	22.94	22.85
7.388	7.340	7.267	7.171	7.054	6.916	6.760	6.587	6.400	6.202	5.996	5.785
2.259	2.116	1.924	1.713	1.508	1.328	1.176	1.050	.946	.860	.787	.725
.525	.355	.258	.202	.165	.140	.121	.105	.096	.085	.074	.074
.063	.037	.027	.018	.016	.012	.012	.01	.01	.01	.01	.01
.006	.00	.00	.00	.00	.00	.00	.00	.00	.00	.00	.00

$\gamma = 4.730$

φ_1	φ_2	φ_3	φ_4	φ_5	φ_6	φ_7	φ_8	φ_9	φ_{10}	φ_{11}	φ_{12}
.01561	.01157	$.0^{2}9191$	$.0^{2}7624$	$.0^{2}6513$	$.0^{2}5685$	$.0^{2}5044$	$.0^{2}4533$	$.0^{2}4115$	$.0^{2}3769$	$.0^{2}3476$	$.0^{2}3225$
.1557	.1156	.09179	.07622	.06508	.05682	.05042	.04531	.04114	.03768	.03476	.03225
1.321	1.0725	.8849	.7468	.6435	:5642	.5019	.4518	.4106	.3762	.3411	.3222
2.676	2.468	2.230	1.999	1.790	1.609	1.454	1.322	1.210	1.114	1.031	.9594
5.015	4.924	4.788	4.615	4.415	4.200	3.979	3.764	3.554	3.238	3.168	2.955
7.122	7.061	6.970	6.851	6.705	6.536	6.350	6.149	5.940	5.727	5.513	5.302
8.734	8.686	8.613	8.517	8.399	8.260	8.102	7.928	7.740	7.542	7.336	7.128

$\gamma = 9.440$

φ_1	φ_2	φ_3	φ_4	φ_5	φ_6	φ_7	φ_8	φ_9	φ_{10}	φ_{11}	φ_{12}
16.22	---	---	---	---	---	15.58	---	---	---	---	14.81
9.310	9.176	9.126	8.863	8.700	8.535	8.369	8.203	8.038	7.875	7.715	7.556
7.729	---	---	---	---	---	6.742	---	---	---	---	5.947
4.880	4.704	4.529	4.357	4.189	4.026	3.869	3.718	3.572	3.433	3.300	3.172
2.545	2.366	2.197	2.040	1.896	1.765	1.646	1.538	1.441	1.354	1.275	1.204
1.055	---	---	---	---	---	.5321	---	---	---	---	.3706
.3802	.3221	.2770	.2436	.2175	.1963	.1789	.1643	.1519	.1412	.1320	.1238
.0385	.0323	.0278	.0244	.0218	.0197	.0179	.0164	.0153	.0141	.0132	.0124
$.0^{2}389$	$.0^{2}327$	$.0^{2}281$	$.0^{2}247$	$.0^{2}220$	$.0^{2}199$	$.0^{2}181$	$.0^{2}166$	$.0^{2}154$	$.0^{2}143$	$.0^{2}134$	$.0^{2}125$
$.0^{3}389$	$.0^{3}327$	$.0^{3}281$	---	---	---	---	---	---	---	---	$.0^{3}125$

$\gamma = 14.16$

φ_1	φ_2	φ_3	φ_4	φ_5	φ_6	φ_7	φ_8	φ_9	φ_{10}	φ_{11}	φ_{12}
13.66	---	---	---	---	---	12.93	---	---	---	---	12.34
10.45	10.33	10.21	10.09	9.966	9.846	9.727	9.609	9.493	9.377	9.263	9.150
8.430	---	---	---	---	---	---	---	---	---	---	---
5.790	5.666	5.545	5.426	5.309	5.194	5.081	4.971	4.862	4.756	4.653	4.551
2.898	2.778	2.663	2.551	2.444	2.341	2.245	2.150	2.061	1.977	1.897	1.821
1.388	1.277	1.178	1.090	1.012	0.9432	.8818	.8271	.7020	.7344	.6950	.6594
.1635	.1446	.1295	.1173	.1072	.09871	.09145	.08518	.07926	.07492	.07060	.06681
.01639	.01448	.01297	.01173	.01074	$.0^{2}9882$	$.0^{2}9155$	$.0^{2}8527$	$.0^{2}7979$	$.0^{2}7498$	$.0^{2}7072$	$.0^{2}6691$
$.0^{2}1640$	$.0^{2}1448$	$.0^{2}1297$	$.0^{2}1174$	$.0^{2}1074$	$.0^{3}9882$	$.0^{3}9155$	$.0^{3}8527$	$.0^{3}7979$	$.0^{3}7498$	$.0^{3}7072$	$.0^{3}6691$

$\gamma = 18.90$

φ_1	φ_2	φ_3	φ_4	φ_5	φ_6	φ_7	φ_8	φ_9	φ_{10}	φ_{11}	φ_{12}
14.00	13.92	13.83	13.74	13.65	13.56	13.47	13.38	13.29	13.20	13.12	13.03
4.055	3.966	3.878	3.795	3.706	3.625	3.544	3.465	3.387	3.311	3.237	3.164
2.703	2.615	2.529	2.447	2.365	2.286	2.211	2.138	2.067	2.013	1.934	1.872
.8407	.7660	.7184	.6684	.6232	.5855	.5509	.5200	.4922	.4671	.4444	.4237
.0898	.0816	.0748	.0690	.0641	.0598	.0561	.0528	.0498	.0472	.0448	.0426
$.0^{2}899$	$.0^{2}817$	$.0^{2}749$	$.0^{2}690$	$.0^{2}640$	$.0^{2}598$	$.0^{2}561$	$.0^{2}528$	$.0^{2}499$	$.0^{2}472$	$.0^{2}448$	$.0^{2}427$
$.0^{3}90$	$.0^{3}82$	$.0^{3}75$	$.0^{3}69$	$.0^{3}64$	$.0^{3}60$	$.0^{3}56$	$.0^{3}53$	$.0^{3}50$	$.0^{3}47$	$.0^{3}45$	$.0^{3}43$
$.0^{4}9$	$.0^{4}8$	$.0^{4}7$	$.0^{4}7$	$.0^{4}6$	$.0^{4}6$	$.0^{4}6$	$.0^{4}5$	$.0^{4}5$	$.0^{4}5$	$.0^{4}4$	$.0^{4}4$

$\gamma = 28.33$

φ_1	φ_2	φ_3	φ_4	φ_5	φ_6	φ_7	φ_8	φ_9	φ_{10}	φ_{11}	φ_{12}
15.70	15.64	15.58	15.52	15.46	15.40	15.34	15.28	15.21	15.15	15.09	15.03
12.72	12.66	12.60	12.55	12.49	12.43	12.37	12.31	12.25	12.20	12.14	12.08
8.851	8.792	8.732	8.675	8.617	8.559	8.502	8.445	8.388	8.332	8.276	8.219
4.621	4.562	4.505	4.447	4.391	4.335	4.280	4.225	4.171	4.117	4.065	4.013
2.449	2.359	2.335	2.279	2.225	2.172	2.119	2.069	2.019	1.971	1.923	1.878
1.053	1.002	.9542	.9102	.8695	.8318	.7968	.7643	.7341	.7059	.6797	.6552
.3857	.3620	.3410	.3222	.3054	.2901	.2722	.2638	.2523	.2417	.2301	.2231
.03914	.03665	.03445	.03250	.03075	.02919	.02778	.02650	.02533	.02426	.02328	.02237
$.0^{3}3916$	$.0^{3}3666$	$.0^{3}3446$	$.0^{3}3251$	$.0^{3}3076$	$.0^{3}2920$	$.0^{3}2779$	$.0^{3}2650$	$.0^{3}2534$	$.0^{3}2426$	$.0^{3}2328$	$.0^{3}2237$

e notation $.0^{8}5$ denotes 5×10^{-9}.

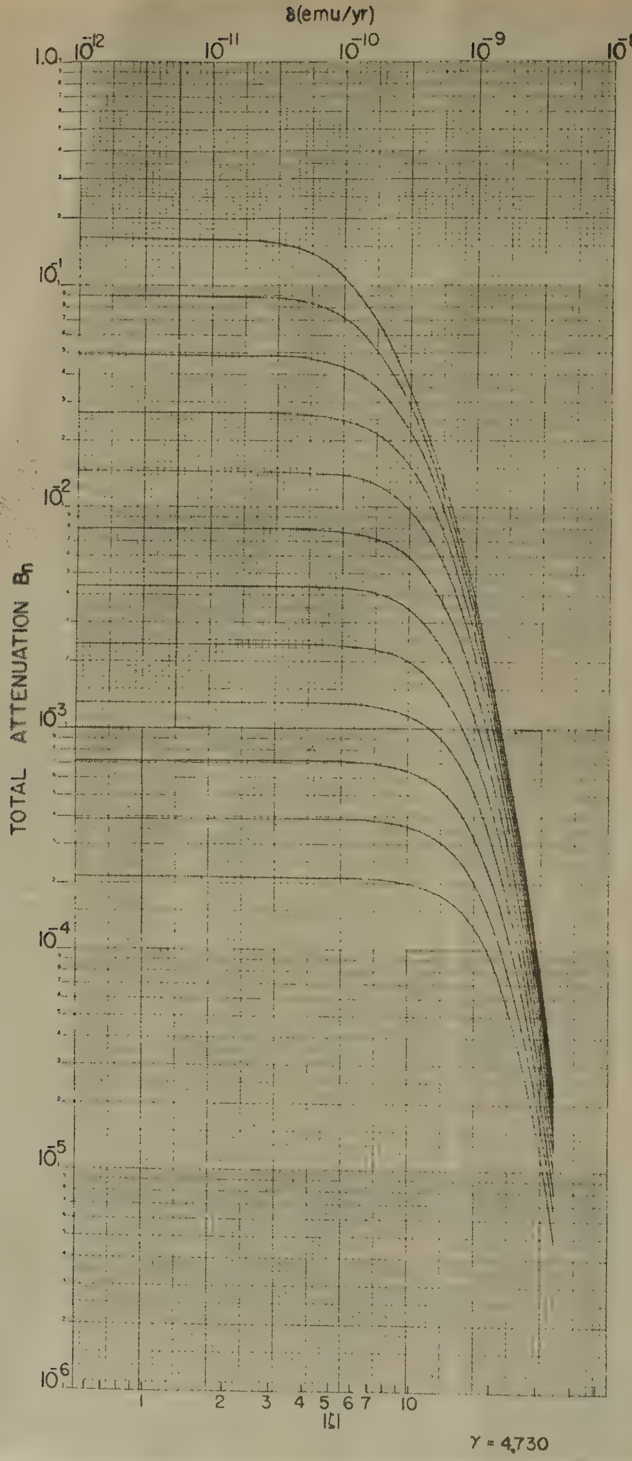

FIG. 1—Total attenuation B_n, defined by Eq. (7), for the first 12 solid harmonics. The uppermost curve corresponds to $n = 1$. Ordinates indicate wave amplitude at the earth's surface of a unit amplitude sinusoidal wave at the core, as a function of frequency

dispersive effect seriously distorts the surface wave-shapes, especially for the rapid aperiodic variations.

Extensive plots showing the relationships between C_n, B_n, ϕ_n as functions of γ and δ, or $|\zeta|$, are compiled in reference [10]. In particular, B_n is plotted (*a*) as a function of δ ($n = 1$ to 12) for the γ-values given above, and (*b*) as a function of γ throughout the range 0 to 35 ($n = 1$ to 6), treating δ as a parameter. Also, all possible ratios B_i/B_j ($j < i = 2, 3, \cdots, 6$) and the phase retardation ϕ_n, for γ-values of 2.000, 9.440, 18.90, and 28.33, are plotted as functions of δ.

IV. EQUIVALENT CONDUCTIVITY

The utility of an equivalent δ (equivalent conductivity) lies in the fact that calculations involving the earth's mantle may be simplified by a choice of the electrical conductivity, such as a constant or an inverse-square law. We next establish such an equivalence for later reference.

For a harmonic of given degree, Figure 2 shows that curves B_n, for different values of γ, are nearly "parallel." This implies that one may establish, for each harmonic, an equivalent δ, δ_c, valid over a large B_n-interval by horizontally translating that B_n-curve for which $\gamma = 0$ (constant electrical conductivity). The translations $\log_{10}\tau = \log_{10}\delta - \log_{10}\delta_c$ of the zero-curve to any chosen γ-curve, for various constant attenuations, are shown in Figure 3. Curves I, II, III, for $n = 6$, correspond to constant physical attenuations 0.800, 0.500, and 0.201. The attenuations of the first harmonic, corresponding to these constant values, are shown in Figure 2 by the Curves I′, II′, III′, and the geometric means between the extreme points ($\gamma = 0$ and $\gamma = 35$) of these curves are shown by Curves I″, II″, III″. Here the physical attenuations are $C_1 = 0.37$, 0.18, and 0.061. The displacements $\log \delta/\delta_c$ are shown in Figure 3, for $n = 1$, for the curves I″, II″, III″, together with the curve III. Curve III represents a total attenuation of amount $B_n = 1.63 \times 10^{-3}$, the corresponding physical attenuations being $C_1 = 0.010$ and $C_6 = 0.204$. In Figure 3, observe that the curves for $n = 6$ are grouped closer together than those for $n = 1$. Curves for n greater (or lesser) than 6 lie below (or above) those for $n = 6$. The results for $n = 12$ have not been included here. However, one may expect this family to be quite compact and to lie somewhat closer to the family $n = 6$ than does the family $n = 1$. For the error incurred by using the translated zero-curves, the reader is referred to reference [10].

If we postulate that the secular field $\dot{H}_r(R_c, \theta, \phi, t)$ would require harmonics of order 12, for an error not larger than, say, 2 or 3 per cent, the translation of an intermediary harmonic, say $n = 6$, would be expected to represent, very roughly, the translation of the whole field. Since the τ-curves for $n = 6$, Figure 3, are quite compact, we arbitrarily choose Curve II in the approximation of δ_c. From the Maclaurin expansion $\log_{10}\tau = a\gamma + b\gamma^2 + c\gamma^3 + \cdots$, we may write

$$\sigma_c = T_c\delta_c = \sigma_0 \frac{T_c}{T} \exp\{-(a\gamma + b\gamma^2 + c\gamma^3 + \cdots) \log_e 10\} \quad \ldots\ldots(9)$$

For Curves II and II″, the first few coefficients are tabulated below. For these curves, the points $\gamma = 2.000$, 9.440, 18.90, 28.33, and $\gamma = 2.000$, 14.16, 28.33, were employed.

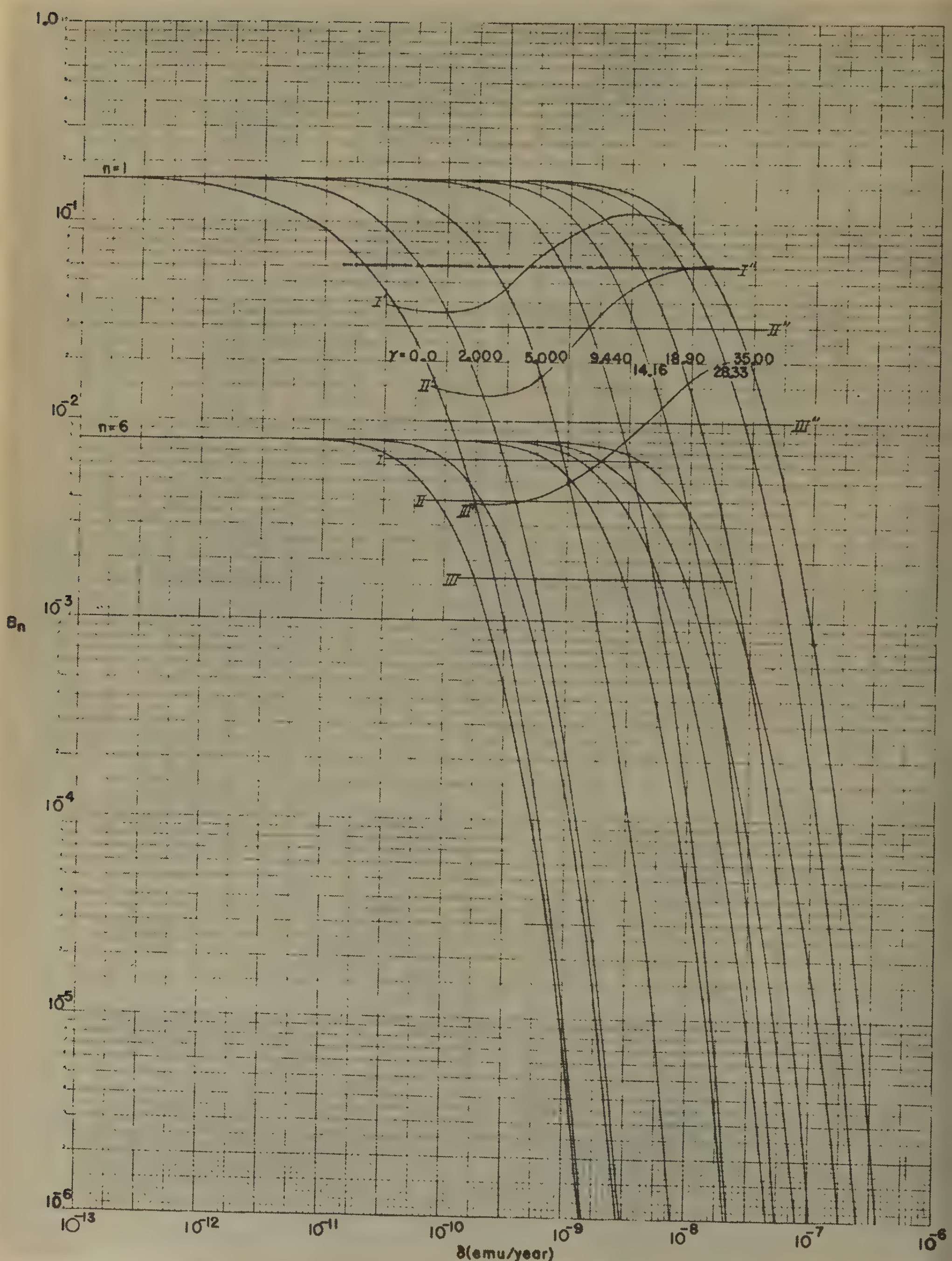
1.0
10^{-1}
10^{-2}
10^{-3}
10^{-4}
10^{-5}
10^{-6}
B_n
n=1
n=6
γ=0.0
2.000
5.000
9.440
14.16
18.90
28.33
35.00
I
I'
II
II'
II''
III
III'
III''
10^{-13}
10^{-12}
10^{-11}
10^{-10}
10^{-9}
10^{-8}
10^{-7}
10^{-6}
δ(emu/year)

FIG. 2

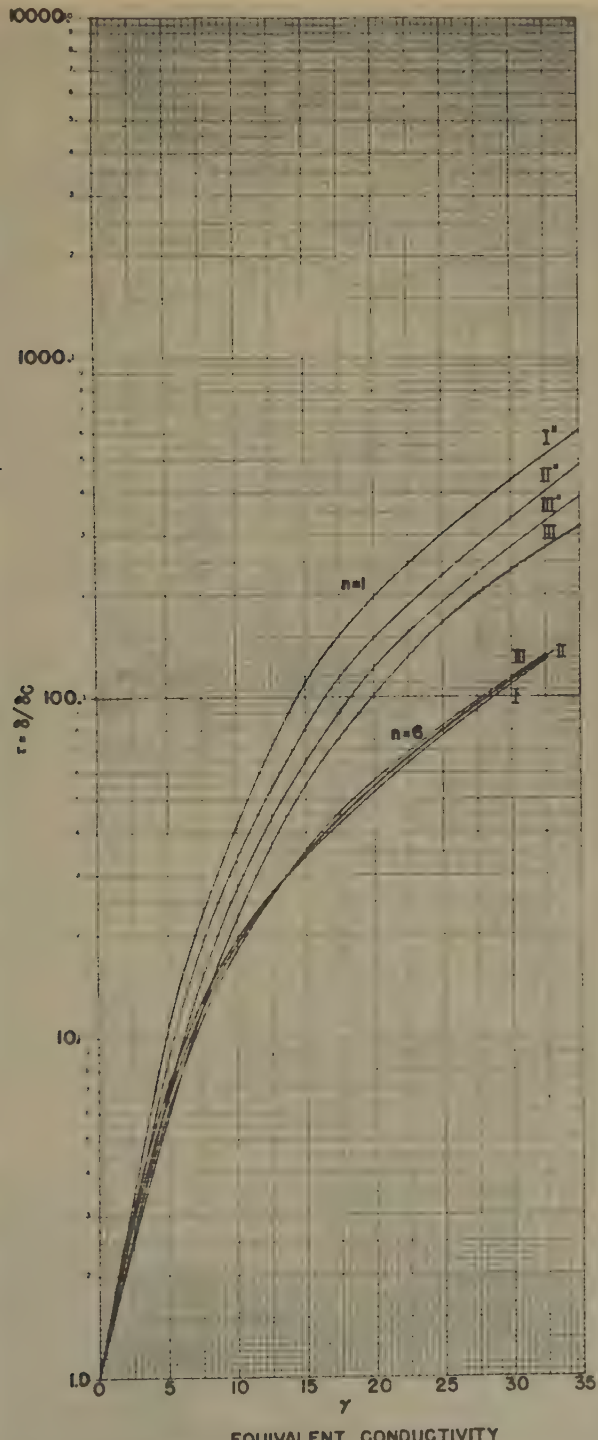
10000
1000
100
10
1.0
0
5
10
15
20
25
30
35
τ = δ/δc
γ
EQUIVALENT CONDUCTIVITY
n=1
n=6
I"
II"
III"
III
II
I

FIG. 3

	$n = 1$	$n = 6$
a	0.202	0.211
b	−0.00599	−0.0113
c	6.89×10^{-5}	0.000324
d	....	-3.60×10^{-6}

With $T_c = T$, we compute the equivalent conductivity in terms of the conductivity σ_0 at the core-mantle boundary.

V. COMPUTATION OF ELECTRICAL CONDUCTIVITY

Using our present model, we estimate σ by a method which replaces the time average of the space-averaged squared field at the core by a random static distribution. We justifiably neglect reflection effects at the earth's surface; otherwise the isoporic lines would show variations in their space derivatives at the shore lines of the continents. The linearity of Eqs. (3) allows us to write $\dot{H}_r$, as well as H_r, in the form of Eq. (5):

$$\dot{H}_r(\rho, \theta, \phi, t) = \rho^{-1} \sum_{n=1}^{\infty} n(n+1) \sum_{m=0}^{n} (\mathfrak{R}_{nc}^m S_{nc}^m + \mathfrak{R}_{ns}^m S_{ns}^m)$$

We next introduce the real total attenuation $B_n(\rho, t)$ and the real phase retardation $\phi_n(\rho, t)$:

$$B_n e^{-i\phi_n} = \rho^{-1}\mathfrak{R}_n(\rho, t)/\mathfrak{R}_n(1, t) \dots\dots\dots\dots\dots\dots (10)$$

Making use of the usual orthogonality relations, the surface average of $|\dot{H}_r|^2$ is

$$h^2 = \sum_{n=1}^{\infty} \frac{1}{2n+1} \left[B_{n0}^2 |a_{n0}|^2 + \frac{1}{2} \sum_{m=1}^{n} (B_{nmc}^2 |a_{nm}|^2 + B_{nms}^2 |b_{nm}|^2) \frac{(n+m)!}{(n-m)!} \right] \dots (11)$$

where $a_{nm} = n(n+1)\, \mathfrak{R}_{nc}^m(1, t)$, $b_{nm} = n(n+1)\, \mathfrak{R}_{ns}^m(1, t)$. Observational values of $B_{nmc}(R_e/R_c, t)a_{nm}$ and $B_{nms}b_{nm}$ are provided by the Carnegie Institution of Washington (ref. [17], p. 42). In terms of associated Legendre polynomials, Vestine's analysis is written

$$\dot{H}_r = \sum_{n=1}^{\infty} \frac{n+1}{n} \left\{ A_n^0 P_n + \sum_{m=1}^{n} \left[\frac{2(n-m)!}{(n+m)!} \right]^{1/2} P_n^m(\cos\theta)[A_n^m \cos m\phi + B_n^m \sin m\phi] \right\} \dots (12)$$

where A_n^m and B_n^m are tabulated. According to (12), the time average of h^2 at the earth's surface is

$$h_t^2 = \sum_{n=1}^{\infty} \frac{V_{nt}}{2n+1}, \qquad V_{nt} = \left(\frac{n+1}{n}\right)^2 \left[|A_n^0|_t^2 + \sum_{m=1}^{n} (|A_n^m|_t^2 + |B_n^m|_t^2) \right] \dots (13)$$

The subscript t denotes the time average. $\sqrt{V_{nt}}$ is tabulated below, Table 3, for $n = 1, 2, \cdots, 6$. The time average was taken only over the four available ten-year

TABLE 3

n	$V_{nt}^{1/2}$ γ/yr	n	$V_{nt}^{1/2}$ γ/yr
1	46.58	4	51.01
2	89.67	5	56.17
3	69.44	6	33.31

epochs 1912.5, 1922.5, 1932.5, and 1942.5. The values of A_n^m, or B_n^m, found separately from their $\dot{X}$ and $\dot{Y}$ analyses, were averaged algebraically. To supplement the data, the straight line $y = -12.26\,n + 110.3$ and the exponential $135.4\,e^{-0.215n}$ were fitted by the method of least squares to the points $(V_{nt}^{1/2}, n)$ for $n = 2, 3, 4, 5, 6$. These curves, together with the plots of $V_n^{1/2}$, for each epoch, and $V_{nt}^{1/2}$, are shown in Figure 4. (Evidently, for the time interval covered by the four epochs, the activity

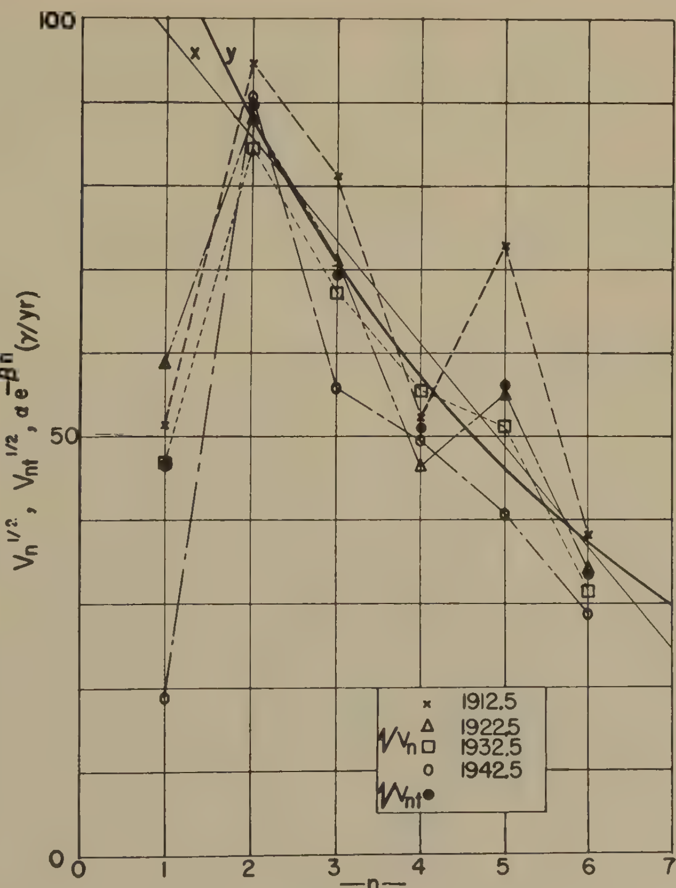

FIG. 4

of the secular field continually diminishes; if one presumes the first six harmonics to be descriptive of the whole secular field, the space-rms field h, computed from Eq. (12), assumes the successive values 67.2, 63.5, 58.9, and 51.9, gammas per year.)

We next compare (13) with the time average of h^2 in (11). $B_n(\rho, t)$ is a slowly varying function of t. Hence, we use only the first term in its Maclaurin expansion. Moreover, its dependence on the subscripts m, c, and s is artificially introduced in satisfying the boundary conditions at the core; the radial differential equation (4) depends only on the order n. Accordingly, we introduce the approximation that $B_n = B_{nic} = B_{njs}$ for all i and j. (For a damped periodic wave of frequency ν, B_n depends only on ν and the conductivity distribution. We may regard the secular field as being grouped about this frequency.) Since the two expressions are identical, term by term, at the earth's surface, we then have

$$B_n = V_{nt}^{1/2}\left\{| a_{n0} |_t^2 + \sum_{m=1}^{n} \tfrac{1}{2}[| a_{nm} |_t^2 + | b_{nm} |_t^2] \frac{(n + m)!}{(n - m)!}\right\}^{-1/2} \quad \ldots\ldots (14)$$

At the core, $B_n = 1$, $\phi_n = 0$, so that $\dot{H}_r$ is expressed in terms of a_{nm} and b_{nm}. The various criteria available for estimating these quantities will be discussed shortly. The ratio B_i/B_j of the total attenuation of the i^{th} to j^{th} solid harmonic, calculated from Table 1 for various γ-values, is represented by the γ-curves B_i/B_j *vs* δ (see ref. [10]). In these graphs, a specified value of B_i/B_j, as may be computed from (14), intersects the various γ-curves at *critical values* of δ. Curves for these points on a γ-δ coordinate system for various number pairs (i, j) may be expected to intersect in a small region of the plane (ideally, at a single point if only one frequency were present; increasing the frequency would increase the ordinate of this point). The values of γ and δ appropriate to the mantle are then the critical values read off the graph.

We now return to the coefficients a_{nm} and b_{nm}. Because of the slow series convergence at the core, we choose as a first, rough approximation

$$| a_{ij} |_t^2\left[\frac{2}{2i + 1}\cdot\frac{(i + j)!}{(i - j)!}\right] = | b_{pq} |_t^2\left[\frac{2}{2q + 1}\cdot\frac{(p + q)!}{(p - q)!}\right]$$

for all i, j, p, and q. From Eq. (14), we therefore compute the ratios $B_i/B_j = [(j + 1)V_{it}/(i + 1)V_{jt}]^{\frac{1}{2}}$. Improvements in these ratios may be obtained from a consideration of the magnetic field at the core.

The bulk of the magnetic topography, for $\dot{H}_r$, has been described in terms of an extensive system of ridges, *in motion*, the function varying rapidly over the core surface (ref. [9]). The cross-sectional shape of a typical ridge at present is unknown. The ridge half-width, however, is sufficiently small (3° to 10° of arc) to render its series expansion quite insensitive to cross-sectional shape. Neglecting these finer details of the ridges and recalling their kinetic nature, we replace the quantities $| a_{nm} |_t^2$ and $| b_{nm} |_t^2$ by the surface average of their corresponding squared coefficients computed from a weighted static distribution which varies rapidly over the core. For a *random distribution* of the function

$$\dot{H}_r(R_c, \theta) = \dot{H}_{r0} \sum_n A_n P_n(\cos \theta), \qquad \dot{H}_{r0} = \text{constant}$$

of axial symmetry, we make use of the Legendre addition theorem and compute the ratio

$$B_i/B_j = | A_j/A_i |\cdot(V_{it}/V_{jt})^{1/2} \quad \ldots\ldots\ldots\ldots\ldots\ldots (15)$$

Our choice of a random distribution seems quite justified. Vestine's secular-variation maps show a relatively rapid regional motion of the ridges superimposed upon the general westerly drift. Taken over a few hundred years, one would, therefore, not expect a ϕ-dependence in the time average of $|\dot{H}_r|^2$. Likewise, there is, at most, a small θ-dependence; the four or five active localized regions at the core occur, evidently, without preference. (If, however, these regions remain within the latitudes, say 75° north and 75° south, the field at the earth's surface would still be large over the polar caps and would therefore tend to mask any small θ-dependence.) The θ-dependence at the earth's surface may be illustrated by the line integral $f(\theta)$ of $|\dot{H}_r|_t^2$ along the parallels of latitude. Table 4 below

TABLE 4

θ	$f(\theta)\gamma/yr$	θ	$f(\theta)\gamma/yr$
0	39.5	180	53.4
10	39.7	170	68.9
20	40.8	160	88.8
30	46.3	150	92.9
40	56.2	140	81.2
50	59.1	130	65.3
60	55.8	120	54.6
70	53.1	110	55.2
80	56.8	100	60.0
90	60.9		

shows $f(\theta)$ computed from Vestine's data (ref. [16]) for 10° intervals of latitude. The time average includes only the four available epochs, which are insufficient to depict the equatorial symmetry.

Figure 5 shows the plots of the ratios B_i/B_j computed from Eq. (15). The coefficients A_n represent the axially symmetric function $f = (\cos\theta - \cos\alpha)/(1 - \cos\alpha)$, $\theta \leq \alpha$; $f \equiv 0$, $\theta \geq \alpha$. Here, $\alpha = 5°$. Figure 5*a* pertains to the original data in Table 3, whereas the exponential fit was employed in Figure 5*b*. The region of greatest convergence of the curves was estimated by locating graphically the minimum of the relative mean deviations of the points of intersection of the curves with the γ-ordinates. We next demonstrate that these critical values of γ are quite independent of the choice of function randomly distributed over the core, as well as of the observed data V_{nt}. For our purpose, several computed critical values of γ are tabulated below.

	From Table 3	*Linear*	*Exponential*
$\alpha = 5°$	5.25	4.75	5.40
$\alpha = 15°$	4.60	5.50	....

The half-angle $\alpha = 1°$ yields practically the same values as $\alpha = 5°$. The average value of the above quantities is $\gamma = 5.10$. Accordingly, we set

$$\gamma_{av} = 5.10 \pm 2 \quad (16)$$

The margin of error is deemed quite generous, in view of the small scatter. Our results indicate that after the initial rapid rise in the first one-third portion of the

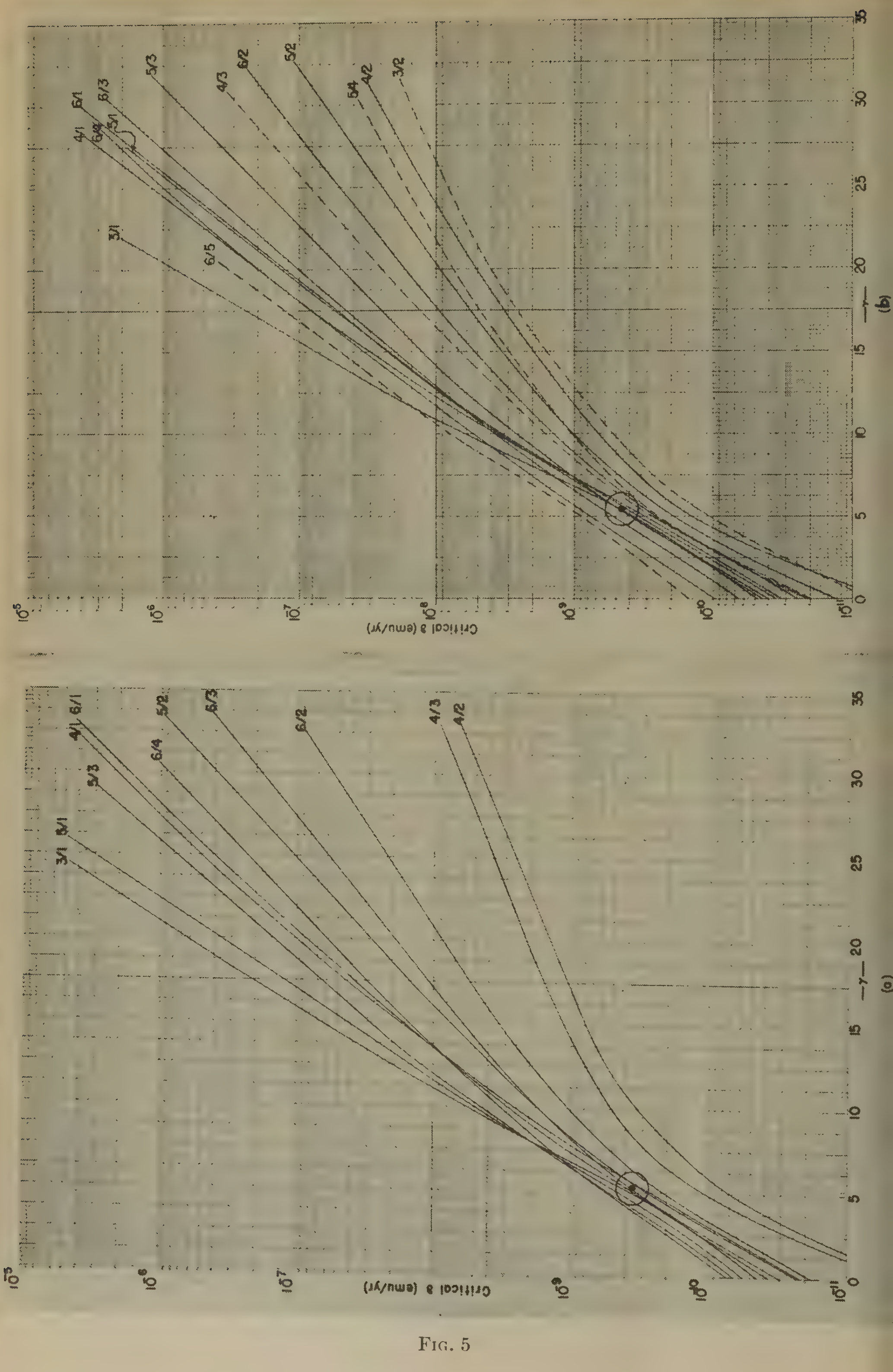

Fig. 5

mantle (ref. [8]), the conductivity levels off. σ at the 1,000-km depth is of the order of one-tenth the value at the core.

The average critical value of δ, from Figure 5, is roughly 4×10^{-10} emu/yr. On the assumption that the secular field is grouped about a wave period of T_e years, the electrical conductivity at the core is

$$\sigma_0 = 4\, T_e \cdot 10^{-10} \text{ emu} \cdots\cdots\cdots\cdots (17)$$

A value of T_e equal to 10 or 100 years would be expected. These results will be corroborated in the next Section, wherein σ_0 will be computed using an aperiodic model (also, see Appendix A).

VI. SOME APERIODIC MODELS

We wish to solve Eq. (4), subject to the following boundary conditions at the core surface:

$$\mathfrak{R}_n(1, t) = F_n(t),\ t > 0 \text{ and } \mathfrak{R}_n(\rho, 0) = 0,\ \rho > 1$$

These relationships are to be employed in the construction of various geometrical distributions at the core. Denote the Laplace transform of $\mathfrak{R}_n(\rho, t)$ by $L\{\mathfrak{R}_n\} = \mathfrak{r}_n(\rho, s)$. The transformed Eq. (4) then becomes

$$\frac{\partial^2}{\partial \rho^2}(\rho \mathfrak{r}_n) = \left\{\frac{n(n+1)}{\rho^2} + k\mu R_c^2 \sigma s\right\}\rho \mathfrak{r}_n \cdots\cdots\cdots (18)$$

$$\mathfrak{r}_n(1, s) = L\{F_n(t)\} = f_n(s)$$

These equations are solved by use of the substitutions (6). We merely replace ω by s. ζ and ν_n then become

$$\zeta \to \zeta_s = i(sk\mu R_c^2 \sigma_0)^{1/2} = (s/\omega)^{1/2}\,|\,\zeta\,|\,i, \qquad |\operatorname{Arg} s| < \pi$$

$$\nu_n \to \nu_n(s) \doteq 2[(n + \tfrac{1}{2})^2 + sk\mu R_c^2 \sigma_1]^{1/2}/|\gamma - 2|$$

When $\gamma \neq 2$, $\rho^{\frac{1}{2}}\, \mathfrak{r}_n(\rho, s) = W_\nu(z)$ satisfies Bessel's differential equation of order $\nu_n(s)$ and argument $z(s)$. Hereafter, it is assumed that $\sigma_1 = 0$, ν_n real. As in Section 5, we require that $\mathfrak{R}_n(\rho, t)$ be of order ρ^{-n-1} as $\rho \to \infty$. The two cases $\gamma > 2$, $\gamma < 2$ thus involve Bessel and Hankel functions of the first kind, respectively. When $\gamma = 2$, the substitutions are singular. Eq. (4), however, is homogeneous in ρ and may therefore be integrated directly. Returning to the case $\gamma > 2$, we therefore write $\mathfrak{r}(\rho, s) = A\rho^{-\frac{1}{2}} J_\nu(z)$. Eq. (18) is satisfied only if we take $A = f(s)/J_\nu(z_c)$, where $z_c = z\rho^{\gamma/2-1} = 2\,\zeta_s/|\,\gamma - 2\,|$. The inverse transform of $\mathfrak{r}(\rho, s)$ is, therefore,

$$\mathfrak{R}(\rho, t) = \frac{\rho^{-1/2}}{2\pi i}\int_{\lambda - i\infty}^{\lambda + i\infty} e^{st} \cdot f(s)[J_\nu(z)/J_\nu(z_c)]\, ds \cdots\cdots\cdots (19a)$$

the integration process being taken over the straight line $Rl\, s = \lambda$. When $\gamma < 2$, the Hankel function $H_\nu^{(1)}$ replaces J_ν. When $\gamma = 2$, we take $\sigma = \sigma_0 \rho^{-2}$. Integrating directly, we obtain the solution $\mathfrak{r}_n(\rho, s) = A\rho^{-\frac{1}{2}} \exp\{-\sqrt{\tfrac{1}{4} + \xi(s)}\, \log \rho\}$, for an expanding wave-front, where $\xi(s) = n(n+1) + k\mu\sigma_0 R_c^2 s$. Eq. (18) requires that $A = f_n(s)$. In this case, the inverse transform is, therefore,

$$\mathfrak{R}_n(\rho, t) = \frac{\rho^{-1/2}}{2\pi i}\int_{\lambda - i\infty}^{\lambda + i\infty} e^{st - \sqrt{1/4 + \xi(s)} \cdot \log \rho} \cdot f_n(s)\, ds \cdots\cdots\cdots (19b)$$

The inversion theorem is valid, provided that $\Re(\rho, t)$ is of bounded variation in a δ-interval about point t and the integral $\int_0^\infty e^{-\lambda t} \mid \Re(\rho, t) \mid dt$ exists in the Lebesgue sense. The integrals (19) may be estimated by the method of steepest descents for various functions $f_n(s)$. In (19a), all the zeros of $J_\nu(z_c)$ lie along the negative real axis in the complex s-plane. To deform the path of integration, it is therefore necessary to consider these singular points of the integrand. Alternately, we may employ the equivalent conductivity, Section IV, to convert the results of simplified calculations using a value of $\gamma = 2$. In Eq. (19b), we substitute

$$\alpha_n + s = s', \qquad \alpha_n = (n + \tfrac{1}{2})^2/\beta^2, \qquad \beta^2 = k\mu\sigma_0 R_c^2$$

Dropping the prime notation, we obtain

$$\Re_n(\rho, t) = \rho^{-1/2} \cdot e^{-\alpha_n t} \cdot \frac{1}{2\pi i} \int_{\alpha_n+\lambda-i\infty}^{\alpha_n+\lambda+i\infty} f_n(s - \alpha_n) \cdot e^{st - \sqrt{s}\beta \log \rho} \cdot ds$$

The right-hand factor is the inverse transform of the function

$$e^{-\sqrt{s}\beta\log\rho} \cdot L\{e^{\alpha_n t} F_n(t)\} = \frac{\beta \log \rho}{2\sqrt{\pi}} L\{t^{-3/2} \cdot e^{-(\beta\log\rho)^2/4t}\} \cdot L\{e^{\alpha_n t} F_n(t)\}$$

Two useful core functions $F_n(t)$ are listed below, together with $\Re_n$:

$F_n(t)$	$\Re_n(\rho, t)$
$e^{-\alpha_n t} S_0(t)$	$\rho^{-1/2} \cdot e^{-\alpha_n t} \cdot \operatorname{erfc}\left(\frac{\log \rho}{2\sqrt{t}}\right)$
$\delta(t)$	$\rho^{-1/2} \cdot e^{-\alpha_n t} \cdot \frac{\beta \log \rho}{2\sqrt{\pi t^3}} \cdot e^{-(\beta\log\rho)^2/4t}$

$S_0(t)$ is the Heaviside unit function. $\delta(t)$ denotes the Dirac delta-function with Laplace transform of unity. Erfc$(x) = 1 - \operatorname{erf}(x)$. Other solutions may be obtained by use of the Faltung integral, or a table of Laplace transforms.

It is worth while to plot the time variation of $\dot{H}_r$ at the earth's surface, assuming an ordinary discontinuity $S_0(t)$ in H_r at the core—that is, a δ-function in $\dot{H}_r$ at the core. The geometrical configuration is formed by taking the difference between two concentric axially symmetric functions of different half-angles $\psi_1 = 5°$ and $\psi_2 = 30°$, each of the form $\dot{H}_r(1, \theta, \phi, t) = \delta(t) \cdot H_{r0}$ $(\cos \theta — \cos \psi)/(1 - \cos \psi)$, whenever $\theta \leq \psi$; otherwise $\dot{H}_r \equiv 0$, $\psi \leq \theta \leq \pi$. The series representation at the core insures a vanishing flux of **H**:

$$\dot{H}_r = \delta(t) \cdot H_{r0} \sum_{n=1}^{\infty} A_n' P_n(\cos \theta), \qquad A_n' = (A_n)_{5°} - (A_n)_{30°} \cdot (A_0)_{5°}/(A_0)_{30°}$$

For values of $\rho > 1$, we thus have, using the above Laplace inverse transformation,

$$\dot{H}_r(\rho, \theta, \phi, t) = H_{r0} \cdot \beta \cdot (\rho t)^{-3/2} \cdot \log \rho \cdot (4\pi)^{-1/2} \cdot e^{-(\beta\log\rho)^2/4t} \sum_{n=1}^{\infty} e^{-\alpha_n t} A_n' P_n(\cos \theta)$$

At the earth's surface, the time t_n required for the n^{th} solid harmonic component

[illegible] of H_r to reach its peak value is inversely proportional to σ_0:

$$t_0\sigma_0 = [illegible] \qquad \ldots\ldots(20)$$

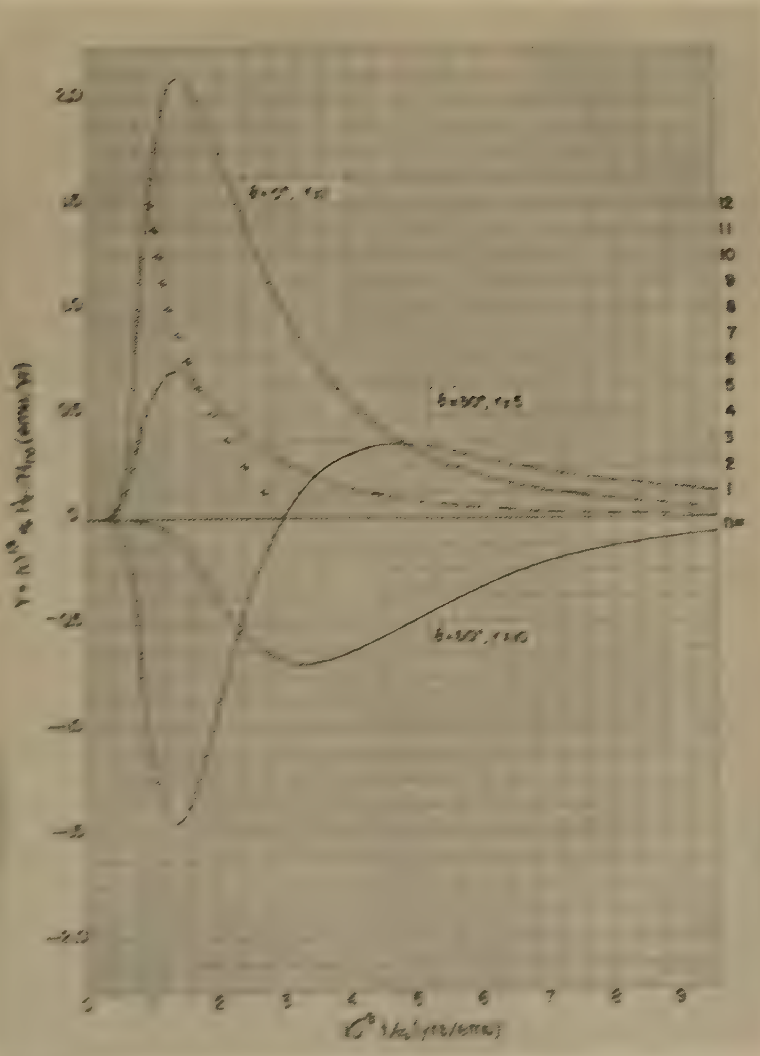

Fig. 6

Figure 6 shows the time variations of H_r at the earth's surface. The three solid curves indicate the values that an observer would expect to measure were he located directly above the region of anomaly, or 30°, or 60° therefrom. The dashed curve is similar to that denoted by $\theta = 0°$, except that the half-angle values employed here are $\theta_1 = 5°$, $\theta_2 = 15°$. The open circles indicate the values of $t_0\sigma_0$ computed by Eq. (20). As the figure shows, the time required for the peak

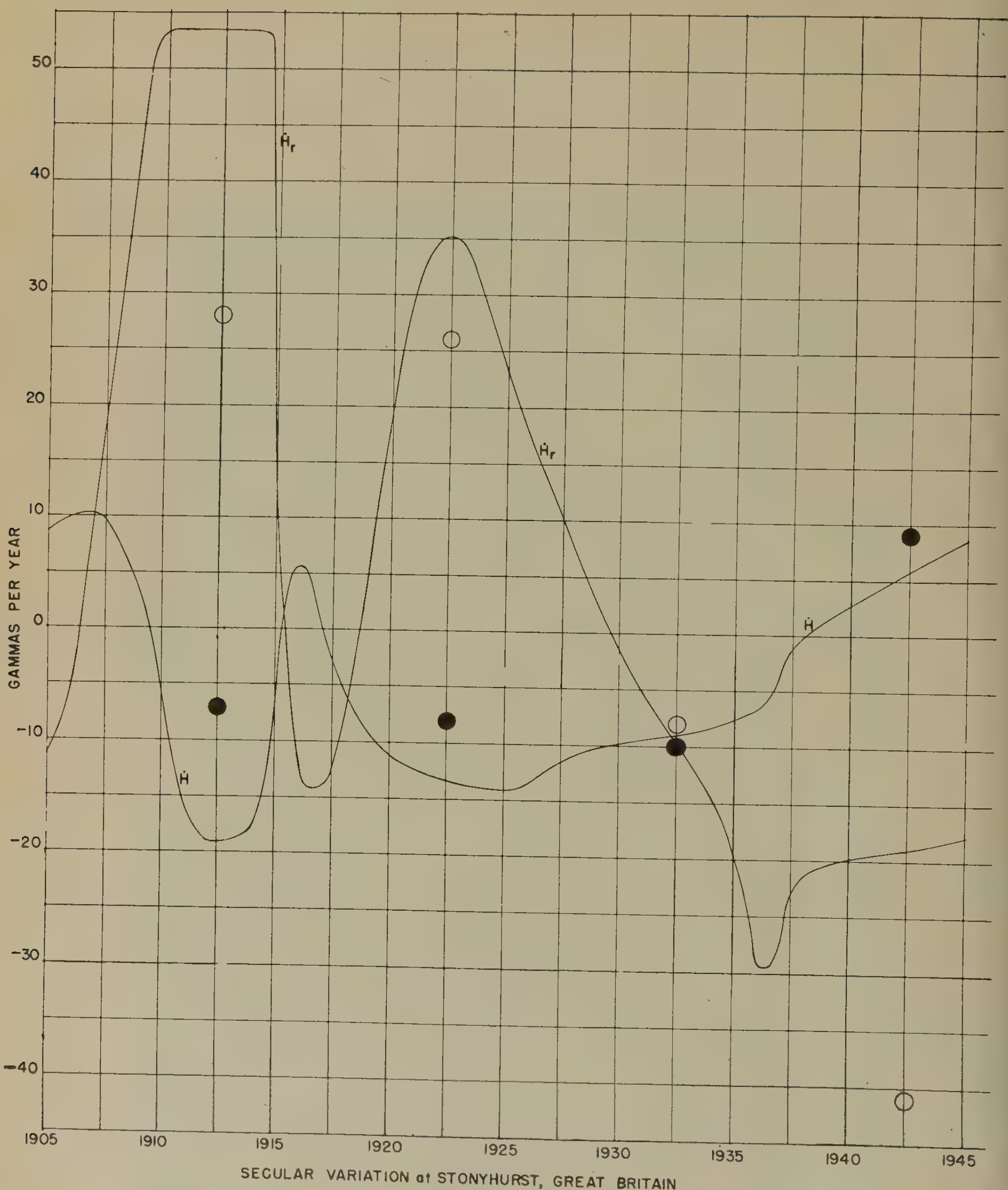

Fig. 7

of the disturbance $\dot{H}_r$ to reach the earth's surface is approximately $10^{-9}t/\sigma_0 = 1.40$ yrs/emu, a quantity representative of the *seventh* solid harmonic. t is estimated within reasonably narrow limits from a consideration of the slopes of the $\dot{H}_r$ curves scaled from magnetic observatory records (see ref. [16]). Figure 7 shows one of the more active records, for Stonyhurst, Great Britain. The rapid, large variation during the interval 1914-15 is quite anomalous; in general, moderate changes in $\dot{H}_r$ require five or ten years, as shown by the region excluding this

neighborhood. A more striking example of this irregular behavior is found, quite singularly, at Dickson, Siberia. During a one-year interval in 1937, the field increased by approximately 150 gammas per year, and then returned to its point of beginning (ref. [10]). A further discussion of these geomagnetic secular-change "impulses" is given by Walker and O'Dea (1952). From all considerations, we estimate that the travel time t for the peak value to reach the earth's surface is

$$t = 0.8 \pm 0.4 \text{ year} \qquad (21)$$

This allows for the possible error introduced in scaling the slopes from the observatory records. Since the latter are gotten from annual averages of the force components, it is difficult to measure accurate fluctuations over smaller times. Using this value of t, the conductivity σ_0, for $\gamma = 2$, is 5.71×10^{-10} emu. Now taking $H_{r0} = 1$ gauss in Figure 6, we see that the maximum value of $\dot{H}_r$ at the earth's surface is approximately 37 γ/yr. Time discontinuities of 2 or 3 gauss at the core are, therefore, entirely compatible with magnetic observatory records. Corresponding to the three values of t in (21), the equivalent conductivities σ_c ($\gamma = 0$) computed from Eq. (9) are, for the sixth solid harmonic, 1.19 emu $< \sigma_c 10^{10} = 2.39$ emu < 3.58 emu.

These results are compared with Runcorn's calculations for a plane wave pulse transmitted through a uniformly conducting semi-infinite medium (see ref. [15]). At the boundary of the medium $x = 0$, and $H_z(0, t) = H_{z0}$ whenever $t > 0$. For $t < 0$, $H_z \equiv 0$. Accordingly, the intensity at any point $x > 0$ is $H_z = H_{z0}$ erfc $\{x \sqrt{\pi\mu\sigma_c/t}\}$. Substituting $x = R_e - R_c$, the time required for the peak of the disturbance $\dot{H}_r$ to reach the earth's surface is given by

$$10^{-9}t/\sigma_c = \tfrac{2}{3}\pi\mu(R_e - R_c)^2 = 5.51 \text{ yrs/emu}$$

Substituting $t = 0.80$ year, we see that these computations, which neglect a spherical space, infer an equivalent conductivity which is too small by a factor of 0.61.

Finally, we wish to discuss the effective period T_e in Eq. (17). Using the value of $\gamma = 5.10$ in Eq. (16), we compute σ_0 for the above three values of σ_c, using Eq. (9). These are 0.791, 1.59, and 2.38, all multiplied by 10^{-9} emu. The corresponding values of T_e in Eq. (17) are, therefore, 1.98, 3.97, and 5.95 years. Judging from the variation of the slopes of the magnetic observatory records (see, for example, Fig. 7), these values are considerably smaller than would be expected. In the next section, we shall, in fact, increase their magnitude to a more reasonable value.

VII. ELECTRICAL CONDUCTIVITY OF THE EARTH'S MANTLE

The derived conductivity distribution is shown in Figure 8 by the solid curve. Values greater than 10 ohms^{-1}/m were derived from the secular magnetic variations, whereas those less than 1 ohm^{-1}/m ($= 10^{-11}$ emu) pertain to the geomagnetic transient variations, S_q and D_{st}. Intermediate values near the knee of the curve are smoothed extrapolations from the inner and outer portions of the mantle. Curves d and e were taken from Lahiri and Price (1939), without actually checking their numerical calculations. Curve e is a limiting distribution compatible with the observed phase difference in P_3^2 of S_q, consisting of a thin surface shell of strength

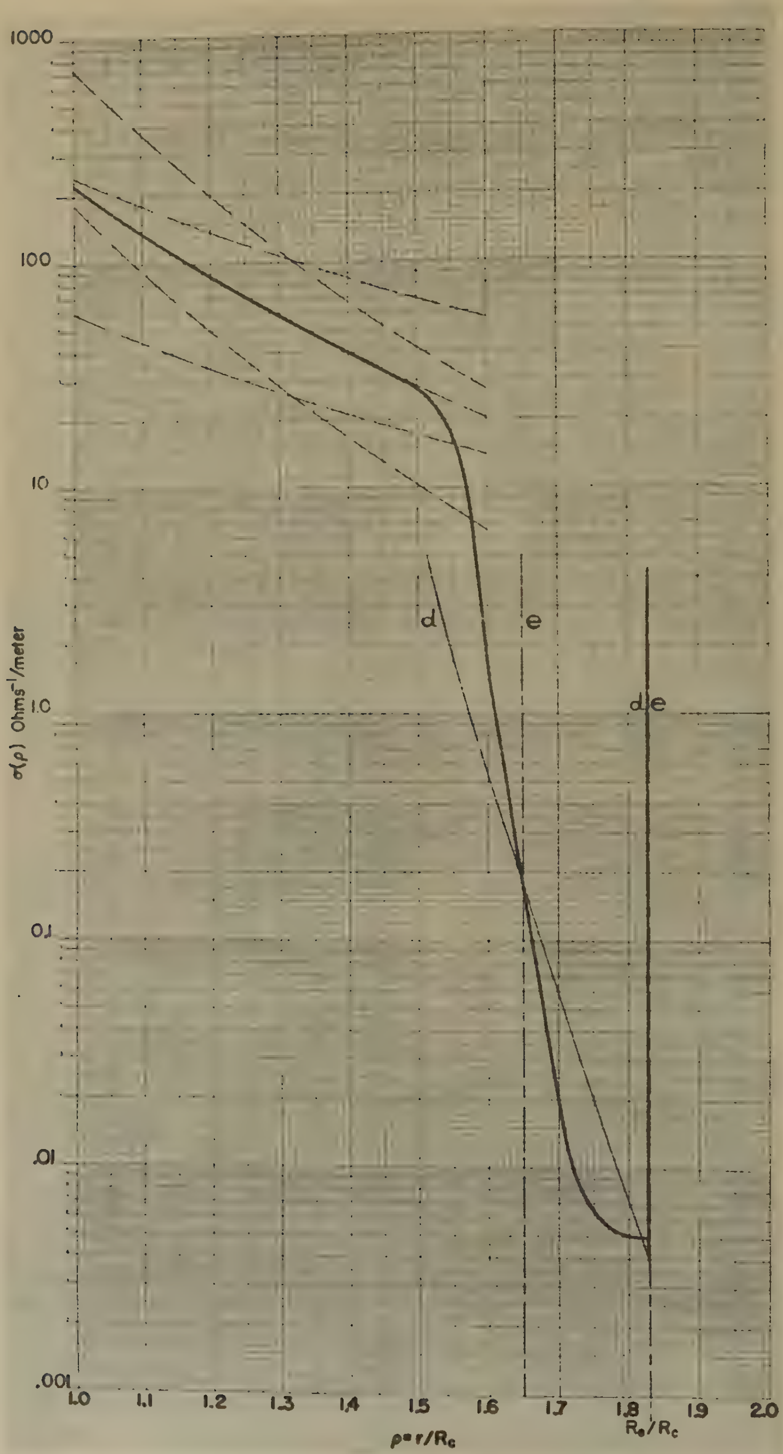

Fig. 8—Electrical conductivity distribution in the earth's mantle

.1 $\times 10^{-6}$ emu-cm—equivalent to a uniform ocean of depth 1.2 km—surrounding highly conducting region in which the radial variation of σ becomes infinite hen $\rho = 1.65$. Curve d consists of a thin shell of strength 2.0×10^{-6} emu-cm—quivalent to a uniform ocean of depth about 0.5 km— surrounding a conducting egion of conductivity $\sigma = 2.0 \times 10^{-4}\rho^{-37}$ emu. Any distribution between Curves and e, such as the chosen heavy line, is compatible with the S_q and D_{st} variations. n Curve e, the highly conducting inner core is partially shielded from the periodic ariations by the oceanic shell, whereas in Curve d, this shielding is due only in art to the oceanic shell, the outer layers, below the crust, being moderately onducting. The value of 2×10^{-6} emu-cm in Curve d is not necessarily a lower mit to the influence of the oceans. The conductivity of dry ground and surface ocks varies roughly between 10^{-16} and 10^{-15} emu, and wet ground and fresh ater exhibit values near 10^{-14} to 10^{-13} emu, whereas sea water is as large as $\times 10^{-11}$ emu. The several continents distributed over the globe would, therefore, e expected to reduce the shielding effects of the oceans. This view is supported by ikitake's studies (refs. [11] and [12]) of the influence of S_q and D_{st} by the presence f a sea bounded by the two meridians, $\pi/2$ apart in longitude. His conclusions dicated that the uniform shell models represent an upper limit to the shielding fects. On the supposition that the oceans present no shielding effect on the ansient variations, it is necessary to suppose that σ near or at the earth's surface, ccording to Lahiri and Price, be as large as 2.3×10^{-13} emu, and that between is region and the lower more highly conducting portion there is one where σ is nsiderably less than this value. The low conductivities of surface objects, however, indicate that this supposition is quite unlikely, and that it seems more robable that the oceans have an effect not too different from that shown by urves d or e.

In the last Section we derived a value $\sigma_0 = 1.59$ emu, for $\gamma = 5.10$, in the nductivity expression $\sigma_0\rho^{-\gamma}$, by using a travel time $t = 0.8$ year in the relation $^{-9}t/\sigma_0 = 1.4$ yrs/emu, scaled from Figure 6 for $\gamma = 2$. This value, however, oes not account for the sudden decrease in σ when $\rho > 1.6$; the travel time through e outer 800 km of the mantle is negligible compared to 0.8 year. On the other and, the conductivity at the 900-km depth has already decreased to at least $10 \cdot \sigma_0$, so that the total wave attenuation in this outer portion of the mantle essentially geometrical. It follows then that the previous calculations of γ remain altered. To correct for σ_0, we use Eq. (20) with $n = 7$. Substituting $t_7 = 0.8 \pm 0.4$ ear and $\rho = 1.600$, in place of 1.829, we obtain the corrected values of σ_0. Using q. (9), the final equivalent conductivity is established, $0.168 < 10^9\sigma_c = 0.336 <$ 671 emu. The conductivity at the core-mantle boundary is $\sigma_0 = 2.23 \times 10^{-9}$ nu, with a γ-value of 5.10. Therefore, the periods T_e in Eq. (17) are now increased a factor of about 1.4 to the values 2.78, 5.57, and 8.35 years. The dashed curves Figure 8 indicates the large margin of error arising from both the travel-time terval in Eq. (21) and the estimated range of γ-values in Eq. (16).

ACKNOWLEDGMENT

The author wishes to express his appreciation to Prof. W. M. Elsasser for merous helpful suggestions and valuable criticism.

References

[1] Chapman, S., and A. T. Price (1930); Phil. Trans. R. Soc., A, **229**, 427.
[2] Chapman, S., and J. Bartels (1940); Geomagnetism, Oxford, Clarendon Press, Vols. 1 and 2.
[3] Copson, E. T. (1935); Theory of Functions of a Complex Variable, London, Oxford University Press.
[4] Elsasser, W. M. (1950); Rev. Modern Phys., **22**, 1.
[5] Elsasser, W. M. (1955); Amer. J. Phys., **23**, 590.
[6] Elsasser, W. M. (1956); Amer. J. Phys., **24**, 85.
[7] Elsasser, W. M. (1956); Rev. Modern Phys., **28**, 135.
[8] Lahiri, B. N., and A. T. Price (1939); Phil. Trans. R. Soc., A, **237**, 509.
[9] McDonald, K. L. (1955); J. Geophys. Res., **60**, 377.
[10] McDonald, K. L. (1956); Tech. Rep. No. 19 (Pt. I) and No. 21 (Pt. II), Earth's Magnetism and Magnetohydrodynamics, Contract Nonr 1288(00), Office of Naval Research.
[11] Rikitake, T. (1950), Bull. Earthquake Res. Inst., Tokyo Univ., **28**, Pts. 1-2.
[12] Rikitake, T. (1951); Bull. Earthquake Res. Inst., Tokyo Univ., **28**, Pts. 3-4.
[13] Rikitake, T. (1951); Bull. Earthquake Res. Inst., Tokyo Univ., **29**, Pt. 1.
[14] Rikitake, T. (1951); Bull. Earthquake Res. Inst., Tokyo Univ., **29**, Pt. 2.
[15] Runcorn, S. K. (1955); Trans. Amer. Geophys. Union, **36**, No. 2.
[16] Vestine, E. H., L. Laporte, I. Lange, C. Cooper, and W. C. Hendrix (1947); Washington, D. C., Carnegie Inst. Pub. 578.
[17] Vestine, E. H., L. Laporte, I. Lange, and W. E. Scott (1947); Washington, D. C., Carnegie Inst. Pub. 580.
[18] Walker, G. B., and P. L. O'Dea (1952); Trans. Amer. Geophys. Union, **33**, 797.

APPENDIX A

A general explicit evaluation of Eq. (19) is given below. The function $f_n(s)$ is restricted to a finite number of simple poles at the points s_{rj} ($j = 1, 2, \cdots, N$), none of which coincide with the zero points of $J_\nu\{z_c(s)\}$, except possibly the point $s = 0$, which otherwise is a regular point of the integrand. The remaining singularities are the simple poles s_j along the negative real s-axis arising from the above zero points. After a deformation of the path of integration to the left, indefinitely, there remains only the residues of the integrand. Summing over the latter points, we therefore obtain ($\gamma > 2$)

$$\Re_n(\rho, t) = \rho^{-1/2} \sum_{j=1}^{N} e^{s_{rj} t} A_j \cdot J_\nu\{z(s_{rj})\}/J_\nu\{z_c(s_{rj})\} + 2\rho^{-1/2} \sum_{j=1}^{\infty} e^{s_j t} f_n(s_j) \frac{s_j J_\nu\{z(s_j)\}}{z_c(s_j) J_{\nu-1}\{z_c(s_j)\}}$$

In the first summation, A_j denotes the j^{th} residue of $f_n(s)$. In the latter summation, in accord with the notation of Section VI, s_j is related to the j^{th} zero x_{cj} of the Bessel function of the first kind, of order ν, by the relation $s_j = -|\gamma - 2|^2 x_{cj}^2/4\beta^2$. Also, $z_c = |z_c| = x_c = z\rho^{\gamma/2-1}$. β has the same meaning as in Section VI. In computing the latter summation, the real parts of z and z_c are made greater than zero when $Rl\, s < 0$ by choosing $-2\pi < \operatorname{Arg} s < 0$. This procedure is permitted since only even powers of these quantities occur in the ratio of the two Bessel functions. In computing the s_j-residues, $J_{\nu-1}$ in the denominator arises from the use of the recurrence relation $J_\nu'(z) = J_{\nu-1}(z) - \nu/z\, J_\nu(z)$ in the Taylor expansion of J_ν about the j^{th} zero point.

When $\gamma = 2$, the point $s = 0$ is a branch point of the integrand. Deformation

of the path of integration indefinitely to the left thus involves integration along the lines $s = u \pm 0i$, $u \leq 0$, together with the closed paths about the N poles of $f_n(s - \alpha_n)$, at the points s'_{rj} . α_n has the meaning given in Section VI. We are led to the following inverse transform

$$\Re_n(\rho, t) = \rho^{-1/2} e^{-t\alpha_n} \left\{ \sum_{j=1}^{N} e^{s'_{rj}t} \rho^{-\beta s'_{rj}{}^{1/2}} B_j \right.$$

$$\left. + \frac{1}{\pi} \int_0^\infty e^{-ut} f_n(-u - \alpha_n) \sin(u^{1/2}\beta \log \rho)\, du \right\},$$

where B_j is the j^{th} residue of $f_n(s - \alpha_n)$ and $Rl\ s^{\frac{1}{2}} \geq 0$ for all s, whereas Im $s^{\frac{1}{2}}$ has the same sign as Im s; $|\operatorname{Arg} s| < \pi$, as in the above case. The term involving the integral combines the two integrations along the line $s = u \pm 0i$. In the event that the point s'_{rj} lies on the negative real axis, the integral assumes the Cauchy principle value.

When $\gamma < 2$, J_ν in the above expression for $\Re_n(\rho, t)$ is replaced by the Hankel function $H_\nu^{(1)}$ of the first kind. The points s_{rj} and s_j now locate the poles of $f_n(s)$ and the zeros, never real, of $H_\nu^{(1)}(z_c)$. To this expression one must add the two integrations along the branch cut $s = u \pm 0i$. These are given by the single expression

$$\frac{\rho^{-1/2}}{2\pi i} \int_0^{-\infty} e^{ut} f_n(u) \{ [H_\nu^{(1)}(z)/H_\nu^{(1)}(z_c)]_{u+0i} - [H_\nu^{(1)}(z)/H_\nu^{(1)}(z_c)]_{u-0i} \}\, du$$

When ν is an integer, the origin is still a branch point of the Hankel functions but a regular point of their ratio, and the integral vanishes. Here, as in the two previous cases, the proof does not depend upon the behavior of $f_n(s)$ at infinity; $f_n(s)$ may be a constant.

To corroborate these results with Section VII, we substitute $A_j = 0$, $\sigma_0 = 2.23 \times 10^{-9}$ emu, $\rho = 1.600$, $R_c = 3.473 \times 10^8$ cm, and $\gamma = 5$. Using these values, the seventh solid harmonic component ($n = 7$) of a δ-function disturbance in $\dot{H}_r$ at the core is computed to pass through its maximum at an elapsed time of approximately one year, in accord with (21).

Journal of Geophysical Research Volume 62, No. 1 March, 1957

NOTE ON INDUCTION DRAG

By K. P. Chopra

Department of Physics, Delhi University, Delhi 8, India

(Received October 6, 1956)

ABSTRACT

An attempt to describe some aspects of induction drag is made in this short paper. The quoted expressions for translational and rotational induction drags of a sphere of infinite electrical conductivity moving in an incompressible fluid of finite electrical conductivity in the presence of a magnetic field may be derived following an earlier paper by the author. An analogy with the viscous drag is drawn, and it is shown that, unlike ordinary viscosity, the hydromagnetic or inductive viscosity is anisotropic in nature. A condition for this second viscosity to play an important role is also obtained. The rest of the paper is devoted to a discussion of the limitations of the results obtained. It is shown that the results hold good for small bodies or weak induction currents. When applied to large bodies or strong currents, the appropriate corrections for the electromagnetic and for electrostatic shielding effects must be applied. An order of magnitude calculation shows that, for bodies of cosmical dimensions, the correction is precisely of the same order as the induction effect itself.

When a magnetized body moves in a conducting medium, currents are induced in the medium, and on account of the dissipation of energy (Joule heat) the body suffers a resistance to its motion. Consider, for example, a uniformly magnetized spherical body of mass m, radius a, magnetic moment ν $(= \frac{1}{2} H_0 a^3)$, moving in an incompressible, inviscid fluid of electrical conductivity σ (in e.s.u.). Then, an induced electric field

$$\mathbf{E} = \frac{1}{c}(\mathbf{v} \times \mathbf{H}) \qquad (1)$$

is produced at any point $P(r, \theta, \varphi)$, and hence currents of density

$$\mathbf{j} = \frac{\sigma}{c}(\mathbf{v} \times \mathbf{H}) \qquad (2)$$

are generated. Here $\mathbf{v}$ is the velocity of the dipole and $\mathbf{H}$ is the dipolar field at P. The total rate of energy dissipation is obtained by multiplying the energy-dissipation function

$$\Phi = \frac{\sigma}{c^2}(\mathbf{v} \times \mathbf{H})^2 \qquad (3)$$

with the volume element surrounding P, and integrating throughout the fluid. Following Chopra (1956), it can be shown that (*i*) the translational induction drag of a spherical dipole moving with uniform velocity $\mathbf{v}$ in a direction inclined to the dipole axis at an angle α is given by

$$R = \frac{2\pi}{5}\left(1 + \frac{1}{2}\sin^2\alpha\right)\frac{\sigma H_0^2 a^3}{c^2} v \qquad (4)$$

and (*ii*) the rotational drag D of the dipole rotating with uniform angular velocity ω about an axis inclined to the axis of the dipole at an angle β is given by

$$D = \frac{2\pi}{3}\left(1 + \frac{1}{4}\sin^2\beta\right)\frac{\sigma H_0^2 a^5}{c^2}\omega \qquad (5)$$

The expressions for the drag experienced by a uniformly magnetized body moving in an incompressible, conducting, and viscous fluid are obtained by combining equations (4) and (5) with the corresponding Stokes' expressions in hydrodynamics. Thus,

$$R' = 6\pi a v\left[\eta + \frac{1}{15}\left(1 + \frac{1}{2}\sin^2\alpha\right)\frac{\sigma H_0^2 a^2}{c^2}\right] \qquad (6)$$

and

$$D' = 8\pi a^3\omega\left[\eta + \frac{1}{4}\left(1 + \frac{1}{4}\sin^2\beta\right)\frac{\sigma H_0^2 a^2}{c^2}\right] \qquad (7)$$

The expression $(\sigma/c^2)\,H_0^2 a^2$ has the dimensions of viscosity and may be rightly called the electromagnetic viscosity. The numerical coefficients of this term in the parentheses of (6) and (7) suggest that, unlike ordinary viscosity, the electromagnetic (or inductive) viscosity is anisotropic in nature. Further, the inductive viscosity is of importance when the inequality

$$H_0 a > c\sqrt{\eta/\sigma} \qquad (8)$$

is satisfied.

Under the action of electromagnetic viscosity alone, the kinetic energy of a body of magnetic moment ν and radius a would fall to $1/e^{\text{th}}$ of its value in a time

$$\tau \sim (\sigma/c^2)^{-1}(ma^3/\nu^2) \qquad (9)$$

where m is the mass of the spherical body. We speak of τ as the decay time. An alternative expression for the decay time in terms of density ρ of the sphere and the magnetic field H_0 is the following:

$$\tau \sim \frac{16\pi}{3}\frac{c^2\rho}{\sigma H_0^2} \qquad (10)$$

It must, however, be remembered that the calculations given above are valid only in the special case when the currents do not seriously modify the magnetic field. If, on the contrary, the magnetic field is actually modified by the induced electric currents, then several other factors need to be taken into account. An illustration follows:

In the case of the sun, various parameters in equation (9) have the values

$$m \sim 10^{33}\text{gm}, \; a \sim 10^{11}\text{cm}, \; \nu \sim 10^{33}\text{e.m.u.}$$

and

$$\sigma/c^2 \sim 10^{-10}\text{e.m.u. (for interstellar gas)}$$

Substituting these values in (9), we have for the decay time

$$\tau \sim 1{,}000 \text{ years}$$

This values of τ is too small compared with the age of the universe. One way to overcome this difficulty would be to assume that there is no relative motion between the spherical body and a part of the fluid surrounding it to the extent of a radius, say, a'. The evidence in support of such a view is not lacking in astrophysics; the outer solar corona has a radius $a' \sim 10a$. According to our calculations, if τ is to be of the order of 10^{10} years, a' should necessarily be of the order of $100a$. This factor alone fails to give a decay time compatible with the age of the universe.

The discrepancy is perhaps due to our neglect of the fact that the currents may be altering the field appreciably. If this happens, the changes in **H** due to these currents cause an electric field **E**$'$ to be produced in a direction opposite to $(1/c)$ $(\mathbf{v} \times \mathbf{H})$, thus reducing the currents appreciably. Then, we must have

$$\mathbf{j} = \sigma[\mathbf{E}' + 1/c \, (\mathbf{v} \times \mathbf{H})] \qquad \text{(11)}$$

where

$$\text{curl } \mathbf{E}' = -\frac{1}{c}\frac{\partial \mathbf{H}}{\partial t} \qquad \text{(12)}$$

and hence

$$\frac{\partial \mathbf{H}}{\partial t} = \text{curl } (\mathbf{v} \times \mathbf{H}) - c \text{ curl } (\mathbf{j}/\sigma) \qquad \text{(13)}$$

With the help of

$$\text{curl } \mathbf{H} = \frac{4\pi}{c}\mathbf{j} \qquad \text{(14)}$$

and

$$\text{div } \mathbf{H} = 0 \qquad \text{(15)}$$

the equation (13) leads to

$$\frac{\partial \mathbf{H}}{\partial t} = \text{curl } (\mathbf{v} \times \mathbf{H}) + \frac{c^2}{4\pi\sigma} \nabla^2 \mathbf{H} \qquad \text{(16)}$$

If l is a length comparable to the size of the sphere, then the order of magnitude considerations give the values vH/l and $c^2H/4\pi\sigma l^2$, respectively, to the two terms on the right of (16). Therefore, the two terms are of the same order if

$$l \sim \frac{c^2}{4\pi\sigma v} \qquad \text{(17)}$$

If $l \ll (c^2/4\pi\sigma v)$, the first term is small compared to the second, and equation (16) reduces approximately to

$$\frac{\partial \mathbf{H}}{\partial t} = \frac{c^2}{4\pi\sigma} \nabla^2 \mathbf{H} \qquad (18)$$

In such a case, the changes in **H** brought about by the induced electric currents are wiped out before they are allowed to arrest appreciable magnitudes by a process akin to diffusion.

On the contrary, if $l \gg (c^2/4\pi\sigma v)$, the first term dominates the second, and (16) becomes approximately

$$\frac{\partial \mathbf{H}}{\partial t} = \text{curl } (\mathbf{v} \times \mathbf{H}) \qquad (19)$$

When this happens, $E' + [(1/c)(\mathbf{v} \times \mathbf{H})]$, and hence the currents $\mathbf{j}$ would vanish completely or reduce to inappreciable magnitudes. The fluid behaves as if it possessed infinite electrical conductivity. Such a phenomenon is called electromagnetic shielding. If the shielding is perfect, the motion of the sphere is unimpeded, while partial shielding merely increases the decay time.

It is evident that the formulae for induction drag quoted in this note are applicable only to small bodies or when the currents are very small. These are certainly not suitable for bodies of solar dimensions, and when applied they should be corrected for appropriate shielding. In our illustrative solar example, if we have $a' \sim 10a$ and $\tau \sim 10^{10}$ years, the shielding should be to the extent of 99.0 per cent, that is, the net electric field

$$E'' = E' + \frac{1}{c}(\mathbf{v} \times \mathbf{H}) \sim 10^{-2} \frac{1}{c}(\mathbf{v} \times \mathbf{H})$$

Apart from the electromagnetic shielding, the mechanical effects of the sphere may be reduced by another effect known as electrostatic shielding, in which the electric field $(1/c)(\mathbf{v} \times \mathbf{H})$ is balanced by an electric field $\mathbf{E}'$ of purely electrostatic origin. Here, the currents produce a piling up of positive charge in front of itself and of negative charge behind, so that the fluid becomes electrically polarized. The sphere proceeds unopposed if the balance of $\mathbf{E}'$ with $(1/c)(\mathbf{v} \times \mathbf{H})$ is very nearly exact. The balance cannot be nearly perfect unless the rate at which the polarization charge is built up is far greater than that at which it is dissipated by conduction through the surrounding material.

The electrostatic shielding takes place only if

$$\text{div } \mathbf{j} \neq 0 \qquad (20)$$

For translational motion, the induced currents do not satisfy this condition. However, in the case of a rotating sphere, it appears that the effect of electrostatic shielding may play some part.

References

[1] Chopra, K. P. (1956); Indian J. Phys., 30, 605-610.

THE SUPERPOSITION OF COSMIC-RAY EFFECTS ON FEBRUARY 23, 1956

BY ROBERT R. BROWN*

Department of Physics, University of New Mexico, Albuquerque, New Mexico

(Received September 8, 1956)

ABSTRACT

The cosmic-ray event of February 23, 1956, represents the superposition of a flare increase and a broad Forbush-type intensity decrease. A model is proposed to account for the cosmic-ray intensity observations during this event.

INTRODUCTION

The cosmic-ray flare event of February 23, 1956, is interesting in that it occurred during a sequence of semiregular intensity decreases and thus serves as an example of the superposition of cosmic-ray effects. The flare increase and the decreases in the period surrounding it have been reported [see 1 of "References" at end of paper] previously. Briefly, the circumstances were as follows: With the outbreak of intense solar activity in January, cosmic-ray decreases were observed in close association with the growth and disk passage of regions of intense activity on the sun. In January, the decrease amounted to about 4 per cent and reached a minimum at approximately the same time as the central meridian passage of the active regions; in February, the decrease amounted to about 8 per cent and was similar to that in January. The flare increase occurred approximately three days after the intensity minimum in February. It was characterized by a rise to maximum intensity, requiring about 20 to 30 minutes, and was followed by a slow decay lasting about seven hours. It has been reported [2] that the decay observed at other stations varied from two to 15 hours, depending on the geomagnetic latitude, and that a time difference for the onset of flare radiation existed, stations located in impact zones [3] receiving particles before those located elsewhere, the time difference amounting to approximately five minutes.

Following the suggestion of Morrison [4] that magnetized clouds emanate from the sun during periods of solar activity, these observations may be interpreted tentatively as due to particles accelerated near the sun, the prompt particles following relatively direct orbits to the impact zones while delayed particles reaching stations located outside of the impact zones only after diffusing through the magnetized clouds.

Recently, Meyer, Parker, and Simpson [5] reported on the cosmic-ray flare data obtained with six neutron monitors distributed over a wide range of geomagnetic latitudes. Their results indicate that the flare radiation incident on the earth an hour or more after the flare had a steep momentum spectrum (power

*Now at the National Science Foundation, Washington 25, D. C.

law with exponent $n \sim -7$) and that the radiation fell off with time roughly as $t^{-3/2}$. These data, together with the time difference for onset, led them to propose the following conditions in interplanetary space: The earth was located in a relatively field-free ($B < 10^{-6}$ gauss) cavity, centered on the sun, with radius somewhat greater than one astronomical unit (1 A.U. = 1.5×10^{13} cm), and surrounded by a shell of finite thickness, in which disordered magnetic fields ($B \sim 10^{-5}$ gauss) existed. These conditions are similar to those proposed by Davis [6] in connection with the interaction of solar corpuscular streams and the magnetic field of the galaxy, except that the radius of the field-free cavity is smaller by a factor of about 10^2.

In this model, particles go out directly from the sun, some following orbits to the earth, while others, on encountering the magnetized shell, diffuse back into the cavity or out through the shell to escape from the solar system. The diffusion of particles in this geometry agrees roughly with the $t^{-3/2}$ result; however, with the spherical cavity, this model indicates that flares occurring on the backside of the sun may yield detectable cosmic-ray intensity increases on the earth.

It is the purpose of this paper to outline an alternate model for this event, which is suggested by the Forbush-type intensity decreases observed prior to the flare.

INTERPLANETARY MODEL

The intensity decreases observed in January and February, lasting from 12 to 14 days and in conjunction with the growth and disk passage of active regions on the sun, suggest that the earth moved through a stream of matter emitted by the sun. The time-correlations of the decreases indicate that the outward velocity of the stream was great enough to give the stream a fairly radial structure, thus suggesting a velocity of about 2,000 km/sec, comparable to that obtained from the time lags of magnetic storms after solar flares [7]. The slow decay of the post-flare radiation on February 23 suggests that the stream was made up of turbulent magnetized clouds, which served as trapping regions for the flare particles.

In attempting to use these suggestions to construct a model for this event, we assume that the magnetic conditions near the earth resulted from the presence of these magnetized clouds sent out from the sun, the magnetic field of the galaxy having been swept away by the background corpuscular emission of the sun, as suggested by Davis [6]. Except for a transition region in the vicinity of the sun, the solar stream is assumed to consist of clouds with dimensions comparable to or greater than solar dimensions arranged in a lobe-like structure which rotates with the sun. The time-associations mentioned above suggest that the broad Forbush-type decreases resulted from the passage of the earth through this stream. The details of this mechanism are not understood at present.

We consider cosmic-ray particles accelerated near the sun during the flare as injected into this stream over a wide range of directions, the particles undergoing a series of magnetic deflections, each depending on the field encountered, the extent of clouds, as well as the Larmor radius in the clouds. We assume that the emission process took place during a time interval of 10 to 15 minutes, somewhat shorter than that required for the flare radiation to reach maximum intensity.

Thus, the advance of particles through the clouds is viewed as initially in the form of a broad front, the leading edge of which varied according to local conditions, and ultimately, after emission processes had ceased, took the form of a slow diffusion out through the clouds. The cosmic-ray intensity variations observed at the earth during the flare, according to this model, resulted from particles from a limited portion of the front coming directly toward the earth, as well as particles from the remaining portions of the front which were returned to the earth after scattering in the magnetized clouds; after the flare ended, the intensity variations were due to the diffusion and leakage of particles out of the lobe.

Assuming that the lobe was roughly symmetrical with respect to the solar radius vector passing through the active regions, we may estimate from the duration of the intensity decreases that the transverse dimensions of the lobe near the earth were roughly two or three times the earth-sun distance. Further, since the flare occurred when the active regions were near the sun's limb, it follows that the prompt flare particles observed at the earth moved at large angles with respect to the axis of the lobe and passed through its outer portions. Considering the turbulent nature of the clouds, we may expect the central portions of the lobe had a greater density of large clouds than the outer portions, the smaller clouds having been swept aside as the large clouds moved outward. The rise in intensity with the onset of the flare indicates that the particles passing through these outer portions were not appreciably deviated from their original directions, while the slow decay suggests the containment of particles in the larger clouds of the lobe. Taking λ as a typical cloud size in the outer part, $R = pc/eB$ as the Larmor radius of a particle, and R_e as the earth-sun distance, we may expect relatively prompt arrival of flare radiation and yet storage in the central portions of the lobe if

$$\lambda < R < R_e = 1.5 \times 10^{13} \text{ cm}$$

This is equivalent to stating that the particles underwent a series of small-angle scatterings in approaching the earth from the sun, but were capable of being contained in trapping regions beyond the earth of dimensions comparable to those suggested by the intensity decreases. This condition is satisfied by taking the cloud size $\lambda \sim 1.5 \times 10^{11}$ cm and the Larmor radius $R \sim 1.5 \times 10^{12}$ cm. Hence, we estimate the magnetic field in the trapping regions as about 10^{-5} gauss.

Next, to obtain appreciable diffusion of particles injected into the central portion of the lobe, we assume a large number of scattering regions were distributed throughout its volume. Taking the lobe as roughly conical in shape and the clouds as spherical, we satisfy this requirement by having the volume of the lobe large compared to that of a typical scattering cloud

$$\frac{\pi r^2 h}{3} \gg \frac{4\pi\lambda^3}{3}$$

where r is the base and h is the altitude of the cone. From the transverse dimensions of the stream, we estimate that r and h were roughly comparable and thus have

$$h^3 \gg 4\,\lambda^3$$

to insure diffusion. This will be satisfied if we take

$$h \sim 10^{14} \text{ cm} \sim 6 \text{ A.U.}$$

for the radial extent of the lobe.

We may obtain the total energy released in the form of cosmic radiation during the flare by using the estimate of Meyer, Parker, and Simpson [5] for the energy density of flare radiation, $\sim 1.2 \times 10^{-10}$ erg/cm^3, and assuming that the flare particles were confined to a region extending out to approximately 2 A.U. from the sun at the time of maximum intensity: this gives

$$E \sim 3 \times 10^{30} \text{ ergs}$$

for the energy release. This value is comparable to that obtained by Meyer, Parker, and Simpson [5], using the spherical model.

It is to be noted that, while $\lambda \sim 1.5 \times 10^{11}$ cm has been used as a typical cloud dimension in the outer part of the lobe, we would expect a large range of cloud sizes present in the lobe. In this connection, it is interesting to observe that this distribution will have a bearing on the diffusion of flare radiation. We may see this by considering the diffusion equation [8]

$$\frac{\partial n}{\partial t} = \frac{c\lambda_{tr}}{3} \nabla^2 n$$

where $n(p)dp$ is the density of particles with momentum in the range $(p, p + dp)$, λ_{tr} is the transport mean free path which determines the diffusion of particles in the medium, and c is the velocity of the particles, approximately equal to the velocity of light. Just as in the case of neutron diffusion, we distinguish between the scattering mean free path λ_{sc} and the transport mean free path λ_{tr} because of the non-isotropic scattering in the clouds. Considering the turbulent clouds to have been in rather close contact, we may estimate the scattering mean free path as approximately equal to the cloud dimensions λ. However, the transport mean free path is somewhat longer, given by

$$\lambda_{tr} = \frac{\lambda_{sc}}{1 - \overline{\cos \theta}}$$

where $\overline{\cos \theta}$ is an average of the cosine of the scattering angle in the clouds. Taking λ/R as a rough estimate of the scattering angle, we see that for λ/R small compared to unity we may write this as

$$\lambda_{tr} \sim 2\left(\frac{R}{\lambda}\right)^2 \lambda_{sc}$$

The distinction between the transport and scattering mean free paths becomes less important when the Larmor radius becomes comparable to the dimensions of a cloud. Under these circumstances, the above approximation breaks down and the transport mean free path goes over to the scattering mean free path given by the cloud dimensions.

As a result of these considerations, we note that the parameters of this model, chosen so as to satisfy the inequality $\lambda < R < R_e$, are such that for protons of

momentum $p \sim 5$ Bev/c, the sun, as seen from the earth through the outer portions of the lobe, was at a distance of less than one transport mean free path. Hence, as indicated above, we may expect relatively prompt and direct arrival of flare particles at the terrestrial impact zones. In contrast to this, both the earth and sun, as seen from the central portions of the lobe where we expect to find larger clouds, were at distances of the order of 15 to 20 mean free paths for these particles. Thus, the central portions served as a large trapping region for flare particles.

Further, we observe that this distribution in cloud sizes would have the effect of making the diffusing medium inhomogeneous, the central portions serving as the main diffusion region and surrounded on all sides by clouds in which the transport mean free path gradually increases as the boundaries of the lobe are approached. The relative sizes of these two regions depend on the Larmor radii of particles, the diffusion region being larger for particles of low momentum. As a result, we expect a more rapid outward diffusion of high momentum particles, giving the post-flare radiation observed at the earth a steeper momentum spectrum than at the source, the sun. Also, the flare decay, as observed at low geomagnetic latitudes, would be of shorter duration than elsewhere.

The time-dependence of the diffusion of particles in this model is difficult to assess because of the geometry and inhomogeneities of the medium. However, certain qualitative observations may be made which will be of some value toward explaining the decay of flare radiation. In particular, the diffusion is viewed as follows: Flare particles sent out from the sun rapidly penetrate the relatively transparent regions, where $\lambda < R$, bordering on the main diffusing medium, particles being scattered out in the process. As the particles encounter more opaque regions, where $\lambda \sim R$, they become trapped and the diffusion into the central regions is slowed down. The diffusion proceeds, the density concentration on the side nearest the sun being reduced, until particles are distributed throughout the trapping volume. To the extent that we may approximate the central region as spherical in shape, the diffusion then follows an exponential decay until the supply of trapped particles is exhausted.

Thus, taking a spherical volume somewhat larger than that which includes the trapping volume to compensate for the inhomogeneity of the medium, we find by straightforward solution of the diffusion equation that the particle density is given by

$$n \sim \frac{N_0}{4\mathcal{R}^2 r}\left(\sin\frac{\pi r}{\mathcal{R}}\right)\exp\left(-\frac{\pi^2 c\lambda}{3\mathcal{R}^2}\,t\right), \qquad r \leq \mathcal{R}$$

where r is the distance from the center of the sphere of radius $\mathcal{R}$ and N_0 is the number of particles trapped at time $t = 0$. The flux of particles out of this volume depends on the gradient of the density at the surface. Using numerical values suggested by the size of the lobe and the mean free path for protons of momentum $p \sim 5$ Bev/c, $\mathcal{R} \sim 2 - 3 \times 10^{13}$ cm and $\lambda \sim 1.5 \times 10^{12}$ cm, we estimate the time constant for exponential decay to be approximately 5×10^3 sec. These estimates apply only after the transient conditions have passed, presumably a few hours after the flare ended.

By way of summary, the lobe model appears capable of accounting for the

rapid rise of flare radiation and its slow decay. In addition, it offers a possible explanation for the steep momentum spectrum of flare particles and the variation of decay time with momentum. In contrast to the spherical model, it rules out the possibility of back-side flare increases because of its geometry.

DISCUSSION

As a result of the observations of the February 23 flare, there seems little doubt that a magnetized medium plays an important role in the motion of flare radiation away from the sun. The main problem, however, is with the conditions in the region between the sun and the earth and the manner in which they were brought about.

Both the lobe and spherical models achieve a rapid rise of flare radiation at the earth by having conditions such that the earth-sun distance is smaller than a transport mean free path; in the lobe model, this results from small clouds being located between the sun and the earth, while in the spherical model from the long Larmor radius in the cavity because of the weak field in this region. Further, in both models, the slow decay results from the outward diffusion of particles trapped in regions of relatively short mean free path. Thus, except for the question of mechanism, the difference between the two models is reduced to one of geometry and its consequences, the question of back-side flare increases.

In regard to mechanisms, the lobe model is based on the corpuscular emission of the sun; in particular, it is assumed that the general emission which varies with the 11-year solar cycle is responsible for sweeping the magnetic field of the galaxy far away from the earth, while the corpuscular streams associated with intense solar activity serve to provide local magnetic fields in which cosmic-ray flare particles diffuse, by transporting fields "frozen" into conducting matter out into the solar system. The spherical model also involves corpuscular emission, but only to the extent necessary to sweep the galactic field from the first few A.U. near the sun. The spherical shell of tangled magnetic fields built up by the pressure of streaming solar matter on the galactic field provides the diffusing medium for flare radiation.

There remain other possibilities for explaining the rapid rise of flare radiation; for example, a hole might be "punched" through the diffusing medium or, as Gold and Morrison [9] suggest, from a rapid ordering of the turbulent magnetic fields by a violent solar process.

Observations of earlier flares, as reported in the literature [10], suggest that prolonged diffusion after a flare event may be typical. If the diffusing medium is established periodically by corpuscular emission from the sun, we may look to the occasional large Forbush-type decrease, as reported with this flare, as an indication of an impending flare event. This speculation, together with questions concerning rise time, decay time, and momentum spectra, will require further observations.

The mechanisms invoked in the lobe and spherical models have been used also to discuss the relatively slow world-wide decreases of cosmic-ray intensity. With the magnetized clouds proposed by Morrison [4], such decreases are viewed as the result of the earth moving through regions which initially, on emission by the sun, were devoid of cosmic rays but are slowly being filled by diffusion from the

outside. The model of Davis [6], based on the interaction of solar streams with the galactic field, views the decreases as due to density changes of particles trapped in the field-free cavity, resulting from increases in the volume of the cavity. From the discussion of the lobe model given above and the spherical shell model by Meyer, Parker, and Simpson [5], it would appear that neither mechanism, by itself, is capable of explaining the superposition of effects observed with the February flare.

For example, the mean free path in clouds of the lobe model required to explain the flare observations is too long, by at least an order of magnitude, to give the slow inward diffusion required to account for the decreases observed prior to the flare. That is to say, diffusion into an empty cloud region would take place in a time comparable to the time required to empty regions filled with flare particles. Similarly, diffusion through the shell of tangled fields required in the spherical model of the flare event is too fast to contain particles long enough so that volume increases of the cavity could account for the intensity decreases.

In view of these difficulties, other possibilities must be considered to account for the Forbush-type decreases. Since the decreases appear to be correlated with the growth and disk passage of active regions, some mechanism involving a solar stream or excitation would seem to be required. Factors which limit the possible mechanisms are the speed with which the disturbance is propagated through interplanetary space and the lack of isotropy, as shown by the close relation of cosmic-ray intensity to activity on the visible hemisphere of the sun. On these grounds, the shell of tangled fields built up by slow corpuscular streams, as proposed by Davis, is too remote to give prompt intensity changes. However, a disturbance emanating from active regions and propagated at a speed close to that of light would remove this objection; the question of isotropy would need to be examined.

Another possibility would involve the interaction of solar streams with the earth's magnetic field. However, considering the difficulties encountered with ring currents [11], the slow intensity variations may indicate the presence of a slowly varying solar component of cosmic radiation. This has been considered earlier [7], but has not been generally accepted because of the tremendous drain on solar resources it represents.

ACKNOWLEDGMENTS

The author is indebted to the Research Corporation for a Frederick Gardner Cottrell Grant. In addition, he wishes to express his appreciation to Profs. P. Meyer, E. N. Parker, and J. A. Simpson for a copy of their manuscript in advance of publication, and to Profs. P. Morrison and K. Greisen for their comments on this problem.

References

[1] R. R. Brown, J. Geophys. Res., **61**, 639 (1956).
[2] H. Elliot and T. Gold, Collection of Cosmic Ray, Solar, Ionospheric and Magnetic Data relating to the Solar Cosmic Ray Outburst, 1956 February 23, Royal Greenwich Observatory (1956).
[3] J. W. Firor, Phys. Rev., **94**, 1017 (1954).
[4] P. Morrison, Phys. Rev., **101**, 1397 (1956).

[5] P. Meyer, E. N. Parker, and J. A. Simpson, Phys. Rev., **104**, 768 (1956).
[6] L. Davis, Phys. Rev., **100**, 1440 (1955).
[7] G. Kuiper (Editor), The Sun, University of Chicago Press, Chicago (1953).
[8] R. Stephenson, Introduction to Nuclear Engineering, McGraw-Hill Book Co., Inc., New York (1954).
[9] P. Morrison, private communication.
[10] L. Biermann, Annual Reviews of Nuclear Science (1953).
[11] S. B. Treiman, Phys. Rev., **89**, 130 (1953).

GEOMAGNETIC AND SOLAR DATA

INTERNATIONAL DATA ON MAGNETIC DISTURBANCES

The time lag between the compilation of *Kp*-indices and that of sudden commencements has now become so great that it is proposed in the future to divide the international data on magnetic disturbances into Parts 1 and 2. Beginning with this issue, in Part 1 are given the usual data on sudden commencements and solar-flare effects, April to June, 1956, by Father A. Romañá, and in Part 2 the geomagnetic planetary three-hour-range indices *Kp*, preliminary magnetic character-figures *C*, average amplitudes *Ap*, and final selected days, July to September, 1956, by Drs. J. Bartels and J. Veldkamp.

PART 1: SUDDEN COMMENCEMENTS AND SOLAR-FLARE EFFECTS, SECOND QUARTER, 1956

S.c.'s given by five or more stations are in italics. Times given are mean values, with special weight on data from quick-run records.

Sudden commencements followed by a magnetic storm or a period of storminess (*s.s.c.*)

1956 April *02d 07h 21m*: sixteen.—*02d 09h 16m*: five.—21d 08h 53m: So Cm Ma.—*21d 11h 01m*: thirty-four.—*21d 13h 56m*: six.—22d 08h 00m: Ma Db El.—*25d 11h 33m*: thirty.—*26d 21h 11m*: forty-four.—*28d 17h 27m*: thirty-one.—*28d 18h 57m*: twenty-one.—*30d 01h 38m*: forty.—*30d 02h 41m*: six.

1956 May *11d 23h 42m*: thirty-four.—*11d 23h 55m*: thirteen.—*13d 22h 22m*: thirteen.—*16d 04h 17m*: thirty-one.—*20d 06h 38m*: forty-one.—23d 10h 11m: Ci Ta Al.—*24d 05h 48m*: fifteen.—29d 13h 11m: Cm Ma.

1956 June *05d 15h 13m*: fifteen.—*23d 18h 06m*: twenty-six.

Sudden commencements of polar or pulsational disturbances (*p.s.c.*)

1956 April *01d 21h 55m*: eleven.— 01d 22h 59m: SM MB Va Hr.—*02d 20h 26m* eighteen.—*03d 03h 29m*: thirteen.—*03d 23h 24m*: five.—04d 03h 08m.—SM Ta.—04d 08h 13m: Ta Hr.—04d 13h 25m: To Am.—*04d 19h 53m*: nine.—05d 13h 44m: Ka Wa To Am.—05d 19h 21m: Ma Db Hb IK.—*07d 00h 38m*: eight.—*09d 20h 50m*: eleven.—10d 05h 51m: Me Ag.—*10d 22h 23m*: six.—10d 23h 45m: He Ta.—*14d 21h 31m*: eight.—16d 17h 57m: IK SM MB.—*17d 00h 16m*: eighteen.—*17d 03h 48m*: five.—*17d 19h 32m*: seven.—17d 20h 36m: Fu Hb.—*18d 20h 57m*: five.—19d 16h 19m: Ab Ma Hb.—*20d 02h 20m*: nine.—20d 18h 44m: Cm Bi.—21d 21h 29m: Cm IK Tn.—21d 22h 14m: MB Hr.—22d 01h 27m: MB Hr.—22d 18h 58m: Tr So.—23d 02h 05m: SM Ta Hr.—26d 03h 21m: Cm Ta Hr.—26d 11h 13m: To Am.—27d 02h 46m: MB El Hr.—*27d 18h 27m*: five.—28d 00h 33m: Cm SM MB Hr.

1956 May 01d 09h 36m: Ta Hr Am.—02d 07h 50m: Me Ag.—03d 00h 07m: Cm Hr.—*04d 11h 34m*: seven.—05d 17h 25m: Es Ab.—05d 20h 02m: Tr So.—07d 19h 28m: So Hb.—13d 09h 44m: Bi Am.—14d 10h 00m: Ta Wa.—*14d 15h 32m*: five.—*14d 21h 19m*: twenty-two.—*15d 17h 03m*: nine.—16d 00h 24m: Tr Ta.—*19d 21h 27m*: fourteen.—20d 20h 16m: Cm Ab.—20d 22h 50m: Tr Ab.—*22d 18h 24m*: nine.—*22d 19h 16m*: six.—23d 22h 23m: Tr Ab El.—*24d 21h 45m*: six.—25d 00h 18m: MB Hr.—26d 01h 16m: CF Ta Va Hr.—*26d 18h 51m*: five.—

26d 23h 02m: six.—27d 23h 21m: Cm Ta El Hr.—29d 18h 34m: So Cm.—31d 03h 03m: Ag Hr.

1956 June *06d 13h 13m*: five.—06d 19h 58m: Tr So Tn.—07d 17h 24m: Ma Hb —08*d* 01*h* 20*m*: eight.—08d 23h 42m: CF El.—10d 17h 27m: Ci Gi SF.—13d 00h 29m: CF Ta MB.—*13d 20h 37m*: five.—*14d 19h 39m*: seven.—15d 01h 36m: Es Va.—*15d 17h 16m*: six.—15d 22h 17m: Tr Gi Tn.—15d 23h 07m: Gi Ta Tn.—17d 20h 55m: Tr. So.—*17d 21h 31m*: twenty-one.—19d 23h 04m: Do Wn Hb Tn.—20d 23h 10m: Do Ta.—*21d 20h 39m*: twenty.—*22d 20h 13m*: eight.—*23d 00h 26m*: sixteen.—*24d 00h 51m*: five.—25d 15h 31m: SF Ta.—25d 21h 21m: Tr So.—30d 11h 47m: Hb Am.

Sudden impulses found in the magnetograms (*s.i. or s.c.*)

1956 April 02d 14h 24m: Hb MB.—*05d 22h 48m*: five.—*06d 08h 13m*: five.—*15d 16h 28m*: twenty-one.—*23d 08h 09m*: six.—29d 11h 47m: Fu IK He El.

1956 May 01d 14h 33m: Tr IK He El.—05d 00h 56m: Hb Qu.—16d 04h 39m: CF El.—*21d 18h 18m*: eighteen.

1956 June: None.

Preliminary Report on Solar-Flare Effects

Effects confirmed by ionospheric or solar observations are in italics.

1956 April *01d 14h 17m*: Le Hu.—01d 14h 30m: Es?.—03d 09h 04m: Cm Ma Db Bi; s.i.: Qu He El Hr.—03d 12h 29m: IK.—*07d 12h 41m*: Hu.—07d 15h 30m: Ma?.— *09d 09h 40m–10h 30m*?: Hr.—12d 06h 47m–07h 10m: El?.—12d 08h 30m–09h 03m: El?.—14d 19h 11m: Hu.—20d 06h 59m: Al.—20d 08h 09m: Al.—*20d 09h 55m–10h 04m*: CF.—21d 11h 34m–11h 39m: Eb.—*22d 10h 09m–10h 14m*: Le CF? IK.—22d 12h 30m–12h 40m: Ch.—23d 05h 48m: Al.—23d 07h 23m: Al.—23d 12h 29m: Me Wn? Cm Ab? Ma Db Ag Ks Hu; p.s.c.: Le.—25d 03h 47m: Al.—26d 09h 45m–10h 00m: Bi.—26d 16h 03m–16h 42m: SJ.

1956 May 01d 12h 37m: Hu.—01d 13h 57m: Hu.—01d 14h 32m–14h 43m?: Eb.—01d 16h 53m: Hu.—04d 07h 55m–08h 30m: El.—06d 18h 27m: Hu.—08d 13h 10m–13h 24m: Le Es Wn Wi Ni Ab Ma? CF Hb IK Eb Ci? Tl? Gi Ks He Hu Hr; p.s.c.: MB.—09d 17h 00m: Ks.—*11d 18h 14m–18h 30m*: Le Es Ni Tl? Ch Tu SJ.—*13d 18h 08m*: Wn Wi Hu; s.c.: Cm.—*18d 08h 39m*: Ni.—20d 17h 31m: Hu.—20d 20h 18m: Hu.—*21d 08h 30m*?: CF.—22d 13h 32m: Hu.—24d 14h 05m: Hu.—24d 20h 40m: Hu.—26d 07h 11m?: Ma.—28d 13h 17m–13h 32m?: Eb Tl.—29d 13h 11m: IK.—*30d 09h 32m–10h 18m*: Wn Wi Ni Cm Ab Ma Db CF IK Eb Tl? He Al El Hr; p.s.c.: Ks Ta; s.c.: MB Bi.—31d 07h 32m: He.—31d 07h 52m–08h 20m: Wn Wi Ni Cm Ab Ma Db CF Hb Eb Tl? Gi Ka Al El Tn Wa Hr.

1956 June 07d 06h 49m: Al.—09d 14h 03m?: Hr.—*24d 12h 55m*: Ni Hr.—29d 19h 10m–20h 27m: Ch.

Ionospheric or solar disturbances without clear geomagnetic effect

1956 June 04d 10h 00m: Hr.—14d 10h 40m: Hr.

Minor disturbances reported by one station only are listed in the De Bilt quarterly circular, but omitted here.

Committee on Rapid Variations and Earth Currents

A. Romañá, *Chairman*, Observatorio del Ebro, Tortosa, Spain

PART 2: Kp, Ap, Ci, AND SELECTED DAYS, THIRD QUARTER, 1956

TABLE 1—*Geomagnetic planetary three-hour-range indices Kp, preliminary magnetic character-figures C, average amplitudes Ap (unit 2γ), and final selected days, July to September, 1956.*

	July 1956									August 1956								
E	1	2	3	4	5	6	7	8	Sum	1	2	3	4	5	6	7	8	Sum
1	2o	2o	3+	3−	3+	4−	3−	3o	23−	4o	2−	1+	2+	3−	2o	2−	2o	18−
2	3−	2−	4o	3−	3−	3+	3+	2+	23−	2+	1+	1+	2+	2o	1+	2−	2o	14+
3	3o	3o	4−	3+	4−	2+	1−	1−	20+	1o	1o	2+	2−	2+	2o	0+	2−	12+
4	1+	3−	3−	2+	1o	1o	1+	1o	13+	2−	1o	0+	0+	1−	1o	1+	2o	8+
5	1+	1+	2+	3o	3−	2o	2−	2+	17−	1o	2o	2−	1−	0+	1−	1o	1o	8+
6	2−	2−	2−	2o	1+	2−	1+	0+	12−	1o	1o	0+	1+	2−	2−	2o	2−	11−
7	0+	1−	1−	0+	1+	1+	1+	1+	7+	1−	2−	1−	1−	0+	1−	2−	2−	8o
8	3+	3+	3−	2o	2−	1+	2o	4+	21−	2−	1+	3−	3−	1+	4−	4−	2+	19+
9	4−	3o	3+	3−	2o	1o	1−	2−	18o	2o	2+	2o	4o	5−	4+	4o	4−	27o
10	1−	2−	2−	2−	1−	2+	5−	4−	17o	3o	3o	2+	1+	2+	2−	1o	3−	17+
11	3+	3+	3o	2−	3−	3−	3−	3o	22+	5o	4o	4o	4+	4o	4+	5+	3+	34+
12	2−	3o	3o	1+	2o	1+	3−	2−	17−	3o	3+	3+	3+	4o	3−	4−	4+	28−
13	3+	2+	1+	2−	3o	4+	5−	4+	25o	1−	1+	1+	2−	2+	1+	2−	2o	12+
14	5o	2o	1+	2−	2o	2o	2+	3o	19+	2o	2o	1o	1+	1−	0+	1o	2o	10+
15	2o	2o	1o	1+	1+	2−	3o	1+	14−	1−	1o	1−	1o	2o	1o	2o	2o	10+
16	2+	2+	2+	1+	2+	2o	1+	2−	16−	1o	0+	0+	1o	1+	3−	2−	2+	11−
17	1o	2o	2−	2−	1−	0+	1+	2o	11−	4−	5−	5−	4o	4o	3−	1+	2−	27−
18	1o	1o	0+	0+	1o	2−	2o	2−	9o	2−	1+	1+	1o	1o	1−	1o	1o	9o
19	3o	2+	2+	2−	3−	3−	3o	4+	22o	1−	0+	1−	0+	1−	1−	0+	1o	5−
20	4−	2o	2+	1+	3o	3−	2+	2+	20−	1o	1o	1+	1−	0+	1o	0+	1−	6+
21	1+	0+	1−	0+	1+	1−	1+	1+	7+	0+	2o	3−	3+	6−	5−	4−	4−	26o
22	2−	1+	1−	1o	1+	2−	1−	2−	10o	3o	2−	2−	2−	3+	2+	3−	3o	19+
23	2o	2−	1+	2−	3+	3o	4o	5o	22o	3o	3−	4−	4−	5+	3+	4−	6o	31+
24	3+	3−	5−	6o	3+	3o	2−	2o	27−	7o	6−	4o	6−	7−	8−	5o	5−	46+
25	3o	3+	4o	5o	4o	3+	3−	4+	30−	4o	4−	4−	4+	5o	6−	4o	4+	35−
26	5−	4o	6−	5+	4+	4+	4o	5o	37+	6+	4+	5+	3+	3−	3+	4+	2+	32o
27	4o	4−	4−	3+	3+	2o	3o	3+	26+	3−	4−	4−	3−	4−	3−	2−	3−	23+
28	3o	3o	3−	5−	3+	3o	5−	4+	29−	4+	3+	2−	2+	3−	3+	2o	2+	22o
29	3−	2−	5o	2+	3−	5+	3−	2o	24+	2−	2o	2o	3−	4o	3o	2+	3−	20+
30	3+	2+	3o	3−	2o	1+	2o	2−	18+	2+	2+	3+	3o	2+	2−	2−	1−	17+
31	1o	1+	2+	2+	5−	3o	2−	2o	18+	1−	1−	1+	5+	4+	4+	4o	3−	23+

	September 1956									Preliminary C, 1956			Average amplitude Ap		
E	1	2	3	4	5	6	7	8	Sum	July	Aug.	Sep.	July	Aug.	Sep.
1	3−	2o	3−	4−	3o	2+	3o	2+	22−	0.7	0.5	0.8	14	10	13
2	5o	8−	8o	7−	5−	4o	4o	3o	43o	0.7	0.4	1.9	14	7	82
3	6−	6+	6o	6−	5o	3o	2+	2o	36o	0.7	0.2	1.5	13	6	48
4	2o	2o	4−	3o	3−	1o	2−	1o	17o	0.3	0.1	0.4	7	4	10
5	3o	3−	2o	2−	1o	1o	1o	2−	14o	0.4	0.1	0.3	8	4	7
6	3+	4−	4−	5−	4+	3+	3+	3+	30−	0.2	0.2	1.0	5	5	23
7	3o	2+	3−	2o	2o	2o	1+	1+	17−	0.2	0.2	0.4	4	4	8
8	1o	1o	4−	5+	8+	8o	6o	3+	37−	0.7	0.9	1.7	13	12	78
9	3−	3−	4+	4+	4+	3−	4o	3+	28+	0.4	1.1	1.1	11	21	22
10	3o	2+	2o	2−	3−	3−	2+	1+	18o	0.7	0.6	0.5	12	9	9
11	2−	3o	2+	3−	2−	2−	2−	2−	16+	0.7	1.5	0.4	14	33	8
12	2−	1o	1−	1o	1+	1+	3o	5−	15−	0.5	1.1	0.6	9	20	10
13	4+	5+	3−	2o	1+	3−	2o	2−	22o	1.1	0.4	0.8	20	6	17
14	0+	1o	1o	1−	1−	1o	1−	1+	7−	0.7	0.2	0.1	13	5	4
15	2+	2−	0+	1+	1−	1−	1−	3+	11o	0.1	0.2	0.3	7	5	6
16	2+	1+	1+	1o	3−	3o	2o	3−	16+	0.3	0.3	0.6	7	6	9
17	1o	2o	1+	2−	2−	1+	2−	1o	12−	0.1	1.0	0.1	5	22	5
18	1+	0o	0+	1−	0+	0+	0+	0+	4−	0.2	0.1	0.0	4	4	2
19	1−	0+	1−	1−	0+	0+	1−	1+	5o	0.8	0.0	0.0	14	3	3
20	2o	4+	4−	4o	5−	5+	4−	4o	32−	0.7	0.0	1.4	11	3	29
21	5o	6o	5o	4+	4−	4−	3o	3−	33+	0.2	1.2	1.3	4	24	35
22	4−	5o	5o	5+	4−	5−	4+	2+	34o	0.2	0.7	1.4	5	11	34
23	4−	3−	4−	3+	2+	2o	1o	1+	20o	0.9	1.2	0.6	16	31	12
24	2−	2−	1o	2o	3−	0+	2+	2−	13+	1.2	1.8	0.4	24	84	6
25	4−	2+	1−	1−	2+	2+	2o	3o	17o	1.1	1.4	0.6	25	35	10
26	3o	4−	3+	3+	2−	2o	1+	0+	19−	1.4	1.3	0.5	41	34	12
27	0+	1−	2−	2+	2+	2o	2+	2−	13+	1.0	0.8	0.4	18	15	6
28	2+	4−	2+	2+	1+	2+	2−	2−	18−	1.0	0.8	0.4	23	14	9
29	1+	1−	1−	1−	2−	1o	2o	2−	10−	1.0	0.7	0.2	20	12	5
30	3−	3−	2+	2o	1o	1−	1−	2o	14o	0.6	0.6	0.3	10	9	7
31										0.7	1.1		12	21	

Table 1—(Concluded)—*Final magnetically selected days, July to September, 1956*

Month	Five quiet days	Ten quiet days	Five disturbed days
1956			
July	7 17 18 21 22	4 5 6 7 15 16 17 18 21 22	13 24 25 26 28
August	4 5 7 19 20	4 5 6 7 14 15 16 18 19 20	11 23 24 25 26
September	14 17 18 19 29	5 14 15 17 18 19 24 27 29 30	2 3 8 21 22

Table 2—*Monthly mean values of Ci, Cp, and Ap*

Index	July 1956	Aug. 1956	Sep. 1956
Mean *Ci*	0.63	0.67	0.67
Mean *Cp*	0.66	0.65	0.69
Mean *Ap*	13	15	18

Committee on Characterization of Magnetic Disturbances

J. Bartels, *Chairman*
University
Göttingen, Germany

J. Veldkamp
Kon. Nederlandsch Meterologisch Instituut
De Bilt, Holland

PROVISIONAL SUNSPOT-NUMBERS FOR OCTOBER TO DECEMBER, 1956

(Dependent on observations at Zurich Observatory and its station at Locarno and Arosa)

Day	Oct.	Nov.	Dec.
1	170	157	163
2	183	175	145
3	192	187	169
4	195	198	194
5	192	220	190
6	160	274	175
7	160	321	173
8	189	295	157
9	198	242	165
10	189	236	204
11	166	256	229
12	175	262	200
13	170	205	184
14	121	205	218
15	108	246	198
16	104	236	186
17	90	231	174
18	106	180	156
19	126	178	151
20	145	180	130
21	150	183	173
22	155	154	193
23	126	165	215
24	167	175	219
25	173	190	229
26	160	130	216
27	154	122	215
28	162	115	202
29	187	164	185
30	216	198	168
31	195		174
Means.......	160.8	202.7	185.5
No. days.....	31	30	31

Mean for quarter: 182.8 (92 days)
Mean for year 1956: 141.4 (366 days)

M. Waldmeier

Swiss Federal Observatory
Zurich, Switzerland

FREDERICKSBURG THREE-HOUR-RANGE INDICES FOR OCTOBER TO DECEMBER, 1956

[$K9 = 500\gamma$; scale-values of variometers in γ/mm: $D = 2.8$; $H = 2.6$; $Z = 3.1$]

Gr. day	October 1956		November 1956		December 1956	
	Values K	Sum	Values K	Sum	Values K	Sum
1	2313 3224	20	3320 3222	17	1111 2223	13
2	4344 4343	29	2112 2333	17	4123 2322	19
3	3333 3333	24	4233 3233	23	2223 3132	18
4	3123 2322	18	3232 2212	17	3222 2322	18
5	1144 2232	19	1100 0122	7	3211 2321	15
6	3223 4323	22	0322 2323	17	1321 2323	17
7	3222 3342	21	3201 2021	11	2222 2222	16
8	4332 2243	23	1122 2111	11	1244 3122	19
9	3222 3232	19	1011 1154	14	1123 2112	13
10	2001 2222	11	5454 5545	37	4534 3233	27
11	1222 2112	13	6556 4346	39	2100 0121	7
12	0001 1112	6	4254 5433	30	0001 2234	12
13	1101 0011	5	4212 3212	17	2343 2222	20
14	1110 0011	5	4643 3355	33	2312 2111	13
15	0000 1111	4	5566 5334	37	1111 1000	5
16	0132 1011	9	6554 3332	31	0111 1000	4
17	1221 1001	8	2223 3222	18	0111 0101	5
18	1301 1001	7	5341 2221	20	0112 3211	11
19	2222 2112	14	0001 2211	7	0011 0112	6
20	2454 4334	29	1113 3332	17	2112 1121	11
21	3444 4333	28	3444 3234	27	1111 1011	7
22	3420 3122	17	3324 4345	28	1112 2011	9
23	4233 2123	20	5234 4221	23	0001 1112	6
24	1311 0021	9	1112 3222	14	3221 1121	13
25	1221 0011	8	1143 7442	26	2233 5333	24
26	3332 3445	27	3100 1110	7	3442 2111	18
27	4544 3233	28	1221 1233	15	0122 2434	18
28	2344 3222	22	5332 2222	21	4343 3443	28
29	2212 2221	14	2222 2233	18	4223 3222	20
30	1132 3321	16	2323 2222	18	2144 2311	18
31	1013 3213	14			2202 2111	11

Robert L. Gebhardt
Observer-in-Charge

Fredericksburg Magnetic Observatory
Corbin, Virginia

PRINCIPAL MAGNETIC STORMS

(Advance knowledge of the character of the records at some observatories as regards disturbances)

Observatory (Observer-in-Charge) (1)	Green-wich date (2)	Storm-time: GMT of begin. (3)	Storm-time: GMT of ending[1] (4)	Sudden commencement: Type[2] (5)	Sudden commencement: Amplitudes[3] D (6)	Amplitudes[3] H (7)	Amplitudes[3] Z (8)	C-figure, degree of activity[4] (9)	Maximal activity on K-scale 0 to 9: Gr. day (10)	Gr. 3-hr. period (11)	K-index (12)	Ranges: D (13)	Ranges: H (14)	Ranges: Z (15
	1956	*h m*	*d h*		′	γ	γ					′	γ	γ
College (C.J.Beers)	Oct. 2	07 00	4 02	.....	....	....	....	ms	2	5	6	140	930	50
									3	5	6			
	Oct. 20	04 00	22 05	.....	....	....	....	ms	20	3,4,5	7	210	1540	69
	Oct. 26	00 27	29 00	s.c.*	−3	−7	−3	ms	28	3	7	180	1170	82
	Nov. 9	20 30	13 05	s.c.*	−17	−31	−21	ms	10	3,7	7	420	1930	139
									11	3	7			
									12	5,6	7			
	Nov. 14	02 00	18 16	.....	....	....	....	s	15	3	8	380	2470	123
	Nov. 20	09 00	23 22	.....	....	....	....	ms	21	3	7	250	1500	85
	Nov. 25	07 00	26 02	.....	....	....	....	s	25	5	9	340	3260	183
	Dec. 12	08 00	14 00	.....	....	....	....	ms	13	6	6	130	770	45
	Dec. 27	10 00	29 00	.....	....	....	....	ms	28	5,6	6	180	940	55
Sitka (J.L.Bottum)	Oct. 2	06 ..	4 02	.....	....	....	....	ms	2	4,5	6	45	460	35
	Oct. 20	05 ..	22 04	.....	....	....	....	ms	20	3,4,5	7	89	763	51
									21	4				
	Oct. 26	13 12	28 23	s.c.	−2	+17	+4	ms	28	4,5	7	106	774	46
	Nov. 9	20 30	13 04	s.c.*	+20	−27	−24	s	10	3	9	244	1458	124
	Nov. 14	02 ..	16 23	.....	....	....	....	s	15	3	9	157	1655	89
	Nov. 20	09 00	23 20	s.c.	+3	−1	−4	ms	23	4	7	66	520	52
	Nov. 25	06 05	26 03	s.c.*	−1	−7	0	s	25	5	9	135	1892	84
	Dec. 10	02 ..	11 00	.....	....	....	....	ms	10	4	6	39	272	33
Witteveen (D.van Sabben)	Oct. 20	03 00	22 05	.....	....	....	....	m	20	3,6,7,8	5	30	150	10
									21	1	5			
	Oct. 26	13 12	27 08	s.c.*	+2	+25	0	ms	26	7	7	60	215	12
									27	1	7			
	Nov. 9	20 30	13 04	s.c.	−6	+87	−2	ms	10	8	6	45	255	15
									11	1,2,8	6			
									12	1	6			
	Nov. 14	02 00	16 21	s.c.	−3	+19	0	ms	14	7	7	40	310	14
	Nov. 22	12 00	23 20	.....	....	....	....	ms	22	8	6	30	155	10
	Nov. 25	11 39	25 19	s.c.	−1	+10	0	ms	25	5	6	30	200	4
	Dec.	None												
Fredericksburg (R.E.Gebhardt)	Oct. 26	00 27	.. ..	s.c.*	+25	−1	0	m	26	8	5	36	169	1[illegible]
		13 12	28 14	s.c.*	+40	−1	+1		27	2	5			
	Nov. 9	20 30	13 04	s.c.*	−5	+103	+43	ms	11	1,4,8	6	34	139	1[illegible]
	Nov. 14	02 ..	16 20	.....	....	....	....	ms	14	2	6	45	246	3[illegible]
									15	3,4	6			
									16	1	6			
	Nov. 25	11 35	26 04	.....	....	....	....	ms	25	5	7	23	213	[illegible]
	Dec.	None												
Tucson (R. F. White)	Oct. 26	13 12	28 14	s.c.	+2	+12	....	m	26	7	5	14	185	[illegible]
									28	3	5			
	Nov. 9	20 30	13 05	s.c.	0	+67	+4	ms	10	1,8	6	18	187	[illegible]
	Nov. 14	02 00	16 12	.....	....	....	....	ms	14	2	6	23	165	[illegible]
									15	3,4	6			
									16	3	6			
	Nov. 22	12 ..	23 15	.....	....	....	....	m	22	5,8	5	13	150	[illegible]
	Nov. 25	12 ..	26 03	.....	....	....	....	m	25	5	6	21	102	[illegible]
	Dec. 27	15 00	29 06	.....	....	....	....	m	27	5	6	15	110	[illegible]
									28	5	1,3			

[1]Approximate time of ending of storm construed as the time of cessation of reasonably marked disturbance movements in t[illegible] traces; more specifically, when the K-index measure diminished to 2 or less for a reasonable period.

[2]s.c. = sudden commencement; s.c.* = small initial impulse followed by main impulse (the amplitude in this case is that of t[illegible] *main impulse only*, neglecting the initial brief pulse; . . . = gradual commencement.

[3]Signs of amplitudes of D and Z taken algebraically; D reckoned positive if towards the east and Z reckoned positive if ver[illegible]cally downwards.

[4]Storm described by three degrees of activity: *m* for moderate (when K-index as great as 5); *ms* for moderately severe (wh[illegible] K = 6 or 7); *s* for severe (when K = 8 or 9).

PRINCIPAL MAGNETIC STORMS—Concluded

bservatory (Observer-n-Charge)	Green-wich date	Storm-time		Sudden commencement				C-figure, degree of ac-tivity[4]	Maximal activity on K-scale 0 to 9			Ranges		
		GMT of begin.	GMT of ending[1]	Type[2]	Amplitudes[3] D	H	Z		Gr. day	Gr. 3-hr. period	K-index	D	H	Z
(1)	(2)	(3)	(4)	(5)	(6)	(7)	(8)	(9)	(10)	(11)	(12)	(13)	(14)	(15)
	1956	*h m*	*d h*		′	γ	γ					′	γ	γ
Juan	Oct. 26	13 11	27 12	s.c.	+1	+10	−3	ms	26	7	6	11	182	42
Vazquez)	Nov. 9	20 30	13 04	s.c.	0	+39	−11	m	10	1,3,5,6,8	5	13	183	43
									11	1,4,8	5			
									12	1,6	5			
	Nov. 14	02 00	16 11	s.c.	+1	+11	−3	ms	14	8	6	17	161	36
									15	3,4,5	6			
	Nov. 25	11 36	26 03	s.c.	0	+5	−2	m	25	5	6	14	84	26
	Dec.	None												
olulu	Oct. 25	13 00	28 14	.....	....	....	....	ms	26	7	6	4	180	16
L.Cleven)	Nov.	None												
	Dec.	None												
tute	Oct. 20	08 26	21 21	.....	....	....	....	ms	21	5,6	6	12	345	48
físico de	Oct. 26	13 12	27 05	s.c.*	+2	+117	−5	ms	26	6	7	9	407	65
ncayo	Nov. 9	20 30	13 03	s.c.	+4	+169	−15	ms	10	6	6	14	425	79
.Giesecke,	Nov. 14	02 00	16 21	s.c.	+1	+30	−2	ms	15	5	7	17	400	72
	Nov. 25	11 40	25 22	.....	....	....	....	s	25	5	8	9	546	50
	Dec. 25	07 53	25 23	s.c.	0	+11	−3	ms	25	5,6	6	13	294	89
	Dec. 27	10 30	29 04	.....	....	....	....	ms	28	6	6	14	289	60
			(Report prepared by M. Casaverde)											
	Oct. 1	20 ..	4 11	.....	....	....	....	m	2	3	5	6	131	29
. Thomson)	Oct. 5	06 32	10 02	.....	....	....	....	m	5	3,4	5	7	144	25
	Oct. 19	15 ..	22 05	.....	....	....	....	ms	20	2	6	8	196	27
	Oct. 26	00 27	29 20	s.c.	+1	+20	−8	ms	26	7	6	7	225	27
	Nov. 9	20 30	13 04	s.c.*	−1	+43	−15	ms	10	1	6	12	308	41
	Nov. 14	02 00	18 15	s.c.	+1	+16	−10	ms	15	4	6	13	226	48
		(*Note*: No record for Nov. 17; details given for storm commencing 14d 02h 00m refer to remainder of assumed period of storm)												
	Nov. 20	06 ..	23 20	.....	....	....	....	m	22	8	5	8	157	36
	Nov. 24	03 50	26 06	.....	....	....	....	ms	25	5	6	9	111	48
	Nov. 27	18 24	3 03	.....	....	....	....	m	28	1	5	11	142	30
								m	2	1	5			
	Dec. 27	15 03	29 04	s.c.	0	+15	−5	m	28	1,3,7	5	11	117	34
	Aug. 11	00 45	12 23	s.c.	−1	+55	−3	m	11	3	...	3	180	20
Lepas,	Aug. 24	00 14	26 03	s.c.	....	+63	....	m	24	5	...	5	208	25
uckuyt)	Sep. 2	02 31	3 14	s.c.	−1	+39	−1	m	2	2	...	4	198	30
	Sep. 8	10 07	9 24	s.c.	−11	+26	−3	m	8	5,6	...	3	327	28
	Sep. 20	04 46	21 12	s.c.	0	+14	−1	m	20	6	...	3	198	....
eroo	Oct. 26	13 12	28 15	s.c.	+1	+27	+5	m	26	7	6	15	164	113
Tillott)	Nov. 9	20 30	13 06	s.c.*	+3	+34	+17	ms	11	8	7	27	216	156
	Nov. 13	21 38	16 24	s.c.	−2	−3	−8	ms	15	4	6	24	154	230+
	Nov. 22	12 10	23 18	.....	....	....	....	m	22	8	5	22	91	117
									23	1	5			
	Nov. 25	08 50	25 19	.....	....	....	....	ms	25	5	7	15	164	76
	Dec. 27	15 02	29 04	s.c.	+1	+32	−3	ms	28	3	6	20	142	111
ngi	Oct. 20	02 56	22 05	.....	....	....	....	m	20	5	5	24	158	56
	Oct. 26	00 26	29 01	s.c.	−2	+19	+6	ms	26	6,7	6	22	206	70
ngham)	Nov. 9	20 29	13 04	s.c.*	−8	−38	+2	ms	11	8	6	28	255	120
									12	5	6			
	Nov. 13	21 38	16 20	s.c.	−3	−4	0	ms	15	4	7	47	240	180
	Dec. 27	15 01	29 04	s.c.	+1	+48	+1	m	28	3	6	21	182	51
rley	Oct. 26	00 27	.. ..	s.c.	0	+25	−1	m	26	....	...	9	83	16
	Oct. 26	13 12	27 14	s.c.*	+1	+32	−4	ms	26	6,7	7	12	180	106
ngton)	Nov. 9	20 30	13 18	s.c.	−4	−20	+22	ms	11	8	6	32	294	187
	Nov. 14	01 59	18 14	s.c.	+1	+19	−4	ms	15	3,4	6	28	291	176
	Nov. 20	02 ..	26 09	.....	....	....	....	ms	25	5	6	23	285	118
	Dec. 25	07 56	26 11	s.c.	0	+37	−3	m	25	3	4	11	105	64
	Dec. 27	15 03	29 10	s.c.	+2	+35	−7	m	28	3	5	20	199	56
	Dec. 30	06 33	31 04	s.c.*	+1	+58	−9	m	31	3	5	19	160	44

ON SUDDEN COMMENCEMENTS OF MAGNETIC STORMS AT HIGHER LATITUDES

This communication describes a type of sudden commencement of magnetic storms not previously discussed in the literature. This type of sudden commencement occurs at higher latitudes, and its characteristics have been studied in magnetograms made at Point Barrow (71.3°N, 156.8°W; gm 68°N), College (64.9°N, 147.8°W; gm 65°N), Cheltenham (38.7°N, 76.8°W; gm 50°N), Tucson (32.3°N, 110.8°N; gm 40°N), San Juan (18.4°N, 66.1°W; gm 30°N), and Honolulu (21.3°N, 158.1°W; gm 21°N), during the period from July 1949 to March 1956.

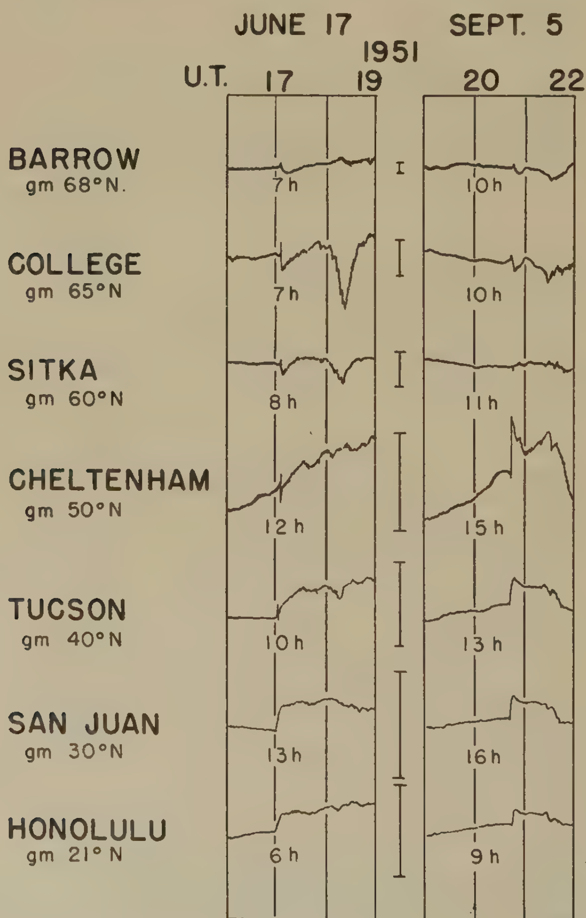

FIG. 1—A new type of sudden commencement of magnetic storms designated as Sc^- (shown by the horizontal component) occurring frequently at higher latitudes. The time is shown by both the universal and local times. The unit scale at each station is 100γ.

During that period, 44 sudden commencements were observed. Twenty-one of them, observed at higher latitudes, were characterized by a small negative impulse preceding the main positive impulse in the horizontal component, and thus were designated as ^{-}Sc (usually denoted by the symbol Sc^*).

The common type of sudden commencement, observed at lower latitudes,

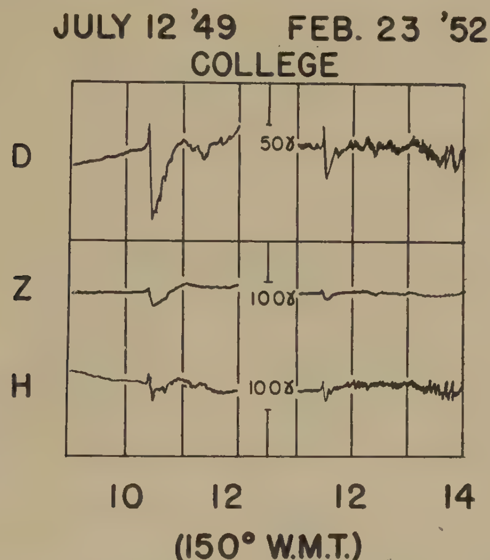

FIG. 2—Sc^{-} in the horizontal and vertical components and the declination at College, Alaska

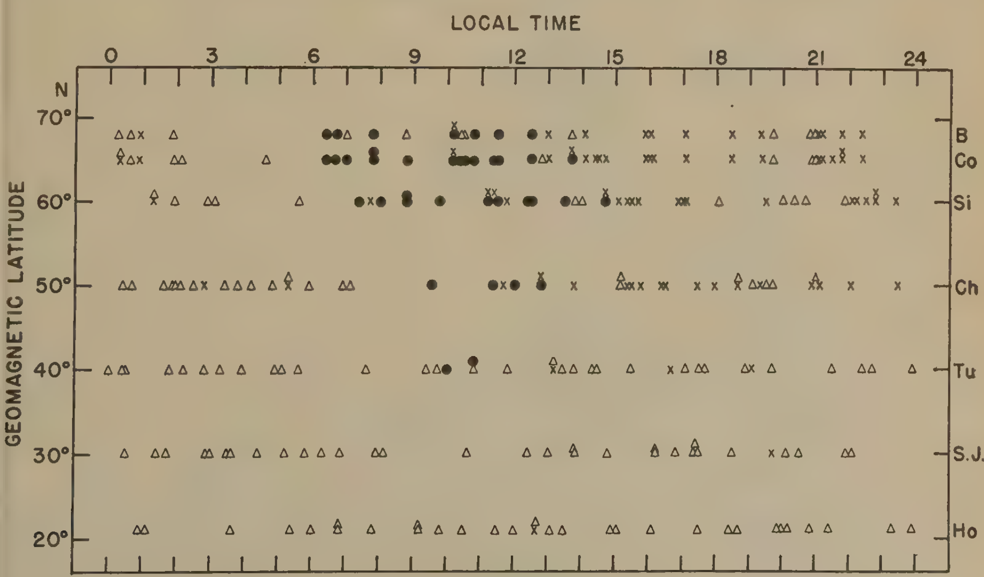

FIG. 3—Three different types of sudden commencement (Δ = Sc, X = ^{-}Sc, and $\cdot$ = Sc^{-}) at Barrow, College, Sitka, Cheltenham, Tucson, San Juan, and Honolulu, plotted against local time of the occurrence

has a single impulse, and is usually designated simply as *Sc*. However, at higher latitudes, this type of sudden commencement does not occur frequently. Only nine storms in the present study showed this single impulse type at all stations.

Fourteen other sudden commencements were of a yet different type at higher latitudes, which I have designated as Sc^-. As shown by the examples in Figure 1, this type of sudden commencement shows a sudden increase in the horizontal component lasting about 1 to 6 minutes, followed by a decrease lasting about 8 to 30 minutes. On June 17, 1951, an Sc^- occurred at stations higher than gm 40°N, although a single *Sc* occurred at San Juan and Honolulu. In the example of September 5, 1951, Barrow and College showed a Sc^-. A ^-Sc occurred clearly at Cheltenham, although the sudden commencement at Sitka showed only a slight decrease. Three other stations show a typical simple *Sc*. Two more examples at College are shown in Figure 2.

In Figure 3, the three different types of sudden commencements (*Sc*, ^-Sc, and Sc^-) at six stations are plotted against their local times of the occurrence. As shown there, Sc^- occurred frequently at higher latitudes during the period

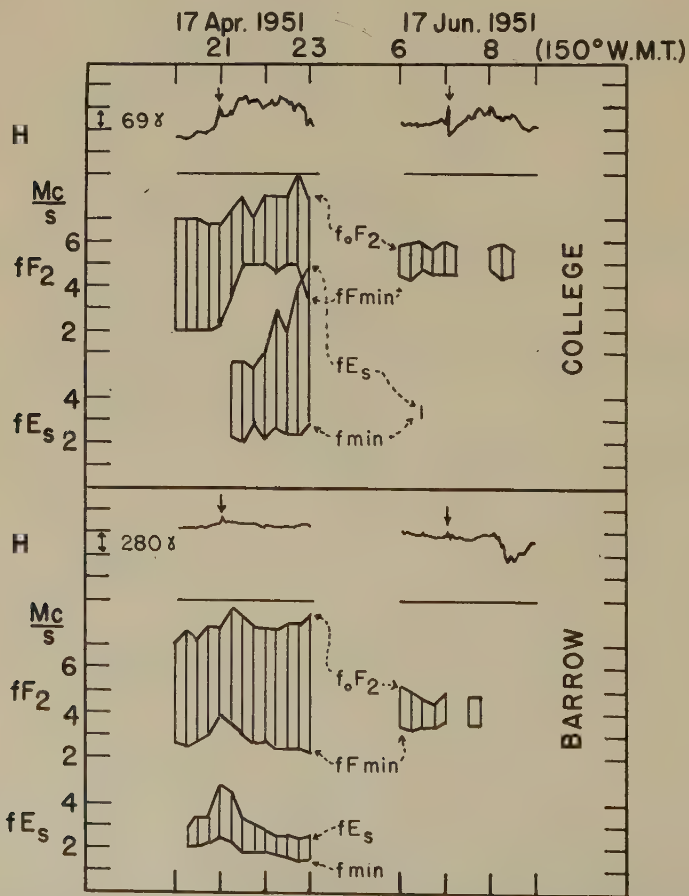

Fig. 4—Sudden commencements of the horizontal component and corresponding ionospheric variations, at Barrow and College, Alaska

from 06^h to 15^h local time. The amplitudes of both increase and decrease impulses were greatest in the zone of 60° to 70° north geomagnetic latitude at about 11^h local time. The decrease may be due to a westward electric current in the upper atmosphere of the earth at the particular location that flows for 8 to 30 minutes after the one to six minutes impulse of the sudden commencement.

Ionospheric variations at Barrow and College, corresponding to sudden commencements of magnetic storms, were also studied. Sometimes a radio blackout or *Es* appearance (or increase) occurred at higher latitudes soon after the occurrence of the sudden commencement, as shown in Figure 4. Several examples among the 26 sudden commencements since January 1951 were discovered in ionograms made at College and Barrow every 15 minutes. These are given in Table 1, which follows.

TABLE 1—*Ionospheric variations at Barrow and College corresponding to sudden commencements of magnetic storms*

Sudden commencement		Ionospheric variation	
Date and time (150°WMT)	Type at *B* and *C**	Time (150°WMT)	Type
14:27, Feb. 26, 1951	^-Sc	*B* 14:27 *C* 14:30	Absorption increases Blackout
20:55, April 17, 1951	*Sc*	*B* 21:00 *C* 21:15	*Es* increases *Es* appears
07:51, June 14, 1951	Sc^-	*C* 08:00	*Es* appears
07:01, June 17, 1951	Sc^-	*B* 07:00–07:30 *C* 07:15–08:00	Blackout Blackout
01:53, Oct. 28, 1951	*Sc*	*B* 02:15–02:30 *C* 02:12–02:42	Absorption increases Blackout
21:32, Mar. 2, 1952	^-Sc	*C* 21:45	Blackout
00:15, Oct. 21, 1952	*Sc*	*C* 00:15	*Es* increases
06:44, Jan. 21, 1956	Sc^-	*B* 06:45 *C* 06:45	*Es* increases *Es* appears
13:42, Mar. 2, 1956	^-Sc	*B* 13:45–14:00 *C* 13:45–14:15	Blackout Blackout

**B* and *C* are Barrow and College.

In conclusion, the author wishes to express his thanks for support of the present study by the Geophysical Research Directorate, Air Force Cambridge Research Center, under contract AF 19(604)-969. He wishes also to express his sincere gratitude to Dr. W. O. Roberts, Mr. A. H. Shapley, Dr. S. Chapman, and Miss

M. B. Wood for their kind help and advice, and to the Central Radio Propagation Laboratories, National Bureau of Standards, for use of magnetograms and ionograms involved in this study and for extending to him the facilities of the Boulder Laboratories.

S. Matsushita

High Altitude Observatory,
University of Colorado,
Boulder, Colorado, October 12, 1956,
On leave from Kyoto University, Kyoto, Japan
(Received October 23, 1956)

COMMENTS CONCERNING THE J. E. HILL AND J. J. GILVARRY ARTICLE, "APPLICATION OF THE BALDWIN CRATER RELATION TO THE SCALING OF EXPLOSION CRATERS"

In a recent paper in this Journal,[1] the origin of the New Quebec crater* was discussed and the authors, although favoring a meteoritic hypothesis themselves, stated that a survey of the site by the Dominion Observatory had failed to produce conclusive evidence. It is the purpose of this Letter to point out that the report[2,3] referred to in the above paper contains the results of a geological and geophysical study, not of the New Quebec crater in Ungava, but of a circular formation, 35 miles in diameter, enclosed by Lakes Manicouagan and Mushalagan, about 150 miles northeast of Seven Islands, Quebec. This study, indeed, suggests considerable doubt about the origin of this latter formation, but this in no way affects any conclusions concerning the New Quebec crater, which is a feature of quite different character.

Recently, Millman[4] has shown that the profile of the New Quebec crater agrees well with the standard form of explosion craters of comparable size. Only in the rim height is there much divergence from the standard profile and this can be explained by glaciation, noted by Harrison,[5] who also pointed out that glacial action is likely to have rendered fruitless any search for meteorite fragments. Routine magnetic observations of the region have been made by W. L. W. Hannaford, of the Division of Geomagnetism, Dominion Observatory, but as yet no systematic search has been made by Observatory personnel to detect magnetic anomalies which might be associated with meteoritic material in or around the crater.

C. S. Beals, *Dominion Astronomer*

Dominion Observatory,
Ottawa, Canada, November 28, 1956
(Received December 1, 1956)

*The crater has been previously referred to as the Ungava Crater and the Chubb Crater. The name New Quebec Crater was adopted by the Canadian Board of Geographical Names, June 3, 1954.

[1]J. E. Hill and J. J. Gilvarry, J. Geophys. Res., 61, 501 (1956).
[2]Sky and Telescope, 14, 374 (1955). [News Notes.]
[3]E. R. Rose, Geological Survey of Canada, Paper No. 55–2 (1955).
[4]P. M. Millman, Pub. Dominion Observatory, 18, 61 (1956).
[5]J. M. Harrison, J. R. Astr. Soc. Can., 48, 16 (1954).

REGARDING THE J. H. MEEK ARTICLE, "A METHOD FOR DRAWING THE GREAT-CIRCLE PATH BETWEEN ANY TWO POINTS ON EARTH"

In a private communication, Mr. W. Galbraith, of the Department of Zoology, Oxford University, has brought to my attention an error in my paper, "A method for drawing the great-circle path between any two points on earth," published in the September 1956 issue (Vol. 61, No. 3, pp. 445-448) of this JOURNAL.

The basic principle (3) was incorrectly quoted from Turner's paper. It is true only for points along the great circle through the center of one grid and parallel to the side common to the adjoining grid. The construction described is correct only for this situation.

As Mr. Galbraith pointed out to me, the great circles from any other points of the first grid diverge in the second grid from equivalent position of that point on the extension of the second grid. This point can be determined by a simple construction if it is not too far from the common boundary, otherwise the direction of the great circle from A through point B in the second grid is found by a proportional construction.

Construction

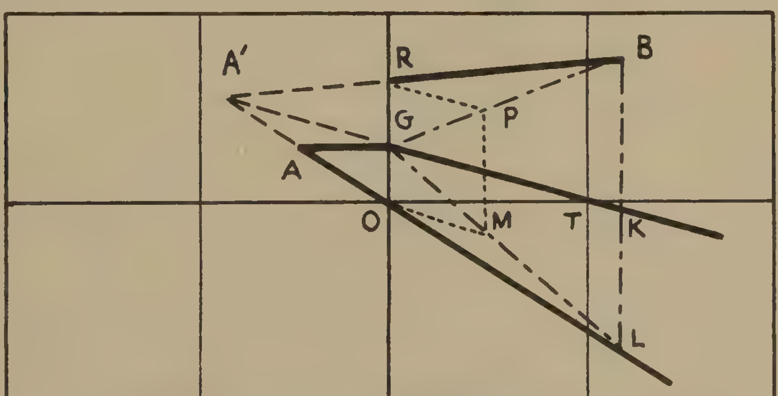

From point A drop a perpendicular to the common boundary. Join its point of intersection (G) to the center of the second grid (T). Join A to the center of the common boundary (O) and produce into the second grid. The intersection of OA and TG produced (A') is the position of A in the second grid. $A'B$ is the required great-circle line in the second grid.

If A' is too far off the chart for construction purposes, the direction of $A'B$ may be found as follows. Drop a vertical line from B cutting GT and AO produced at K, L, respectively. Join GL, GB. Through O draw a straight line parallel to GT cutting GL at M. Draw the vertical from M to cut GB at P. Draw a line through P parallel to TG cutting GO produced at R. R is the point of intersection of the required great circle on the common boundary of the two grids. If point A is on the left-hand half of the grid, the lines GT and AO will converge to the point antipodal to A, to the right of the second grid. Construction must be made to equivalent points on the right-hand boundary of the second grid.

J. H. MEEK

DIRECTORATE OF PHYSICAL RESEARCH (GEOPHYSICS).
DEFENCE RESEARCH BOARD,
Ottawa, Canada, December 13, 1956

(Received December 20, 1956)

ERRATUM IN ARTICLE, "PHYSICAL PROPERTIES OF THE ATMOSPHERE FROM 90 TO 300 KILOMETERS"

Attention was called by Mr. F. S. Johnson[1] to the fact that Figure 2 of the article, "Physical properties of the atmosphere from 90 to 300 kilometers," published in the September 1956 issue (Vol. 61, No. 3, p. 520) of this Journal, did not agree with the density values given in Table 1. Upon checking the illustrative figure, it was found that by mistake of the authors the wrong figure had been included. The correct Figure 2, consistent with Tables 1 and 2 and with the text, is given below.

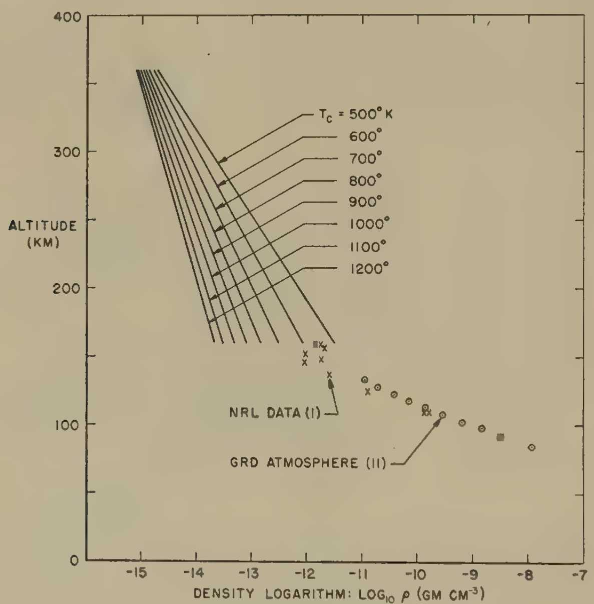

FIG. 2
ALLOWABLE VALUES AND SLOPES FOR DENSITY CURVE AT CRITICAL ALTITUDE

H. K. Kallmann*
W. B. White**
H. E. Newell, Jr.***

*Institute of Geophysics, University of California,
Los Angeles, California, December 13, 1956;
**The Rand Corporation,
Santa Monica, California;
***Naval Research Laboratory,
Washingron, D. C.

(Received December 15, 1956)

[1]Present address: Missile Systems Division, Lockheed Aircraft Corporation, Van Nuys, California.

LARGE INCREASE OF COSMIC-RAY INTENSITY FOLLOWING SOLAR FLARE ON FEBRUARY 23, 1956

In a Letter to Editor* under the above title, the increase of cosmic-ray intensity during the solar flare of February 23, 1956, was shown graphically for Cheltenham and Godhavn. The increase observed at Huancayo and at Ciudad Universitaria, Mexico, D.F., was briefly described on the basis of preliminary reports. The purpose of this note is to correct errors on the graph for Godhavn, which arose from typographical mistakes in the cabled results, and to provide details of the increase at Huancayo, Mexico, and Christchurch. Figure 1 herewith shows the results for five stations. The lengths of the horizontal bars through the points in Figure 1 indicate the time interval over which the intensity was averaged.

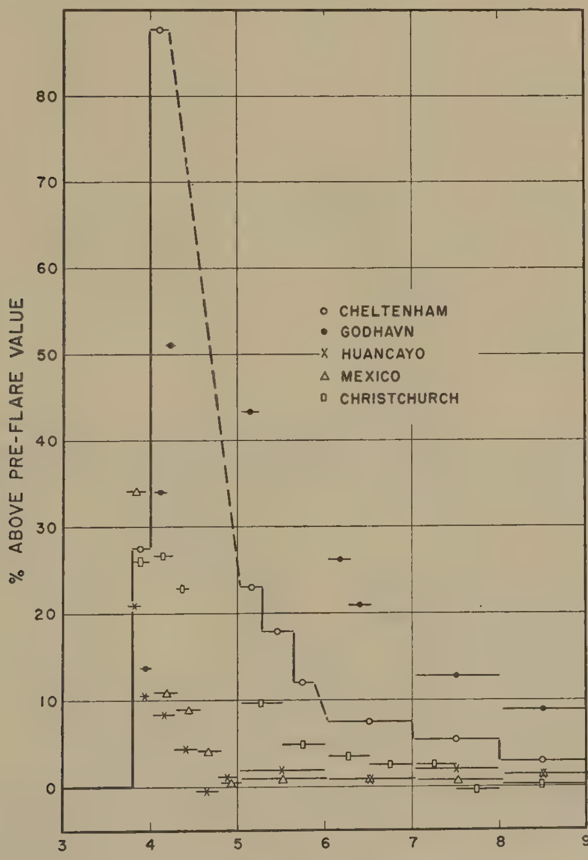

FIG. 1-COSMIC-RAY INTENSITY FOLLOWING SOLAR FLARE AT 0330 GMT, FEBRUARY 23, 1956

For each of five stations, Table 1 gives the values of cosmic-ray ionization (in units of 0.1 per cent) for each of the indicated GMT time intervals. The standard deviation of hourly values is about 0.7 per cent, which barely warrants tabulating

*S. E. Forbush, J. Geophys. Res., 61, 155-156 (1956).

Table 1. Cosmic-ray ionization between 00 00 and 12 00 GMT February 23, 1956[1]

Godhavn		Cheltenham		Mexico		Huancayo		Christchurch	
GMT h m h m	0.1%	GMT h m h m	0.1%	GMT h m h m	0.1%	GMT h m h m	0.1%	GMT h m h m	0.1%
00 03- 01 00	+ 4	00 02 - 01 00	- 9	00 04 - 01 02	+ 6			00 03 - 01 00	- 5
01 03 02 00	- 6	01 02 02 00	0	01 04 02 02	- 1	01 02 - 01 59	0	01 03 02 00	- 2
02 03 03 00	+ 4	02 02 03 00	+ 6	02 04 03 02	- 5	02 02 02 59	+ 6	02 03 03 00	+ 1
03 03 03 53	- 1	03 02 03 48	+ 2	03 04 03 44	- 1	03 02 03 45	- 5	03 03 03 48	+ 7
03 53[2] 04 00	+136	03 48[2] 04 00	+277	03 44[2] 03 57	+340	03 45[2] 03 54	+204	03 48[2] 04 00	+266
						03 54 03 59	+100		
04 03 04 12	+333	04 02 04 12	+878	04 04 04 19	+108	04 02 04 17	+ 78	04 03 04 16	+273
04 12 04 17	+509			04 19 04 34	+ 88	04 17 04 32	+ 38	04 16 04 26	+235
				04 34 04 49	+ 40	04 32 04 47	- 10		
				04 49 05 02	+ 4	04 47 04 59	+ 6		
05 03 05 15	+432	05 02 05 17	+232	05 04 06 02	+ 7	05 02 05 59	+ 14	05 03 05 31	+103
		05 17 05 39	+181					05 31 06 00	+ 55
		05 39 05 52	+122						
06 03 06 17	+260	06 02 07 00	+ 76	06 04 07 02	+ 8	06 02 06 59	+ 4	06 03 06 31	+ 42
06 17 06 32	+208							06 31 07 00	+ 32
07 03 08 00	+126	07 02 08 00	+ 55	07 04 08 02	+ 6	07 02 07 59	+ 15	07 03 07 31	+ 32
								07 31 08 00	+ 4
08 03 09 00	+ 87	08 02 09 00	+ 31	08 04 09 02	+ 13	08 02 08 59	+ 9	08 03 09 00	+ 9
09 03 10 00	+ 65	09 02 10 00	+ 26	09 04 10 02	+ 7	09 02 09 59	+ 8	09 03 10 00	+ 9
10 03 11 00	+ 42	10 02 11 00	+ 16	10 04 11 02	+ 5	10 02 10 59	+ 15	10 03 11 00	+ 14
11 03 12 00	+ 29	11 02 12 00	+ 15	11 04 12 02	+ 7	11 02 11 59	+ 14	11 03 12 00	+ 9

1) Tabular values are departures of the average for the indicated interval. (in units of 0.1%) from the average for 4 hrs. preceding the increase.
2) Estimated time for start of increase.

Note: For 2 or 3 minutes near beginning of hour electrometer needle is earthed.

these to 0.1 per cent; nevertheless, the values for shorter intervals are also given to 0.1 per cent to avoid confusion. Table 1 also includes the estimated GMT at which the increase commenced. These times are probably not in error by more than one minute.

Scott E. Forbush

Department of Terrestrial Magnetism,
Carnegie Institution of Washington,
Washington 15, D. C., January 11, 1957
(Received January 11, 1957)

EMISSION FROM SODIUM VAPOR EJECTED INTO THE EARTH'S ATMOSPHERE AT NIGHT

At 1042 PM on 1 November 1956, 2 kilograms of sodium metal were ejected in vapor form into the earth's atmosphere from 60 to 140 km along the trajectory of an Aerobee rocket. An easily visible yellow glow and persistent trail were observed. Measurements of the altitude and the intensity of the emission were obtained from photometric measurements and simultaneous two-site photography with Super-Schmidt cameras which recorded the emission over the entire 80-km region. At 60 km, the glow was visible and a dim persistent trail was photographed.

The brightness of the glow and the trail decreased with altitude until at about 90 km neither were visible, although the glow was photographed. Around 90 km, the glow brightened and, at 105 km, a very bright glow and long persistent trail were observed. The glow decreased approximately exponentially with altitude, dimming to below the visibility limit at 120 km. Portions of the trail persisted for about 30 seconds. Between 120 km and 135 km, no emission was observed visually, but a very dim glow was photographed. At about 140 km, the glow was again very bright and persistent. Since this is the peak of the rocket trajectory, variations of brightness with altitude for this region are not available. However, both photometric and visual observations indicate that the highest region was the brightest, having a surface brightness of 10^{11} photon/cm^2. Also, it is known from the photometer record that the emission at all altitudes was primarily sodium D at 5890A.

Considering current knowledge and theories concerning atmospheric sodium and the sodium airglow, the observations in the lower regions are not surprising. The significance of this observation is that the variation of the excitation process with altitude has now been measured. Although the results do not allow a unique determination of the exact process which is acting, the observations agree with the proposals which consider the vertical distribution of molecular and atomic oxygen to be of primary importance for the explanation of the sodium night glow.

The emission from the 140-km region and the 105-km region cannot be due to the same process. The brightness of the emission in the upper region clearly shows that the tenuous high atmosphere can extract and store relatively large amounts of solar energy. Preliminary laboratory experiments indicate that sodium vapor in the presence of active nitrogen produces a relatively intense emission. Because of the low density at 140 km, the chemi-luminescent reactions which produce the emission must be of the two-body type. The necessary energy might be obtained by formation of N_2 ; cross-sections and reaction rates for such processes are not well known. Alternately, and more probably, the energy may be obtained from metastable states of atmospheric constituents such as the 2D state of atomic nitrogen, although little knowledge is available on the abundance of such states at 140 km.

The observations indicate that three different excitation processes are operating at different altitudes. If by further experiment the specific processes can be determined, this experimental method may lead to a measure of the density and distribution of the constituents involved in this region of the atmosphere.

John F. Bedinger and Edward Manring

Geophysical Research Directorate,
U.S. Air Force Cambridge Research Center,
Bedford, Massachusetts, February 25, 1957
(Received February 28, 1957)

NOTES

(1) *IGY observations of the ionosphere*—A group of scientists has left the Boulder Laboratories of the National Bureau of Standards for a year in the Antarctic, where they will operate five widespread research stations. The men at each post will collect continuous data with the C-4 ionosphere recorder, an instrument that beams short pulses into the upper atmosphere, measuring the time required for them to travel there and back. A range of from 1 to 25 megacycles is covered in 15 seconds. A reading will be made automatically at least every 15 minutes. The same kind of ionospheric observations will be carried out by scientists working simultaneously in more than 75 such stations located throughout the world as part of the International Geophysical Year program.

(2) *Centenary of the birth of Sir J. J. Thomson*—On December 18, 1956, the centenary of the birth of one of the most remarkable physicists of our time was celebrated. He proved wise and skilled as an administrator in his Mastership of Trinity College. He was a specialist in the field of electric discharge in gases. Important, too, was his part in building up the great school of physics at the Cavendish Laboratory at Cambridge University.

(3) *Announcement of Committee on Extension to the Standard Atmosphere*—A new extension to the 20-km ICAO Standard Atmosphere (the accepted U.S. standard) is being adopted by about 23 United States scientific and engineering organizations. This extension provides tables of atmospheric parameters up to 300 km. Because of their great need for such tables and because many have active high-altitude research programs, these organizations met in November 1953 to seek agreement upon a single representation of the atmosphere compatible with the best available data. The United States Weather Bureau of the Department of Commerce and the Geophysics Research Directorate, Air Force Cambridge Research Center of the Air Research and Development Command co-sponsored this movement. Extensive tables expanding the basic framework are currently under preparation at the Geophysics Research Directorate and will follow closely the format of the ICAO Standard Atmosphere which appears as ICAO Document 7488, NACA TN 3182, and NACA Report 1235; moreover, additional information, important at higher altitudes, such as gravity ratio and molecular weight, will be included. Supplemental information to describe the variability of the atmosphere and other parameters will be issued later as appendices. Preliminary copies of these tables, in a form analogous to the NACA TN 3182 should be available in limited quantities during 1957. It is planned to have the final edition printed by the United States Government Printing Office, and made available to the public through the Superintendent of Documents, Washington, D.C. Efforts will be made to obtain international acceptance for the lowest portion (20 to 32 km) of the tables.

(4) *Thirty-eighth annual meeting of the American Geophysical Union*—The thirty-eighth annual meeting of the American Geophysical Union will be held in Washington, D.C., April 29-May 1, 1957. The plans of the various Sections are now materializing, and it is anticipated that all Sections will have meetings.

There will also be general meetings of the Union as a whole, including a Smoker on the evening of April 29, a general evening session of the Bowie Medal Award on the evening of April 30, and a general session in the afternoon of May 1.

(5) *Eleventh General Assembly of the International Union of Geodesy and Geophysics*—The eleventh general assembly of the I.U.G.G. will be held in Toronto, Canada, September 3-14, 1957. The seven Associations composing the Union are now formulating their plans and programs for this triennial meeting.

(6) *Symposium on Systems for Information Retrieval*—The School of Library Science of Western Reserve University, in conjunction with its Center for Documentation Research, will present on April 15, 16, and 17, 1957, the United States first comprehensive demonstration of systems presently in use for the organization, storage, and retrieval of recorded information, together with a symposium on information-handling problems and technique. Co-sponsor of these activities is the Council on Documentation Research, a group recently formed by representatives of organizations in government, industry, and education for the stimulation of effective cooperation among those who produce, organize, and use information of all types in all fields.

(7) *Sesquicentennial of the United States Coast and Geodetic Survey*—The 150th anniversary of the founding of the United States Coast and Geodetic Survey will be observed during 1957 with issuance of a commemorative postage stamp, dinners, and meetings of scientific groups. Open house will be observed at the Survey headquarters in the Commerce Department, Washington, D.C., on May 20, 1957. The Survey was established on February 10, 1807, under President Thomas Jefferson, and was the first technical bureau in the Federal Government.

(8) *Geomagnetic activities of the United States Coast and Geodetic Survey*—One volume of the MHV series of publications was issued, giving magnetic hourly values and reproductions of magnetograms, year 1952, for Tucson.

Colonel Alejandro Forch of Chile, Sr. Augusto Llano of Chile, and Mr. Radomir Turajlic of Yugoslavia have been studying the methods and procedures of the Coast and Geodetic Survey in office and field work in geomagnetism.

(9) *New section of sun-earth relationships, Boulder Laboratories, National Bureau of Standards*—A new section of sun-earth relationships at the Boulder Laboratory of the National Bureau of Standards, in charge of Alan H. Shapley, radio physicist and vice-president of the U.S. National Committee for the IGY, has been announced. The section will centralize work that Shapley has been engaged in at Boulder, Colorado, for some time. It will also permit a more closely coordinated program in the study of the sun and its effects on radio communication, the use of geophysical data to forecast short-wave radio communication conditions, and the scientific coordination of the many Bureau field-stations that are making radar-type observations of the upper atmosphere.

(10) *Spring meeting of URSI*—The spring meeting of the International Scientific Radio Union (URSI) is scheduled this year for the Hotel Willard in Washington, D.C., on May 22-25, 1957. The anticipated co-sponsors this year will include the IRE Professional Groups on Antennas and Propagation, and on Microwave Theory and Techniques. A combined technical session of interest to all participants is scheduled for the morning of May 23, to be followed by one or more sessions in each

of the following fields: Commission 1—Radio Measurements and Standards; Commission 2—Radio and Troposphere; Commission 3—Ionospheric Radio; Commission 4—Radio Noise of Terrestrial Origin; Commission 5—Radio Astronomy; Commission 6—Radio Waves and Circuits; and Commission 7—Radio Electronics.

(11) *Twelfth General Assembly of URSI*—By invitation of the U.S.A. National Committee of the International Scientific Radio Union (URSI) and the National Academy of Sciences, the XIIth General Assembly of URSI will be held at Boulder, Colorado, August 22 to September 5, 1957. Local hosts will include the University of Colorado, the Boulder Laboratories of the National Bureau of Standards, the High Altitude Observatory, and the City of Boulder. Headquarters for the Assembly and rooms for the technical sessions will be in the Memorial Center of the University of Colorado. Facilities will also be provided in the Boulder Laboratories of the National Bureau of Standards. Meetings of the General Assembly are held every three years, rotating among the member nations of the Union. This is the second in the United States of America, the 1927 meeting have been in Washington, D.C.

(12) *Personalia*—Prof. *Sydney Chapman* was appointed Gauss professor of geophysics of the Academy of Sciences at Göttingen for 1956-57. This professorship was founded in connection with the celebration of the Gauss centenary.

Dr. *Ernest H. Vestine*, formerly Chairman of the Section of Analytical Geophysics, Department of Terrestrial Magnetism, Carnegie Institution of Washington, has accepted a position with the RAND Corporation, of Santa Monica, California. During the latter half of 1956, on leave of absence from the Carnegie Institution, he headed the newly-created Data Coordination Center for the International Geophysical Year, 1957-58, with offices in the National Academy of Sciences, Washington, D.C.

Dr. *Thorndike Saville*, dean of the New York University College of Engineering for the last 20 years, has announced that he will retire with the start of the 1957 fall term, one year ahead of the time set by the University for retirement of faculty members. He will then act in a private advisory capacity as consultant in the fields of his authority—water supply, hydrology, and coastal engineering. Dr. Saville has been a leader not only in engineering education but also in the engineering profession.

Dr. *Charles E. Bunnell*, formerly president (1935-40) of the University of Alaska, died on November 1, 1956, at the age of 78. He was the first president of the Alaska Agricultural College and School of Mines (now University of Alaska), 1922-35.

Dr. *Gustave J. H. Swoboda* died at Geneva, Switzerland, on September 4, 1956, at the age of 63. He was widely known as the administrative head of the pre-war International Meteorological Organization. At the time of his death, he was professor of meteorology at Istanbul, Turkey.

(13) *Corrigendum*—In printing Dr. S. K. Runcorn's corrigendum in the December 1956 issue of this Journal, page 758, the designation "I25d" was inadvertently omitted *following* the dittoed words "should be" in line 4 of the listed correct declinations and inclinations. Also the Imnaha River series were prefixed by "I", which in the Journal was erroneously printed as "1".

LIST OF RECENT PUBLICATIONS

BY W. E. SCOTT

Department of Terrestrial Magnetism,
Carnegie Institution of Washington,
Washington 15, *D.C.*

(Received January 4, 1957)

A—*Terrestrial Magnetism*

ALLCOCK, G. McK., AND L. H. MARTIN. Simultaneous occurrence of 'dawn chorus' at places 600 km. apart. Nature, **178**, 937-938 (Oct. 27, 1956). [Letter to Editor.]

ALMOND, M., AND J. A. CLEGG. Remanent magnetism of some dolerites, basalts and volcanic tufts from Tasmania. Phil. Mag., Ser. 8, **1**, No. 8, 771-782 (1956).

AMBERLEY OBSERVATORY, Magnetic results for 1954. Wellington, R. E. Owen, Govt. Printer, 56 pp. (1955).

BARTELS, J., AND J. VELDKAMP. International data on magnetic disturbances, second quarter, 1956. J. Geophys. Res., **61**, No. 4, 741-743 (1956).

BLOEMBERGEN, N. Magnetic resonance in ferrites. Proc. Inst. Radio Eng., **44**, No. 10, 1259-1269 (1956).

BODLE, R. R. Cheltenham three-hour-range indices *K* for July to September, 1956. J. Geophys. Res., **61**, No. 4, 744 (1956).

BOUŠKA, J. Distribution of the geomagnetic field in Bohemia and Moravia-Silesia (epoch 1950.0). Geofysikální sborník, No. 20-35, 222-223 (1956). [Memorial issue in honor of Dr. B. Šalamon's 75th anniversary.]

CLEGG, J. A., E. R. DEUTSCH, AND D. H. GRIFFITHS. Rock magnetism in India. Phil. Mag., **1**, No. 5, 418-431 (1956).

DAS, A. K. Effect of lightning discharges on magnetographs. Nature, **178**, 815 (Oct. 13, 1956).

DUCLAUX, F., J. L. BUREAU, B. LEPRÊTRE, M. VADELL, ET R. WILL. Valeurs moyennes horaires du champ magnétique terrestre, Tamanrasset 1953-1954. L'Institut de Météorologie et de Physique du Globe de l'Algérie, Fasc. No. 15, 33-38 (March 1956).

DUDLEY, J. D. Penetration of a time-dependent magnetic field through a thin conducting layer of spherical shape. Salt Lake City, University of Utah, Dept. of Phys., Tech. Rep. No. 22, 29 pp. + 2 figs., mim. (Oct. 1, 1956).

EGEDAL, J. On the computation of lunar daily variations in geomagnetism. Two simple methods. Pub. Danske Meteorol. Inst., comm. magnétiques, No. 22, 25 pp. (1956).

EGEDAL, J. The lunar-diurnal magnetic variation and its relation to the solar-diurnal variation. J. Geophys. Res., **61**, No. 4, 748-749 (1956). [Letter to Editor.]

ESPERSEN, J., P. ANDREASEN, J. EGEDAL, AND J. OLSEN. Measurements at sea of the vertical gradient of the main geomagnetic field during the *Galathea* Expedition. J. Geophys. Res., **61**, No. 4, 593-624 (1956).

FOUREY, A. Declinaison magnétique a El Abiod Sidi Cheikh de 1948 à 1954. L'Institut de Météorologie et de Physique du Globe de l'Algérie, Fasc. No. 15, 39-44 (March 1956).

GIORGI, M., E F. MOLINA. La variazione "Sq" all'Osservatorio di Gibilmanna. Ann. Geofis., Roma, **9**, No. 1, 17-30 (1956). [Abstract in English.]

GRAHAM, J. W. Paleomagnetism and magnetostriction. J. Geophys. Res., **61**, No. 4, 735-739 (1956).

HERMANUS MAGNETIC OBSERVATORY. Magnetic observations, 1951-1952. Govt. Printer, Pretoria, 112 pp. (1953-6) 31 cm.

Hermanus Magnetic Observatory. The secular variation programme of the Hermanus Magnetic Observatory (Officer in charge: A. M. Van Wijk). Progress report, 1953. Results of observations at the secular variation field stations in South Africa, 1952-53. Pretoria, Govt. Printer, 34 pp. + charts (rec'd Sept. 18, 1956).

Helwan Observatory. Magnetic report for the year 1945. Published under the direction of Prof. A. H. Samaha, Director of Helwan Observatory. Cairo University Press, 23 pp. (1955). 34 cm.

Helwan Observatory. Magnetic report for the year 1946. Published under the direction of Prof. A. H. Samaha, Director of Helwan Observatory. Cairo University Press, 25 pp. (1955). 34 cm.

Istanbul-Kandilli Observatory. Annuaire magnétique, année 1950. Observatoire Astronomique et Géophysique d'Istanbul-Kandilli, Service du Magnétisme Terrestre, 58 pp. (1955). 28 cm.

Istanbul-Kandilli Observatory. Annuaire magnétique, année 1954. Observatoire Astronomique et Géophysique d'Istanbul-Kandilli, Service du Magnétisme Terrestre, 56 pp. (1955). 28 cm.

Kato, S. Horizontal wind systems in the ionospheric E region deduced from the dynamo theory of the geomagnetic S_q variation. Part II. Rotating earth. Kyoto, J. Geomag. Geoelectr., **8**, No. 1, 24-37 (1956).

Knapp, D. G. Arctic aspects of geomagnetism. Chief of Naval Operations for Polar Projects, U. S. Navy, Pub. No. OPNAV P03-10, 65 pp. (1956).

Maeda, H. Horizontal wind systems in the ionospheric E region deduced from the dynamo theory of the geomagnetic S_q variation. Part I—Non-rotating earth. [For Part II, see S. Kato.] Kyoto, J. Geomag. Geoelectr., **7**, No. 4, 121-132 (1955).

Maeda, H. Daily variations of the electrical conductivity of the upper atmosphere as deduced from the daily variations of geomagnetism, Part II. Non-equatorial regions. Rep. Ionosphere Res. Japan, **10**, No. 2, 49-68 (1956).

Mauersberger, P. Zur Bestimmung des äusseren Anteils des geomagnetischen Haupt feldes. Beitr. Geophysik, **65**, Heft 3, 191-206 (1956).

Mauersberger, P. Das Mittel der Energiedichte des geomagnetischen Hauptfeldes an der Erdoberfläche und seine säkulare Änderung. Beitr. Geophysik, **65**, Heft 3, 207-215 (1956).

McDonald, K. L. Penetration of the secular field through a mantle with variable conductivity. Part II. Salt Lake City, University of Utah, Dept. of Phys., Tech. Rep. No. 21, 40 pp. + 15 figs., mim. (Aug. 1, 1956).

Nagata, T., and M. Ozima. Anomalous increase in thermo-remanent magnetization of ferromagnetic minerals—Magnetic interaction between different constituents in ferromagnetic minerals. J. Geomag. Geoelectr., **7**, No. 4, 105-120 (1956).

Nairn, A. E. M. Relevance of paleomagnetic studies of Jurassic rocks of continental drift. Nature, **178**, 935-936 (Oct. 27, 1956). [Letter to Editor.]

Namikawa, T. Magneto-hydrodynamic oscillations of a conducting liquid mass rotating in a uniform magnetic field. J. Geomag. Geoelectr., **7**, No. 4, 97-104 (1955).

Niemegk, Adolf-Schmidt-Observatorium. Ergebnisse der Beobachtungen am Adolf-Schmidt-Observatorium für Erdmagnetismus in Niemegk in den Jahren 1946 bis 1950 (bearbeitet von G. Fanselau und H. Wiese). Berlin, Geomag. Inst. u. Obs. Potsdam/Niemegk, 123 pp. (1956). [Published under the auspices of the Meteorologischer Dienst der Deutschen Demokratischen Republik.]

Niemegk, Adolf-Schmidt Observatorium. Ergebnisse Jahrbuch 1953 mit wissenschaftlichen Mitteilungen (bearbeitet von H. Wiese). Berlin, Geomag. Inst. u. Obs. Potsdam/Niemegk, 127 pp. (1956). [Published under the auspices of the Meteorologischer Dienst der Deutschen Demokratischen Republik.]

Oguti, T. Notes on the morphology of SC. Rep. Ionosphere Res. Japan, **10**, No. 2, 81-90 (1956); also Geophys. Notes, **9**, No. 1 (1956).

Parker, E. N. On the geomagnetic storm effect. J. Geophys. Res., **61**, No. 4, 625-637 (1956).

Piddington, J. H. Hydromagnetic wave in ionized gas. M. Not. R. Astr. Soc.. **115**, No. 6, 671-683 (1956).

Pratap, R. The effect of inclination of the geomagnetic axis on the *Sq* variations. Bull. Calcutta Math. Soc., **47**, No. 2, 115-124 (1956).

Průhonice Observatory. Výsledky Geomagnetických Měření na Observatoři Průhonice u Prahy za Rok 1954. Československ. Akad. Věd, Geofys. Ustav, 107 pp. (1956).

Quetta, Geomagnetic Observatory. Annual summary of geomagnetic observations at Quetta, 1953-1954 (S. N. Naqui, director; S. A. A. Kazmi, officer-in-charge). Pakistan Meteorological Service, Geophys. Rev., **1**, Pt. II—Geomagnetism, No. 4, 121 pp. (1955). 24 cm.

Rao, V. B. Magnetic properties of magnetite. Geophysics, **21**, No. 4, 1100-1110 (1956).

Rikitake, T. Magneto-hydrodynamic oscillations of a conducting fluid sphere under the influence of the Coriolis force. Bull. Earthquake Res. Inst., Tokyo Univ., **34**, Pt. 2, 139-156 (1956).

Roche, A. Sur la date de la dernière inversion du champ magnétique terrestre. Paris, C.-R. Acad. sci., **243**, No. 11, 812-814 (1956).

Romañá, A., y J. O. Cardús. La amplitud de la variación magnetica diurna en las proximidades del Ecuador. Observatorio del Ebro, Misc. Pub. No. 14, 40 pp. (1955).

San Fernando. Anales del Instituto y Observatorio de Marina publicados de orden de la superioridad. Seccion 3—Observaciones meteorológicas y magnéticas correspondientes a los años 1951-1952. San Fernando, Imprenta del Observatorio de Marina, iii + 76, iii + 76 (1956). 34 cm.

San Fernando, Anales del Instituto y Observatorio de Marina publicados de orden de la superioridad. Seccion 3—Observaciones meteorológicas y magnéticas correspondientes a los años 1953-1954. San Fernando, Imprenta del Observatorio de Marina, iii + 76, iii + 76 (1956). 34 cm.

Shotton, F. W. Some aspects of the New Red desert in Britain. Liverpool and Manchester Geol. J., **1**, Pt. 5, 450-465 (1956). [See p. 452 relating to position of magnetic poles.]

Tamanrasset, Magnétisme terrestre à Tamanrasset de 1948 à 1952. L'Institut de Météorologie et de Physique du Globe de l'Algérie, Fasc. No. 14, 1-12 (January 1956).

Tandon, J. N. Geomagnetic activity and solar *M*-regions for the current epoch of the sunspot minimum. Indian. J. Phys., **30**, No. 4, and Proc. Indian Assoc. Cultivation Science, **39**, No. 4, 153-168 (1956).

Tromsø, Auroral Observatory. Observations 1954. Bergen, Norska Inst. Kosmisk Fysikk, No. 38, 43 pp. (1956). [Contains results of magnetic, ionospheric, and ozone observations for the year 1954; also annual means of *D*, *H*, and *Z* for the years 1930-1954.]

Van Vleck, J. H. Fundamental theory of ferro- and ferri-magnetism. Proc. Inst. Radio Eng., **44**, No. 10, 1248-1258 (1956).

Volland, H. Zur Theorie des Sonnenfinsternis-Effektes im Erdmagnetfeld. J. Atmos. Terr. Phys., **9**, Nos. 2/3, 131-143 (1956).

Whitham, K., and E. I. Loomer. The diurnal and annual motions of the north magnetic dip pole. J. Atmos. Terr. Phys., **8**, No. 6, 349-351 (1956). [Research note.]

Wiese, H. Tiefentellurik (Erforschung von grossräumigen Zonen erhöhter elektrischer Leitfähigkeit im Erdinneren durch erdmagnetische Variationen). Abh. Geomag. Inst. u. Obs. Potsdam-Niemegk, 36 pp. (1956). [Published under the auspices of the Meteorologischer Dienst der Deutschen Demokratischen Republik.]

Yokoyama, I. Geomagnetic studies of Volcano Mihara. 7th paper. (Possible thermal process related to changes in the geomagnetic field.) Bull. Earthquake Res. Inst., Tokyo Univ., **34**, Pt. 1, 21-32 (1956).

Zmuda, A. J., and J. F. McClay. A method of interpolating magnetic data under conditions of mutual consistency. J. Geophys. Res., **61**, No. 4, 667-672 (1956).

B—*Terrestrial Electricity*

Clarke, C., and B. J. Byrne. The location of thunderstorms by a single-station high-frequency ranging technique. J. Atmos. Terr. Phys., **9**, No. 4, 210-228 (1956).

Hepburn, F. Man's study of lightning. Sci. Prog., **44**, No. 176, 635-646 (1956).

Schonland, B. F. J. The lightning discharge. (Reprint from Handbuch der Physik, Edited by S. Flügge.) Springer-Verlag, Berlin, **22**, 576-628 + 43 figs. (1956).

C—*Cosmic Rays*

Aarons, J., and W. R. Barron. Sudden absorption of atmospherics due to increase in cosmic ray intensity. Nature, 178, 277-278 (Aug. 4, 1956). [Letter to Editor.]

Barut, A. O. Anisotropy of cosmic rays due to galactic rotation. Nuovo Cimento, **4**, No. 3, 661-665 (1956).

Biermann, L. Der Ursprung der Kosmischen Strahlung. Phys. Bl., **12**, Heft 9, 396-402 (1956).

Brown, R. R. Time variations of cosmic-ray intensity. J. Geophys. Res., **61**, No. 4, 639-646 (1956).

Danielson, R. E., P. S. Freier, J. E. Naugle, and E. P. Ney. Heavy primary cosmic radiation at the equator. Phys. Rev., **103**, No. 4, 1075-1081 (1956).

Elliott, H., and P. Rothwell. The solar daily variation of the cosmic ray intensity. Phil. Mag., Ser. 8, **1**, No. 7, 669-676 (1956).

Elsasser, W., E. P. Ney, and J. R. Winckler. Cosmic-ray intensity and geomagnetism. Nature, **178**, 1226-1227 (Dec. 1, 1956).

Fowler, P. H., and C. J. Waddington. The energy distribution of cosmic ray particles over northern Italy. Phil. Mag., Ser. 8, **1**, No. 7, 637-650 (1956).

Hoyle, F. Suggestion concerning the nature of the cosmic-ray cutoff at sunspot minimum. Phys. Rev., **104**, No. 1, 269-270 (1956). [Letter to Editor.]

Jory, F. S. Selected cosmic-ray orbits in the earth's magnetic field. Phys. Rev., **103**, No. 4, 1068-1075 (1956).

Koshiba, M., and M. Schein. Time variation of primary heavy nuclei in cosmic radiation. Phys. Rev., **103**, No. 6, 1820-1824 (1956).

Maeda, K. Atmospheric latitude effect on cosmic radiation. Rep. Ionosphere Res. Japan, **10**, No. 1, 9-14 (1956).

Parker, E. N. Modulation of primary cosmic-ray intensity. Phys. Rev., **103**, No. 5, 1518-1533 (1956).

Ray, E. C. Effects of a ring current on cosmic radiation. II. Impact zones. Iowa City, State University of Iowa, Dept. of Phys., Pub. SUI-56-13, 14 pp. + table + 2 figs., mim. (August 1956).

Tandberg-Hanssen, E. On the interpretation of sudden decreases in cosmic rays from the sun. Astroph. Norvegica, **5**, No. 9, 241-258 (1956).

Winckler, J. R. Cosmic-ray increase at high altitude on February 23, 1956. Phys. Rev., **104**, No. 1, 220 (1956).

D—*Upper Air Research*

Aarons, J. Low frequency electromagnetic radiation 10-900 cycles per second. J. Geophys. Res., **61**, No. 4, 647-661 (1956).

Australia, Commonwealth of. Ionospheric predictions series H handbook for use with publications of the Ionospheric Prediction Service. Dept. of the Interior, Pub. IPS-H1, 22 pp., mim. (Oct. 1956).

Banerjee, S. S., and P. G. Surange. Scattering of radio waves and the horizontal gradient of ionization in the ionosphere. Science and Culture, **21**, No. 12, 750-753 (1956). [Letter to Editor.]

Baral, S. S. Ionospheric prediction methods and the probable sources of error. Indian J. Phys., **30**, No. 4, and Proc. Indian Assoc. Cultivation Science, **39**, No. 4, 189-205 (1956).

Barber, N. F. A correlation treatment of fading signals. J. Atmos. Terr. Phys., **8**, No. 6, 318-330 (1956).

Bates, D. R., and B. L. Moiseiwitsch. Origin of the Meinel hydroxyl system in the night airglow. J. Atmos. Terr. Phys., **8**, No. 6, 305-308 (1956).

Berg, O. E., and L. H. Meredith. Meteorite impacts to altitude of 103 kilometers. J. Geophys. Res., **61**, No. 4, 751-754 (1956). [Letter to Editor.]

Berthier, P. Étude spectrophotométrique de la luminescence nocturne des bandes des molécules OH et O_2 atmosphérique. Ann. Géophys., **12**, No. 2, 113-143 (1956).

Beynon, W. J. G., and J. O. Thomas. The calculation of the true heights of reflection of radio waves in the ionosphere. J. Atmos. Terr. Phys., **9**, No. 4, 184-200 (1956).

OOKER, H. G. Turbulence in the ionosphere with applications to meteor-trails, radio-star scintillation, auroral radar echoes, and other phenomena. J. Geophys. Res., **61**, No. 4, 673-705 (1956).

OOKER, H. G., AND R. COHEN. A theory of long-duration meteor-echoes based on atmospheric turbulence with experimental confirmation. J. Geophys. Res., **61**, No. 4, 707-733 (1956).

ROWN, R. A. Lunar variations of the *F*2 layer at Ibadan. J. Atmos. Terr. Phys., **9**, Nos. 2/3, 144-154 (1956).

HAMBERLAIN, J. W. Resonance scattering by atmospheric sodium—I. Theory of the intensity plateau in the twilight airglow. J. Atmos. Terr. Phys., **9**, Nos. 2/3, 73-89 (1956).

HAMBERLAIN, J. W., AND B. J. NEGAARD. Resonance scattering by atmospheric sodium—II. Nightglow theory. J. Atmos. Terr. Phys., **9**, No. 4, 169-178 (1956).

HVOJKOVÁ, E. Eigenschaften der Ionosphärischen *F*-Schicht II. Prague, Bull. Astron. Inst. Czechoslovakia, **7**, No. 5, 99-104 (1956).

LARK, C., AND A. M. PETERSON. Motion of sporadic-*E* patches determined from high-frequency backscatter records. Nature, **178**, 486-487 (Sept. 1, 1956). [Letter to Editor.]

ELOBEAU, F., ET K. SUCHY. L'absorption ionosphérique à Dakar. J. Atmos. Terr. Phys., **9**, No. 1, 45-50 (1956).

OMINICI, P. Comportamento della ionosfera a Roma durante l'eclisse parziale di sole del 30 giugno 1954. Ann. Geofis., Roma, **9**, No. 1, 107-131 (1956). [Abstract in English.]

ONAHUE, T. M. A calculation of the sodium dayglow intensity. J. Geophys. Res., **61**, No. 4, 663-666 (1956).

UNGEY, J. W. The effect of ambipolar diffusion in the night-time *F* layer. J. Atmos. Terr. Phys., **9**, Nos. 2/3, 90-102 (1956).

LLIS, G. R. On the propagation of whistling atmospherics. J. Atmos. Terr. Phys., **8**, No. 6, 338-344 (1956).

RITZOVÁ, L. A comparison of values of the air density gradient and original velocities of meteors obtained by different methods. Prague, Bull. Astron. Inst. Czechoslovakia, **7**, No. 5, 104-106 (1956).

ARTLEIN, C. W. The aurora borealis. Chief of Naval Operations for Polar Projects, U. S. Navy, Pub. No. OPNAV P03-6, 17 pp. (1956).

ARNISCHMACHER, E., ET K. RAWER. L'interprétation des observations du vent ionosphérique suivant la méthode des "fading." Paris, C.-R. Acad. sci., **243**, No. 9, 747-750 (1956).

ARNISCHMACHER, E., ET K. RAWER. Résultats d'observations systématiques du vent ionosphérique dans la région *E*. Paris, C.-R. Acad. sci., **243**, No. 9, 782-783 (1956).

NES, C. O. Electron resonance in ionospheric waves. J. Atmos. Terr. Phys., **9**, No. 1, 56-70 (1956).

NES, C. O. Diurnal variations in forward-scattered meteor signals. J. Atmos. Terr. Phys., **9**, No. 4, 229-232 (1956).

RONO, M., AND T. KITAMURA. A dynamo theory in the ionosphere. J. Geomag. Geoelectr., **8**, No. 1, 9-23 (1956).

KKYO, N. The scattering of electromagnetic waves by plasma oscillations. J. Geomag. Geoelectr., **8**, No. 1, 1-8 (1956).

NTEN, D. M. Resonance scattering by atmospheric sodium -III. Supplementary considerations. J. Atmos. Terr. Phys., **9**, No. 4, 179-183 (1956).

NTEN, D. M., F. E. ROACH, AND J. W. CHAMBERLAIN. A photometric unit for the airglow and aurora. J. Atmos. Terr. Phys., **8**, No. 6, 345-346 (1956).

CKSON, J. E., J. A. KANE, AND J. C. SEDDON. Ionosphere electron-density measurements with the Navy Aerobee-Hi rocket. J. Geophys. Res., **61**, No. 4, 749-751 (1956). [Letter to Editor.]

NES, A. V. Ca II emission lines in the twilight spectrum. Nature, **178**, 276-277 (Aug. 4, 1956). [Letter to Editor.]

TADIA, K. M. Sporadic echoes from the *E* region over Ahmedabad. J. Atmos. Terr. Phys., **8**, No. 6, 331-337 (1956).

EPECHINSKY, D. On the existence of a "Q.L."-"Q.T." "transition-level" in the ionosphere and its experimental evidence and effect. J. Atmos. Terr. Phys., **8**, No. 6, 297-304 (1956).

NDBLAD, B. A. Combined visual and radar observations of Perseid meteors. Göteborg, Medd. Lund Astr. Obs., Ser. I, No. 189, 98 pp. (1956).

Little, C. G., W. M. Rayton, and R. B. Roof. Review of ionospheric effects at VHF and UHF. Proc. Inst. Radio Eng., **44**, No. 8, 992-1018 (1956).

Lyon, A. J., and A. J. G. Moorat. Accurate height measurements using an ionospheric recorder. J. Atmos. Terr. Phys., **8**, No. 6, 309-317 (1956).

Mariani, F. Densita ellettronica in una ionsfera non isoterma. Ann. Geofis., Roma, **9**, No. 1, 43-62 (1956). [Abstract in English.]

Mariani, F. Temperatura e densità elettronica nella regione F della ionosfera. Ann. Geofis., Roma, **9**, No. 2, 245-271 (1956).

McNichol, R. W. E., H. C. Webster, and G. G. Bowman. A study of "spread-F" ionospheric echoes at night at Brisbane. I. Range spreading (experimental); II. Interpretation of range spreading. Aust. J. Phys., **9**, No. 2, 247-271 and 272-285 (1956).

Minnis, C. M. The effective recombination coefficients in the E and $F1$ layers during the solar eclipse of 25 February 1952. J. Atmos. Terr. Phys., **9**, No. 1, 36-44 (1956).

Minnis, C. M., G. H. Bazzard, and H. C. Bevan. Ionospheric changes associated with the solar event of 23 February 1956. J. Atmos. Terr. Phys., **9**, No. 4, 233-234 (1956). [Research note.]

Morel-Viard, J. Luminosité aurorale produite par des protons de direction quelconque. Paris, C. R. Acad. sci., **243**, No. 3, 292-295 (1956).

Omholt, A. Characteristics of auroras caused by angular dispersed protons. J. Atmos. Terr. Phys., **9**, No. 1, 18-27 (1956).

Omholt, A. Secondary processes due to absorption of the Lyman lines emitted from aurorae. J. Atmos. Terr. Phys., **9**, No. 1, 28-35 (1956).

Ratcliffe, J. A. Some aspects of diffraction theory and their application to the ionosphere. Rep. Progr. Phys., **19**, 188-267 (1956). [Pub. by Physical Society, London.]

Saha, A. K. On the determination of electron density distribution in the ionospheric regions from $h' - f$ records. Indian J. Phys., **30**, No. 9, and Proc. Indian Assoc. Cultivation Science, **41**, No. 9, 464-479 (1956).

Sales, G. S. A summarization of turbulence and ionospheric "wind" measurement theories with application of the latter to preliminary data at 75 kc/s. Pennsylvania State University, Ionosphere Res. Lab., Sci. Rep. No. 88, 113 pp., mim. (Aug. 1, 1956).

Sarma, N. V. G., and A. P. Mitra. Some aspects of the geomagnetic distortion of the F_2 region at equatorial latitudes. J. Sci. Industr. Res., New Delhi, B, **15**, No. 6, 320-322 (1956). [Letter to Editor.]

Satyanarayana, R., K. Bakhru, and S. R. Khastgir. Polarization of the echoes from the E_s and F regions. J. Sci. Industr. Res., New Delhi, B, **15**, No. 7, 331-339 (1956).

Scrimger, J. A., and D. M. Hunten. Observation of atmospheric sodium in absorption. Nature, **178**, 753-754 (Oct. 6, 1956).

Sengupta, P. K. Origin of the zodiacal light and the variation of its brightness. Indian J. Phys., **30**, No. 6, and Proc. Indian Assoc. Cultivation Science, **40**, No. 6, 285-291 (1956).

Sinno, K. On the radio propagation disturbances. J. Radio Res. Lab. Japan, **3**, No. 13, 155-160 (1956).

Skinner, N. J., and R. W. Wright. Equatorial ionospheric absorption. J. Atmos. Terr. Phys., **9**, Nos. 2/3, 103-117 (1956).

Störmer, C. The polar aurora. Clarendon Press, Oxford, xix + 403 + 216 figs. + 34 pls. (1955). [International Monographs on Radio.]

Szendrei, M. E., and M. W. McElhinny. Recombination and attachment in the $F1$ and $F2$ layers during the solar eclipse of 25 December 1954. J. Atmos. Terr. Phys., **9**, Nos. 2/3, 118-130 (1956).

Thomas, J. A. Sporadic E at Brisbane. Aust. J. Phys., **9**, No. 2, 228-246 (1956).

Vassy, E. Physique de l'atmosphère. Tome I—Phénomènes d'émission dans l'atmosphère. Paris, Gauthier-Villars, I, vi + 338 (1956). [Contains chapters on structure of the atmosphere, aurora, night sky light, corpuscular emission phenomena, meteorites, and lightning.]

Vegard, L. Composition, variations and excitation of the auroral luminescence spectra. Norske Vid.-Akad., Oslo, Geofys. Pub., **19**, No. 9, 51 pp. + pls. (1956).

Wait, J. R. The amplitude and phase of the low frequency ground wave near a coast line. Boulder, Colo., Nation. Bur. Stan., NBS Rep. No. 5014, 10 pp. + 2 figs., mim. (Aug. 31, 1956).

Wait, James R. On the mode theory of V.L.F. ionospheric propagation. Boulder Laboratories. Nation. Bur. Stan., NBS Rep. No. 5022, 18 pp., mim. (Oct. 10, 1956).

Wait, J. R., and A. Murphy. Multiple reflections between the earth and the ionosphere in V.L.F. propagation. Nation. Bur. Stan., Boulder, NBS Rep. No. 5019, 11 pp. + 8 figs., mim. (Sept. 14, 1956).

Wark, D. Q. A determination of the line-width of the λ6300 line of oxygen in the twilight sky. Nature, **178**, 689-691 (Sept. 29, 1956). [Letter to Editor.]

E—*Radio Astronomy*

Baldwin, J. E. A survey of the integrated radio emission at a wave-length of 3.7 m. Mon. Not. R. Astr. Soc., **115**, No. 6, 684-689 (1956).

Baldwin, J. E. The distribution of the galactic radio emission. Mon. Not. R. Astr. Soc., **115**, No. 6, 690-700 (1956).

Baldwin, J. E., and F. G. Smith. Radio emission from the extragalactic nebula M87. Observatory, **76**, No. 893, 141-144 (1956).

Bok, B. J. A national radio observatory. Sci. Amer., **195**, No. 4, 56-64 (1956).

Bracewell, R. N. Strip integration in radio astronomy. Aust. J. Phys., **9**, No. 2, 198-217 (1956).

Ellis, G. R. On the propagation of radio waves through the upper ionosphere. J. Atmos. Terr. Phys., **9**, No. 1, 51-55 (1956).

Hanbury Brown, R., H. P. Palmer, and A. R. Thompson. Polarization measurements on three intense radio sources. Mon. Not. R. Astr. Soc., **115**, No. 5, 487-492 (1956).

Hauge, Ø. Statistical investigations of solar radio bursts on 200 Mc/s. Astroph. Norvegia, **5**, No. 8, 227-240 (1956).

Lamden, R. J., and A. C. B. Lovell. The low frequency spectrum of the Cygnus (19N4A) and Cassiopeia (23N5A) radio sources. Phil. Mag., Ser. 8, **1**, No. 8, 725-737 (1956).

Marshall, L. Production of the sun's non-thermal radio emission by Čerenkov radiation. Astroph. J., **124**, No. 2, 469-475 (1956).

Mills, B. Y. The radio source near the galactic centre. Observatory, **76**, No. 891, 65-67 (1956).

Mills, B. Y., A. G. Little, and K. V. Sheridan. Emission nebulae as radio sources. Aust. J. Phys., **9**, No. 2, 218-227 (1956).

Müller, H. Über die Randverdunkelung der radiofrequenten Sonnenstrahlung. Zs. Astroph., **39**, 160-187 (1956).

Ryle, M. Radio galaxies. Sci. Amer., **195**, No. 3, 205-220 (1956).

Tandon, J. N. Radio Astronomy. Science and Culture, **22**, No. 1, 4-11 (1956).

Williams, D. R. W., and R. D. Davies. The measurement of the distance of radio sources by interstellar neutral hydrogen absorption. Phil. Mag., Ser. 8, **1**, No. 7, 622-636 (1956).

F—*Earth's Crust and Interior*

Ahrens, L. H., K. Rankama, and S. K. Runcorn (Eds.). Physics and chemistry of the earth, McGraw-Hill Book Co., Inc., New York, 317 pp. (1956). 23 cm. [Progress Series in Physics and Chemistry of the Earth.]

Aldrich, L. T., G. W. Wetherill, and G. L. Davis. Determinations of radiogenic Sr^{87} and Rb^{87} of an interlaboratory series of lepidolites. Geochim. et Cosmochim. Acta, **10**, No. 4, 238-240 (1956). [Geochemical note.]

Beck, A., J. C. Jaeger, and G. Newstead. The measurement of the thermal conductivities of rocks by observations in bore holes. Aust. J. Phys., **9**, No. 2, 286-296 (1956).

de Sitter, L. U. The strain of rock in mountain-building processes. Amer. J. Sci., **254**, No. 10, 585-604 (1956).

Deutsch, S., F. G. Houtermans, et E. E. Picciotto. Étude de la radioactivité de météorites métalliques par la méthode photographique. Geochim. et Cosmochim. Acta, **10**, No. 3, 166-184 (1956).

Egyed, L. Determination of changes in the dimensions of the earth from paleographic data. Nature, **178**, 534 (Sept. 8, 1956). [Letter to Editor.]

Forester, R. D. SKP and related phases. Bull. Seis. Soc. Amer., **46**, No. 3, 185-201 (1956).

GUTENBERG, B. Great earthquakes 1896-1903. Trans. Amer. Geophys. Res., **37**, No. 5, 608-614 (1956).

GUTENBERG, B., J. P. BUWALDA, AND R. P. SHARP. Seismic explorations on the floor of Yosemite Valley, California. Bull. Geol. Soc. Amer., **67**, No. 8, 1051-1078 (1956).

GUTENBERG, B., AND C. F. RICHTER. Magnitude and energy of earthquakes. Ann. Geofis., Roma, **9**, No. 1, 1-15 (1956).

HERZOG, L. F., AND W. H. PINSON, JR. Rb/Sr age, elemental and isotopic abundance studies of stony meteorites. Amer. J. Sci., **254**, No. 9, 555-566 (1956).

JEFFERY, P. M. The radioactive age of four Western Australian pegmatites by the potassium and rubidium methods. Geochim. et Cosmochim. Acta, **10**, No. 3, 191-195 (1956).

KASAHARA, K. Strain energy in the visco-elastic crust. Bull. Earthquake Res. Inst., Tokyo Univ., **34**, Pt. 2, 157-165 (1956).

KEMP, W. R. G., P. G. KLEMENS, AND G. K. WHITE. Thermal and electrical conductivities of iron, nickel, titanium, and zirconium at low temperatures. Aust. J. Phys., **9**, No. 2, 180-188 (1956).

PATTERSON, C. Age of meteorites and the earth. Geochim. et Cosmochim. Acta, **10**, No. 4, 230-237 (1956).

ST. AMAND, P. Two proposed measures of seismicity. Bull. Seis. Soc. Amer., **46**, No. 1, 41-45 (1956).

WESSERBURG, G. J., R. J. HAYDEN AND K. J. JENSEN. A^{40}-K^{40} dating of igneous rocks and sediments. Geochim. et Cosmochim. Acta, **10**, No. 3, 153-165 (1956).

G—*Miscellaneous*

BABCOCK, H. W. The sun's general magnetic field. Nature, **178**, 533 (Sept. 8, 1956). [Letter to Editor.]

BLACKWELL, D. E. A study of the outer corona from a high altitude aircraft at the eclipse of 1954 June 30. Mon. Not. R. Astr. Soc., **115**, No. 6, 629-649 (1956).

BYRAM, E. T., T. A. CHUBB, H. FRIEDMAN, AND J. E. KUPPERIAN, JR. Observations of the intensity of solar Lyman-alpha emission. Astroph. J., **124**, No. 2, 480-482 (1956). [Note.]

CHOVITZ, B., AND I. FISCHER. A new determination of the figure of the earth from arcs. Trans. Amer. Geophys. Union, **37**, No. 5, 534-545 (1956).

DAUVILLIER, A. L'origine des planètes (essai de cosmogonie). Presses Universitaires de France, Paris, 224 pp. (1956).

FERRARO, V. C. A., AND P. C. KENDALL. On azimuthal solar magnetic fields. Astroph. J., **124**, No. 2, 443-446 (1956).

GOLD, T. High-energy particles in solar flares. Nature, **178**, 487 (Sept. 1, 1956). [Letter to Editor.]

JEFFERIES, J. T. The $H\alpha$ emission of prominences. Mon. Not. R. Astr. Soc., **115**, No. 6, 617-628 (1956).

PAGE, R. M. Cosmological theories—ancient and modern. J. Wash. Acad. Sci., **46**, No. 8, 244-252 (1956).

PRZYBYLSKI, A. A variational method for improving model stellar atmospheres. Mon. Not. R. Astr. Soc., **115**, No. 6, 650-660 (1956).

SCOTT, W. E. John Adam Fleming, 1877-1956. J. Geophys. Res., **61**, No. 4, 589-592 (1956).

SCOTT, W. E. List of recent publications. J. Geophys. Res., **61**, No. 4, 759-767 (1956).

WALDMEIER, M. Die Variation der monochromatischen Gesamtemission der Sonnenkorona im 11 jährigen Zyklus. Zs. Astroph., **39**, 219-231 (1956).

WALDMEIER, M. Provisional sunspot-numbers for July to September, 1956. J. Geophys. Res., **61**, No. 4, 744 (1956).

WHIPPLE, F. L. The scientific value of artificial satellites. J. Frank. Inst., **262**, No. 2, 95-109 (1956).

WILSON, J. T. Geophysics. Chief of Naval Operations for Polar Projects, U. S. Navy, Pub. No. OPNAV P03-21, 11 pp. (1956).

WOOD, M. B. A study of magnetic maps of the sun. Astroph. J., **124**, No. 2, 447-450 (1956).

ZIRIN, H. The temperature and equilibrium of hydrogen in solar prominences. Astroph. J., **124**, No. 2, 451-460 (1956).

NOTICE

When available, single unbound volumes can be supplied at $6 each and single numbers at $2 each, postpaid.

Charges for reprints and covers

Reprints can be supplied, but prices have increased considerably and costs depend on the number of articles per issue for which reprints are requested. It is no longer possible to publish a schedule of reprint charges, but if reprints are requested approximate estimates will be given when galley proofs are sent to authors. Reprints without covers are least expensive; standard covers (with title and author) can be supplied at an additional charge. Special printing on covers can also be supplied at further additional charge.

Fifty reprints, without covers, will be given to institutions paying the publication charge of $8 per page.

Alterations

Major alterations made by authors in proof will be charged at cost. Authors are requested, therefore, to make final revisions on their typewritten manuscripts.

Orders for back issues and reprints should be sent to Editorial Office, 5241 Broad Branch Road, N.W., Washington 15, D. C., U.S.A.

Subscriptions are handled by The Editorial Office, 5241 Broad Branch Road, N.W., Washington 15, D. C., U.S.A.

CONTENTS—Concluded